



HAL
open science

CO₂ photocatalytic conversion through porous monoliths

Sophie Bernadet

► **To cite this version:**

Sophie Bernadet. CO₂ photocatalytic conversion through porous monoliths. Other. Université de Bordeaux, 2018. English. NNT : 2018BORD0172 . tel-02000296

HAL Id: tel-02000296

<https://theses.hal.science/tel-02000296>

Submitted on 1 Feb 2019

HAL is a multi-disciplinary open access archive for the deposit and dissemination of scientific research documents, whether they are published or not. The documents may come from teaching and research institutions in France or abroad, or from public or private research centers.

L'archive ouverte pluridisciplinaire **HAL**, est destinée au dépôt et à la diffusion de documents scientifiques de niveau recherche, publiés ou non, émanant des établissements d'enseignement et de recherche français ou étrangers, des laboratoires publics ou privés.

THÈSE PRÉSENTÉE
POUR OBTENIR LE GRADE DE
DOCTEUR DE
L'UNIVERSITÉ DE BORDEAUX

ÉCOLE DOCTORALE DE SCIENCES CHIMIQUES
SPÉCIALITÉ PHYSICO-CHIMIE DE LA MATIÈRE CONDENSÉE

Par Sophie BERNADET

**Conversion photocatalytique du CO₂
sur monolithe poreux**

Sous la direction de : Rénal BACKOV
(co-directeur : Serge RAVAINÉ)

Soutenue le 30 Novembre 2018

Membres du jury :

Mme ZAKRI, Cécile
M. BOISSIERE, Cédric
M. GARCIA, Hermenegildo
Mme LACOMBE, Sylvie
M. VALLEE, Renaud
M. FECANT, Antoine

Professeure, CNRS/CRPP
Directeur de Recherche, CNRS/UPMC
Professeur, Univ. Valencia/ICT
Directrice de Recherche, CNRS/IPREM
Directeur de Recherche, CNRS/CRPP
Ingénieur de Recherche, IFPEN

Présidente
Rapporteur
Rapporteur
Examinatrice
Invité
Invité

« Entre
Ce que je pense
Ce que je veux dire
Ce que je crois dire
Ce que je dis
Ce que vous avez envie d'entendre
Ce que vous croyez entendre
Ce que vous entendez
Ce que vous avez envie de comprendre
Ce que vous croyez comprendre
Ce que vous comprenez
Il y a dix possibilités qu'on ait des difficultés à communiquer.

Mais essayons quand même... »

L'encyclopédie du savoir relatif et absolu

Bernard Werber

Remerciements

Tout d'abord, je tiens à remercier la Professeure Cécile Zakri (Directrice du Centre de Recherche Paul Pascal, CRPP), M. Luc Nougier (Directeur de la direction Catalyse, Biocatalyse et Séparation, IFP Energies Nouvelles) et M. Tivadar Cseri (Directeur du département CATalyse par les Métaux et les solides Acido-Basiques, CATMAB, IFP Energies Nouvelles) pour m'avoir permis d'intégrer leur laboratoire pendant ces années de thèse.

J'adresse mes vifs remerciements aux Professeur Hermenegildo Garcia et Directeur de Recherche Cédric Boissière pour avoir accepté et pris le temps de juger mes travaux de thèse en la qualité de rapporteur, ainsi qu'à la Professeure Cécile Zakri pour avoir présidé le jury lors de ma soutenance, et la Directrice de Recherche Sylvie Lacombe pour avoir été examinatrice.

Je souhaite également exprimer ma gratitude envers les différents collaborateurs de ce projet pour leur investissement dans les travaux réalisés ainsi que les échanges constructifs qui ont eu lieu. D'une part, Sylvie Lacombe et Mickael Le Behec, de l'Institut des Sciences Analytiques et de Physico-Chimie pour l'Environnement et les Matériaux (IPREM) de l'Université de Pau, pour avoir appliqué les matériaux synthétisés à la photopurification de l'air, et ouvrir ainsi leur champ d'application. Par ailleurs, le Professeur Renaud Vallée et le doctorant Duc-Minh Ta, du CRPP, pour les mesures quantitatives de pénétration des photons au sein de ces matériaux synthétisés, apportant une preuve de concept.

Je tiens à remercier chaleureusement mes encadrants : les Professeurs Serge Ravaine (L'Avant-gardiste) et Rénal Backov (L'Optimiste), et le Docteur Antoine Fécant (Le Pragmatique). Ce trio forme une AOP équipe de travail des plus performantes dans la concrétisation de projet innovant d'envergure. Travailler à leur côté m'a permis d'évoluer autant d'un point de vue scientifique, que personnel, et je leur en suis extrêmement reconnaissante. Leur ambition, leur savoir, et leur rigueur m'ont énormément inspiré.

Au cours de ma première année de thèse effectuée au sein du CRPP, j'ai eu l'opportunité de recevoir beaucoup d'aide permettant de faire avancer mes travaux de thèse.

Tout d'abord, je tiens à remercier les stagiaires qui ont travaillé autour de ce projet comme Alexandre Dubouil, ou d'autres que j'ai eu l'opportunité d'encadrer : Aurélie Boulot, Marina Koleski,

Remerciements

Maxime Teixeira, et Raphaël Schrader. Merci à vous tous pour vos travaux et votre contribution dans ce projet.

Un grand merci particulier à Stéphanie Exiga pour son travail sur la synthèse de monolithes, son soutien quotidien, ses anecdotes et sa bonne humeur. Merci également aux autres membres de la cellule chimie qui m'ont aidé et soutenu Frédéric Louerat, Xavier Brilland, et Mbolotiana Rajaoarivelo.

Merci à Armand, co-doctorant (et maintenant Docteur, Félicitations !) sous la direction du Professeur Rénal Backov, avec qui j'ai commencé cette aventure et partagé un grand nombre de bons moments au laboratoire et dans les bars de Bordeaux.

Je souhaite également remercier toutes les personnes que j'ai côtoyé et qui permettent au laboratoire de fonctionner, comme l'administration et service comptabilité avec Corinne Amengual, Caroline Legrand, Béatrice Dupin, Elisabeth Hortolland et Evangéline Lounissi ; le service informatique avec Sandrine Maillet, Jean-Luc Laborde et Philippe Hortolland ; l'atelier avec Philippe Barboteau et Emmanuel Texier ; le service bâtiment avec Lionel Chevalier et Stéphane Bechemin ; mais également, Lionel Buisson et Pascal Merzeau à l'instrumentation ; Ahmed Bentaleb, Annie Février, Eric Laurichesse, Isabelle Ly et Hassan Saadaoui à la plateforme technique ; Emmanuelle Hamon à la cellule Transform ; et Béatrice Huynh-Tan et Nathalie Touzé à l'accueil. Merci particulièrement à Isabelle Ly et Christine Picard pour leur formation aux microscopes électroniques.

Un merci tout particulier à Nadine Laffargue, ma co-bureau et bibliothécaire du CRPP, dont la vie est si tumultueuse qu'on pourrait en écrire un livre « Les malheurs de Nadine ». Merci pour ton écoute constante, ta rage de vivre, ton franc parlé et tes conseils. Tu resteras une image forte de ma thèse ! Merci également à Eric Laurichesse, Emmanuelle Hamon, Véronique Schmitt et Nadine pour les discussions enflammées que l'on a pu avoir les midis durant mon stage de Master 1. De cette période de stage, je retiens également les amis formidables que je me suis fait : Céline Hubert et Christophe Coutant, avec qui je passe encore de fabuleux moments.

Merci à Manou (Emmanuel Suraniti), avec qui j'ai pu partager quotidiennement cette année de thèse, et qui a fait preuve d'une écoute exceptionnelle et d'un soutien sans faille. Il a toujours su m'encourager et me faire part de ses conseils avisés. Je ne pourrais jamais assez te remercier !

J'aimerais également remercier toutes les personnes qui, dans d'autres laboratoires voisins du CRPP, ont participé à l'avancée de ces travaux de thèse, à commencer par Sonia Buffière et Eric Lebraud de l'ICMCB/Placamat ; et Marc Birot et Marie-Anne Dourges de l'ISM.

En début de deuxième année, j'ai rejoint IFP Energies Nouvelles, dans le département CATMAB de façon définitive et ai alors pu évoluer au jour le jour au contact de gens exceptionnels.

Tout d'abord, je souhaite exprimer ma profonde gratitude et adoration envers Eugénie Tavernier, qui a partagé mon quotidien et dont le soutien sans faille m'a permis d'arriver jusqu'au bout

Remerciements

de cette aventure. Ton pragmatisme indéniable, ta détermination sans égale, et ta douceur maternelle resteront des vertus modèles à mes yeux. Merci pour tout ce que tu m'as apporté !

Un grand merci à Audrey Bonduelle, qui a suivi et contribué à l'avancée des travaux, et avec qui j'ai pu avoir de longues conversations enrichissantes.

Je souhaite remercier toutes les personnes du département, et plus, que j'ai côtoyé et qui ont illuminé mes journées : Carine Guégan, Carine Chollet, Clara Mancia, Romain Chenevier, Adrien Berliet, Marie Velly, Laurent Renaudot, Charles Leroux, Cédrik Popelin, Margauld Chancerel, Sophie Bailly, Brigitte Pigeat, Pascal Galguen, Delphine Marti, Sylvie Lacombe, Malika Boualleg, Amandine Cabiac, Vincent Coupard, Céline Chizallet.

Merci aussi à toutes les personnes du département Physique et Analyse, pour leur expertise, leur patience face à ces matériaux complexes, et leur constante bonne humeur : Hedwige Poncet, Anne-Lise Taleb, Florian Moreau, Véronique Lefebvre, Yannick Blouet, Sylvie Massot-Jeudy, Christian Tracol, Carole Bobin, Marine Collaudin, Nathalie Crozet, Isabelle Cléménçon, Olivier Delpoux, Thomas Coquet, Sébastien Selles, Nathalie Texier, Sylvain Carbonneaux, Denis Gasquet, Denis Roux, Nicolas Girod (« Cette technique marche pour l'immense majorité des échantillons, SAUF les tiens »), et Jérémy Gajan. Ce fût un réel plaisir de travailler avec vous !

Je souhaite également remercier Patrice Arzac pour avoir effectué, toujours avec le sourire, les multiples travaux dans le laboratoire pour que le μ GC se sente bien et soit performant, et à Victor Lameiras Franco Da Costa pour sa contribution à l'élaboration du modèle cinétique. Merci à Nathalie Farrenq et Marie-Claude Beaufile, pour leur assistance et leur disponibilité.

Un merci tout particulier à Charlotte Loustau Cazalet (alias Chachou) qui a été un pilier d'exception pendant ces trois années, et ce, depuis notre rencontre dans un bus avec Kévinou. Ton ingéniosité, ton optimisme et ton soutien constant ont fait de nos pauses une vraie bouffée d'air frais. Merci également à Dina Lofficial (alias Dinou), ex-doctorante en photocatalyse, qui m'a apporté ses connaissances de chercheuse en la matière, et bien plus. Ton charisme, ta fonce-attitude, et ton soutien m'ont permis d'affronter les moments les plus durs de cette thèse avec légèreté. Je suis chanceuse de vous compter parmi mes amis !

Merci également à tous les autres doctorants qui ont partagé mon quotidien : Angélique et Damien, rabatteurs pour le déjeuner ; Ana Theresa (mon petit rayon de soleil) et Ester, mes co-bureau ; et tous les autres (dont certains sont Docteur à présent), Kévin, Carole, Lina, Joël, Alexis, Adrien, Paulo, Etienne, Emile, Cora, Caro, Ana Rita, Marisa, Céline, Julie, Audrey, Larissa, ...

Je tiens à adresser mes remerciements les plus sincères aux membres de ma famille :
À toi, Mamounette, qui a toujours su tirer le meilleur de moi et m'accompagner dans les épreuves de ma vie sans jamais douter de mes compétences et mes qualités, je t'en serai éternellement reconnaissante. J'espère te montrer aujourd'hui que tous les efforts que tu as fournis pour m'élever,

Remerciements

m'apporter tout ce dont j'ai besoin, et me fournir les armes pour voler de mes propres ailes, ont servi. Je te dois cette réussite !

À toi, Patou, mon modèle ... C'est grâce à toi que j'ai eu l'ambition de faire une thèse. Ta force, ta patience, ta détermination et ton intelligence m'ont guidé tout au long de ces trois ans. Je suis honorée de partager le grade de Docteur avec toi ! À Augustin et Mathilde, ces merveilleux enfants qui égailent notre famille, et dont les photos m'ont donné le sourire chaque jour !

À toi, Papounet, pour ton aide inépuisable, tes précieux conseils, ton perfectionnisme à toute épreuve, ta disponibilité malgré la préparation chronophage de ta certification, ton expertise certifiée et ton soutien. Merci d'être frère de moi !

À toi, Mida, pour ton soutien, ta compréhension, tes conseils, et tous ces moments complices. Hvala vam što ste bili deo moje porodice !

À mes grands-parents, inconditionnellement fiers de leur petits-enfants. Merci !

À Antje, plus proche que jamais !

À ma belle-famille, Sylvie, Luigi, Loré, Julien, Lana, Valentin, Chris, Mathilde, et Guido, pour faire partie de ma vie, m'avoir soutenu, et me partager vos moments familiaux si ressourçant.

À Bryan, pour avoir partagé 5/6 de ma vie de thésarde, et avoir tenu bon. Merci pour ta patience face à mes longues histoires de problèmes de paillasse, ta contribution à la thèse en confectionnant des outils plus pratiques pour poncer et mesurer mes monolithes, ton attention lors des répétitions improvisées de communications orales, ta persévérance pour te rappeler de tous les noms de mes collègues, ta présence à la pause-café de l'autre côté du grillage pour se voir 5 minutes dans la journée, ton aide pour sortir du lit les matins de réveil tôt, ton soutien quotidien, ta joie de vivre communicative, ton admiration, ton amour. J'ai hâte de vivre avec toi, tous ces bons moments qui nous attendent !

À Papi Michel, Alain, et Joël, partis trop tôt...

Résumé

L'augmentation de la teneur en dioxyde de carbone (CO₂) dans l'atmosphère et l'épuisement des ressources énergétiques fossiles nécessitent une réaction sociétale urgente face à un dérèglement climatique planétaire effectif, tout en assurant l'approvisionnement futur en énergie.

En chiffres, la concentration actuelle en CO₂ dans l'atmosphère est de 411 ppm (au 21 avril 2018 ¹), laquelle dépasse largement sa fluctuation naturelle, entre 180 et 300 ppm, sur les 800 000 dernières années ². D'un point de vue énergétique, la consommation mondiale d'énergie devrait passer de 15-17 TW en 2010 ³ à 25-27 TW en 2050 ⁴, soit une augmentation de 47 à 80% en quarante ans. En 2017, 81% de la demande totale en énergie était fournie par l'utilisation de combustibles fossiles. Toutefois, la prise de conscience de la nécessité d'une transition énergétique vers une production bas-carbone existe puisqu'un quart de la production mondiale d'électricité est assurée par des énergies renouvelables, ce qui représente le taux de croissance en volume le plus élevé par rapport à toute autre source d'énergie en 2017 ⁵. Ces chiffres témoignent de l'effort qui doit être soutenu pour réduire cette forte dépendance aux combustibles fossiles, comme le souligne l'Agence internationale de l'énergie (AIE). En considérant le scénario de développement durable décrit dans World Energy Outlook 2017 ⁶, les sources d'énergie à faible émission de carbone doivent doubler leur part dans le bouquet énergétique pour atteindre 40% en 2040.

Parmi les sources d'énergies renouvelables déployées à grande échelle pour la production d'énergie électrique, on peut citer le solaire (panneaux photovoltaïques) et le vent (éoliennes). Ceux-ci convertissent l'irradiation solaire ou la force du vent en énergie électrique. Cependant, alors que nos sociétés passent de l'ère du tout pétrole à celle du zéro carbone, le stockage massif de l'énergie est le principal défi technologique auquel nous serons naturellement confrontées en raison de l'intermittence de ces sources. Les nouvelles technologies alternatives basées sur la conversion de l'électricité en énergie chimique sont au cœur de la recherche. En particulier, l'électrolyse de l'eau est un moyen envisageable de stocker l'électricité sous forme d'hydrogène. Afin d'éviter de superposer les étapes de conversion/transformation qui induisent nécessairement des pertes de rendements, des voies directes pour convertir l'énergie solaire en énergie chimique sont en phase de développement plus ou moins avancé selon les domaines et associé au processus de photosynthèse naturelle (biocarburants de 1^{ère}, 2^{ème} ou 3^{ème} génération) ou artificielle (photocatalyse pour la production d'hydrogène - le « *water splitting* » - ou la réduction du dioxyde de carbone en hydrocarbures). Dans ce projet de thèse, c'est la photoconversion du CO₂ qui sera l'objet de l'étude ; elle permet la production d'hydrocarbures à fort contenu énergétique en utilisant l'énergie solaire. Les hydrocarbures, qu'on imagine produits par

l'utilisation d'émissions anthropiques de CO₂, peuvent alors être utilisés comme combustibles pour produire de l'énergie. Cette consommation d'hydrocarbures appelés, « carburant solaires » (*solar fuel* en termes anglo-saxons) libère à nouveau du CO₂, qui pourra être réutilisé dans un nouveau procédé de photoconversion. Cela permettrait d'intégrer le CO₂ émis par la combustion de carburants dans un cycle global du carbone. Le CO₂ deviendrait un vecteur énergétique (dans la mesure où il serait disponible en quantité et bon marché) permettant de substituer l'utilisation de combustibles fossiles à celle des carburants solaires ⁷.

Le projet de thèse s'inscrit dans la thématique de la conversion directe du CO₂ par photocatalyse hétérogène. La photocatalyse a fait l'objet d'une attention considérable au cours des dernières années et a été utilisée dans un large éventail de domaines de recherche, notamment dans les domaines environnementaux, énergétiques et de chimie fine. En se basant sur la percée du « *water splitting* » rapportée par Fujishima et Honda en 1972 ⁸, les propriétés photocatalytiques de certains matériaux ont été utilisées pour convertir l'énergie solaire en énergie chimique, (c'est-à-dire en hydrogène et/ou en hydrocarbures ⁹), pour éliminer les polluants et bactéries sur les surfaces de matériaux, dans l'air ou l'eau. Parmi les nombreux photocatalyseurs, le TiO₂ a été le plus largement étudié et utilisé dans de nombreuses applications en raison de ses fortes capacités oxydantes pour la décomposition des polluants organiques, sa superhydrophilie, sa stabilité chimique, sa longue durabilité, sa non-toxicité et son faible coût.

Le processus global de la photocatalyse hétérogène consiste en une succession de processus complexes impliquant des étapes élémentaires se déroulant à la surface du matériau (adsorption des réactifs, diffusion, réaction des intermédiaires en surface et recombinaison en surface des charges photogénérées) et dans son volume (absorption des photons, génération, diffusion et recombinaison en volume). La complexité du mécanisme de la photocatalyse hétérogène révèle des limites que la communauté scientifique cherche à repousser le plus loin possible. Ces limitations peuvent être induites par l'effet d'écrantage, par des phénomènes d'adsorption ou par la recombinaison des porteurs de charge. Par conséquent, les performances catalytiques revendiquées dans la littérature pour la photoconversion du CO₂ ou plus largement la production de carburants solaires, sont encore éminemment faibles au regard de l'émergence des procédés à l'échelle industrielle. Aujourd'hui, même avec les meilleurs photocatalyseurs, les vitesses de conversion du CO₂ sont encore très faibles (de l'ordre de quelques dizaines à quelques centaines $\mu\text{mole}\cdot\text{h}^{-1}\cdot\text{g}^{-1}$) ⁷. La plupart des travaux mentionnés dans la littérature se concentrent sur la modification physico-chimique des semi-conducteurs afin d'améliorer l'utilisation des porteurs de charge photogénérés en minimisant le phénomène de recombinaison par des effets architecturaux spécifiques (hétérojonctions), l'addition de métal comme co-catalyseur, ou de dopants ^{10,11}. Bien que ces voies de recherche soient intéressantes et aient permis des avancées substantielles, une voie, qui reste très peu étudiée et constitue par conséquent un grand défi, concerne l'optimisation de la diffusion de flux de photons au sein du lit (photo)catalytique. En effet, les photocatalyseurs actuels se présentent sous forme de couche mince due à la faible pénétration des

photons dans la matière dense. Une amélioration de la diffusion des photons dans la profondeur du lit catalytique permettrait l'intensification du processus en volume et donc une réduction de l'empreinte au sol des futurs systèmes de production de carburants solaires.

Ainsi, le projet de thèse propose la mise en œuvre d'un photocatalyseur dans des matériaux tridimensionnels nommés HIPEs (High Internal Phase Emulsion)¹² pour répondre au défi de la collecte des photons. Ces matériaux tridimensionnels sont des monolithes à porosité hiérarchisée. La structure multi-échelles a fait ses preuves pour optimiser les propriétés de transport des matériaux. Le comportement du fluide est intrinsèquement hiérarchisée, alimentant efficacement les parois des macropores, qui peuvent accueillir la phase active^{13,14,15,16}. Au-delà de l'interaction avec les fluides, les structures poreuses ont également prouvé leur capacité à interagir avec la lumière. Par exemple, la distribution périodique et monodisperse en taille des pores confère aux cristaux photoniques la capacité de contrôler la pénétration des photons et de piéger la lumière¹⁷. Cependant, ces matériaux diffusent une seule longueur d'onde de la lumière liée à la taille des pores. Les éponges photoniques (« photonic sponge », en anglais) ont ensuite été introduites par Carbonell *et al.*¹⁸ pour favoriser la diffusion de la lumière dans une large région spectrale en raison de la composition polydisperse des particules ou des pores. Inspirés par le monde vivant, Zhou *et al.*¹⁹ ont reproduit l'architecture hiérarchique 3D des feuilles pour améliorer la multidiffusion de la lumière. L'objectif de ces structures est d'augmenter le temps de séjour des photons et leur profondeur de pénétration pour augmenter la probabilité de rencontre entre les photons et la phase active, et intensifier le processus photocatalytique. Lorsqu'elles sont purement inorganiques, ces mousses HIPEs ont récemment été utilisées comme capteurs de lumière dans le domaine des lasers aléatoires^{20,21} où du TiO₂ a été ajouté pendant le processus sol-gel pour augmenter l'indice de réfraction du squelette inorganique, optimisant ainsi le libre parcours moyen de transport des photons dans les mousses²².

En d'autres termes, la thèse vise à étudier les systèmes photocatalytiques composés de semi-conducteurs dispersés dans des monolithes à porosité hiérarchisée, pour la réduction du dioxyde de carbone en présence d'eau, en tant qu'agent sacrificiel. Un des avantages potentiels de ces solides réside dans la multiplication des interfaces de contact réactives (CO₂ et photons)-semi-conducteur, en volume et non plus sur une surface, et donc dans une meilleure collecte/diffusion de la lumière dans le matériau.

Le premier chapitre présente un état de l'art des principes et des approches en recherche dans le domaine de la photocatalyse (et plus particulièrement en photoréduction du dioxyde de carbone), la compréhension des interactions entre la lumière et la matière, ainsi que le domaine des outils de la chimie intégrative utilisés dans la synthèse des architectures poreuses. D'après cette étude bibliographique, les méthodes chimiques tels que l'ajout d'un co-catalyseur métallique, le dopage à l'azote ou le mélange de phases cristallines du TiO₂ permettent de repousser les limites de la photocatalyse par une meilleure séparation de phase et/ou une extension de la collecte des photons à la part du visible du spectre solaire. De plus, structurer la mésoporosité et la macro-porosité d'un catalyseur ou d'un support de catalyseur semble constituer une approche physique intéressante pour améliorer le

Résumé

rendement énergétique des procédés photocatalytiques. Cet effet de porosité souligne l'importance de son rôle dans les interactions lumière-matière. Pour décrire la propagation de la lumière dans un matériau, la théorie de la diffusion constitue un outil mathématique très utile, notamment par la détermination du libre parcours moyen de transport des photons au sein des matériaux.

Le chapitre II détaille les protocoles de synthèse des matériaux étudiés au cours du projet, les différentes techniques de caractérisation physico-chimique utilisées, ainsi que le montage de l'unité de tests et les quantités utilisées pour l'évaluation des performances photocatalytiques. Les matériaux poreux synthétisés et mis en œuvre dans le cadre de ces travaux, nommés $\text{TiO}_2@\text{Si}(\text{HIPE})\text{s}$, sont obtenus par les effets synergiques de gabarits des mésophases lyotropes (micelles concentrées) du TTAB (Trimethyl(Tetradecyl)Amonium Bromide) qui créent la mésoporosité (diamètres des pores de 2 nm à 50 nm) et d'émulsions directes concentrées du dodécane induisant la macroporosité connectée (diamètres des pores supérieurs à 50 nm), combinés au procédé sol-gel qui condense la phase hydrophile continue à base de TEOS (TetraEthylOrthoSilicate). Comme le squelette inorganique est constitué de silice amorphe, la microporosité (diamètre des pores inférieur à 2 nm) repose sur la répartition statistique de tétraèdres de SiO_4 dans l'espace géométrique. Ainsi, l'utilisation de l'émulsion comme gabarit souple pour la genèse des matériaux macrocellulaires fournit une forte porosité hiérarchique, en particulier une macrostructure auto-supportée de forme modulable. En raison de son faible coût, de sa stabilité chimique, de ses performances photocatalytiques et de ses propriétés physico-chimiques, le TiO_2 est la phase active utilisée dans ce projet et incorporée à la structure par imprégnation d'un précurseur, le TTIP (Titanium isopropoxide). Pour comprendre le comportement de ces matériaux par rapport à la photoréduction du CO_2 , et pour mettre en relation les performances obtenues avec leurs propriétés physico-chimiques, un ensemble de caractérisations multi-échelles a été mis en œuvre. Les macropores permettent d'abaisser considérablement les gradients de pression à l'intérieur de la structure, assurant ainsi l'intégrité du matériau lorsque des fluides y circulent. Cette propriété est essentielle lors de l'imprégnation du TiO_2 . Ainsi, ces macropores ont été visualisés et caractérisés par MEB (Microscopie Electronique à Balayage) et par porosimétrie à intrusion de mercure. La distribution du TiO_2 dans la matrice de silice a été évaluée par microsonde de Castaing et observée par MEB et MET (Microscopie Electronique à Transmission). Les micro- et méso-structures sont le lieu où se produisent l'adsorption, la désorption et les réactions. Il est donc important de connaître la structure des matériaux à ces échelles. A cet effet, les analyses par spectrométrie de Fluorescence des rayons X (FX), MET, diffraction des rayons X (DRX) et spectroscopie en réflectance diffuse UV-Visible ont permis de quantifier et caractériser la phase active, tandis que la physisorption de l'azote permettait de déterminer la surface spécifique développée. La porosité hiérarchique du matériau joue un rôle clé dans la diffusion multiple de la lumière, tout comme l'indice de réfraction des diffuseurs. Ainsi, le libre parcours moyen de transport des photons a été évalué par une méthode laser pulsée. L'évaluation du comportement des matériaux synthétisés et de la poudre commerciale de TiO_2 P25 vis-à-vis de la photoréduction du CO_2 a été réalisée sur l'installation schématisée Figure 1. Les paramètres importants sont que les essais

Résumé

photocatalytiques ont été effectués à température ambiante, à pression atmosphérique et en conditions anaérobies. Les principales quantités utilisées dans l'évaluation de la performance photocatalytique étaient la vitesse moyenne de consommation d'électrons photogénérés normalisé par unité de masse ou de surface irradiée et la sélectivité moyenne envers les produits détectés par chromatographie en phase gazeuse.

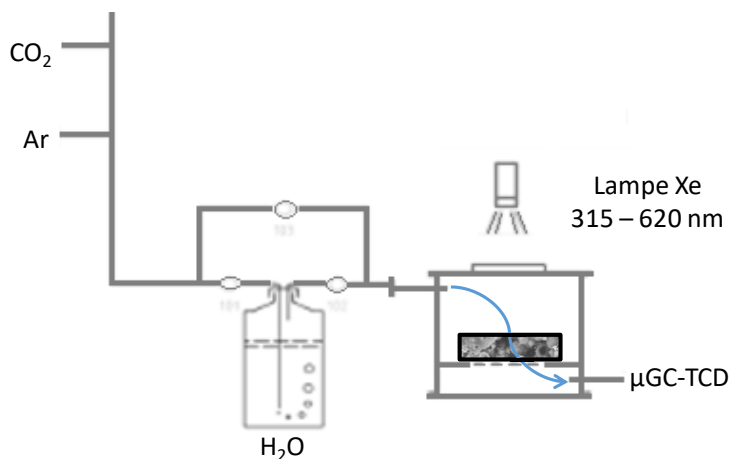


Figure 1: Représentation schématique du montage utilisé pour les tests photocatalytiques

Les propriétés physico-chimiques des matériaux auto-supportés (Figure 2 A) sont décrites dans le chapitre III et discutées vis-à-vis de la modification de différents paramètres de synthèse. Les Si(HIPE)_s et TiO₂@Si(HIPE)_s présentent une porosité élevée (de 70 à 90%), avec une grande proportion de micro et macropores. Les micropores fournissent une taille caractéristique principalement inférieure à 1 nm et polydispense. Les macropores sont décrits par des caractères polydispenses et bimodaux, la taille des pores s'étendant d'environ 10 nm à quelques microns (Figure 2 B). Les pores sont reliés par des fenêtres cellulaires internes de centaines de nanomètres, et l'agrégation des sphères creuses de silice forme des fenêtres cellulaires externes de quelques microns (Figure 2 C). De plus, la structure silicique de type vermiculaire a été induite par l'arrangement de la phase mésoscopique (les micelles de tensio-actifs, Figure 2 D). L'imprégnation du TiO₂ implique un blocage des micropores induit par la nucléation hétérogène du TiO₂ sur les mésopores et/ou les micropores (Figure 2 E), et une réduction de moitié de la surface BET (d'environ 1000 à 500 m².g⁻¹). Pour des raisons de reproductibilité et de répétabilité, un monolithe (Si(HIPE) et/ou TiO₂@Si(HIPE)) par lot a été consacré à la réalisation des caractérisations représentatives de chaque lot. Les méthodes d'imprégnation ont un fort impact en fonction du type I (en une étape) ou II (en deux étapes) sur les phases cristallines du TiO₂. La raison principale en est très probablement la création de liaisons Ti-O-Si promues par la méthode d'imprégnation en deux étapes, qui influencent la cristallisation et bloquent le TiO₂ à proximité de la matrice silicique sous forme amorphe. Quelle que soit la porosité de Si(HIPE), la phase cristalline de TiO₂ reste constante à 100% anatase par la méthode d'imprégnation en deux étapes. Seules les tailles des cristallites varient d'environ 10 à 25 nm. Les paramètres de synthèse (X) qui influencent le plus la morphologie finale du matériau sont la fraction volumique en huile, la température de calcination de la silice et la vitesse de rotation

Résumé

pendant l'émulsification. A partir des échantillons de X-TiO₂@Si(HIPE), l'influence de la surface spécifique du TiO₂, de la surface BET et du diamètre médian des pores a pu être étudiée sur les performances photocatalytiques. De plus, les expériences de diffusion de la lumière mettent en évidence le contraste de la pénétration des photons dans un lit de poudre ou un monolithe. Plus le diamètre médian de l'ouverture des pores est grand, plus le libre parcours moyen de transport des photons l_t est important (Figure 3), et donc la pénétration des photons. La visualisation de la pénétration des photons a été réalisée par imprégnation d'un sel d'or et réduction de celui-ci sous irradiation UV (Figure 2 F). Ces résultats vont dans le sens de lier les caractéristiques morphologiques et structurales au principe de la photocatalyse.

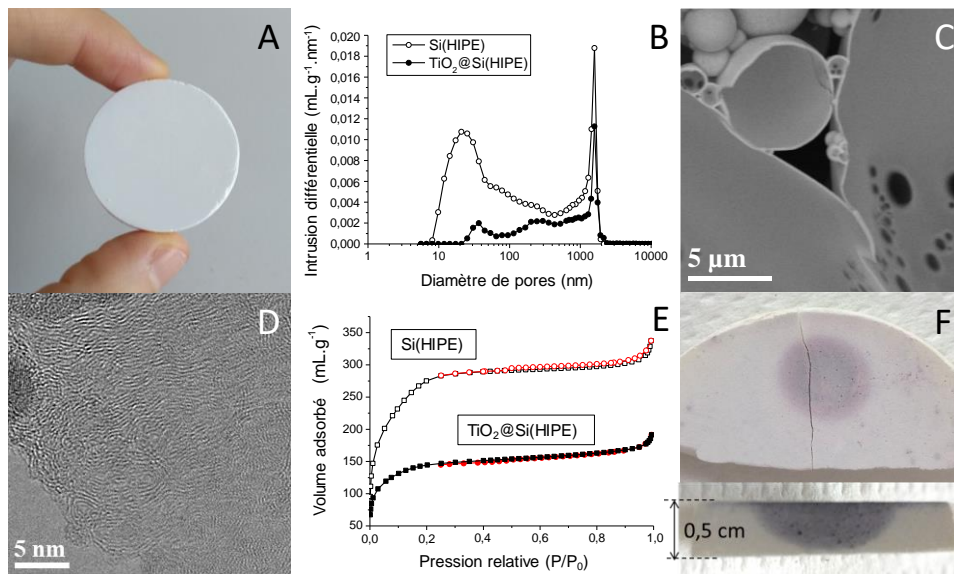


Figure 2: (A) Photographie d'un monolithe TiO₂@Si(HIPE), (B) Distribution de taille de pores d'un Si(HIPE) (cercle noir) et d'un TiO₂@Si(HIPE) (cercle plein noir), (C) Cliché MEB d'une fenêtre cellulaire externe, (D) Cliché MET d'une paroi de silice, (E) Isothermes d'azote d'un Si(HIPE) (symboles vides) et d'un TiO₂@Si(HIPE) (symboles pleins). (□) et (■) branches d'adsorption, (○) et (●) branches de désorption

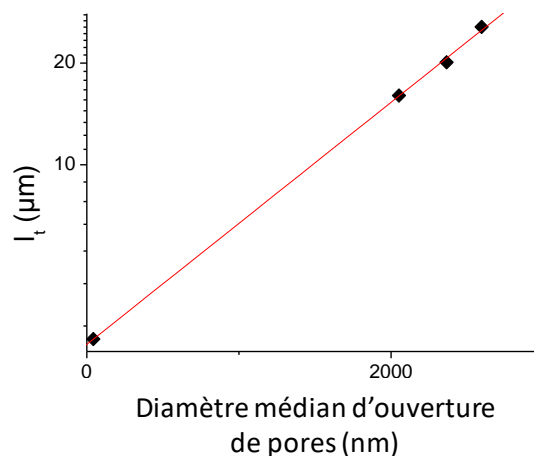


Figure 3: Libres parcours moyen de transport des photons l_t par rapport aux diamètres médian d'ouverture de pores pour le lit de poudre du TiO₂ P25 et de trois TO₂@Si(HIPE)s. Le coefficient de corrélation correspondant est $R^2 = 0,9995$.

Le chapitre IV propose une description du comportement des matériaux synthétisés et de la poudre de TiO₂ P25 (photocatalyseur de référence) concernant la photoréduction du CO₂ dans nos conditions. Afin de mieux comprendre les phénomènes impliqués, un modèle macro-cinétique a été développé, basé sur les formalismes de Langmuir-Hinshelwood pour les réactifs et Eley-Rideal pour les photons. Il considère les photons comme des réactifs au même titre que le CO₂ et H₂O. En confrontant le modèle à quatre matériaux étudiés en fonction de l'épaisseur du lit catalytique, les descripteurs k_0 , K et α ont pu être évalués. La constante k_0 décrit le taux de paires électron-trou photogénérées et a montré que le TiO₂ P25 présente la meilleure performance photocatalytique intrinsèque. La constante K décrit l'impact des réactions inverses sur les performances. Plus la constante K est élevée, plus on peut supposer que le taux de réactions inverses est faible. Par ailleurs, cette constante semble être liée en particulier à la contribution spécifique en surface du TiO₂. Ensuite, le coefficient d'atténuation α est significativement réduit en utilisant des monolithes poreux et semble être lié en particulier aux diamètres médians d'ouverture des pores et au libre parcours moyen de transport des photons.

Grâce à l'étude des paramètres influençant la performance photocatalytique de la poudre commerciale de TiO₂ P25, il a été possible de mettre en évidence les comportements clés des matériaux concernant la photoréduction du CO₂. L'alimentation en photons semble notamment être l'étape limitante dans nos conditions. La formation d'oxygène (co-produit de la réaction) réduit considérablement les performances du TiO₂ à mesure que l'épaisseur du lit catalytique augmente, et ré-orienté ainsi les réactions en fin de lit vers la production d'H₂O, de CO et de CO₂ (réoxydation par le dioxygène formé du dihydrogène ou des hydrocarbures produits). Néanmoins, il a été montré que la dilution de la phase active TiO₂ dans une matrice silicique limite l'importance de ces réactions inverses. Des tests photocatalytiques de référence et des analyses complémentaires ont confirmé que la production d'hydrocarbures était bien issue de la réduction photocatalytique du CO₂ contenu dans la phase gaz en présence d'eau, et non de contamination résiduelle sur les solides.

Pour comparer les matériaux testés à différentes épaisseurs, les corrélations établies lors de la mise en œuvre du modèle ont été utilisées afin de calculer les constantes k_0 pour chaque matériau de la série X-TiO₂@Si(HIPE), où X est le paramètre de synthèse modifié. Leur étude a montré que le taux de paires électron-trou photogénérées est d'autant plus élevé que la taille des cristallites de TiO₂ est grande. Ce comportement pourrait être lié à la densité de défauts plus élevés pour les cristallites de petite taille. De plus, ce taux diminue, dans la gamme étudiée, contre-intuitivement à mesure que la contribution de la surface spécifique du TiO₂ augmente. En outre, la méthode d'imprégnation du TiO₂ dans le Si(HIPE) influence fortement la sélectivité. En effet, lorsque les cristallites de TiO₂ sont issues de l'imprégnation du précurseur de TiO₂, elles dirigent préférentiellement les produits vers le méthane et l'éthane. *A contrario*, lorsque les particules de TiO₂ incorporées dans le Si(HIPE) sont issues de l'imprégnation d'une suspension colloïdale de poudre de TiO₂, la part d'hydrogène est deux fois plus importante que pour le TiO₂ issu d'un précurseur. L'intimité du contact TiO₂/TiO₂ et TiO₂/SiO₂ mériterait donc d'être étudiée pour mieux comprendre l'influence du type d'imprégnation.

Résumé

La mise en œuvre et l'optimisation des matériaux $\text{TiO}_2@\text{Si}(\text{HIPE})$ a permis d'atteindre des performances extrêmement intéressantes pour la photoréduction du CO_2 . En effet, des vitesses de consommation d'électrons (normalisé par unité de surface irradiée) ont été mesurées jusqu'à 5 fois supérieures à celle obtenue par le lit de poudre optimal du TiO_2 P25 ; la raison évoquée étant une épaisseur utile pour les monolithes jusqu'à 20 fois supérieure à celle des lits de poudre, ayant pour conséquence une efficacité volumique de ces systèmes (Figure 4). De plus, les sélectivités ont montré une formation préférentielle d'hydrocarbures à haute valeur énergétique : méthane et éthane.

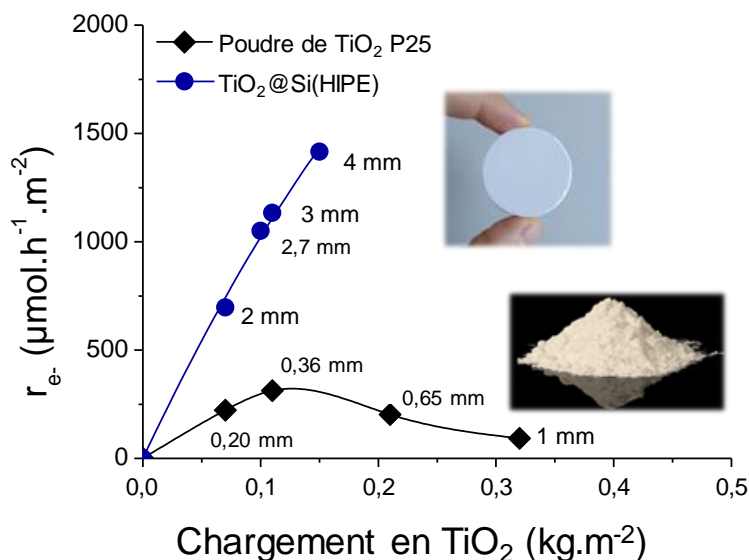


Figure 4: Comparaison des performances photocatalytiques de la poudre de TiO_2 P25 et d'un monolithe $\text{TiO}_2@\text{Si}(\text{HIPE})$ en fonction de la charge en TiO_2

Au-delà des performances élevées induites par la meilleure pénétration des photons au sein du matériau, les matériaux synthétisés dans le cadre de cette étude présentent plusieurs avantages. Parmi ceux-ci, on peut citer la mise en œuvre d'un mode de préparation issu de la chimie douce, ce qui implique une faible dépense énergétique lors de la synthèse. De plus, la structure poreuse de la silice présente une bonne résistance mécanique et permet ainsi de disposer de matériaux manipulables facilement (par rapport à un matériau pulvérulent).

Malgré les points forts mis en évidence, des points restent à améliorer. Tout d'abord, concernant la préparation des matériaux, la synthèse du matériau nécessite environ deux mois, principalement en raison du temps nécessaire à la délicate étape de séchage pour l'élimination progressive du solvant utilisé dans la dégradation de la phase organique structurante. Des travaux de développement en utilisant des techniques de séchage plus rapides qui préservent l'intégrité du matériau, comme le séchage supercritique, pourrait être entrepris. Deuxièmement, les lots de matériaux présentaient parfois des différences sur le plan des caractéristiques physico-chimiques dues à certaines étapes de synthèse encore trop manuelle. A cette fin, une synthèse automatisée pourrait permettre d'éliminer le caractère opérateur-dépendant induit par l'émulsification manuelle. Au cours du projet, un montage comprenant l'utilisation

Résumé

d'une agitation mécanique à l'aide d'une pale et l'incorporation du dodécane à l'aide d'un pousse-seringue a été utilisé pour l'étude de l'influence de la vitesse de rotation sur la morphologie de la matrice silicique. Une étude plus détaillée de la conception des pales et de la vitesse de rotation devrait être envisagée pour rendre ce processus reproductible.

Selon ce travail de thèse, le coefficient d'atténuation de la lumière α diminue avec le diamètre médian de l'ouverture des pores lorsque la diffusion multiple est en jeu. Ainsi, pour aller plus loin dans la structuration du matériau, l'augmentation de la taille des pores serait alors favorable à la pénétration des photons en profondeur. Pour ce faire, une diminution des contraintes en cisaillement lors de l'émulsification et/ou une réduction de la fraction volumique de l'huile (paramètres influençant fortement la distribution de taille de pores) augmenterait la taille des gouttelettes d'huile et donc la taille des pores après frittage. Dans la continuité d'une amélioration de la pénétration des photons et donc de la réalisation de procédés photocatalytiques en volume, une diffusion des photons qui suivrait la loi de Mie pourrait être favorisée et combinée à la diffusion multiple. En effet, ce mode de diffusion de la lumière induit une diffraction anisotrope par les objets diffusants de telle sorte que la propagation des photons dans la direction du rayonnement incident est intensifiée (i.e. dans la profondeur du matériau). Cette diffusion est obtenue par des objets diffusants monodisperses en taille et de taille caractéristique du même ordre de grandeur que la longueur d'onde du faisceau incident. Afin de synthétiser de tels objets, la synthèse de gabarits (« hard templates ») peut être envisagée. Par exemple, en synthétisant des billes de latex de taille adaptée et monodisperses, elles peuvent être incorporées dans le sol de départ des Si(HIPE)s. Après frittage et donc dégradation des billes, les parois de silice des $\text{TiO}_2@Si(\text{HIPE})s$ pourraient alors présenter des pores de taille contrôlée et monodisperses, agissant comme objets diffusants et dirigeant les photons de l'UV en profondeur. Si la phase active incorporée permet d'absorber dans le visible, cette technique est également réalisable en adaptant la taille des billes de latex à la longueur d'onde ciblée.

En ce qui concerne la phase active, l'influence du rapport anatase/rutile n'a pu être analysée en raison de l'absence d'une série cohérente. Pour comparer rigoureusement les proportions anatase/rutile, celles-ci doivent être le seul paramètre à considérer. Les matériaux synthétisés avec des proportions anatase/rutile variables présentaient soit différentes tailles de cristallites, soit différentes formes (poudre vs monolithe). Une méthode de synthèse contrôlant à la fois les proportions de phases et la taille des cristallites permettrait alors d'étudier ce paramètre. En outre, il est à noter que l'imprégnation n'a été réalisée qu'avec de l'oxyde de titane pendant le projet. Cependant, la méthode de préparation mise au point dans le cadre de ces travaux peut être généralisée à toute phase active sous forme de suspension colloïdale. Des clusters de photocatalyseurs absorbant dans le visible de manière intrinsèque ou par des modifications chimiques (ajout de dopant, co-catalyseur...) peuvent donc être incorporés et améliorer les performances photocatalytiques des $SC@Si(\text{HIPE})s$. Au-delà de la phase active incorporée, des modifications chimiques du support peuvent également être envisagées. Il a été observé dans la littérature qu'une hétérojonction entre deux semi-conducteurs améliore l'absorption des photons et la

Résumé

séparation des porteurs de charge. Par exemple pour une hétérojonction anatase/rutile, le rutile présentant une énergie de band gap plus faible que l'anatase, il permet d'absorber une plus grande part des photons issus de rayonnement solaire. Puis, la migration des électrons en surface de l'anatase permet de les séparer des trous restant dans le rutile. On peut alors imaginer de modifier la matrice silicique pour lui conférer des propriétés semi-conductrices, alors en contact avec le TiO_2 imprégné tout en préservant la porosité hiérarchique. Pour ce faire, un sel de métal de transition divalent M^{2+} pourrait être incorporé dans le sol de départ des Si(HIPE)s afin de former une phase méta-silicate (MSiO_3) après traitement thermique (substitution des atomes de Si par les éléments M). Ces types de matériau peuvent s'apparenter aux minéraux colorés tel que le Chrysocolle ($\text{CuSiO}_3, n\text{H}_2\text{O}$) présentant une couleur vert bleu à brun noir. Une structure colorée implique l'absorption de photons dans le spectre du visible. Ainsi, une plus grande part du spectre solaire pourrait être absorbée, donc un plus grand nombre de charges photogénérées permettrait les réactions de réduction du CO_2 et oxydation de H_2O après migration des charges à l'interface $\text{MSiO}_3/\text{TiO}_2$.

Au regard du modèle cinétique, en le confrontant à de nouveaux profils de performances photocatalytique en fonction de l'épaisseur de lit, les descripteurs utilisés dans la description des phénomènes en jeu pourraient être affiner. De même qu'une étude mécanistique, en faisant par exemple varier le ratio molaire CO_2 sur H_2O , apporterait des informations complémentaires sur la sélectivité des produits. En affinant l'identification des paramètres influençant les niveaux de performances des réactions, le modèle se généraliserait à la prédiction des conditions opératoires optimales, en plus de la morphologie des matériaux à synthétiser.

De manière connexe à l'étude en photoréduction du CO_2 , des essais en lien avec la purification de l'air ont été réalisés à l'IPREM-Pau par Mickael Le Behec et Sylvie Lacombe. Les mesures d'adsorption et de minéralisation de l'acétone et du toluène ont été très prometteuses. D'une part, les valeurs d'adsorption de l'acétone et du toluène ont montré que les $\text{TiO}_2@\text{Si(HIPE)s}$ peuvent atteindre des niveaux significativement élevés même par rapport aux matériaux connus pour être très capacitifs comme le charbon actif ou le Quartzel. D'autre part, les taux de minéralisation du toluène et de l'acétone étaient au moins aussi bons que ceux obtenus par les applications de pointe connues. De plus, les $\text{TiO}_2@\text{Si(HIPE)s}$ ont permis d'obtenir des activités photocatalytiques très stables, contrairement au Quartzel. En effet, une désactivation rapide a été observée avec ce matériau, caractérisée par une diminution de la production de dioxyde de carbone et un jaunissement significatif du matériau pendant la phase de test d'irradiation. Ainsi au-delà de la réduction du CO_2 , d'autres applications sont envisageables, comme la photopurification de l'air, voire de l'eau.

Références du résumé

- (1) Moduloo.net. La concentration de CO₂ dans l'atmosphère vient de passer un cap jamais atteint depuis des millions d'années [https://reporterre.net/La-concentration-de-CO₂-dans-l-atmosphere-vient-de-passer-un-cap-jamais-atteint](https://reporterre.net/La-concentration-de-CO2-dans-l-atmosphere-vient-de-passer-un-cap-jamais-atteint) (accessed Oct 14, 2018).
- (2) Smol, J. P. Climate Change: A Planet in Flux. *Nature* **2012**, *483*, S12–S15.
- (3) Fontecave, M. Energy for a Sustainable World. From the Oil Age to a Sun-Powered Future. Von Nicola Armaroli Und Vincenzo Balzani. *Angewandte Chemie* **2011**, *123* (30), 6836–6837.
- (4) Lewis, N. S.; Nocera, D. G. Powering the Planet: Chemical Challenges in Solar Energy Utilization. *PNAS* **2006**, *103* (43), 15729–15735.
- (5) Renewables <https://www.iea.org/geco/renewables/index.html> (accessed Oct 14, 2018).
- (6) WEO 2017 <https://www.iea.org/weo2017/#section-5-1> (accessed Oct 14, 2018).
- (7) Habisreutinger, S. N.; Schmidt-Mende, L.; Stolarczyk, J. K. Photocatalytic Reduction of CO₂ on TiO₂ and Other Semiconductors. *Angewandte Chemie International Edition* **2013**, *52* (29), 7372–7408.
- (8) Fujishima, A.; Honda, K. Electrochemical Photolysis of Water at a Semiconductor Electrode. *Nature* **1972**, *238* (5358), 37–38.
- (9) Inoue, T.; Fujishima, A.; Konishi, S.; Honda, K. Photoelectrocatalytic Reduction of Carbon Dioxide in Aqueous Suspensions of Semiconductor Powders. *Nature* **1979**, *277*, 637–638.
- (10) Chang, X.; Wang, T.; Gong, J. CO₂ Photo-Reduction: Insights into CO₂ Activation and Reaction on Surfaces of Photocatalysts. *Energy Environ. Sci.* **2016**, *9* (7), 2177–2196.
- (11) Kosten, E. D.; Kayes, B. M.; Atwater, H. A. Experimental Demonstration of Enhanced Photon Recycling in Angle-Restricted GaAs Solar Cells. *Energy Environ. Sci.* **2014**, *7* (6), 1907–1912.
- (12) Silverstein, M. S. Emulsion-Templated Porous Polymers: A Retrospective Perspective. *Polymer* **2014**, *55* (1), 304–320.
- (13) Ungureanu, S.; Deleuze, H.; Sanchez, C.; Popa, M. I.; Backov, R. First Pd@Organo–Si(HIPE) Open-Cell Hybrid Monoliths Generation Offering Cycling Heck Catalysis Reactions. *Chem. Mater.* **2008**, *20* (20), 6494–6500.
- (14) Ungureanu, S.; Deleuze, H.; Babot, O.; Achard, M.-F.; Sanchez, C.; Popa, M. I.; Backov, R. Palladium Nanoparticles Heterogeneous Nucleation within Organically Grafted Silica Foams and Their Use as Catalyst Supports toward the Suzuki–Miyaura and Mizoroki–Heck Coupling Reactions. *Applied Catalysis A: General* **2010**, *390* (1), 51–58.
- (15) Brun, N.; Babeau Garcia, A.; Deleuze, H.; Achard, M.-F.; Sanchez, C.; Durand, F.; Oestreicher, V.; Backov, R. Enzyme-Based Hybrid Macroporous Foams as Highly Efficient Biocatalysts Obtained through Integrative Chemistry. *Chem. Mater.* **2010**, *22* (16), 4555–4562.
- (16) Brun, N.; Babeau-Garcia, A.; Achard, M.-F.; Sanchez, C.; Durand, F.; Laurent, G.; Birot, M.; Deleuze, H.; Backov, R. Enzyme-Based Biohybrid Foams Designed for Continuous Flow Heterogeneous Catalysis and Biodiesel Production. *Energy Environ. Sci.* **2011**, *4* (8), 2840–2844.
- (17) Likodimos, V. Photonic Crystal-Assisted Visible Light Activated TiO₂ Photocatalysis. *Applied Catalysis B: Environmental* **2018**, *230*, 269–303.
- (18) Carbonell, E.; Ramiro-Manzano, F.; Rodríguez, I.; Corma, A.; Meseguer, F.; García, H. Enhancement of TiO₂ Photocatalytic Activity by Structuring the Photocatalyst Film as Photonic Sponge. *Photochem. Photobiol. Sci.* **2008**, *7* (8), 931–935.
- (19) Zhou, H.; Guo, J.; Li, P.; Fan, T.; Zhang, D.; Ye, J. Leaf-Architected 3D Hierarchical Artificial Photosynthetic System of Perovskite Titanates Towards CO₂ Photoreduction Into Hydrocarbon Fuels. *Scientific Reports* **2013**, *3*, 1667.
- (20) Gaikwad, P.; Ungureanu, S.; Backov, R.; Vynck, K.; Vallée, R. A. L. Photon Transport in Cylindrically-Shaped Disordered Meso-Macroporous Materials. *Opt. Express, OE* **2014**, *22* (7), 7503–7513.
- (21) Bachelard, N.; Gaikwad, P.; Backov, R.; Sebbah, P.; Vallée, R. A. L. Disorder as a Playground for the Coexistence of Optical Nonlinear Effects: Competition between Random Lasing and Stimulated Raman Scattering in Complex Porous Materials. *ACS Photonics* **2014**, *1* (11), 1206–1211.

- (22) Gaikwad, P.; Bachelard, N.; Sebbah, P.; Backov, R.; Vallée, R. A. L. Competition and Coexistence of Raman and Random Lasing in Silica-/Titania-Based Solid Foams. *Advanced Optical Materials* **2015**, 3 (11), 1640–1651.

TABLE OF CONTENTS

INTRODUCTION	1
CHAPTER I	7
1 PHOTOCATALYSIS	11
1) PRINCIPLE.....	11
A. FUNDAMENTALS.....	11
B. SEMICONDUCTOR ROLE.....	12
C. LIMITATIONS	14
2) PHOTOCATALYST, CASE OF TiO ₂	17
A. PHYSICOCHEMICAL CHARACTERISTICS OF TiO ₂	17
B. MODIFIED TiO ₂	18
C. MORPHOLOGICAL MODIFICATION	20
2 LIGHT-MATTER INTERACTION	22
1) INTRODUCTION TO DIFFUSION.....	23
2) MULTI-DIFFUSION THEORY	24
A. DIFFUSION EQUATION	24
B. BOUNDARY CONDITIONS AND STATIONARY SOLUTION	25
C. FULL TIME-DEPENDENT SOLUTION.....	27
3 INTEGRATIVE CHEMISTRY FOR GENESIS OF POROUS ARCHITECTURES	28
1) ALVEOLAR MATERIALS BEARING HIERARCHICAL POROSITY	28
A. NOTIONS OF PORES AND TEXTURAL PARAMETERS	28
B. SYNTHETIC PATHWAYS OF 3D SYSTEMS	30
2) INORGANIC POLYMERIZATION: SILICA-BASED SOL-GEL PROCESS	35
A. GENERALITIES	35
B. HYDROLYSIS MECHANISMS.....	37
C. CONDENSATION MECHANISMS AND SOLS GROWTH.....	37



4	<u>PHD PROJECT AND AIM</u>	39
5	<u>REFERENCES</u>	40
	CHAPTER II	47
1	<u>SYNTHESES OF MONOLITHS BEARING HIERARCHICAL POROSITY</u>	51
	1) SILICA MATRIX SYNTHESIS.....	51
	A. CONDENSATION STAGE	51
	B. WASHING STAGE	52
	C. DRYING STAGE	52
	D. CALCINATION TREATMENT: ORGANIC CALCINATION AND SILICA SINTERING	53
	2) TiO ₂ IMPREGNATION	53
	A. PRECURSOR SOLUTION	53
	B. IMPREGNATION STAGE	54
	C. HEAT TREATMENT.....	55
2	<u>CHARACTERIZATIONS</u>	55
	1) STRUCTURAL AND MORPHOLOGICAL CHARACTERIZATIONS	55
	A. MACROSCOPIC LENGTH SCALE.....	55
	B. MESO- AND MICROSCOPIC LENGTH SCALE.....	60
	2) ELECTRONIC CHARACTERIZATION: DIFFUSE REFLECTANCE UV-VISIBLE SPECTROSCOPY	67
	3) LIGHT DIFFUSION CHARACTERIZATION.....	68
	A. GOLD SALT IMPREGNATION METHOD.....	68
	B. PULSED LASER METHOD	68
3	<u>PHOTOCATALYTIC TESTS</u>	70
	1) SET UP	70
	A. REACTOR.....	70
	B. DEVICES	71
	C. PROCEDURE.....	72

2) EVALUATION OF PHOTOCATALYTIC PERFORMANCES	73
A. PHOTOCATALYTIC ACTIVITIES	74
B. SELECTIVITY	76
4 CONCLUSION.....	76
5 REFERENCES	77
CHAPTER III.....	79
1 MORPHOLOGICAL DESCRIPTIONS.....	83
1) Si(HIPE): SILICA MATRIX.....	83
A. MACROSCOPIC LENGTH SCALE.....	83
B. MESO- AND MICROSCOPIC LENGTH SCALE.....	85
C. REPRODUCIBILITY AND REPEATABILITY	87
2) TiO ₂ @Si(HIPE)	88
A. MACROSCOPIC LENGTH SCALE.....	88
B. MESO- AND MICROSCOPIC LENGTH SCALE.....	91
C. REPRODUCIBILITY AND REPEATABILITY	93
3) CONCLUSION	94
2 INFLUENCE OF SPECIFIC PARAMETERS	94
1) TiO ₂ STRUCTURE AND PARTICLE MORPHOLOGY	94
A. IMPREGNATION METHODS OVER PARTICLE MORPHOLOGY	95
B. CALCINATION TREATMENT OVER TiO ₂ STRUCTURE	100
C. IMPREGNATION METHODS OVER TiO ₂ STRUCTURE	103
2) MORPHOLOGICAL Si(HIPE) MODIFICATIONS	105
A. OIL VOLUME FRACTION (ϵ).....	105
B. OIL CHAIN LENGTH (C_x)	107
C. CALCINATION TREATMENT (T)	109
D. LOCAL SHEAR (v)	111



E. THICKNESS (t).....	113
3) CONCLUSION	114

3 LIGHT DIFFUSION.....	114
4 CONCLUSION.....	117
5 REFERENCES	118

CHAPTER IV.....	121
1 PROOF OF CONCEPT AND EXPERIMENTAL LIMITATION	125
1) PRELIMINARY TESTING	125
A. POWDER VS. MONOLITH	125
B. CRITICAL PARAMETERS.....	127
2) TiO ₂ @Si(HIPE) BEHAVIOR.....	132
A. CO ₂ PHOTOREDUCTION PROCESS THROUGH TiO ₂ @Si(HIPE).....	132
B. CO ₂ PHOTOREDUCTION ENHANCEMENT THROUGH TiO ₂ @Si(HIPE).....	134
2 KINETIC MODELLING	137
1) MODEL DESCRIPTION	137
A. HYPOTHESES	138
B. PHOTON QUANTITY DESCRIPTION	138
C. ACTIVE SITE DESCRIPTION	139
D. GLOBAL EQUATION RATE.....	140
2) CONFRONTATIONS WITH EXPERIMENTAL RESULTS	141
A. MATERIAL DESCRIPTION	141
B. PARAMETER FITTING.....	142
C. K COEFFICIENT CORRELATION	144
D. LIGHT ATTENUATION COEFFICIENT CORRELATIONS	145
3 TiO₂@Si(HIPE) BEHAVIOR UNDERSTANDING	146



1) TiO ₂ SPECIFIC SURFACE AREA	147
2) TiO ₂ SSA CONTRIBUTION	148
3) MEDIAN PORE DIAMETER	150
4) SYNTHESIZED AND COMMERCIAL TiO ₂ : INFLUENCE OF TiO ₂ ORIGIN	150

<u>4 CONCLUSION.....</u>	<u>151</u>
<u>5 REFERENCES</u>	<u>154</u>
<u>CONCLUSION AND PERSPECTIVES</u>	<u>157</u>
<u>ANNEXES.....</u>	<u>163</u>



Introduction

Rising carbon dioxide (CO₂) level in the atmosphere and the fossil energy resource depletion raise serious concerns about global warming and future energy supply.

In figures, these concerns correspond to a current CO₂ concentration of 411 ppm (in April 21, 2018 ¹) which far exceeds its natural fluctuation, between 180 and 300 ppm, over the past 800,000 years ². From an energy point of view, global energy consumption is estimated to increase from 15-17 TW in 2010 ³ to 25-27 TW in 2050 ⁴, an increase from 47 to 80% in forty years. In 2017, 81% of total energy demand was still met by fossil fuels. However, a quarter of global electricity generation was met by renewables, which represents the highest growth rate compared to any energy source in 2017 ⁵. This is a demonstration of the effort that must be sustained to reduce this high dependence on fossil fuels, as highlighted by the International Energy Agency (IEA). In the Sustainable Development Scenario described in World Energy Outlook 2017 ⁶, low-carbon sources double their share in the energy mix to 40% in 2040.

The most famous renewable energies currently available for industrial energy production are photovoltaic panels and wind turbines. These convert solar irradiation or wind force into electrical energy. However, massive electricity storage is the main technological challenge currently facing our societies as they move from the all-oil to the zero-carbon era. New alternative technologies based on conversion into chemical energy are at the heart of the research. In particular, water electrolysis is a possible way of storing electricity in the form of hydrogen, which can be easily stored and transported. Direct pathways for converting solar energy into chemical energy exist and are currently expanding, such as water splitting. In this thesis project, particular attention is paid to CO₂ photoconversion. Indeed, this allows the hydrocarbons production offering high energy potential by using solar energy and exploiting anthropogenic CO₂ emissions. Hydrocarbons can then be used as fuels to produce energy. This consumption of photogenerated hydrocarbons releases CO₂ again, which will be re-used in a new photoconversion process. This would then allow it to reintegrate into the carbon cycle, which would significantly limit carbon dioxide emission increase. The CO₂ would then become a cheap and abundant raw material that would replace, at least in part, fossil fuels ⁷.

Photocatalysis has been the focus of considerable attention in recent years being used in a variety of products across a broad range of research areas, including especially environmental and energy-related fields (Figure 5). Based on the water splitting breakthrough reported by Fujishima and Honda in 1972 ^{8,9}, the photocatalytic properties of certain materials have been used to convert solar energy into chemical energy including hydrogen and hydrocarbons, and to remove pollutants and bacteria on wall surfaces and in air and water. Of the many different photocatalysts, TiO₂ has been the most widely studied and used in many applications because of its strong oxidizing abilities for the decomposition of organic pollutants, superhydrophilicity, chemical stability, long durability, nontoxicity, and low cost.

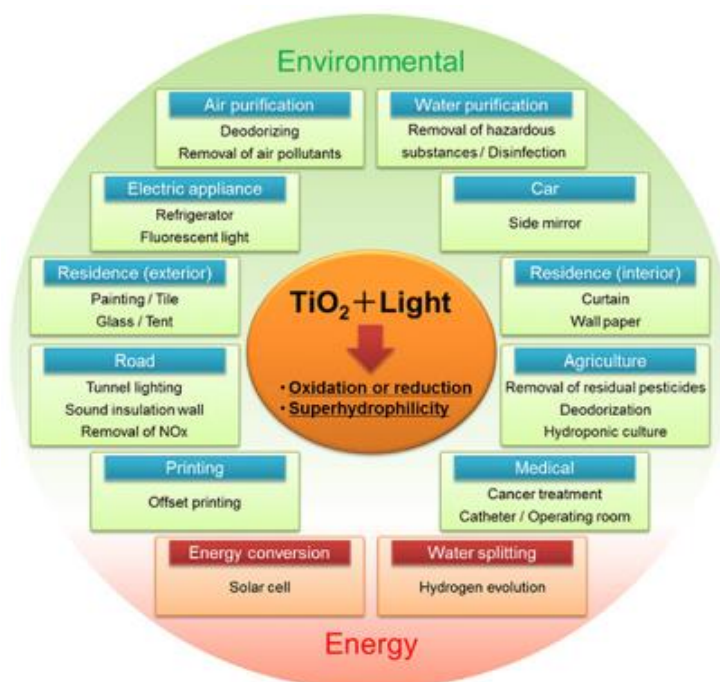


Figure 5: Applications of TiO_2 photocatalysis ¹⁰

The thesis project is in line with the theme of direct CO_2 conversion through heterogeneous photocatalysis. The overall heterogeneous photocatalysis process consists of a succession of complex processes involving elementary steps occurring on the surface of the material (adsorption of reagents, diffusion and reaction of intermediates on the surface) and in its volume (photon absorption, generation, diffusion and recombination by volume and charge surface). The complexity of the heterogeneous photocatalysis mechanism reveals limits that the scientific community is trying to push as far as possible. These limitations could be induced by screening effect, by adsorption phenomena, or photogenerated charge carrier recombination. The result is catalytic performance that is still crippling when considering the emergence of industrial processes. Today, even with the best photocatalysts, reaction rates of CO_2 conversion are still very low (in the range of a few tens to hundreds $\mu\text{mole} \cdot \text{h}^{-1} \cdot \text{g}^{-1}$) ⁷. Most of the works mentioned in the literature focus on the semiconductor physicochemical modification in order to improve the photogenerated charge carriers use by minimizing the recombination phenomenon through specific architectural effects (heterojunctions), metal addition as co-catalyst, or dopants ^{11,12}. While these research routes are interesting, a big challenge of optimizing photon penetration persists and forces the two-dimensional character of current photocatalysts. The global performance of a photocatalytic transformation results from a combination of several steps. Today, progress in this field requires a better knowledge of these steps. Determining their respective roles and their dependencies on each other can help to better identify the limiting steps.

Thus, the thesis project proposes a photocatalyst implementation in a three-dimensional material labelled HIPEs (High Internal Phase Emulsion) ¹³ to address the photon harvesting challenge. These three-dimensional materials are monoliths with hierarchical porosity. The multi-scale structure has

proven to optimize material transport properties. The fluid behavior is intrinsically hierarchical and combines a mass transport system that efficiently feeds the macropore walls, which host the active phase^{14,15,16,17}. Beyond the interaction with fluids, porous structures have also proven their ability to interact with light. For example, photonic crystals play on the monodisperse periodical distribution of voids in order to control the photon motion and trap light¹⁸. However, such materials scatter light in a single wavelength linked to pore size. Photonic sponges were then introduced by Carbonell *et al.*¹⁹ to promote light scattering in a broad spectral region due to polydisperse composition of either particles or voids. Inspired by the living world, Zhou *et al.*²⁰ replicated leaf's 3D hierarchical architecture to enhance light scattering and light multi-diffusion. The objective of such structures is to increase the photon residence time and their penetration depth to increase the encounter probability between photons and the active phase and intensify the photocatalytic process.

In summary, the thesis aims to study photocatalytic systems such as semiconductor dispersed in monoliths bearing hierarchical porosity for the carbon dioxide reduction in the presence of a sacrificial agent, water. One of the potential advantages of these solids lies in the multiplication of reactive contact interfaces (CO₂ and photons)-semiconductor, in a volume and no longer on a surface and in a better collection/diffusion of light in the material. The understanding of involved phenomena is addressed by a complete physico-chemical characterization of materials and a model implementation.

The first chapter presents the principles and research approaches in the photocatalysis field, considerations related to understanding the interactions between light and matter, as well as the tools of integrative chemistry used in the synthesis of porous architectures.

Chapter II details the protocols for synthesizing the materials studied during the project, the different physicochemical characterization techniques used, as well as the setup performing the tests and the quantities used in the evaluation of photocatalytic performance.

The physicochemical properties of the materials are described in Chapter III and discussed regarding the various synthetic parameters.

Chapter IV focuses on describing the behavior of synthesized materials and TiO₂ P25 powder (reference photocatalyst) concerning CO₂ photoreduction under our conditions. In order to better understand the phenomena involved, a kinetic model is implemented and used to extract the descriptors related to the observed behaviors.

References of the introduction

- (1) Moduloo.net. La concentration de CO₂ dans l'atmosphère vient de passer un cap jamais atteint depuis des millions d'années <https://reporterre.net/La-concentration-de-CO2-dans-l-atmosphere-vient-de-passer-un-cap-jamais-atteint> (accessed Oct 14, 2018).
- (2) Smol, J. P. Climate Change: A Planet in Flux. *Nature* **2012**, *483*, S12–S15.
- (3) Fontecave, M. Energy for a Sustainable World. From the Oil Age to a Sun-Powered Future. Von Nicola Armaroli Und Vincenzo Balzani. *Angewandte Chemie* **2011**, *123* (30), 6836–6837.

-
- (4) Lewis, N. S.; Nocera, D. G. Powering the Planet: Chemical Challenges in Solar Energy Utilization. *PNAS* **2006**, *103* (43), 15729–15735.
 - (5) Renewables <https://www.iea.org/geco/renewables/index.html> (accessed Oct 14, 2018).
 - (6) WEO 2017 <https://www.iea.org/weo2017/#section-5-1> (accessed Oct 14, 2018).
 - (7) Habisreutinger, S. N.; Schmidt-Mende, L.; Stolarczyk, J. K. Photocatalytic Reduction of CO₂ on TiO₂ and Other Semiconductors. *Angewandte Chemie International Edition* **2013**, *52* (29), 7372–7408.
 - (8) Fujishima, A.; Honda, K. Electrochemical Photolysis of Water at a Semiconductor Electrode. *Nature* **1972**, *238* (5358), 37–38.
 - (9) Inoue, T.; Fujishima, A.; Konishi, S.; Honda, K. Photoelectrocatalytic Reduction of Carbon Dioxide in Aqueous Suspensions of Semiconductor Powders. *Nature* **1979**, *277*, 637–638.
 - (10) Nakata, K.; Fujishima, A. TiO₂ Photocatalysis: Design and Applications. *Journal of Photochemistry and Photobiology C: Photochemistry Reviews* **2012**, *13* (3), 169–189.
 - (11) Chang, X.; Wang, T.; Gong, J. CO₂ Photo-Reduction: Insights into CO₂ Activation and Reaction on Surfaces of Photocatalysts. *Energy Environ. Sci.* **2016**, *9* (7), 2177–2196.
 - (12) Kosten, E. D.; Kayes, B. M.; Atwater, H. A. Experimental Demonstration of Enhanced Photon Recycling in Angle-Restricted GaAs Solar Cells. *Energy Environ. Sci.* **2014**, *7* (6), 1907–1912.
 - (13) Silverstein, M. S. Emulsion-Templated Porous Polymers: A Retrospective Perspective. *Polymer* **2014**, *55* (1), 304–320.
 - (14) Ungureanu, S.; Deleuze, H.; Sanchez, C.; Popa, M. I.; Backov, R. First Pd@Organo–Si(HIPE) Open-Cell Hybrid Monoliths Generation Offering Cycling Heck Catalysis Reactions. *Chem. Mater.* **2008**, *20* (20), 6494–6500.
 - (15) Ungureanu, S.; Deleuze, H.; Babot, O.; Achard, M.-F.; Sanchez, C.; Popa, M. I.; Backov, R. Palladium Nanoparticles Heterogeneous Nucleation within Organically Grafted Silica Foams and Their Use as Catalyst Supports toward the Suzuki–Miyaura and Mizoroki–Heck Coupling Reactions. *Applied Catalysis A: General* **2010**, *390* (1), 51–58.
 - (16) Brun, N.; Babeau Garcia, A.; Deleuze, H.; Achard, M.-F.; Sanchez, C.; Durand, F.; Oestreicher, V.; Backov, R. Enzyme-Based Hybrid Macroporous Foams as Highly Efficient Biocatalysts Obtained through Integrative Chemistry. *Chem. Mater.* **2010**, *22* (16), 4555–4562.
 - (17) Brun, N.; Babeau-Garcia, A.; Achard, M.-F.; Sanchez, C.; Durand, F.; Laurent, G.; Birot, M.; Deleuze, H.; Backov, R. Enzyme-Based Biohybrid Foams Designed for Continuous Flow Heterogeneous Catalysis and Biodiesel Production. *Energy Environ. Sci.* **2011**, *4* (8), 2840–2844.
 - (18) Likodimos, V. Photonic Crystal-Assisted Visible Light Activated TiO₂ Photocatalysis. *Applied Catalysis B: Environmental* **2018**, *230*, 269–303.
 - (19) Carbonell, E.; Ramiro-Manzano, F.; Rodríguez, I.; Corma, A.; Meseguer, F.; García, H. Enhancement of TiO₂ Photocatalytic Activity by Structuring the Photocatalyst Film as Photonic Sponge. *Photochem. Photobiol. Sci.* **2008**, *7* (8), 931–935.
 - (20) Zhou, H.; Guo, J.; Li, P.; Fan, T.; Zhang, D.; Ye, J. Leaf-Architected 3D Hierarchical Artificial Photosynthetic System of Perovskite Titanates Towards CO₂ Photoreduction Into Hydrocarbon Fuels. *Scientific Reports* **2013**, *3*, 1667.

Chapter I

Bibliography

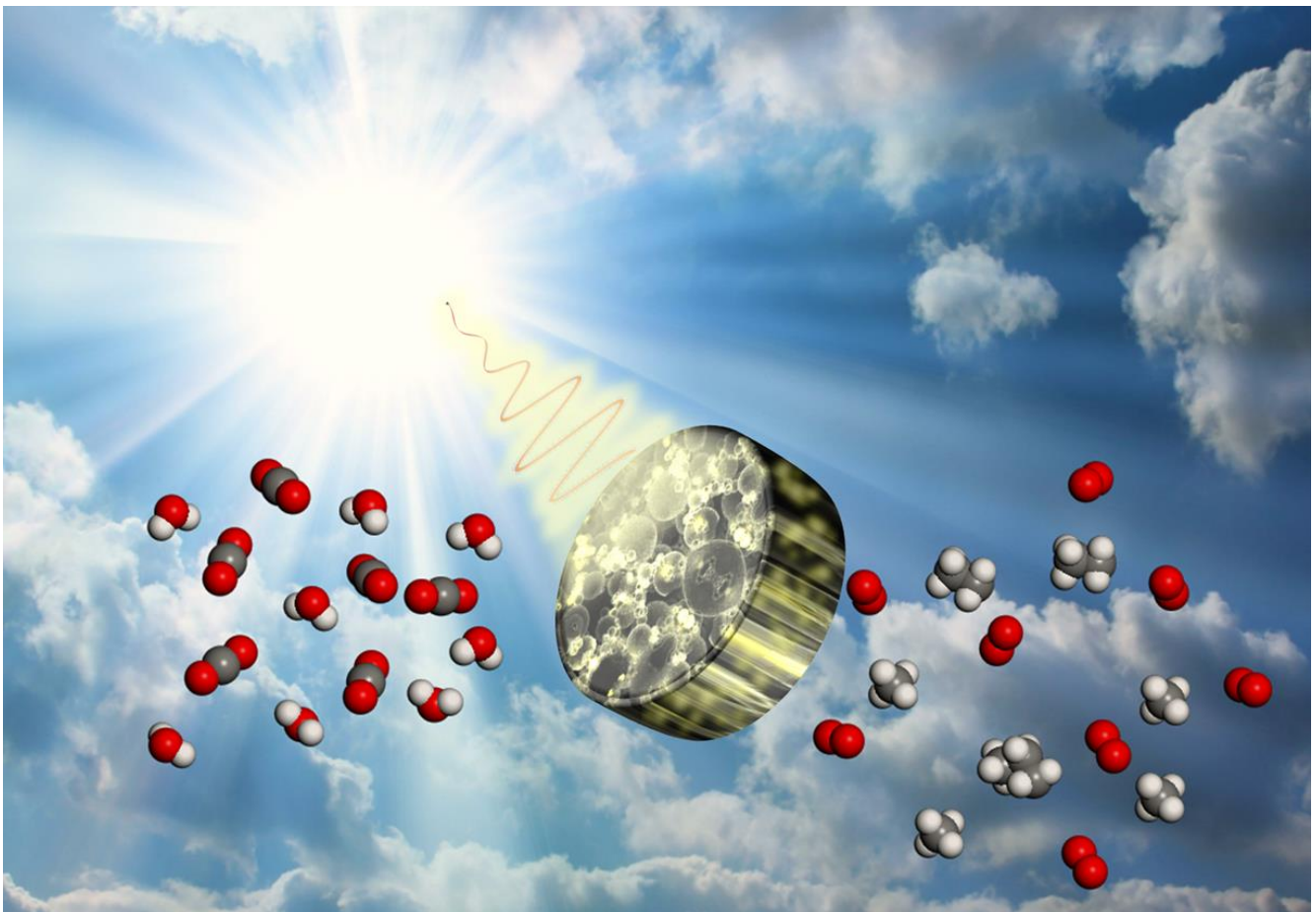


TABLE OF CONTENTS

1	<u>PHOTOCATALYSIS</u>	11
1)	PRINCIPLE	11
A.	FUNDAMENTALS	11
B.	SEMICONDUCTOR ROLE	12
C.	LIMITATIONS	14
2)	PHOTOCATALYST, CASE OF TiO ₂	17
A.	PHYSICOCHEMICAL CHARACTERISTICS OF TiO ₂	17
	Generalities	17
	Crystal structures	18
B.	MODIFIED TiO ₂	18
	Doping modification: visible light response	18
	Co-catalyst modification: charge carrier separation	18
	Crystalline phase mixture	19
C.	MORPHOLOGICAL MODIFICATION	20
2	<u>LIGHT-MATTER INTERACTION</u>	22
1)	INTRODUCTION TO DIFFUSION	23
2)	MULTI-DIFFUSION THEORY	24
A.	DIFFUSION EQUATION	24
B.	BOUNDARY CONDITIONS AND STATIONARY SOLUTION	25
C.	FULL TIME-DEPENDENT SOLUTION	27
3	<u>INTEGRATIVE CHEMISTRY FOR GENESIS OF POROUS ARCHITECTURES</u>	28
1)	ALVEOLAR MATERIALS BEARING HIERARCHICAL POROSITY	28
A.	NOTIONS OF PORES AND TEXTURAL PARAMETERS	28
B.	SYNTHETIC PATHWAYS OF 3D SYSTEMS	30
	Soft templates: foams and emulsions	31
	Controlled phase separation	33
	Hard templates	34
2)	INORGANIC POLYMERIZATION: SILICA-BASED SOL-GEL PROCESS	35
A.	GENERALITIES	35
B.	HYDROLYSIS MECHANISMS	37

Chapter I - Bibliography

Acid-catalyzed hydrolysis	37
Base-catalyzed hydrolysis	37
C. CONDENSATION MECHANISMS AND <i>SOLS</i> GROWTH.....	37
<u>4 PHD PROJECT AND AIM.....</u>	<u>39</u>
<u>5 REFERENCES</u>	<u>40</u>

1 Photocatalysis

Photocatalysis is by definition “the acceleration of a photoreaction by the action of a catalyst”¹. This implies that light and a photocatalyst are both necessary to influence a reaction. In the photocatalysis field, more generally in catalysis, one can distinguish between homogeneous and heterogeneous catalysis. The first one is commonly referring to a liquid-liquid interface, between reactants and catalyst. The second one is related to the liquid-solid and gas-solid interfaces. In the following of this manuscript, we will evolve in the context of heterogeneous photocatalysis involving a solid photocatalyst, commonly named semiconductor, and gaseous reactants.

1) Principle

The fundamentals of photocatalysis are described in the first part. Then, the semiconductor essential role, as well as the photocatalysis process limitations will be detailed as part of our reaction of interest: CO₂ photoreduction involving water.

a. Fundamentals

The initial photocatalytic step is based on light absorption by the semiconductor (SC). Semiconductors are characterized by their bandgap (written “E_g”), which corresponds to the energy gap between the top of the valence band (VB) and the bottom of the conduction band (CB)¹. When the light source emits photons providing a higher energy (hν) than the semiconductor bandgap, then this one will be able to absorb photons: the photocatalyst is in an excited state. The energy provided by the light radiation allows the promotion of an electron (e⁻) from the valence band to the conduction band. This step leaves an unoccupied state within the valence band, commonly called “hole” and denoted h⁺. This leads to the generation of an electron-hole pair ($h\nu \xrightarrow{SC} e_{CB}^- + h_{VB}^+$)².

Then, the generated free charge carriers migrate within the semiconductor and conduct to several pathways of de-excitation. On the one hand, the successful transfer of the carriers to the acceptor (A) and donor (D) molecules adsorbed at the surface, which leads to the desired redox reactions: $A_{ads} + e_{CB}^- \rightarrow A_{ads}^-$ and $D_{ads} + h_{VB}^+ \rightarrow D_{ads}^+$. On the other hand, the carriers can recombine with their opposite charge counterparts trapped on the surface, or in the catalyst volume (Figure I. 1). Indeed, in absence of acceptor and donor molecules, the carriers recombine releasing energy in the form of either heat or photons³. The semiconductor reactivity is limited by this process, which is predominant. For instance, the average lifetime of an electron in a colloidal TiO₂ sample is about 30 ps².

An efficient photocatalyst should be both able to adsorb reactants and absorb effective photons (hν ≥ E_g) under a low recombination rate⁴. Thereby, the photocatalytic system efficiency is dependent on charge carrier number and their lifetime, the reactants adsorption and desorption rates, as well as the involved redox reactions rates².

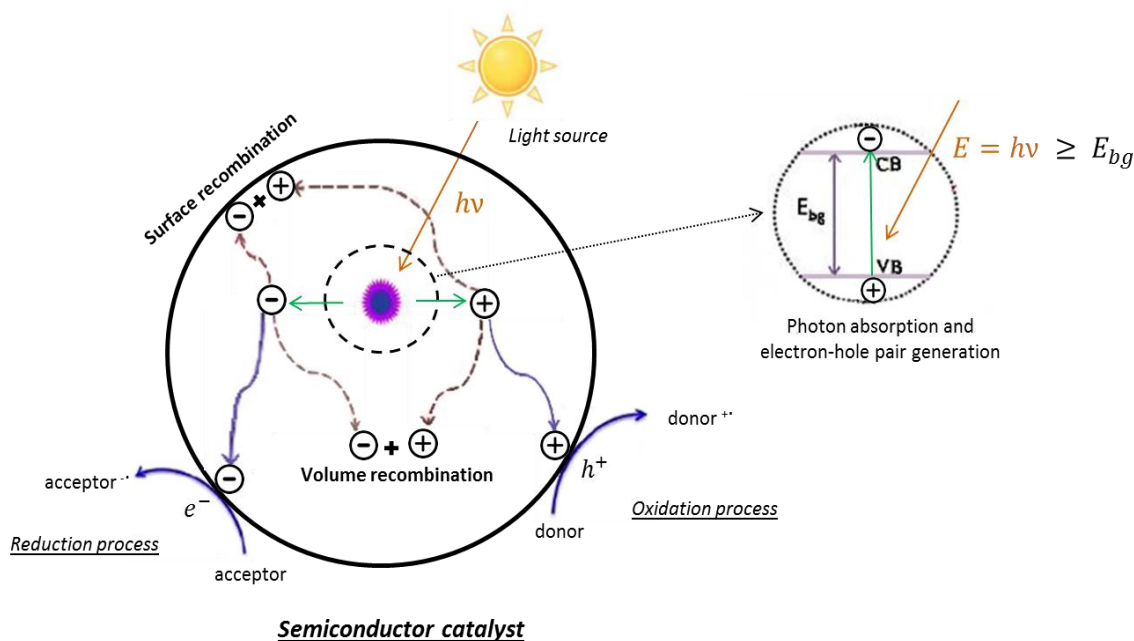


Figure I. 1: Mechanism and pathways for photocatalytic oxidation and reduction processes on the surface of heterogeneous photocatalyst ⁵

From a thermodynamic point of view, when conditions are met to allow redox reactions to take place, those of oxidation will occur at potentials lower than that of the valence band, and those of reduction at potentials higher than that of the conduction band. Thus, both conduction and valence band potentials are decisive for the formation and conversion of desired products and reactants, respectively. The selection of the appropriate semiconductor is essential toward the implementation of a photoconversion system ³.

b. Semiconductor role

Beyond the production of hydrocarbons (oxygenated or not), the results of Inoue *et al.* ⁶ show the influence of the irradiation time and the type of semiconductor on hydrocarbon production yields. The CO₂ photoconversion cannot be carried out using Si catalyst, because its valence band which does not offer enough positive potential to permit the oxidation of H₂O (Figure I. 2). Especially, the selection of adapted semiconductor is driven by the redox potentials of the targeted reactants. Here, it is necessary to use a semiconductor whose energy level of its conduction band is more negative than the redox potential of CO₂ (acceptor) and, at the same time, that its valence band more positive than the redox potential of H₂O (donor).

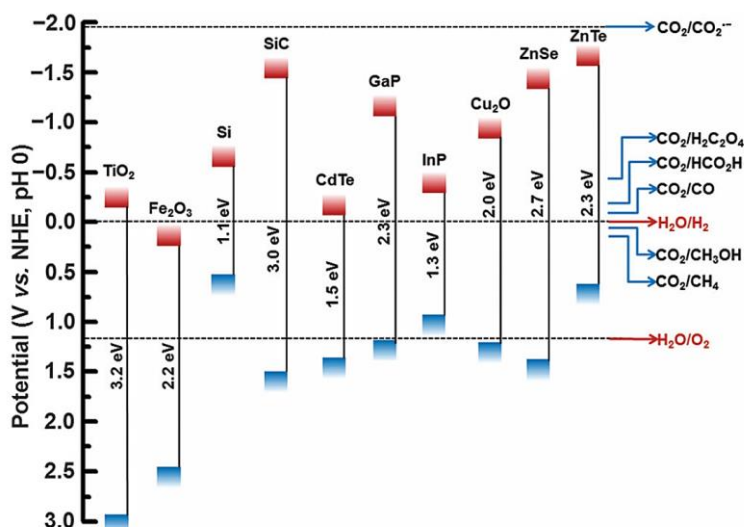


Figure I. 2: Band-edge positions of some typical semiconductor photocatalysts relative to the energy levels of the redox couples involved in the reduction of CO_2 ⁷, where CB and VB are represented with red and blue squares respectively

Once the choice of an appropriate catalyst has been made, the photocatalytic efficiency of CO_2 reduction is mainly governed by: (i) the efficiency of light collection (ii) charge separation (due to charge conduction properties, governed by the dielectric constant of the semiconductor), as well as (iii) surface reactions (adsorption kinetics of reactants and desorption of products)³. The charge separation is a key parameter about the multielectronic reactions (Figure I. 1). In fact, these reactions need a large number of effective electrons on the surface.

Table I. 1: Oxidation-reduction reactions and associated potentials of gaseous elements, involved in CO_2 photoreduction in presence of water and calculated from $\Delta_r G^0$ ⁸

Product	Reaction	E^0 (V vs. NHE)	Eqn
Carbon monoxide	$\text{CO}_2 + 2\text{H}^+ + 2\text{e}^- \rightarrow \text{CO} + \text{H}_2\text{O}$	-0.10	(I. 1)
Hydrogen	$2\text{H}^+ + 2\text{e}^- \rightarrow \text{H}_2$	0	(I. 2)
Propane	$3\text{CO}_2 + 20\text{H}^+ + 20\text{e}^- \rightarrow \text{C}_3\text{H}_8 + 6\text{H}_2\text{O}$	0.155	(I. 3)
Ethane	$2\text{CO}_2 + 14\text{H}^+ + 14\text{e}^- \rightarrow \text{C}_2\text{H}_6 + 4\text{H}_2\text{O}$	0.162	(I. 4)
Methane	$\text{CO}_2 + 8\text{H}^+ + 8\text{e}^- \rightarrow \text{CH}_4 + 2\text{H}_2\text{O}$	0.19	(I. 5)
Oxygen	$2\text{H}_2\text{O} \rightarrow \text{O}_2 + 4\text{H}^+ + 4\text{e}^-$	1.23	(I. 6)

Among the reduction reactions mentioned in Table I. 1, the water reduction in dihydrogen (Eqn I. 2) represents the heart of research on water splitting to produce hydrogen as energetic vector. In the case of photoreduction of CO_2 , this reaction is a side one and in strong competition with the reduction of CO_2 to CH_4 , for instance. Indeed, despite its more negative potential ($E_{redox}^0(\text{H}^+/\text{H}_2) = 0 \text{ V} <$

$E_{redox}^0(CO_2/CH_4) = 0.19 V$, vs. NHE, pH = 0), the formation reaction of H_2 requires only two electrons, instead of eight for CH_4 ³, so it is kinetically favored even if thermodynamically less favorable.

c. Limitations

As described by Herrmann⁹, the overall process of heterogeneous photocatalysis can be decomposed into independent five steps:

1. Transfer of the reactants from the fluid phase to the surface
2. Adsorption of a least one of the reactants
3. Reaction in the adsorbed phase
4. Desorption of the products
5. Removal of the products from the interface region

Specifically, step 3 contains all the photoelectronic processes and can be sub-divided as follows:

- 3.1. Absorption of the photons by the solid
- 3.2. Creation of electron-hole pairs
- 3.3. Electron transfer reactions

These three steps are at the heart of the limitations of photocatalysis, especially regarding CO_2 photoreduction.

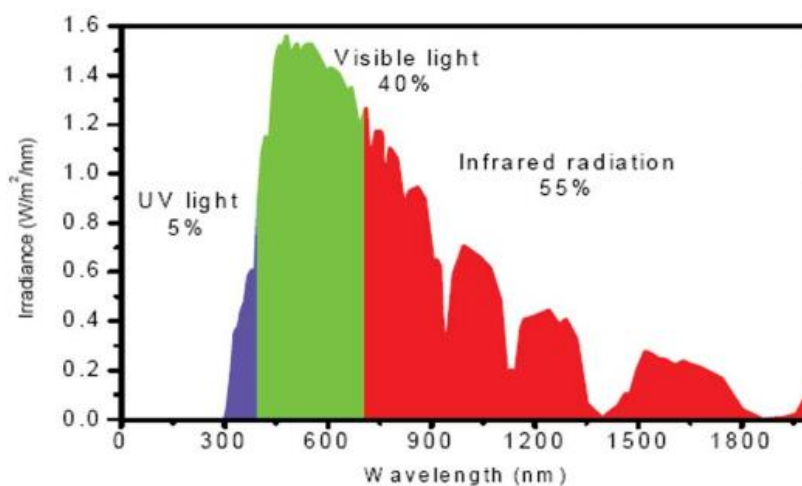


Figure I. 3: Solar spectrum reaching the Earth's surface after being filtered by the different gases in the atmosphere¹⁰

Furthermore, as alternative technology, a strong limiting parameter is the absorbable wavelength range by semiconductors. Many pristine semiconductors are activated by UV irradiation, related to the bandgap energy of semiconductors. Then, those semiconductors can absorb only 5% of the solar electromagnetic spectrum (Figure I. 3), which obviously limits the yields. To improve this point, a modulation of band-edge potentials is needed. Modulation may be performed on the

semiconductor, and usually metal ions (ferric, tungstate, etc), or non-metal ions (carbon, nitrogen etc) doping of semiconductors has a positive effect on the photoactivity in the visible part of the solar spectrum ¹¹. The combination of photosensitizers such as organic dyes or quantum dots with semiconductors allows one to reach interesting band-edge potentials ¹².

Light-harvesting is also a weight factor for photocatalytic yields. First, within the semiconductor, the extinction of light follows the exponential law:

$$I = I_0 * e^{-\alpha l} \quad \text{Eqn I. 7}$$

Where l is the penetration distance of the light and α the reciprocal absorption length. According to Hagfeldt and Grätzel ¹³ and Eqn I. 7, for bulk TiO₂ only 10% of incident light with a wavelength of 320 nm are transmitted through a 390 nm thick sample. In other words, light penetrates at best up to 600 nm (Figure I. 4 left), due to absorption. Strikingly, for colloidal suspension of TiO₂ nanoparticles, light penetration is also limited, due to diffusion. For high catalyst quantities, Herrmann ⁹ highlighted a screening effect of excess particles, which masks part of the photosensitive surface. This phenomenon results in the reaction rate, r , independent of the catalyst mass (Figure I. 4 right). Against this lack of light penetration, it could be considered to use thin films over a given area. To visualize what this surface would be, Domen *et al.* ¹⁴ exemplified this for a more mature technology (than CO₂ photoconversion), the water splitting. They suggested that to provide one-third of the projected energy needs of human society in 2050 from solar energy, a 250 000 km² area with a solar energy conversion efficiency of 10% would be required, corresponds to 1% of the earth's desert area.

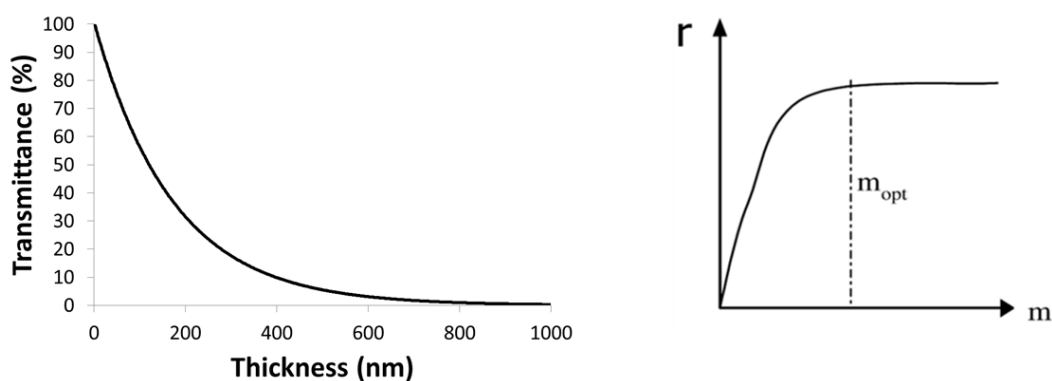


Figure I. 4: (left) Light penetration in bulk TiO₂, (right) Screening effect for $m > m_{opt}$ in TiO₂ slurry ⁹

As aforementioned, CO₂ photoreduction reactions are in competition with electron/hole recombination. This phenomenon is governed by the capacity of photocatalytic system to separate charge carriers. To be aware about the importance of the charge carrier recombination, Bahnemann *et al.* ¹⁵ propose to compare the time of possible photoinduced events, obtained by time-resolved analysis (Figure I. 5). It appears clearly that surface or bulk recombination need short time to occur compared to interfacial charge transfer. These values are dependent on the particle sizes and electronic structures of

the semiconductors. These are both scientific challenges on which researchers have focused their attention to improve the charge carrier separation.

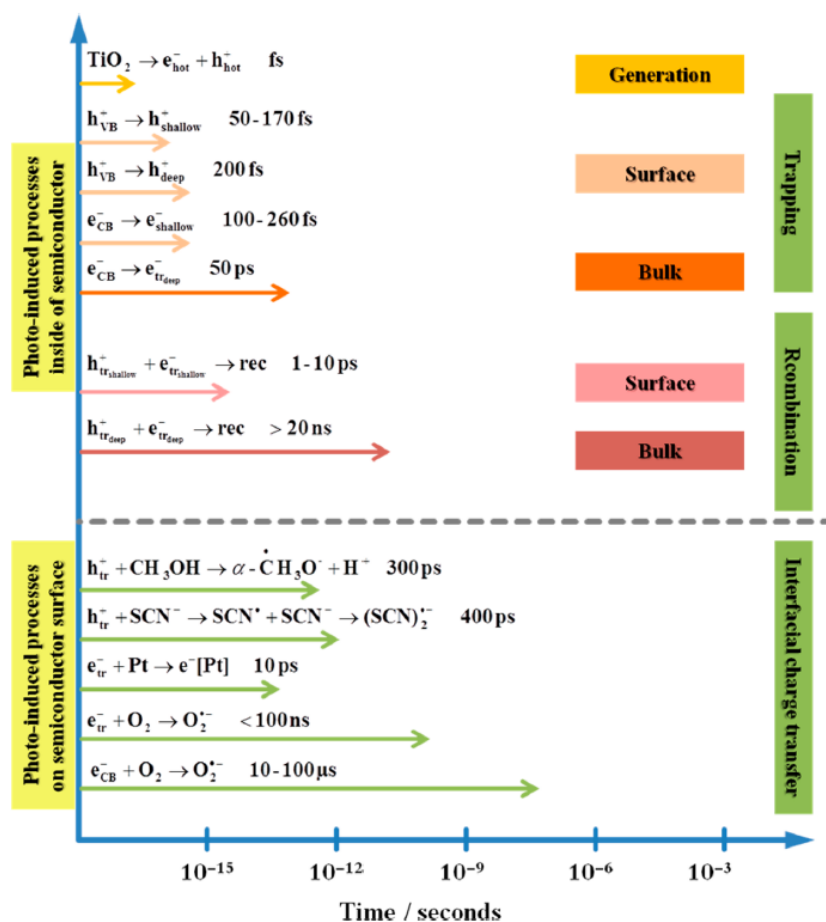


Figure I. 5: Overview of the possible photoinduced events inside and on the surface of a TiO_2 photocatalyst in the time scale region from femtoseconds to microseconds ¹⁵

The electron efficiency is commonly evaluated by the quantum yield. This is an apparent one, because diffusion, absorption, and migration of charge carriers are all considered. Losses of efficient electron are usually ascribed to recombination rate, which is considered as the limiting step of a photoconversion process. Moreover, photon diffusion through a material could also be a relevant origin of an efficient electron lack.

Beyond physicochemical limitations, the huge number of photocatalytic test conditions (e.g. lamp power) and evaluation (e.g. units) used confuses the information (Table A 1, Table A 2, Table A 3,¹⁶ in annex). In consequence, systems comparison between publications becomes difficult and each study must set the scene (e.g. P25 commercial TiO_2 powder as reference test) to evaluate photocatalytic performances.

2) Photocatalyst, case of TiO₂

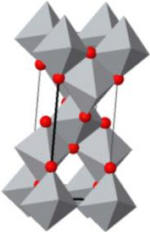
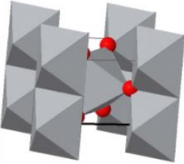
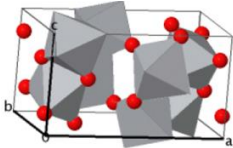
The definition proposed by Parmon *et al.*¹⁷ considers photocatalyst as “a substance that is able to produce, by absorption of light quanta, the chemical transformations of the reaction participants, repeatedly coming with them into the intermediate chemical interactions and regenerating their chemical composition after cycle of such interactions”.

a. Physicochemical characteristics of TiO₂

Of the many different photocatalysts, TiO₂ has been the most widely studied and used in many applications because of its strong oxidizing abilities for the decomposition of organic pollutants, superhydrophilicity, chemical stability, long durability, nontoxicity, and low cost.

Generalities

Table I. 2: Lattice parameters, bandgap energy, density and refractive index of the three crystalline phases of TiO₂. [a] the data are from 9852 ICSD records for anatase, 33837 for rutile and 36408 for brookite. [b] the data come from the reference¹⁸ [c] the data comes from the reference¹⁹

	ANATASE	RUTILE	BROOKITE
Elementary framework representation ^[a]			
Lattice parameters (Å) ^[a]	a = 3.7842 c = 9.5146	a = 4.5924 c = 2.9575	a = 9.174 b = 5.4492 c = 5.1382
E_g (eV) ^[b]	3.2	3.0	3.3
Density (g/cm⁻³) ^[a]	3.88	4.13	4.26
Refractive index ^[c]	2.5	2.7	2.6

Titanium dioxide has three major allotropic phases: anatase (tetragonal), rutile (tetragonal) and brookite (orthorhombic). The size dependence of the stability of various TiO₂ phases has recently been reported²⁰. Rutile is the most stable phase for particles above 35 nm in size. Anatase is the most stable phase for nanoparticles below 11 nm. Brookite has been found to be the most stable for nanoparticles in the range 11-35 nm range. Some of their properties are summarized in Table I. 2. All three are active in photocatalysis, but they offer different activities for photocatalytic reactions. The brookite has rarely been studied because of its metastability²¹. However, anatase, rutile, as well as anatase / rutile mixed-

phase have been the subject of numerous studies. In particular, the Degussa TiO₂ (P25) composed of a mix of about 80% anatase and 20% rutile, is used today as a reference for photocatalytic performance tests, due to its high photocatalytic activity^{22,23}.

Crystal structures

The TiO₂ crystalline structure consists of a sequence of TiO₆ octahedra sharing edges or vertices. The structures obtained differ by these octahedra assembly. Thus, the crystalline structure of anatase can be described as a three-dimensional sequence of TiO₆ octahedra bound by the edges. Each octahedron shares four edges. The structure of the brookite can be described from zig-zag octahedra chains where the TiO₆ groups are bound by the edges. These links form planes in the x and z directions. The connection between these plans is made in the direction y by the pooling of vertices. Each octahedron shares three edges. The rutile structure consists of linear sequences in the z direction of TiO₆ octahedra sharing edges. The connection between the chains is established by pooling vertices in the x and y directions. Each octahedron shares two opposite edges. The distortion of the structure increases as the number of edges shared between TiO₆ octahedra is large. The atomic packing factor increases in the opposite direction. These factors may involve differences in reactivity between polymorphs.

b. Modified TiO₂

To overcome the limitations of photo-catalysis, many ways of improving semiconductors have been explored. Two in particular are well known to address the problems of absorbed range of photons and charge carrier separation: the doping pathway and that by adding a co-catalyst, respectively. The influence of structuring a catalyst or catalyst support will be developed later. These considerations open up new possibilities for light trapping.

Doping modification: visible light response

The possibility of extending the absorption range of TiO₂ to the visible range by non-metallic atoms was discovered in 1986 by Sato²⁴. The presence of the NH₄Cl impurity has been demonstrated, certainly resulting from the hydrolysis of TiCl₄. These materials showed absorption at 434 nm and a photocatalytic activity 10 times greater than P25 in the case of oxidation of carbon monoxide. In recent years, much research has been done on the subject, revealing the possibility of extending the absorption spectrum of TiO₂ to the visible by a wide variety of non-metallic elements, such as N^{25,26,27,28}, C²⁹, S³⁰, B³¹, P³² and F³³.

Co-catalyst modification: charge carrier separation

By adding a metal co-catalyst, a heterojunction M/TiO₂ is created. The deposited metals on the surface of TiO₂ usually act as a sink for photo-generated charge carriers and can thus improve charge transfer processes at the interfaces. Inside the M/TiO₂ system, the photo-excited electrons are supposed to be transferred from the TiO₂ conduction band to the metal particles, while the holes remain on its

surface³⁴. A multitude of M/TiO₂ systems, where M is a metal such as Au^{35,36}, Pd³⁷, Pt³⁸, Cu³⁹ or Fe⁴⁰, have been tested in order to improve especially the separation of the charge carriers. Ishitani and Inoue⁴¹ have demonstrated their effect on the CO₂ conversion and the selectivity towards products by photo-deposition of a co-catalyst on TiO₂ P25 particles. The works of Wang *et al.*³⁸ particularly illustrate the size effects of the metal particles deposited on the separation of charge carriers.

By adding a semiconductor to the M/SC system (for example Pt-TiO₂), it is possible to create a structure called "Z-scheme", denoted SC2/M/SC1, representative of the energy scheme of natural photosynthesis⁴².

Crystalline phase mixture

Considering band gap energies, it seems obvious that there may be a significant difference in the photocatalytic performance of the three allotropic phases of TiO₂. These performances should logically be classified in ascending order as follows (under solar irradiation): brookite < anatase < rutile. Rutile holds the weakest band gap, and therefore absorbs photons in a wider range of wavelengths. However, Zhang *et al.*¹⁸ have shown that the nature of the gap, direct or indirect, strongly influences the electronic properties of the semiconductor. Indeed, rutile and brookite have a direct type gap (Figure I. 6) In this case, the electrons generated by the light irradiation can directly recombine with the holes of the valence band, by relaxing energy in the form of irradiation (photons). However, anatase has an indirect band gap and therefore requires the assistance of phonon¹ to make recombination possible (Figure I. 6). Thus, the charge carrier lifetime is longer for anatase and improves its photocatalytic activity.

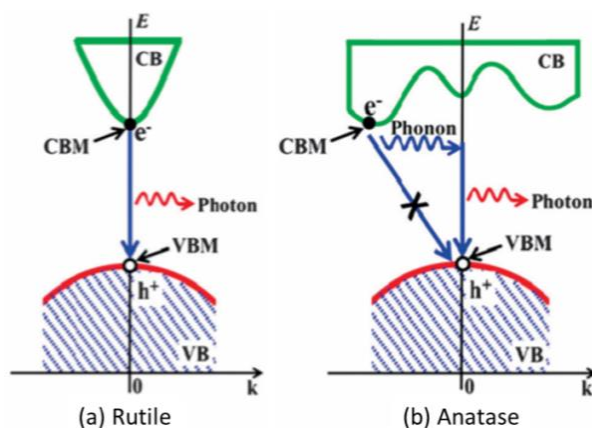


Figure I. 6: Recombination processes of photogenerated electrons and holes for a direct (a) and indirect (b) band gap¹⁸

¹ In physics of condensed matter, a phonon denotes a quantum of vibrational energy: when a vibrational mode of a crystal, with a defined frequency ν , gives or gains energy, it can occur only by blocks of $h\nu$ energy. This block is considered as a quasi-particle, called phonon⁴³.

For the P25 high photocatalytic activity, Hurum *et al.*²² proposed an explanation in which rutile plays an antenna role. Due to its weak bandgap energy (compared to anatase), a larger number of photons is absorbed. Then, photogenerated electrons in the rutile phase migrate rapidly to lower energy levels of the anatase one and then to its surface. According to the authors, the electron transfer rate depends to the crystallite size of rutile. Thus, the contact between two crystal structures and the crystallite sizes^{44,45,35} are both parameters that strongly influence the charge carrier separation and so, enhance the photocatalytic activity of the system (Figure I. 7).

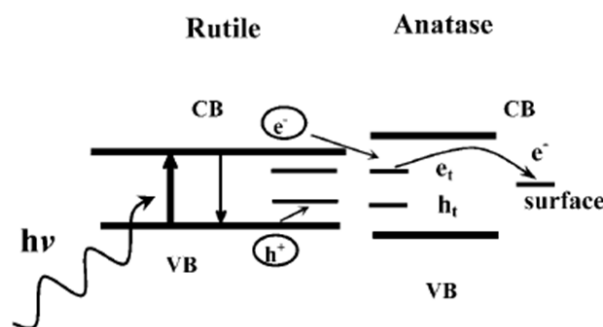


Figure I. 7: Model proposed by the authors where rutile plays the role of antenna, followed by a separation of charges²²

Beyond the nature of the heterojunction, the proportion between the two semiconductors in contact is also a key parameter. Zhao and Liu *et al.*²¹ studied the anatase / brookite ratio of the photocatalytic system during CO₂ conversion. From the CO production rates, the best proportion is the one involving 75% of anatase and 25% of brookite. This result seems consistent with the anatase / rutile proportion put forward by P25.

c. Morphological modification

In 1986, Anpo *et al.*⁴⁶ have shown that TiO₂ anchored into a silica structure makes it possible to improve products formation resulting from the photo-catalytic reduction of CO₂ in the presence of water. On this principle, they published in 2012 an article in which the performances of different TiO₂/SiO₂ systems were exposed⁴⁷. Figure I. 8 below illustrates the results obtained. To facilitate reading, a descriptive table of structures is joined.

The yields show that the use of a support structure in which TiO₂ is incorporated brings about a real improvement. The production of methane via the TS-1 structure indicates that the transfer of thin-layer shaping (TiO₂ powder) to a three-dimensional structure plays a decisive role. Similarly, the comparison between the TiO₂ powder and the TiMCM-41 structure highlights the importance of mesopores. The high photocatalytic activity of TiMCM-48 highlights the synergy of mesopores and three-dimensional structure⁴⁸. The palladium loading added to this structure also shows the impact of the Pd/TiO₂ heterojunction on the selectivity (orientation towards the production of methane at the expense of methanol)⁴⁹.

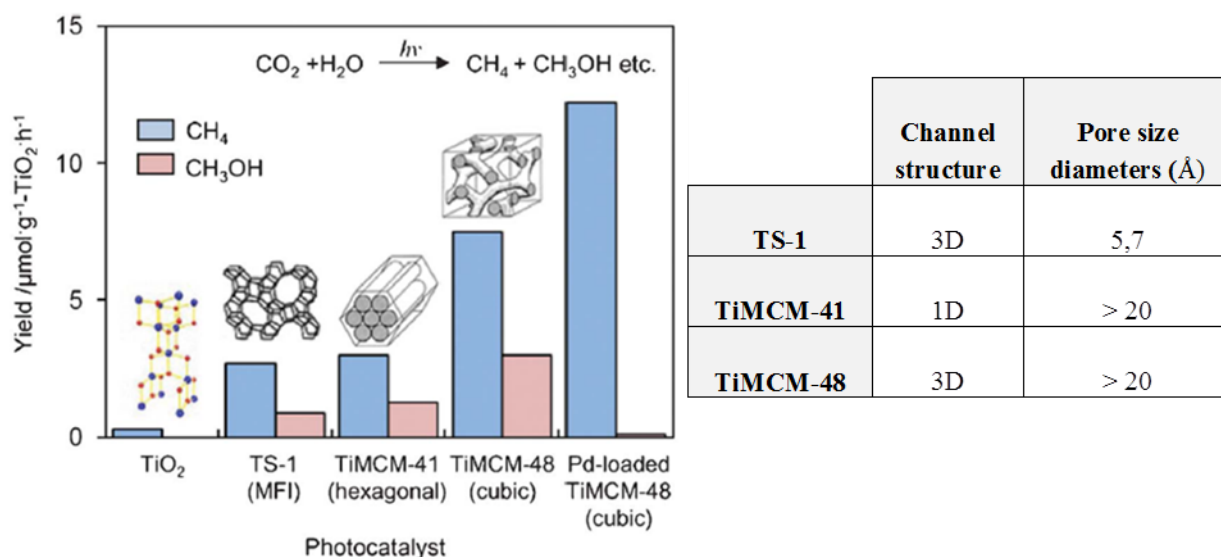


Figure I. 8: Methane and methanol yields on various catalysts: TiO_2 powder, TS-1 (zeolite), Ti-MCM-41, Ti-MCM-48 (molecular sieves), and Ti-MCM-48 loaded with Pd, and structures associated⁴⁷

Carbonell *et al.*⁵⁰ work in 2008 on structuring TiO_2 as a photonic sponge. A TiO_2 porous film bearing different calibrated pore diameters is synthesized to obtain highly scattering properties over a very wide wavelength range in the visible spectral region (Figure I. 9). The resulting photonic sponge exhibited a 3.3-fold higher initial succinonitrile photocatalytic degradation than analogous unstructured films.

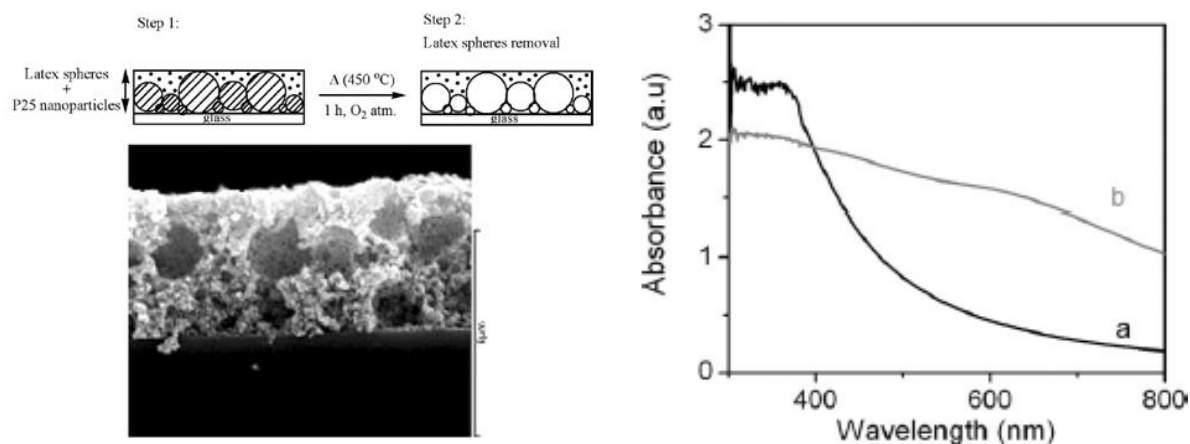


Figure I. 9: Preparation process of photonic sponges and SEM image of a cross section of a photonic sponge sample (left), and diffuse reflectance UV-Vis spectra of (a) 3 μm -thick film of P25 (b) 3 μm -thick photonic sponge (right)⁵⁰

Until now, one of the limitations of these photocatalytic systems is that large photonic crystals could not be prepared. Moreover, the preparation procedures developed up to now yield materials in which the concentration of defects is high enough to suppress or at least hinder the desirable properties. In accordance with their structuring strategy, Aprile *et al.*⁵¹ have reviewed the influence of semiconductor spatial structure on its photocatalytic activity. Especially they have concluded that

while many current approaches to influence the photocatalytic activity enhancement is based on chemical composition modification, control of the particle size and spatial organization of TiO₂ nanoparticles is also a powerful methodology to improve the photocatalytic efficiency.

Furthermore, Wang *et al.*⁵² synthesized TiO₂ monolithic particles comprising macro- and mesoporosity. To carry out photocatalytic evaluation, they packed monolithic particles (0.2-0.3 mm) into an 11 cm long 2.4 mm diameter fixed bed tubular reactor and studied the conversion yield of ethylene feed. Then, to emphasize the interest of macroporosity, they compare monolithic particles of anatase TiO₂ (T350 sample) before and after grinding (Figure I. 10). T350 samples provide similar behavior, with a rapid increase of conversion and then a plateau. However, this plateau is 1.5 times greater with the presence of macroporosity. The authors associate this enhancement to the macrochannels which act as a light-transfer path for introducing incident photon flux into the inner surface of mesoporous TiO₂.

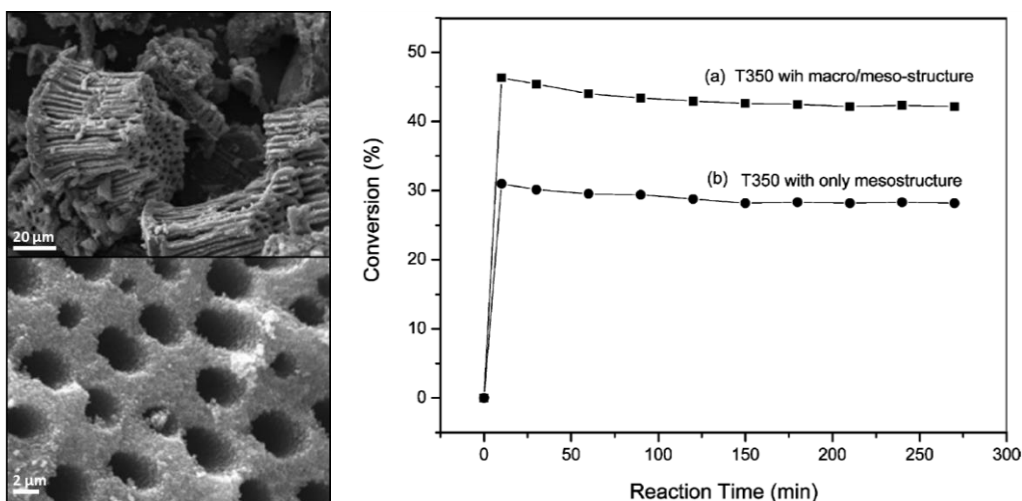


Figure I. 10: SEM images of T350 sample (left) and its photocatalytic activity (a) before and (b) after grinding (right)⁵²

To tackle photocatalysis limitations, a range of chemical methods have proven their worth. Structuring the meso- and macro-porosity of a catalyst or a catalyst support seems to deliver an interesting physical approach to improve photocatalytic yield. This porosity effect emphasizes the significant role played by the photon flux in the photocatalysis process and its dependence on light-matter interactions.

2 Light-Matter interaction

In photocatalytic processes, photons must be considered as reagents in the same way as chemical reactants (CO₂ and H₂O in this study). To understand how to optimize the use of this reactant and determine whether it represents a limiting step depending on conditions or materials, it is essential to understand its behavior.

1) Introduction to diffusion

Light is in constant interaction with the matter around us and gives rise to various phenomena such as the light scattering that meets the surface of a wall, its refraction when it passes through a glass, or its partial absorption and partial reflection by a plant leaf.

A common example used to put forward the phenomenon of light diffusion in a medium is the color of the sky. Light diffusion in the atmosphere originates from the scattering light by molecules in all directions (Rayleigh scattering)⁵³. The blue light is 6 times more scattered by these small molecules (N_2 , O_2 , ...) than of the red light. Thus, the sky appears blue because eye mainly receives in majority the blue fraction of the light spectrum displayed by the sun.

Light diffusion is then closely dependent on the size of the objects that light encounters and leads to the dissociation of three diffusion regimes. In addition to "Rayleigh scattering", "Mie scattering" corresponds to the light interaction with scatterers providing characteristic size comparable to the wavelength of the incident light. It is characterized by the formation of a "photonic nanojet", *i.e.* the scattered light has a strong anisotropy in intensity. Figure I. 11 compares these both different regimes. In short, the two regimes allow light to be diffused in all directions, with a different degree of anisotropy.

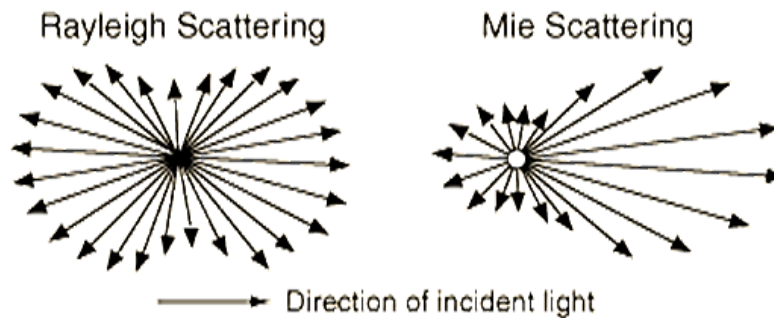


Figure I. 11: Comparison of Rayleigh and Mie scattering regimes⁵⁴

Finally, if the scatterers' dimensions are much larger than the wavelength of light, geometric optics and light rays describe the propagation of light. Figure I. 12 compares the two extreme regimes: particle diameter much smaller than the wavelength (a) and much larger (b).

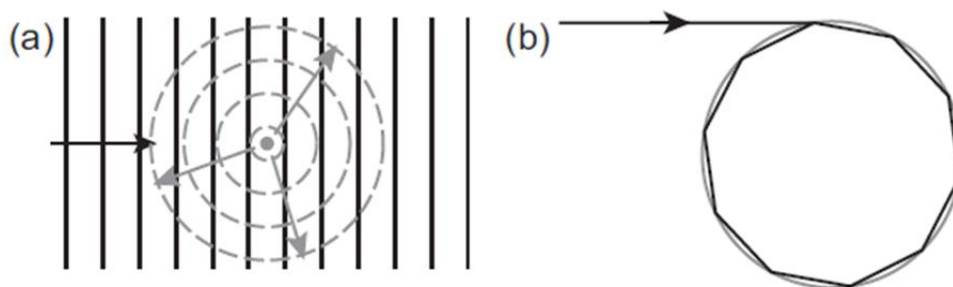


Figure I. 12: Comparison of extreme diffusion regimes (a) diffusion described by the Rayleigh regime, (b) geometrical optics⁵³

To trap light inside a material for photocatalytic purposes, a combination of these different phenomena can be a solution. By structuring the materials appropriately, it is possible to increase the interaction between the photons and the active phase. For a photocatalytic application, the longer the residence time of the light in the materials the more it will have the chance to activate a large number of catalytic sites. This remark makes particular sense in the case of a three-dimensional material compared to conventional thin-film systems, since multi-diffusive processes may play a major role.

2) Multi-diffusion theory

To discuss light diffusion inside 3D materials, a key parameter to know is the photon transport mean free path. A mathematical description of the experimentally measurable transmittance T ⁵⁵ versus either the thickness of the samples or the photons' times of flight can be obtained by solving the diffusion equation, as shown in the following section.

a. Diffusion equation

When light travels through a disordered porous material, it is multiple scattered. Multiple scattering theory is the mathematical formalism that is used to describe the propagation of a wave through a collection of scatterers. Examples are acoustical waves traveling through porous media, or light scattering from water droplets in a cloud⁵⁶. Straight or ballistic propagation, which is characteristic in a homogeneous medium, is not adapted here to describe the transport of light. Disordered porous materials may be associated with an isotropic random dielectric medium, and the standard diffusion model is used to quantitatively describe light transport in such a material.

The diffuse approximation considers a random walk of photons and imposes a continuity equation for the light intensity $I(\vec{r}, t)$ depending on space and time, and disregarding interference effects. To define the application limits of this approximation, it is necessary to introduce here a parameter, the scattering mean free path, l_s . It corresponds to the average distance between two consecutive scattering events. Then, diffusive approximation applies when $\lambda \ll l_s \ll L$, and $k\lambda \gg 1$, where k is the light wave vector. In other words, the diffusive approximation applies when several scattering events occur before the λ -wavelength light leaves the L -thick sample in a dilute medium. After several scattering events, the light propagation is completely randomized. The transport mean free path, l_t , is defined as the average distance after which the intensity distribution becomes isotropic and is the characteristic length in the regime of multiple scattering.

As a reminder, the continuity equation states that a change in density in any part of the system is due to inflow and outflow of material into and out of that part of the system:

$$\frac{\partial \phi}{\partial t} + \nabla \cdot j = 0 \quad \text{Eqn I. 8}$$

Where ϕ is the density, and j is the flux of the diffusing material. The diffusion equation can be obtained from this when combined with the phenomenological Fick's first law, which states that the flux of the diffusing material in any part of the system is proportional to the local density gradient:

$$j = -D(\phi, r)\nabla\phi(r, t) \quad \text{Eqn I. 9}$$

Then, diffuse light propagates in space (r) and time (t) according to the diffusion equation as follow in such a medium:

$$\frac{\partial I(\bar{r}, t)}{\partial t} - D \cdot \nabla^2 I(\bar{r}, t) = S(\bar{r}, t) - \frac{v_e}{l_i} I(\bar{r}, t) \quad \text{Eqn I. 10}$$

Where, $S(\bar{r}, t)$ is the light source, $I(\bar{r}, t)$ is the light intensity, and v_e is the energy velocity. Multiple scattering increases the interaction between light and the system. When the material which composes the system presents absorption, its effect is increased in a diffusive propagation⁵⁷. The inelastic absorption length, l_i , is the average depth at which light propagates ballistically (straightforward) in a homogeneous medium before being attenuated by a factor e. The diffusive absorption length, l_a , is the distance light propagates diffusively before being absorbed. Inside a diffusive and absorbing material, l_a is the penetration depth of the diffusive light. Diffuse light propagates a greater distance than in a homogeneous material to reach the same depth ($l_a < l_i$). However, both are not independent functions and are related by the following relation, introducing the transport mean free path (that is the length over which the photon propagation direction is randomized), l_t ⁵⁸:

$$l_a = \sqrt{\frac{l_t \cdot l_i}{3}} \quad \text{Eqn 11}$$

The diffusion equation is a very general and practical description of numerous transport processes in physics. In the case of light diffusion, it describes how light intensity spreads through the system with a rate of transport dictated by the diffusion constant, D . The larger the diffusion constant, the faster the transport processes. The whole diffuse transport may be truncated by absorption, which is introduced in the diffusion equation through the inelastic scattering term $\tau_i = v_e/l_i$, where the inelastic or absorption time τ_i is the characteristic time over which light is absorbed in the sample.

b. Boundary conditions and stationary solution

In this study case, the system is considered with a slab geometry, i.e. infinite for x and y directions and limited between $z=0$ and $z=L$, where L is the sample thickness. The diffusion equation can be solved once the boundary conditions are specified. It is assumed that there is no incoming flux through the boundaries, the only flux going from the boundary toward the inside of the slab is the reflected part of the outgoing flux⁵⁹:

$$J_+(z = 0^+) = -R_l J_-(z = 0^+) \quad \text{Eqn I. 12}$$

$$J_-(z = L^-) = -R_r J_+(z = L^-) \quad \text{Eqn I. 13}$$

Where R_l and R_r are reflection coefficients of the left (input) and right (output) boundaries, respectively. The coherent radiation incident on the slab is assumed to become randomized within a distance z_p , which is shown in Figure I. 13. The incoming coherent flux is replaced by a source of diffusive radiation at the plane $z = z_p$, with a strength equal to the incident flux.

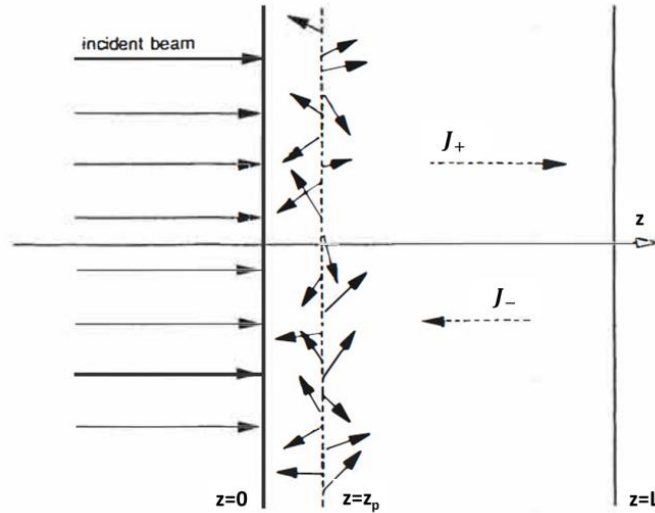


Figure I. 13: Geometry used for the calculation of the intensity profile inside the slab of random media. A plane wave incident on the slab is replaced by a source of diffusive radiation positioned at distance z_p from the material input⁶⁰

Usually boundary conditions for photon diffusion are written not for fluxes but for intensities. In this case it is incorrect to take zero intensity at the boundaries for diffuse photons inside the medium. To solve this problem, extrapolation lengths z_{el} and z_{er} beyond the boundary in which the intensity drops to zero is generally introduced. They are defined as solutions of the following equations:

$$\begin{cases} I(z = -z_{el}) = 0 \text{ for } z < 0 \\ I(z = L + z_{er}) = 0 \text{ for } z > L \end{cases} \quad \text{Eqn I. 14}$$

Where, z_{el} and z_{er} are the extrapolation lengths, which are the positions where the diffuse light intensity is zero and, might be different at the front and back surfaces (if their reflectivities are different)⁵⁸. Commonly, these lengths are set to be identical $z_e = z_{el} = z_{er}$. Then, the solution for Eqn I. 14 is⁶⁰:

$$\begin{cases} z_e = \frac{1}{2\alpha} \ln \left(\frac{1 + \alpha z_0}{1 - \alpha z_0} \right) \\ z_0 = \frac{2}{3} l_t \left(\frac{1 + R}{1 - R} \right) \end{cases} \quad \text{Eqn I. 15}$$

Where α is the inverse absorption length. The source of diffusing photons is provided by photons scattered away from the incident beam. This source is commonly introduced as an exponentially

decaying one $S(z) = S(0) \cdot \exp(-z/z_p)$ or a delta one $S(z) = S(0) \cdot \delta(z - z_p)$. Then, the stationary solution of Eqn I. 10 with boundary conditions Eqn I. 14, and for a delta source can be written in the form:

$$I(z) = I(z_p) \begin{cases} \sinh[\alpha(z + z_e)]/\sinh[\alpha(z_p + z_e)], z < z_p \\ \sinh[\alpha(L + z_e - z)]/\sinh[\alpha(L + 2z_e)], z > z_p \end{cases} \quad \text{Eqn I. 16}$$

$$I(z_p) = \frac{S_0}{\alpha D} \frac{\sinh[\alpha(z_p + z_e)] \sinh[\alpha(L + z_e - z_p)]}{\sinh[\alpha(L + 2z_e)]} \quad \text{Eqn I. 17}$$

Moreover, the total normalized transmission through the slab can be expressed as ⁶⁰:

$$T(L) = \frac{J_{transmitted}(L)}{J_{incident}} = \frac{1}{\alpha z_e} \frac{\sinh[\alpha(z_p + z_e)] \sinh[\alpha z_e]}{\sinh[\alpha(L + 2z_e)]} \quad \text{Eqn I. 18}$$

c. Full time-dependent solution

The full analytical solution of the time-dependent diffusion equation with boundary conditions is given by Patterson *et al.* ⁶¹, and adapted for a slab geometry infinite in x and y directions by Garcia *et al.* ⁵⁸:

$$T(t) = \frac{e^{-\frac{t}{\tau_i}}}{4t(4\pi t D)^{3/2}} \left(\sum_{j=-\infty}^{+\infty} A e^{-\frac{A^2}{4Dt}} - \sum_{j=-\infty}^{+\infty} B e^{-\frac{B^2}{4Dt}} \right),$$

$$A = (1 - 2j)(L + 2z_e) - 2(z_p + l_t),$$

$$B = (2j + 1)(L + 2z_e),$$

$$\tau_i = \frac{l_i^2}{D},$$

$$D = \frac{cl_t}{3n_{eff}} \quad \text{Eqn I. 19}$$

Where n_{eff} is the effective material refraction index if that is a multi-constituent one. According to the Eqn I. 19, light that follows shorter optical paths through the slab is transmitted at earlier times, while light that performs longer random walks emerges at much longer times.

The stationary and time-dependent solutions of the diffusion equations allow to determine the crucial parameters l_t and l_i through fitting of experimental curves either by the expression $T(L)$ given in Eqn I. 18 if transmittance T through the samples has been measured as a function of thickness L of the sample, or by the expression $T(t)$ given in Eqn I. 19 if transmittance out through a sample has been measured as a function of time t (time of flights of photons in the medium).

Diffusion theory constitutes thus a useful mathematical tool for describing the light propagation within a material. The main challenge of optimizing solar irradiation efficiency in the whole set of

artificial photo-driven processes concerns the light harvesting. Furthermore, the intrinsic 3D architecture within natural leaves strongly favors light harvesting in photosynthesis process⁶² *via* a synergy of the light-matter interaction phenomena (focusing of light by the lens-like epidermal cells, the multiple scattering and absorbance of light within the veins' porous network, and so forth). Then, Zhou *et al.*⁶³ replicated this leaf's 3D hierarchical architecture and compared its photocatalytic performances to that of its corresponding powder constituents. They found that leaf-architecture exhibit about 1.5-fold improvement in activities. Inspired by the living world, this work promotes the synthesis of hierarchically porous architectures improving light confinement.

3 Integrative chemistry for genesis of porous architectures

The concept of integrative chemistry, where the final function of the compound induces the skills needed to reach it, opens the way for rational approach to the design of innovative functional architectures, functions ranging from catalysis to optics via sensors or phase separation methods, and so on⁶⁴. Then, materials properties are highly dependent on their architectures. This phenomenon can be observed in nature where materials possess architectures which confer to the organisms the best properties according to their need (diatom frustules, butterfly wings, ...) ⁶⁵. Scientists have been researching to reproduce principles or structures described in animals or plants, and scale-up to human needs⁶⁶.

In this part, different synthesis processes are described for the genesis of complex architectures in a first part. Then, we subsequently focus on the sol-gel process, such as a tool of integrative chemistry.

1) Alveolar materials bearing hierarchical porosity

As mentioned above, a multi-scale porosity must have a great interest, especially for light-matter interactions regarding the targeted applications in this manuscript, but also for fluid transport⁶⁷. The following parts deal with parameters used to describe porous materials and synthetic pathways to formulate alveolar materials with hierarchical porosity.

a. Notions of pores and textural parameters

A porous material is a biphasic medium composed of a solid continuous phase and a fluid dispersed phase⁶⁸. Porous materials have cavities or channels, called pores, whose walls are responsible for an increase in the specific area. Porosity or void fraction is a quantification of the void spaces in a material. It is defined by the ratio:

$$\phi = \frac{V_p}{V_t} = \frac{\text{Volume of pores}}{\text{Total volume}} \quad \text{Eqn I. 20}$$

Where, total volume represents the volume occupied by the entire material, also called apparent volume. A value of porosity can be alternatively calculated from the bulk density ρ_{bulk} , and solid phase density (if no pores) ρ_0 . Then:

$$\phi = 1 - \frac{\rho_{bulk}}{\rho_0} \quad \text{Eqn I. 21}$$

Directly related to the concept of porosity, there are several types of densities which provide complementary information, especially on the nature of the porosity (Figure I. 14):

- **“Real” density**: excluding any form of porosity, ρ_0
- **“Skeletal” density**: including “closed” porosity, which is inaccessible pores set (blue ring)
- **“Apparent” density**: including all pores, especially “open” or “connected” ones, which are accessible by an external fluid (green ring).

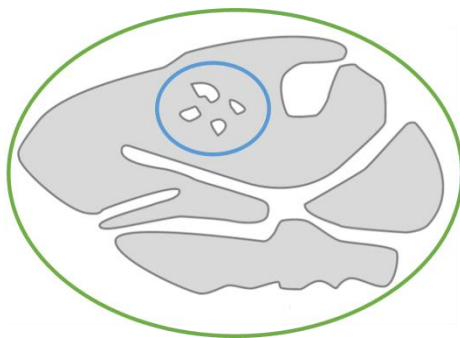


Figure I. 14: Overview of a porous grain ⁶⁹

Nevertheless, since the notion of accessibility depends closely on the probe fluid used to characterize the material, it clearly appears that each of the densities defined above is relative and may thus take on a different value depending on the employed technique ⁶⁷.

For powder, another kind of density could be distinguished, the so-called **“packing” density**. Its value depends on how powder is packed and is defined as the ratio between the mass of introduced powder over the cell volume.

The properties of a porous solid depend essentially on the geometry (Figure I. 15) and size of the pores as well as their distribution (Figure I. 16). According to the International Union of Pure and Applied Chemistry (IUPAC), there are three types of pores: macropores whose width is greater than 50 nm; mesopores whose width is between 2 and 50 nm; and micropores whose width is less than 2 nm.

Two other characteristic quantities of porous materials deserve also to be emphasized. On the one hand, the surface area represents the interface area between the solid and fluid phases per unit mass volume. It is noted S_{BET} , in relation to the BET (Brunauer-Emmett-Teller) method used to determine its value. On the other hand, the porous media are differentiated by the connectivity that exists between the

pores. Intuitively, fluid flows associated with the passage of a wave in the middle are sinuous ⁷⁰. The tortuosity T characterizes this phenomenon.

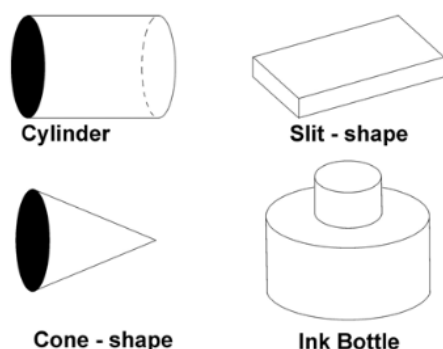


Figure I. 15: Pores geometry classification ⁷¹

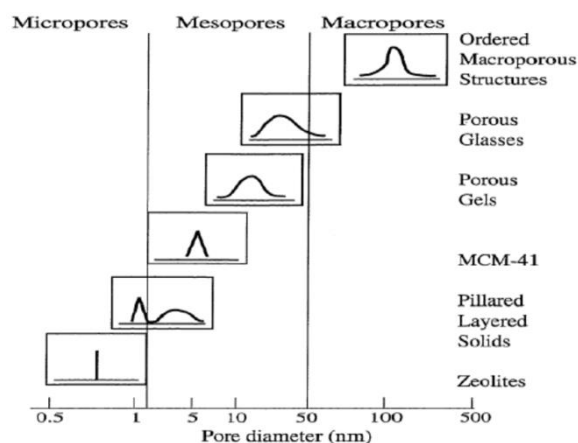


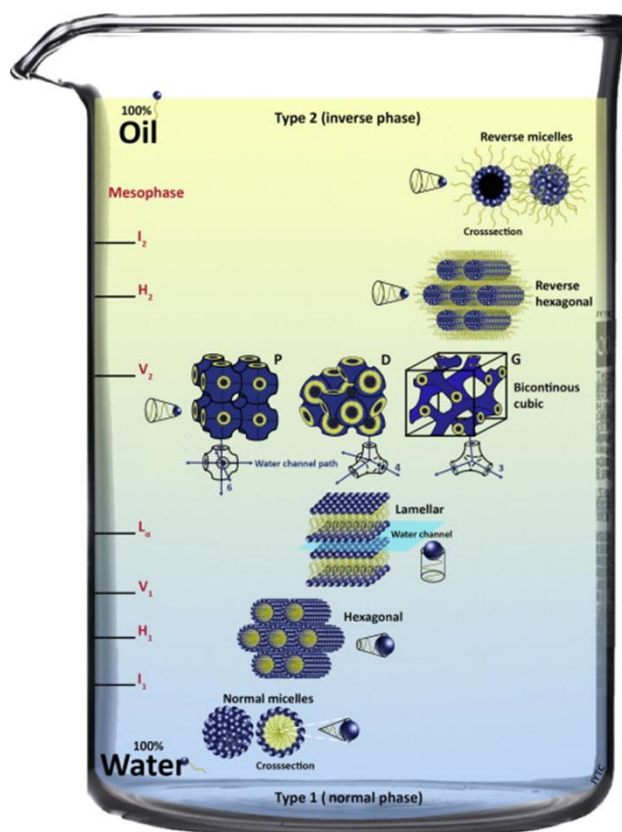
Figure I. 16: Schematic illustrating pore size distribution of some porous materials ⁷²

In general, the properties deployed by a material, and more particularly by a porous medium, are directly related to these morphological and / or structural characteristics. Chapter II will describe the characteristics of the materials synthesized during the project.

b. Synthetic pathways of 3D systems

The genesis of complex entities (multi-scale, multi-functional, ...) by integrative chemistry method is based on combinations of nature, morphology and structure of compounds, where chemical reactors can be now rationally positioned within the geometric space. For alveolar materials bearing hierarchical porosity, i.e. multi-scale porosity, each porosity scale is derived from the structuring, the arrangement of the elements used during the synthesis.

Concretely, the microstructure is based on the connectivity of basic molecular patterns. These patterns can be organic monomers (assembled by polymerization), alkoxydes (by hydrolysis-condensation), supra-molecules (self-assembled by weak bonds), or also mineral salts. The synthesis of this microstructure in the project framework will be detailed in the next part for silica sol-gel process. Secondly, the constituent elements of the microstructure have the possibility of organizing themselves at the mesoscopic scale, around templates ⁶⁴. Currently, these templates are mostly organic and organized *via* weak bonds, typically amphiphilic molecules (or particles) ⁷³. At the mesoscopic length scales, template-effect can also be induced by phase separation, spinodal decomposition, hydrodynamic instabilities, that will extend at the macroscopic length scale.



After removing them, mesopores are formed whose shape depends on the supramolecular assembly of the amphiphilic entities (for concentrations above CMC, critical micelle concentration): for instance, lamellar, hexagonal or worm-like phase (Figure I. 17⁷⁴). According IUPAC, these phases are called lyotropic mesophases and defined as mesophase formed by dissolving an amphiphilic mesogen in a suitable solvent, under appropriate conditions of concentration, temperature, and pressure⁷⁵.

Figure I. 17: An illustration of the main types of lyotropic liquid crystal phases depending on the interface curvature (molecular shape or concentration in water)

Then, micro- and mesostructures can be organized at the macroscopic length scale. This one is often produced by taking advantage of complex fluids in using metastable thermodynamic templates like for examples foams, emulsions, instabilities hydrodynamic phenomena of phase separation or the application of external shaping mode (electro spinner, spray dryer, extrusion). These techniques are detailed in following part. Furthermore, the generation of a macrostructure, and more precisely of a macroporosity, can be envisaged by the incorporation of porogens called hard templates, and will be stated in the last part.

Soft templates: foams and emulsions

Two categories of bi-phasic system composed of two non-miscible phases can be found: foams (air-liquid foam) and emulsions (bi-liquid foam). Foams and emulsions are then ternary systems which are composed of a liquid as continuous phase, amphiphilic molecules (or particles), and a non-miscible phase dispersed in the continuous one⁷⁶. Emulsions typically involve an oil and an aqueous phase. Note that two types of emulsion are distinguished: the so-called direct emulsion, for which oil is dispersed in water, and the so-called inverse one, where water is dispersed in oil. To disperse the non-miscible phase (air or liquid), an input of energy into the system is required, such as mechanical agitation. Then, interfaces between both phases are created and metastable. The amphiphilic molecules then act as stabilizer to maintain the bi-phasic system over time. The cohesion of a liquid is due to molecular attractive forces such as Van der Waals forces and hydrogen bonds. In consequence, creating an interface imply to counter these forces. In this sense, saturation of the interfaces by amphiphilic

molecules, typically surfactants, makes it possible to lower the energy required to destroy the intermolecular bonds per unit of surface created.

Nevertheless, these systems remain metastable over time (the surfactants expand the time scale) and tend towards a situation of thermodynamic equilibrium resulting in a macroscopic phase separation. Destabilization of such systems involves the following phenomena: creaming or sedimentation (according to the density of the dispersed phase), flocculation (aggregates formation), drainage and coalescence (disappearance of the film separating two droplets or bubbles and their fusion), and Ostwald ripening (droplets or bubbles fusion governed by Laplace law)^{77,78}.

On a dimensional point of view, the bubbles of foam can reach diameters between 10 microns and a few millimeters⁷⁹. Undeniably, the step of template (air) elimination is not necessary. As regards the emulsions, the size of the dispersed droplets is typically of the order of one micrometer, in a range from 0.1 to 100 μm ⁷⁶. In addition, the dispersed phase elimination is potentially achievable by a simple liquid extraction.

The use of "air-liquid" systems for obtaining macrocellular materials is promising. However, the conservation of calibrated monolithic structures is strongly dependent on the drainage, and its control is generally delicate. In addition, the inorganic monoliths obtained often have a relatively low mechanical strength, thus considerably limiting the possible applications⁶⁷. In the following, "liquid-liquid" systems will be then emphasized.

As mentioned before, an emulsion is a system comprising two immiscible liquids, one of which is dispersed in the other, and stabilized by surfactants. The relative affinity of a surfactant for water and oil is often characterized by a number dimensionless, called HLB (Hydrophilic Lipophilic balance), and introduced in 1949 by W. C. Griffin⁸⁰. Its value indicates in which phase the surfactant is the most soluble. Then, the lipophilic character of a surfactant helps to anticipate the types of emulsion (W/O or O/W) it will form since, according to Bancroft's rule⁸¹. Besides, the addition of surfactant to a bi-phasic system decreases the interfacial tension between the two phases as the surfactant concentration increases. Thus, the HLB method makes it possible to apprehend the stability and the final nature of the emulsion.

Furthermore, by raising the dispersed phase volume fraction above 70%, random compact arrangement of droplets can be obtained, leading to a High Internal Phase Emulsion (HIPE)⁸². Then, droplet act as templates around which the continuous phase reacts and form the micro- and meso-structure. So that when the dispersed phase is removed, the resulting structure reveals a very open structure. This kind of emulsion is classified as concentrated emulsion^{83,84}. It is justified by a chemical reaction initiated at the oil/water interface, then considered as reactors. Interfaces act as macroscopic defects where the nucleation enthalpy will be minimized because then considered as a heterogeneous nucleation. For example, during the precursors condensation that will form the first germs, solid/liquid interfaces appear, which have an energy cost. This energy cost is counterbalanced by the energy of volume gained during the formation of germs. This phenomenon is visualized by a small material shrinkage. Moreover,

chemical reactions are spatially confined in a concentrated emulsion. Then, a chemical reaction can propagate from a reactor to another, generating a monolithic material. Monoliths are defined as bulk gels (smallest dimension ≥ 1 mm) cast to shape and processed without cracking⁸⁵, *i.e.* remaining self-standing character.

Controlled phase separation

The use of the phase separation mechanism, via a spinodal decomposition process, for the integration of a controlled macroporosity within silica gels, was introduced as early as 1992 by K. Nakanishi *et al.*⁸⁶. Generally, this process involves a ternary system composed of an inorganic precursor (typically silicon alkoxide), a solvent (often acidified water) and an organic additive (typically a polymer) (Figure I. 18). The structuration of the porous material is based on a kinetic competition between phase separation and solidification.

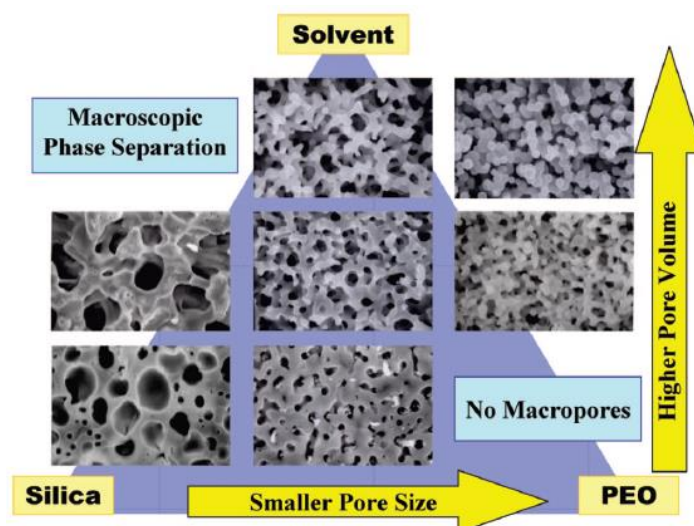


Figure I. 18: Schematic relations between starting compositions and resultant gel morphologies in a pseudoternary [silica/poly(ethylene oxide)/solvent] system⁸⁷

In addition to temperature, pH, and species concentrations, the modification of the polymer chemical nature, *i.e.* modification of its interactions with the hydrolysed precursor, governs the final morphology of the gel. It is thus possible to vary both the pore sizes (from 50 nm to 50 microns) and their connectivity. However, gels thus obtained suffer from a lack of mechanical strength. A dissolution-condensation step in a basic solution is necessary to improve their mechanical resistance⁸⁸.

Several examples of improved catalytic reactions or adsorption processes in liquid media have been highlighted using this type of monolith^{89,52}. Despite the success of this method, the difficulty of controlling separately the different porosity levels as well as the need for the post-condensation step for obtaining of a monolith led to the search for alternatives.

Hard templates

The hard template use for the genesis of macroporous materials has been especially reported by S. Davis *et al.*⁹⁰ in 1997, who used a bacterium made of co-aligned filaments (*Bacillus Subtilis*) in order to obtain macroporous fibers made of silica. Later, this strategy was extended to include organic chitin skeletons from the cuttlefish⁹¹, followed by frustules of diatoms⁹². For all these systems, the principle is to impregnate the natural structure with the sol precursor of the material desired, and to trigger the sol-gel reaction. Although natural materials allow the synthesis of interesting structures, some applications require specific structures that cannot be synthesized by this method because of the lack of suitable templates in nature.

Another approach aims at separately synthesizing organic calibrated particles, called colloidal crystal, and incorporating them in a gel. After gel ageing, organic templates are removed by a thermal treatment. Thus, by modulating the diameter of spherical organic templates, (typically from 200 nm to 1 μm), inorganic skeletons with hierarchical porosity can be easily obtained. This process was extended by B. T. Holland *et al.*⁹³ to the polymerization of various metal alkoxide sols for the synthesis of macroporous alumina, zirconia, and titanium oxide. Typically, templates are often polystyrene ones. Especially, Ramiro-Manzano *et al.*⁹⁴ take advantage on the multiple particle sizes that could be obtained to synthesize a photonic sponge of TiO_2 with apollony architecture (Figure I. 19), to optimize the light trapping.

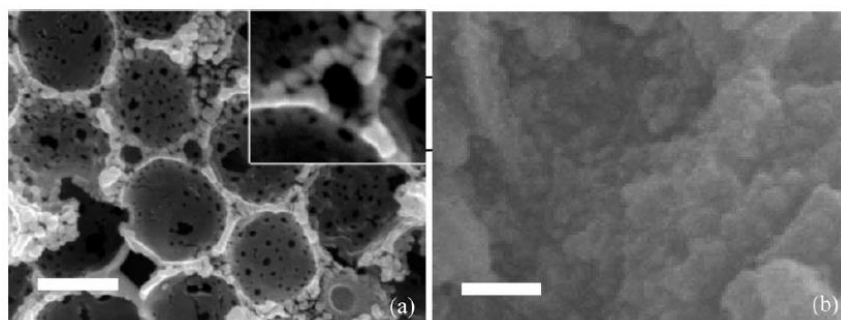


Figure I. 19: SEM images of titania nanoparticles arranged in a photonic sponge architecture (a) or in a packed manner. Scale bars: 1 μm .⁹⁴

Beyond polystyrene, polymethyl methacrylate particles are also widely used^{95 96}. Since the successful synthesis of mesoporous molecular sieves⁹⁷, template methods have been extended widely to various colloids⁹⁸, and surfactants⁹⁹. Consequently, porous silica materials with various morphology and pore shapes has been synthesized in the past 20 years, such as spheres, vesicles, tubular particles, core-shell particles with double shells and so on¹⁰⁰. However, the materials are often obtained in the form of powder or small size monoliths, due to the critical step of template removing by either thermal or chemical means.

2) Inorganic polymerization: silica-based sol-gel process

The sol-gel path makes it possible to synthesize materials, whose structure is controllable. Sol-gel chemistry is one of the tools of integrative chemistry leading to materials with hierarchical porosity. The following information is essentially extracted from “Sol-Gel Science”, written by C. J. Brinker *et al.* ¹⁰¹. There are two ways of sol-gel synthesis: the inorganic route or, the metallo-organic pathway, from metal alkoxides, which interests us in this part.

The starting sol is a colloidal suspension in which the dispersed phase has a characteristic size (≈ 1 -1000 nm) such that the gravitational forces are negligible, and the interactions are dominated by short-span forces, such as Van der Waals, and by the surface charges. This sol can be of different forms: a colloidal suspension of solid particles in liquid, liquid or solid particles in a gas; or a dispersion of liquid drops in another liquid (emulsion). The process of sol-gel chemistry is carried out under the conditions of soft chemistry, and involves solution polymerization reactions of organic species, from molecular precursors. These precursors are generally metal alkoxides, of the form $M(OR)_n$, where M is a metal with a degree of oxidation n, and OR an alkoxide group corresponding to a deprotonated alcohol. The polymerization reactions lead to the development of oxide frameworks ¹⁰².

The most used and studied metal alkoxide is tetraethylorthosilicate (TEOS), $Si(OEt)_4$. After activation of the TEOS precursor by hydrolysis, the condensation of the species results in the formation of the silica gel. In this part, the mechanisms of hydrolysis and condensation for SiO_2 case will be described, as well as the various resulting gels.

a. Generalities

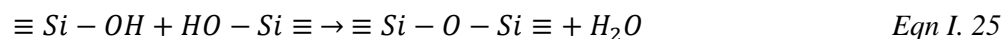
The first step of this solution polymerization is therefore hydrolysis. At first, it leads to the formation of hydroxyl functions around the metal atom, and then a nucleophilic substitution reaction occurs to deprotonate the water molecules solvating the alkoxide. The alkyl groups are then removed in the form of alcohol. Hydrolysis can be partial (*Eqn I. 22*) or, under certain conditions, complete (*Eqn I. 23*):



This step is very slow with pure water. Therefore, it requires the addition of a catalyst, acid or basic, which influences the final gel form (§3.2.c). In addition, it has been seen that the hydrolysis reaction is generally faster and complete under acidic conditions, while highest condensation rate is obtained at around pH 4.

Following the activation of the precursor, the condensation step takes place and can be done on two ways. The condensation of two alkoxides of which only one has been hydrolyzed is the olation (*Eqn I.*

24). However, when it occurs between two hydrolyzed alkoxides, then is oxolation (Eqn I. 25). Generally, one or the other of these reactions depends on the ratio $r = H_2O/Si$: for $r \ll 2$, the mechanism forming the alcohol is favored; whereas for $r \geq 2$, the mechanism forming water is favored.



The sequence of the condensation reactions leads to the formation of oligomers, then to a three-dimensional framework bonded by siloxane bridges, Si-O-Si. During these mechanisms, a characteristic parameter can be determined, the *gel point*. It is defined as the time at which the last gel-forming bond is formed and results in a sudden change in viscoelastic properties¹⁰³, the “caking” of the sol. The gel is defined as a substance that contains a continuous solid skeleton enclosing a continuous liquid phase. Then, the last precursors present in the liquid phase still react with each other or with the skeleton of the gel, during the so-called ageing stage. Finally, the syneresis phenomenon occurs for certain gels. The formation of bonds or the attraction between particles leads to the framework shrinkage and the expulsion of the solvent present in the pores. This phenomenon is visible both during condensation and during drying. It is then possible to distinguish two types of dry gel. The first is *xerogel*, resulting from drying under normal conditions of evaporation of the solvent. Due to the capillary pressures imposed by the drying, the dried material has a reduction on its volume by a factor of 5 to 10, compared to the volume of the wet gel. However, when the drying is carried out under supercritical conditions, the absence of liquid-vapor interface eliminates the capillary pressures. The material does not undergo a shrinkage and the resulting gel is called *aerogel*. To finalize the synthesis of these materials and obtain a structure with great mechanical strength, it is necessary to perform a heat treatment, allowing the densification of the structure. A summary of the different steps and products formed is shown Figure I. 20.

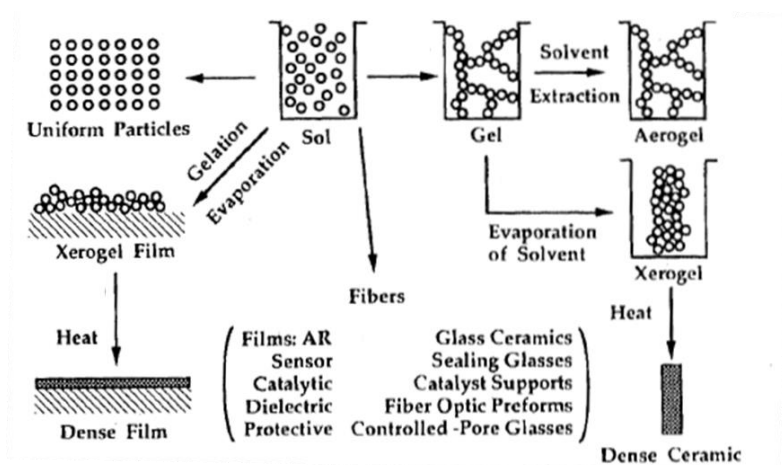


Figure I. 20: Overview of the steps involved in the sol-gel process¹⁰¹

b. Hydrolysis mechanisms

Hydrolysis occurs by the nucleophilic attack of the oxygen present in the water molecule on the silicon atom. This reaction is largely influenced by the steric and inductive effects which differ according to the type of used catalyst, acid or basic. In both cases, the mechanism supported by the scientific community is a bimolecular nucleophilic displacement reaction (S_N2 -Si reactions) involving pentacoordinate intermediates or transition states.

Acid-catalyzed hydrolysis

Under acidic conditions, the alkoxide group is protonated in a rapid first step. Electron density is withdrawn from silicon, making it more electrophilic and thus more susceptible to be attacked by water. The water molecule attacks from the rear and acquires a partial positive charge. The positive charge of the protonated alkoxide is correspondingly reduced, making alcohol a better leaving group. The transition state decays by displacement of alcohol accompanied by inversion of the silicon tetrahedron (Figure I. 21).

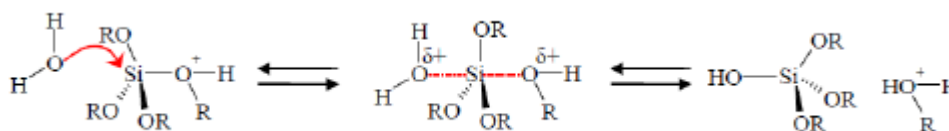


Figure I. 21: Hydrolysis of a silicon alkoxide in an acid medium ⁶⁵

Base-catalyzed hydrolysis

Under basic conditions, the first step is a rapid dissociation of water to produce nucleophilic hydroxyl anions. The hydroxyl anion then attacks the silicon atom, according to an S_N2 -Si mechanism in which OH^- displaces OR^- with inversion of the silicon tetrahedron (Figure I. 22).

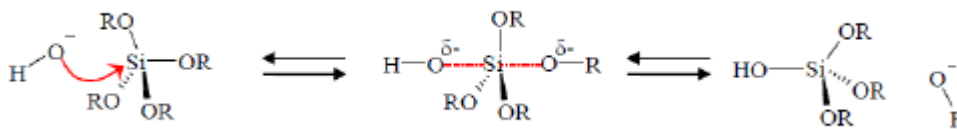


Figure I. 22: Hydrolysis of a silicon alkoxide in a basic medium ⁶⁵

The catalyst choice influences the mechanism without changing either the type of intermediate or involved reaction.

c. Condensation mechanisms and *sols* growth

Although the condensation of silanols can proceed thermally without involving catalysts, their use especially in organosilanes is often helpful. To clearly visualize the catalyst impact on the condensation reaction, Figure I. 23 shows the pH-dependence of the average condensation rate.

According to Figure I. 23, there is a minimum close to pH 2, which corresponds to the isoelectric point of the silica ($pI_{\text{silica}} = 2.1$). It makes it possible to define the domain, $pH < 2$, for which the silanol groups on the surface are protonated, and $pH > 2$, for which they are deprotonated.

Under acidic conditions ($pH < 2$), the protonation of silanols brings the electrophilic nature out of the silicon atom, favoring any nucleophilic attack. Thus, the lower the pH, the greater the kinetics of condensation. The most favorably protonated silanol groups are those which logically have the most marked base character. In other words, they are those which carry the most protonated hydroxide groups, *i.e.* the monomers and the ends of the polymerized chains. Thus, in strongly acidic medium, the kinetics of reactions are such that the hydrolysis is almost complete when the condensation begins. This induces the formation of open and branched particulate networks. When the pH increases towards the isoelectric point of silica, the silicic species are neutral, which strongly reduces the surface energies and thus leads to the formation of weakly-branched structures characterized by a low fractal dimension, $d_f \approx 2$ (Euclidian nature).

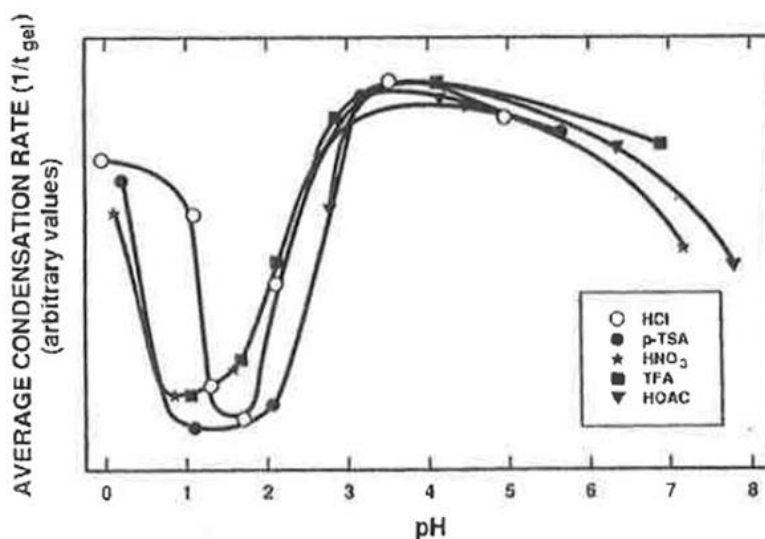


Figure I. 23: Evolution of the condensation rate as a function of the pH for different catalysts ¹⁰¹

Under more basic conditions ($pH > 6$), the most deprotonated silanols are the most condensed. The reaction rate progressively increases as the condensation progress. Monomers are added to highly condensed clusters; whose density increases with pH. In addition, the high concentration of hydroxyl ions destabilizes the siloxane bridges by increasing the coordination of the silicon atoms. Then, a dissolution-precipitation phenomenon occurs leading to particle densification. The basic pathway therefore tends to the formation of Euclidean objects (definition at the end of the part), all the denser as the pH is away from the silica isoelectric point. The so-called Stöber process ¹⁰⁴ takes place under these conditions. After nucleation, growth and ripening, it results in the formation of spherical particles, dense and monodisperse in size.

At pH conditions, the ratio $r = H_2O/Si$, which also strongly influences the final structure of the material, is added. For instance, at a neutral pH, for a ratio r much less than 4 (empirically determined

value), hydrolysis is the limiting step, *i.e.* some sites remain non-hydroxylated (partial hydrolysis). The nucleation/growth competition is then in favor of a growth mechanism. This results in mass or surface fractal objects, or uniformly porous objects as a function of the number of non-hydroxylated sites.

As a reminder, mass and surface fractal objects are distinguished from Euclidean objects as follows. In the first case, the mass m of the fractal object increases with the radius r of the object according to $m \propto r^{d_f}$, where d_f is called the mass fractal dimension and $d_f < 3$, while $m \propto r^3$ for an Euclidean object. That is, the larger the object, the less dense it is (*e.g.* trees). In the case of surface fractal objects, their area S increases more rapidly than r^2 : $S \propto r^{d_s}$ where d_s is the surface fractal dimension. For example, a crumpled sheet of paper has a mass that increases along r^3 , while its crumpled surface is fractal.

4 PhD project and aim

The photochemical CO₂ conversion requires meeting certain conditions to become competitive and take part in the energy mix, as a renewable energy: use low-cost systems that deliver energy efficiency above 10%¹⁰⁵, produce fuels that can be easily stored and transported, and use renewable resources. Indeed, one of the major disadvantages of renewable energies lies in the intermittent nature of the resources which leads to consider its storage for a large-scale upgrading.

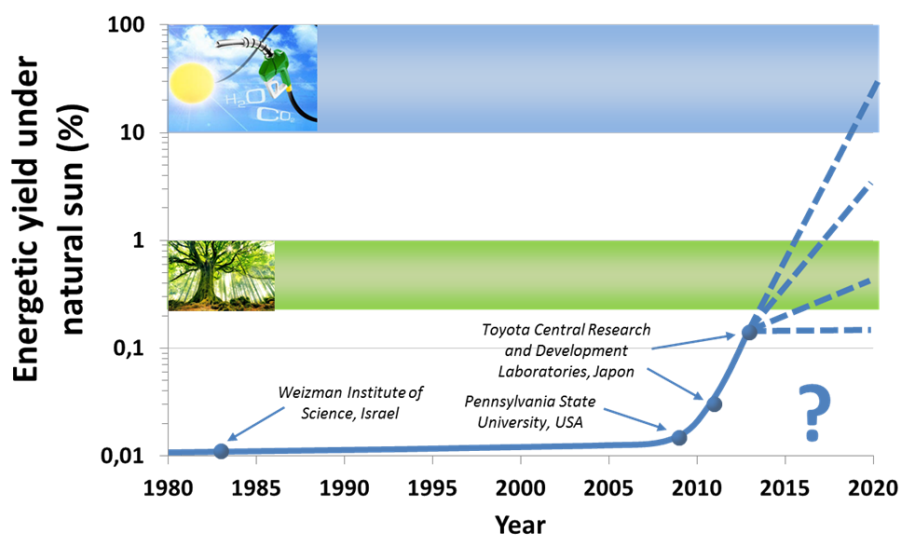


Figure I. 24 :Significant progress in converting carbon dioxide into solar fuels¹⁰⁶

In recent years, CO₂ has been successfully converted using sunlight into high value-added hydrocarbons. However, reaction rates and selectivity in desired products such as methane, and C₂₊ are still too low to consider industrial applications (Figure I. 24). Main drawbacks are arising from the photocatalytic process itself, *i.e.* light trapping and harvesting, charge separation-recombination and transportation, surface and backward reactions, and need to be optimized. In this perspective, main

research topics deal with: the modification of the intrinsic properties of semiconductors, the discovery of new architectures or composite structures developing optimized heterojunctions and the use of new molecular complexes as dyes for sensitized solar cells and photocatalysts¹⁰⁷. To develop effective photo-induced processes, equal importance must be given to the photocatalysis fundamental processes, photoreactor design and catalyst synthesis. It is therefore necessary to increase the surface/volume ratio of the photo-active materials in use, addressing thus a severe foot-print penalty.

In this project, the proposed strategy consists in solid foams bearing a hierarchically organized porosity to achieve a three-dimensional CO₂ photoconversion. These porous materials¹⁰⁸ are obtained by the synergistic template effects of lyotrope mesophases (concentrated micelles) that create the mesoporosity (pore diameters ranging from 2 nm to 50 nm) and oil-in-water concentrated emulsions inducing the connected macroporosity (pore diameters above 50 nm), combined with the sol-gel process that condenses the continuous hydrophilic phase. As the inorganic skeleton is amorphous silica, the microporosity (pore diameters below 2 nm) relies on the SiO₄ tetrahedral statistical repartition within the geometric space. Thereby, the use of emulsion as soft template for the genesis of macrocellular materials provides a powerful hierarchical porosity, especially a modular self-standing macrostructure. These self-standing foams are labelled Si(HIPE)¹⁰⁹, and they can be hybridized to reach applications mainly dedicated toward heterogeneous catalysis¹¹⁰. Being purely inorganic, these foams have been recently employed as light scavengers for application devoted toward the field of random lasing^{111,112} where TiO₂ has been added during the sol-gel process to increase the inorganic skeleton refractive index, thereby optimizing the photon mean-free-path within the foams¹¹³. Then, due to its low-cost, chemical stability, photocatalytic performances, and physic-chemical properties, TiO₂ is a great candidate as active phase.

In this intensification objective of artificial photo-driven processes, the synthesis of TiO₂@Si(HIPE)s materials, as well as their multi-scale characterizations, and the evaluation of their photocatalytic performance for CO₂ photoreduction involving water, will be described and discussed in the following chapters.

5 References

- (1) Parmon, V.; Emeline, A. V.; Serpone, N. Glossary of Terms in Photocatalysis and Radiocatalysis. *International Journal of Photoenergy* **2002**, *4*, 91–130.
- (2) Guillard, C.; Kartheuser, B.; Lacombe, S. La Photocatalyse: Dépollution de l'eau Ou de l'air et Matériaux Autonettoyants. *Techniques de l'ingénieur* **2011**, No. J 1 270.
- (3) Xie, S.; Zhang, Q.; Liu, G.; Wang, Y. Photocatalytic and Photoelectrocatalytic Reduction of CO₂ Using Heterogeneous Catalysts with Controlled Nanostructures. *Chem. Commun.* **2016**, *52*, 35–59.
- (4) Herrmann, J.-M. Heterogeneous Photocatalysis: Fundamentals and Application to the Removal of Various Types of Aqueous Pollutants. *Catalysis Today* **1999**, *53*, 115–129.

- (5) Tahir, M.; Amin, N. A. S. Advances in Visible Light Responsive Titanium Oxide-Based Photocatalysts for CO₂ Conversion to Hydrocarbon Fuels. *Energy Conversion and Management* **2013**, *76*, 194–214.
- (6) Inoue, T.; Fujishima, A.; Konishi, S.; Honda, K. Photoelectrocatalytic Reduction of Carbon Dioxide in Aqueous Suspensions of Semiconductor Powders. *Nature* **1979**, *277*, 637–638.
- (7) Chang, X.; Wang, T.; Gong, J. CO₂ Photo-Reduction: Insights into CO₂ Activation and Reaction on Surfaces of Photocatalysts. *Energy Environ. Sci.* **2016**, *9*, 2177–2196.
- (8) Université du Maine. Les Dosages Acido-Basiques.
- (9) Herrmann, J.-M. Heterogeneous Photocatalysis: State of the Art and Present Applications. *Topics in Catalysis* **2005**, *34*, 49–65.
- (10) Zayat, M.; Garcia-Parejo, P.; Levy, D. Preventing UV-Light Damage of Light Sensitive Materials Using Highly Protective UV-Absorbing Coating. *Chem. Soc. Rev.* **2007**, *36*, 1270–1281.
- (11) Etacheri, V.; Di Valentin, C.; Schneider, J.; Bahnemann, D.; Pillai, S. C. Visible-Light Activation of TiO₂ Photocatalysts: Advances in Theory and Experiments. *Journal of Photochemistry and Photobiology C: Photochemistry Reviews* **2015**, *25*, 1–29.
- (12) Verbruggen, S. W. TiO₂ Photocatalysis for the Degradation of Pollutants in Gas Phase: From Morphological Design to Plasmonic Enhancement. *Journal of Photochemistry and Photobiology C: Photochemistry Reviews* **2015**, *24*, 64–82.
- (13) Hagfeldt, A.; Grätzel, M. Light-Induced Redox Reactions in Nanocrystalline Systems. *Chem. Rev.* **1995**, *95*, 49–68.
- (14) Maeda, K.; Domen, K. Photocatalytic Water Splitting: Recent Progress and Future Challenges. *J. Phys. Chem. Lett.* **2010**, *1* (18), 2655–2661.
- (15) Schneider, J.; Matsuoka, M.; Takeuchi, M.; Zhang, J.; Horiuchi, Y.; Anpo, M.; Bahnemann, D. W. Understanding TiO₂ Photocatalysis: Mechanisms and Materials. *Chem. Rev.* **2014**, *114* (19), 9919–9986.
- (16) Li, K.; Peng, B.; Peng, T. Recent Advances in Heterogeneous Photocatalytic CO₂ Conversion to Solar Fuels. *ACS Catal.* **2016**, *6* (11), 7485–7527.
- (17) Parmon, V. Photocatalysis as a Phenomenon: Aspects of Terminology. *Catalysis Today* **1997**, *39*, 137–144.
- (18) Zhang, J.; Zhou, P.; Liu, J.; Yu, J. New Understanding of the Difference of Photocatalytic Activity among Anatase, Rutile and Brookite TiO₂. *Phys. Chem. Chem. Phys.* **2014**, *16* (38), 20382–20386.
- (19) Davis, K. A. Titanium Dioxide. *J. Chem. Educ.* **1982**, *59* (2), 158.
- (20) Zhang, H.; Banfield, J. F. Understanding Polymorphic Phase Transformation Behavior during Growth of Nanocrystalline Aggregates: Insights from TiO₂. *J. Phys. Chem. B* **2000**, *104* (15), 3481–3487.
- (21) Zhao, H.; Liu, L.; M. Andino, J.; Li, Y. Bicrystalline TiO₂ with Controllable Anatase–Brookite Phase Content for Enhanced CO₂ Photoreduction to Fuels. *Journal of Materials Chemistry A* **2013**, *1* (28), 8209–8216.
- (22) Hurum, D. C.; Agrios, A. G.; Gray, K. A.; Rajh, T.; Thurnauer, M. C. Explaining the Enhanced Photocatalytic Activity of Degussa P25 Mixed-Phase TiO₂ Using EPR. *J. Phys. Chem. B* **2003**, *107* (19), 4545–4549.
- (23) Ohno, T.; Sarukawa, K.; Tokieda, K.; Matsumura, M. Morphology of a TiO₂ Photocatalyst (Degussa, P-25) Consisting of Anatase and Rutile Crystalline Phases. *Journal of Catalysis* **2001**, *203* (1), 82–86.
- (24) Sato, S. Photocatalytic Activity of NO_x-Doped TiO₂ in the Visible Light Region. *Chemical Physics Letters* **1986**, *123* (1), 126–128.
- (25) Asahi, R.; Morikawa, T.; Ohwaki, T.; Aoki, K.; Taga, Y. Visible-Light Photocatalysis in Nitrogen-Doped Titanium Oxides. *Science* **2001**, *293* (5528), 269–271.
- (26) Sathish, M.; Viswanathan, B.; Viswanath, R. P.; Gopinath, C. S. Synthesis, Characterization, Electronic Structure, and Photocatalytic Activity of Nitrogen-Doped TiO₂ Nanocatalyst. *Chem. Mater.* **2005**, *17* (25), 6349–6353.
- (27) Emeline, A. V.; Kuznetsov, V. N.; Rybchuk, V. K.; Serpone, N. Visible-Light-Active Titania Photocatalysts: The Case of N-Doped TiO₂s—Properties and Some Fundamental Issues. *International Journal of Photoenergy* **2008**, *2008* (258394), 1–19.

- (28) Akple, M. S.; Low, J.; Qin, Z.; Wageh, S.; Al-Ghamdi, A. A.; Yu, J.; Liu, S. Nitrogen-Doped TiO₂ Microsheets with Enhanced Visible Light Photocatalytic Activity for CO₂ Reduction. *Chinese Journal of Catalysis* **2015**, *36*, 2127–2134.
- (29) Khan, S. U. M.; Al-Shahry, M.; Ingler, W. B. Efficient Photochemical Water Splitting by a Chemically Modified N-TiO₂. *Science* **2002**, *297* (5590), 2243–2245.
- (30) Tachikawa, T.; Tojo, S.; Fujitsuka, M.; Majima, T. Influences of Adsorption on TiO₂ Photocatalytic One-Electron Oxidation of Aromatic Sulfides Studied by Time-Resolved Diffuse Reflectance Spectroscopy. *J. Phys. Chem. B* **2004**, *108* (19), 5859–5866.
- (31) Zhao, W.; Ma, W.; Chen, C.; Zhao, J.; Shuai, Z. Efficient Degradation of Toxic Organic Pollutants with Ni₂O₃/TiO₂-XB_x under Visible Irradiation. *J. Am. Chem. Soc.* **2004**, *126* (15), 4782–4783.
- (32) Lin, L.; Lin, W.; Zhu, Y.; Zhao, B.; Xie, Y. Phosphor-Doped Titania —a Novel Photocatalyst Active in Visible Light. *Chem. Lett.* **2005**, *34* (3), 284–285.
- (33) Yu, J. C.; Yu; Ho; Jiang; Zhang. Effects of F- Doping on the Photocatalytic Activity and Microstructures of Nanocrystalline TiO₂ Powders. *Chem. Mater.* **2002**, *14* (9), 3808–3816.
- (34) Ni, M.; Leung, M. K. H.; Leung, D. Y. C.; Sumathy, K. A Review and Recent Developments in Photocatalytic Water-Splitting Using TiO₂ for Hydrogen Production. *Renewable and Sustainable Energy Reviews* **2007**, *11* (3), 401–425.
- (35) Valden, M.; Lai, X.; Goodman, D. W. Onset of Catalytic Activity of Gold Clusters on Titania with the Appearance of Nonmetallic Properties. *Science* **1998**, *281* (5383), 1647–1650.
- (36) Tang, J. Interaction between Noble Metal Nanoparticles and Light for Contaminant Decomposition. *ChemSusChem* **2010**, *3* (7), 800–801.
- (37) Yui, T.; Kan, A.; Saitoh, C.; Koike, K.; Ibusuki, T.; Ishitani, O. Photochemical Reduction of CO₂ Using TiO₂: Effects of Organic Adsorbates on TiO₂ and Deposition of Pd onto TiO₂. *ACS Appl. Mater. Interfaces* **2011**, *3* (7), 2594–2600.
- (38) Wang, W.-N.; An, W.-J.; Ramalingam, B.; Mukherjee, S.; Niedzwiedzki, D. M.; Gangopadhyay, S.; Biswas, P. Size and Structure Matter: Enhanced CO₂ Photoreduction Efficiency by Size-Resolved Ultrafine Pt Nanoparticles on TiO₂ Single Crystals. *J. Am. Chem. Soc.* **2012**, *134* (27), 11276–11281.
- (39) Adachi, K.; Ohta, K.; Mizuno, T. Photocatalytic Reduction of Carbon Dioxide to Hydrocarbon Using Copper-Loaded Titanium Dioxide. *Solar Energy* **1994**, *53* (2), 187–190.
- (40) Nguyen, T.-V.; Wu, J. C. S. Photoreduction of CO₂ in an Optical-Fiber Photoreactor: Effects of Metals Addition and Catalyst Carrier. *Applied Catalysis A: General* **2008**, *335* (1), 112–120.
- (41) Ishitani, O.; Inoue, C.; Suzuki, Y.; Ibusuki, T. Photocatalytic Reduction of Carbon Dioxide to Methane and Acetic Acid by an Aqueous Suspension of Metal-Deposited TiO₂. *Journal of Photochemistry and Photobiology A: Chemistry* **1993**, *72* (3), 269–271.
- (42) Lofficial, D. Photosynthèse Artificielle: Élaboration de Matériaux Composites Pour La Valorisation de CO₂ Par Photocatalyse, Université de Lyon, 2015.
- (43) Jean, V. Modélisation Du Transport de Phonons Dans Les Semi-Conducteurs Nanostructurés, Université de Lorraine, 2014.
- (44) Subramanian, V.; Wolf, E. E.; Kamat, P. V. Catalysis with TiO₂/Gold Nanocomposites. Effect of Metal Particle Size on the Fermi Level Equilibration. *J. Am. Chem. Soc.* **2004**, *126* (15), 4943–4950.
- (45) Tahiri Alaoui, O.; Herissan, A.; Le Quoc, C.; Zekri, M. el M.; Sorgues, S.; Remita, H.; Colbeau-Justin, C. Elaboration, Charge-Carrier Lifetimes and Activity of Pd-TiO₂ Photocatalysts Obtained by Gamma Radiolysis. *Journal of Photochemistry and Photobiology A: Chemistry* **2012**, *242*, 34–43.
- (46) Anpo, M.; Nakaya, H.; Kodama, S.; Kubokawa, Y.; Domen, K.; Onishi, T. Photocatalysis over Binary Metal Oxides. Enhancement of the Photocatalytic Activity of Titanium Dioxide in Titanium-Silicon Oxides. *J. Phys. Chem.* **1986**, *90* (8), 1633–1636.
- (47) Mori, K.; Yamashita, H.; Anpo, M. Photocatalytic Reduction of CO₂ with H₂O on Various Titanium Oxide Photocatalysts. *RSC Adv.* **2012**, *2* (8), 3165–3172.
- (48) Anpo, M.; Yamashita, H.; Ikeue, K.; Fujii, Y.; Zhang, S. G.; Ichihashi, Y.; Park, D. R.; Suzuki, Y.; Koyano, K.; Tatsumi, T. Photocatalytic Reduction of CO₂ with H₂O on Ti-MCM-41 and Ti-MCM-48 Mesoporous Zeolite Catalysts. *Catalysis Today* **1998**, *44* (1), 327–332.

- (49) Anpo, M.; Yamashita, H.; Ichihashi, Y.; Fujii, Y.; Honda, M. Photocatalytic Reduction of CO₂ with H₂O on Titanium Oxides Anchored within Micropores of Zeolites: Effects of the Structure of the Active Sites and the Addition of Pt. *J. Phys. Chem. B* **1997**, *101* (14), 2632–2636.
- (50) Carbonell, E.; Ramiro-Manzano, F.; Rodríguez, I.; Corma, A.; Meseguer, F.; García, H. Enhancement of TiO₂ Photocatalytic Activity by Structuring the Photocatalyst Film as Photonic Sponge. *Photochem. Photobiol. Sci.* **2008**, *7* (8), 931–935.
- (51) Aprile, C.; Corma, A.; Garcia, H. Enhancement of the Photocatalytic Activity of TiO₂ through Spatial Structuring and Particle Size Control: From Subnanometric to Submillimetric Length Scale. *Phys. Chem. Chem. Phys.* **2008**, *10* (6), 769–783.
- (52) Wang, X.; Yu, J. C.; Ho, C.; Hou, Y.; Fu, X. Photocatalytic Activity of a Hierarchically Macro/Mesoporous Titania. *Langmuir* **2005**, *21* (6), 2552–2559.
- (53) Van Soest, G. Experiments on Random Lasers, Université d'Amsterdam, 2001.
- (54) Nave, R. Mie Scattering.
- (55) Ishimaru, A. *Wave Propagation and Scattering in Random Media*; Elsevier Inc, 1978.
- (56) Lagendijk, A.; van Tiggelen, B. A. Resonant Multiple Scattering of Light. *Physics Reports* **1996**, *270* (3), 143–215.
- (57) Garcia Fernandez, P. D. From Photonic Crystals to Photonic Glasses through Disorder, Universidad Autonoma de Madrid, 2008.
- (58) García, P. D.; Sapienza, R.; Bertolotti, J.; Martín, M. D.; Blanco, Á.; Altube, A.; Viña, L.; Wiersma, D. S.; López, C. Resonant Light Transport through Mie Modes in Photonic Glasses. *Phys. Rev. A* **2008**, *78* (2), 023823.
- (59) Zhu, J. X.; Pine, D. J.; Weitz, D. A. Internal Reflection of Diffusive Light in Random Media. *Phys. Rev. A* **1991**, *44* (6), 3948–3959.
- (60) Garcia, N.; Genack, A. Z.; Lisyansky, A. A. Measurement of the Transport Mean Free Path of Diffusing Photons. *Phys. Rev. B* **1992**, *46* (22), 14475–14479.
- (61) Patterson, M. S.; Chance, B.; Wilson, B. C. Time Resolved Reflectance and Transmittance for the Noninvasive Measurement of Tissue Optical Properties. *Appl. Opt., AO* **1989**, *28* (12), 2331–2336.
- (62) Niinemets, Ü.; Sack, L. Structural Determinants of Leaf Light-Harvesting Capacity and Photosynthetic Potentials. *Progress in Botany* **2006**, *67*, 385–419.
- (63) Zhou, H.; Guo, J.; Li, P.; Fan, T.; Zhang, D.; Ye, J. Leaf-Architected 3D Hierarchical Artificial Photosynthetic System of Perovskite Titanates Towards CO₂ Photoreduction Into Hydrocarbon Fuels. *Scientific Reports* **2013**, *3*, 1667.
- (64) Backov, R. Combining Soft Matter and Soft Chemistry: Integrative Chemistry towards Designing Novel and Complex Multiscale Architectures. *Soft Matter* **2006**, *2* (6), 452–464.
- (65) Depardieu, M. Chimie Intégrative Pour La Synthèse de Matériaux Fonctionnels Avancés, Université de Bordeaux, 2014.
- (66) Sanchez, C.; Arribart, H.; Giraud Guille, M. M. Biomimetism and Bioinspiration as Tools for the Design of Innovative Materials and Systems. *Nature Materials* **2005**, *4* (4), 277–288.
- (67) Brun, N. Chimie Intégrative Pour La Conception de Matériaux Poreux Fonctionnels Avancés et Applications, Université de Bordeaux, 2010.
- (68) Sing, K. S. W.; Schüth, F. Definitions, Terminology, and Classification of Pore Structures. In *Handbook of Porous Solids*; Wiley-Blackwell, 2008; pp 24–33.
- (69) Rouquerol, F.; Luciani, L.; Llewellyn, P.; Denoyel, R.; Rouquerol, J. Texture des matériaux pulvérulents ou poreux. *Techniques de l'ingénieur* **2003**, No P 1050.
- (70) Leclaire, P. Caractérisation Physique de Matériaux Poreux Pour l'étude Des Interactions Acoustique/Structure, Université Paris 7 - D. Diderot, 2005.
- (71) Zdravkov, B. D.; Čermák, J. J.; Šefara, M.; Janků, J. Pore Classification in the Characterization of Porous Materials: A Perspective. *Cent.Eur.J.Chem.* **2007**, *5* (2), 385–395.
- (72) ALOthman, Z.; ALOthman, Z. A. A Review: Fundamental Aspects of Silicate Mesoporous Materials. *Materials* **2012**, *5* (12), 2874–2902.
- (73) Depardieu, M.; Nollet, M.; Schmitt, V.; Backov, R. Integrative Chemistry: Positioning Chemical Reactors within the Geometric Space as a Tool for the Design of Advanced Functional Materials. *Comptes Rendus Chimie* **2016**, *19* (1), 216–230.
- (74) Chong, J. Y. T.; Mulet, X.; Boyd, B. J.; Drummond, C. J. Chapter Five - Steric Stabilizers for Cubic Phase Lyotropic Liquid Crystal Nanodispersions (Cubosomes). In *Advances in Planar Lipid*

- Bilayers and Liposomes*; Iglič, A., Kulkarni, C. V., Rappolt, M., Eds.; Academic Press, 2015; Vol. 21, pp 131–187.
- (75) Barón, M.; Stepto, R. F. T. Definitions of Basic Terms Relating to Polymer Liquid Crystals (IUPAC Recommendations 2001). *Pure and Applied Chemistry* **2002**, *74* (3), 493–509.
- (76) Brochette, P. Émulsification - Élaboration et étude des émulsions. *Techniques de l'ingénieur* **1999**, No J 2150.
- (77) Flesinski, L. Etude de La Stabilité Des Émulsions et de La Rhéologie Interfaciale Des Systèmes Pétrole Brut/Eau: Influence Des Asphaltènes et Des Acides Naphténiques, Université de Pau et des pays de l'adour, 2011.
- (78) Guillermic, R.-M. Propriétés Physico-Chimiques Des Mousses: Études Approfondies Sur Des Mousses Modèles et Études Exploratoires Sur de Nouvelles Mousses, Université de Rennes 1, 2011.
- (79) Carn, F. Intégration Entre Chimie Douce et Fluides Complexes Pour La Genèse d'architectures Poreuses Hiérarchisées: Synthèses, Caractérisations et Application, Université de Bordeaux 1, 2006.
- (80) Griffin, W. C. Classification of Surface-Active Agents by "HLB." *Journal of Cosmetic Science* **1949**, *1* (5), 311–326.
- (81) Bancroft, W. D. The Theory of Emulsification, V. *J. Phys. Chem.* **1913**, *17* (6), 501–519.
- (82) Silverstein, M. S. Emulsion-Templated Porous Polymers: A Retrospective Perspective. *Polymer* **2014**, *55* (1), 304–320.
- (83) Leal-Calderon, F.; Schmitt, V.; Bibette, J. *Emulsion Science: Basic Principles*, 2nd ed.; Springer-Verlag: New York, 2007.
- (84) Binks, B. P. Chapter 1: Emulsions — Recent Advances in Understanding. In *Modern Aspects of Emulsion Science*; 1998; pp 1–55.
- (85) Brinker, C. J.; Scherer, G. W. CHAPTER 1 - Introduction. In *Sol-Gel Science*; Brinker, C. J., Scherer, G. W., Eds.; Academic Press: San Diego, 1990; pp xvi–18.
- (86) Nakanishi, K.; Soga, N. Phase Separation in Silica Sol-Gel System Containing Polyacrylic Acid I. Gel Formation Behavior and Effect of Solvent Composition. *Journal of Non-Crystalline Solids* **1992**, *139*, 1–13.
- (87) Nakanishi, K.; Tanaka, N. Sol-Gel with Phase Separation. Hierarchically Porous Materials Optimized for High-Performance Liquid Chromatography Separations. *Acc. Chem. Res.* **2007**, *40* (9), 863–873.
- (88) Nakanishi, K. Pore Structure Control of Silica Gels Based on Phase Separation. *Journal of Porous Materials* **1997**, *4* (2), 67–112.
- (89) Galarneau, A.; Sachse, A.; Said, B.; Pelisson, C.-H.; Boscaro, P.; Brun, N.; Courtheoux, L.; Olivieri-Tran, N.; Coasne, B.; Fajula, F. Hierarchical Porous Silica Monoliths: A Novel Class of Microreactors for Process Intensification in Catalysis and Adsorption. *Comptes Rendus Chimie* **2016**, *19* (1), 231–247.
- (90) Davis, S. A.; Burkett, S. L.; Mendelson, N. H.; Mann, S. Bacterial Templating of Ordered Macrostructures in Silica and Silica-Surfactant Mesophases. *Nature* **1997**, *385*, 420–423.
- (91) Ogasawara, W.; Shenton, W.; Davis, S. A.; Mann, S. Template Mineralization of Ordered Macroporous Chitin-Silica Composites Using a Cuttlebone-Derived Organic Matrix. *Chem. Mater.* **2000**, *12* (10), 2835–2837.
- (92) Anderson, M. W.; Holmes, S. M.; Hanif, N.; Cundy, C. S. Hierarchical Pore Structures through Diatom Zeolitization. *Angewandte Chemie* **2000**, *112* (15), 2819–2822.
- (93) Holland, B. T.; Blanford, C. F.; Stein, A. Synthesis of Macroporous Minerals with Highly Ordered Three-Dimensional Arrays of Spheroidal Voids. *Science* **1998**, *281* (5376), 538–540.
- (94) Ramiro-Manzano, F.; Atienzar, P.; Rodriguez, I.; Meseguer, F.; Garcia, H.; Corma, A. Apollony Photonic Sponge Based Photoelectrochemical Solar Cells. *Chem. Commun.* **2007**, *0* (3), 242–244.
- (95) Wang, C.; Yan, J.; Cui, X.; Cong, D.; Wang, H. Preparation and Characterization of Magnetic Hollow PMMA Nanospheres via in Situ Emulsion Polymerization. *Colloids and Surfaces A: Physicochemical and Engineering Aspects* **2010**, *363* (1), 71–77.
- (96) Davis, M.; Ramirez, D. A.; Hope-Weeks, L. J. Formation of Three-Dimensional Ordered Hierarchically Porous Metal Oxides via a Hybridized Epoxide Assisted/Colloidal Crystal Templating Approach. *ACS Appl. Mater. Interfaces* **2013**, *5* (16), 7786–7792.

-
- (97) Kresge, C. T.; Leonowicz, M. E.; Roth, W. J.; Vartuli, J. C.; Beck, J. S. Ordered Mesoporous Molecular Sieves Synthesized by a Liquid-Crystal Template Mechanism. *Nature* **1992**, 359 (6397), 710–712.
- (98) Ahmed, A.; Clowes, R.; Myers, P.; Zhang, H. Hierarchically Porous Silica Monoliths with Tuneable Morphology, Porosity, and Mechanical Stability. *J. Mater. Chem.* **2011**, 21 (15), 5753–5763.
- (99) Ravetti-Duran, R.; Blin, J.-L.; Stébé, M.-J.; Castel, C.; Pasc, A. Tuning the Morphology and the Structure of Hierarchical Meso–Macroporous Silica by Dual Templating with Micelles and Solid Lipid Nanoparticles (SLN). *J. Mater. Chem.* **2012**, 22 (40), 21540–21548.
- (100) Peng, J.; Liu, J.; Liu, J.; Yang, Y.; Li, C.; Yang, Q. Fabrication of Core–Shell Structured Mesoporous Silica Nanospheres with Dually Oriented Mesochannels through Pore Engineering. *J. Mater. Chem. A* **2014**, 2 (21), 8118–8125.
- (101) Brinker, C. J.; Scherer, G. W. *Sol-Gel Science*; Elsevier, 1990.
- (102) Le procédé sol-gel : utilisation par RESCOLL http://rescoll.fr/le-procedee-sol-gel__trashed/ (accessed Oct 14, 2018).
- (103) Robin, G.; Vander Meulen, F.; Wilkie-Chancellier, N.; Martinez, L.; Haumesser, L.; Fortineau, J.; Griesmar, P.; Feuillard, G. Détermination Du Temps de Gel Par Mesures de La Vitesse de Phase et de l'atténuation d'une Onde Ultrasonore. In *10ème Congrès Français d'Acoustique*; SFA, S. F. d'Acoustique-, Ed.; Lyon, France, 2010; p .
- (104) Stöber, W.; Fink, A.; Bohn, E. Controlled Growth of Monodisperse Silica Spheres in the Micron Size Range. *Journal of Colloid and Interface Science* **1968**, 26 (1), 62–69.
- (105) Stechel, E. B.; Miller, J. E. Re-Energizing CO₂ to Fuels with the Sun: Issues of Efficiency, Scale, and Economics. *Journal of CO₂ Utilization* **2013**, 1, 28–36.
- (106) Fécant, A.; Toulhoat, H. Pour la Science N°459 - Janvier 2016 - Pourquoi rêvons-nous ? *Pourlascience.fr*. 2016, pp 56–63.
- (107) Fontecave, M.; Fécant, A.; Uzio, D. Editorial: IFP Energies Nouvelles International Conference: Photo4E – Photocatalysis for Energy, 15–17 October 2014, Solaize, France. *Oil Gas Sci. Technol. – Rev. IFP Energies nouvelles* **2015**, 70 (5), 791–798.
- (108) Carn, F.; Colin, A.; Achard, M.-F.; Deleuze, H.; Sellier, E.; Birot, M.; Backov, R. Inorganic Monoliths Hierarchically Textured via Concentrated Direct Emulsion and Micellar Templates. *J. Mater. Chem.* **2004**, 14 (9), 1370–1376.
- (109) Brun, N.; Ungureanu, S.; Deleuze, H.; Backov, R. Hybrid Foams, Colloids and beyond: From Design to Applications. *Chem. Soc. Rev.* **2011**, 40 (2), 771–788.
- (110) Roucher, A.; Depardieu, M.; Pekin, D.; Morvan, M.; Backov, R. Inorganic, Hybridized and Living Macrocellular Foams: “Out of the Box” Heterogeneous Catalysis. *The Chemical Record* **2018**, 18 (7–8), 776–787.
- (111) Gaikwad, P.; Ungureanu, S.; Backov, R.; Vynck, K.; Vallée, R. a. L. Photon Transport in Cylindrically-Shaped Disordered Meso-Macroporous Materials. *Opt. Express* **2014**, 22 (7), 7503–7513.
- (112) Bachelard, N.; Gaikwad, P.; Backov, R.; Sebbah, P.; Vallée, R. A. L. Disorder as a Playground for the Coexistence of Optical Nonlinear Effects: Competition between Random Lasing and Stimulated Raman Scattering in Complex Porous Materials. *ACS Photonics* **2014**, 1 (11), 1206–1211.
- (113) Gaikwad, P.; Bachelard, N.; Sebbah, P.; Backov, R.; Vallée, R. A. L. Competition and Coexistence of Raman and Random Lasing in Silica-/Titania-Based Solid Foams. *Advanced Optical Materials* **2015**, 3 (11), 1640–1651.

Chapter II

Experimental procedures

This chapter consists of three parts dedicated to the experimental procedures: syntheses, characterizations and photocatalytic tests. The first presents the protocols used to synthesize in two steps the porous monoliths. First, the porous silica matrix synthesis, structured at all scales, and then the active phase impregnation. The second section details the principle of the routinely used characterization techniques. Their specific application to synthesized materials is discussed. Finally, the last part develops the set-up, and especially the procedure carried out for the photocatalytic tests. Besides, the quantities applied to evaluate the photocatalytic performances of materials are described.

TABLE OF CONTENTS

1	<u>SYNTHESES OF MONOLITHS BEARING HIERARCHICAL POROSITY</u>	51
1)	SILICA MATRIX SYNTHESIS	51
A.	CONDENSATION STAGE	51
B.	WASHING STAGE	52
C.	DRYING STAGE	52
D.	CALCINATION TREATMENT: ORGANIC CALCINATION AND SILICA SINTERRING	53
2)	TiO ₂ IMPREGNATION	53
A.	PRECURSOR SOLUTION	53
B.	IMPREGNATION STAGE	54
C.	HEAT TREATMENT	55
2	<u>CHARACTERIZATIONS</u>	55
1)	STRUCTURAL AND MORPHOLOGICAL CHARACTERIZATIONS	55
A.	MACROSCOPIC LENGTH SCALE	55
	Photographs and designations	56
	Scanning Electron Microscopy (SEM)	56
	Electron Probe Micro Analysis (EPMA)	58
	Mercury intrusion porosimetry	59
B.	MESO- AND MICROSCOPIC LENGTH SCALE	60
	Elemental analysis	60
	Isothermal sorption	62
	Transmission Electron Microscopy (TEM)	64
	X-ray diffraction (XRD)	65
2)	ELECTRONIC CHARACTERIZATION: DIFFUSE REFLECTANCE UV-VISIBLE SPECTROSCOPY	67
3)	LIGHT DIFFUSION CHARACTERIZATION	68
A.	GOLD SALT IMPREGNATION METHOD	68
B.	PULSED LASER METHOD	68
3	<u>PHOTOCATALYTIC TESTS</u>	70
1)	SET UP	70
A.	REACTOR	70
B.	DEVICES	71

Chapter II – Experimental procedures

C. PROCEDURE.....	72
2) EVALUATION OF PHOTOCATALYTIC PERFORMANCES	73
<hr/>	
A. PHOTOCATALYTIC ACTIVITIES	74
Global activity per mass	74
Global activity per surface.....	75
B. SELECTIVITY	76
<u>4 CONCLUSION.....</u>	<u>76</u>
<u>5 REFERENCES.....</u>	<u>77</u>

1 Syntheses of monoliths bearing hierarchical porosity

The label HIPE (High Internal Phase Emulsion) is referring to the high porosity offered by the synthesized materials, making the use of either direct or reverse emulsion as macroscopic templates. HIPEs are defined by the volume ratio of the emulsion internal phase (the droplets) over the total volume, which is generally required to be at least 74%¹. The term TiO₂@Si(HIPE) consists of a silica HIPE, formulated by sol-gel process, in which titanium dioxide (TiO₂) is incorporated. Moreover, TiO₂/Si(HIPE) structures have also been produced by co-polycondensation, i.e. in one step, of TiO₂ and Si alkoxide precursors². However, this method only allowed TiO₂ loading rates of less than 20% by weight to be obtained, due to the low mechanical strength of final structures. Thus, only the formulation of materials in two steps will be developed in this part: silica matrix synthesis and then, TiO₂ impregnation/nucleation.

Synthesis of silica porous matrices will be developed in the first following part. In the second one, the methods describing the TiO₂ impregnation will be detailed. These are the routine protocols that are described. During the project, some parameters were modified, and will be mentioned in the following chapters when relevant. Steps, products, and devices will be specified in both parts. The effect of synthesis parameters on the textural structure of materials will be discussed in Chapter III.

1) Silica matrix synthesis

The fundamentals of this synthesis were first described by Florent Carn³.

a. Condensation stage

To prepare up to 5 monoliths, 16 g of aqueous solution of TTAB (Myristyltrimethylammonium bromide, purity \geq 99%, Sigma-Aldrich) at 35% by weight was poured and mixed with 5 mL of HCl (hydrochloric acid, purity = 37%, VWR Chemicals) in a mortar. Once the mixture was homogeneous, 5g of TEOS (TetraEthylOrthoSilicate) were added. Note that the TEOS used must come from a bottle opened for less than a month. The gaseous sky present after opening the bottle contains water molecules which deteriorate the reactivity of the TEOS. The TTAB solution-HCl-TEOS mixture was manually stirred until complete hydrolysis of the TEOS (single-phase mixture). Then, 35 g of dodecane were incorporated drop by drop into the mortar, shearing with the pestle, to form a direct and concentrated emulsion. Once the sol was formulated, it was poured into 5.5 cm diameter Petri dishes or propylene pots. The sol amount poured by container depends on the desired final monolith thickness (e.g. one sol poured into two propylene pots leads to two around 1.3 cm thick monoliths). Finally, the filled containers

were placed in a desiccator containing some distilled water, to avoid the monolith to dry and crack during the condensation of the TEOS.

b. Washing stage

At this stage, the materials were silica gels, with a porosity filled still with dodecane.

After about one week, the condensation was complete, resulting in the formation of the gel. The Petri dishes were then immersed in distilled water. By capillarity, water was seeping between the monolith and the Petri dish. The oil (the majority phase of the material at this stage) being less dense than water, the gels were rising to the surface of the water. They were thus transferred into 500 mL crystallizers (1 crystallizer per batch). These were filled with THF (TetraHydroFuran) to dissolve the dodecane. To avoid evaporation of the solvent, the crystallizers were placed in a desiccator throughout the washing period. Once the dodecane was completely dissolved, the materials were reduced to a silica structure, denser ($d_{\text{SiO}_2} = 2.65 \text{ g.cm}^{-3}$) than the solvent ($d_{\text{THF}} = 0.889 \text{ g.cm}^{-3}$) and fell to the bottom of the crystallizer. The washing bath was then changed to a THF/acetone mixture in the volume proportions 70:30. The operation was repeated twice, 24 hours apart, to ensure proper dissolution of the dodecane.

c. Drying stage

At this stage, the materials were wet silica gels, with a porosity filled with solvent.

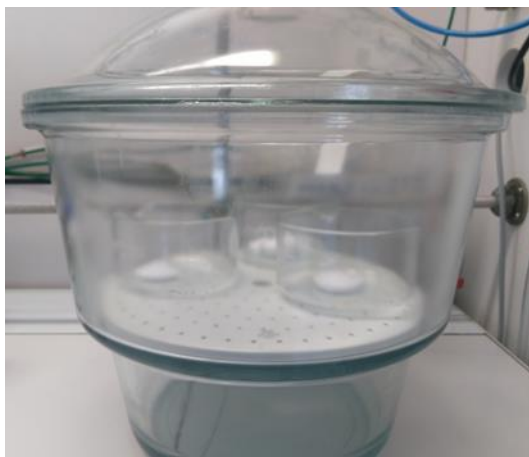


Figure II. 1: Drying step in desiccator

The crystallizers, containing the silica matrices and the THF/acetone mixture, were then emptied of the solvent and placed in a drying desiccator. Initially, the monoliths were left to evaporate with the desiccator closed until the THF/acetone mixture present in the material established a vapor/liquid balance (Figure II. 1). To accelerate the drying of the materials, two paper strips were positioned face to face between the lid and the desiccator container. Thus, the vapor/liquid balance was shifted in favor of solvent evaporation. The operation was repeated three times; about three days between each step,

adding the strips of paper one on top of the other. Once four paper thicknesses had been reached, the monoliths were almost dry and can be removed from the desiccator. The crystallizers are then covered with an aluminum film, in which many holes were perforated with a needle, to finalize the drying gently and avoid any cracking of the material. These were left for about one week or two for thicker monoliths (meaning $> 5\text{mm}$).

d. Calcination treatment: organic calcination and silica sintering

At this stage, the materials were dry silica gels, only bearing a porosity of about 64%.

Once dry, the monoliths were ready to undergo a sintering stage, with the objective of densify their structure (sintering) and giving them good mechanical properties, i.e. the ability to be handleable and self-supported. For this, a heat treatment was carried out. When the materials, placed in a crucible, were in the muffle furnace (Nabertherm L3 model), a first rise in temperature was operated at $2^{\circ}\text{C}\cdot\text{min}^{-1}$ to reach 120°C , where a 2 hours-dwell was done. A second rise at $2^{\circ}\text{C}/\text{min}$ and a 2 hours-dwell at 180°C were applied. This first part ensures the total extraction of the remaining water adsorbed and the structural water present within the material. The next step consists in a new temperature rise at a rate of $2^{\circ}\text{C}\cdot\text{min}^{-1}$, and then a plateau for 5 hours when reaching 650°C . Finally, the temperature was lowered by inertia of the furnace, until it returned to room temperature. The temperature rise ramps can be modified and adapted to the shape of the material. Indeed, the larger the dimension of the material, the more insulating the silica is.

2) TiO₂ impregnation

At this stage, the materials were silica matrices, bearing a porosity of about 90% (due to the contraction of the material occurring throughout sintering).

To incorporate TiO₂ into the silica matrices, four methods were used. Here are first described impregnation solutions, then impregnation stage and finally heat treatment.

a. Precursor solution

The four impregnation solutions used during the syntheses can be divided into two categories: TiO₂ powder slurry and TiO₂ precursor solutions. On the one hand, the slurry contained crystallized particles. On the other hand, TiO₂ precursor solutions contain alcoholate monomer and TiO₂ oligomers with limited size. In this second case, three parameters were varied: the presence and concentration of alcohol, the pH and the titanium precursor concentration. To quantitatively compare the last two parameters, two molar ratios are introduced: i) $[\text{H}_2\text{O}]/[\text{Ti}]$, and ii) $[\text{H}^+]/[\text{Ti}]$.

The first set of solution was prepared from commercial powder of TiO₂: Aeroxide® P25, purity $\geq 99.5\%$, purchased from Sigma-Aldrich. Then, P25 TiO₂ powder was mixed in an aqueous solution acidified with HNO₃ ⁴ (purity $\geq 69\%$, purchased from VWR Chemicals), at pH = 2.2. For the second

category of solution, the products used were (in the order of incorporation): distilled water, isopropanol iPrOH (purity $\geq 99\%$, purchased from VWR Chemicals), hydrochloric acid HCl (purity $\geq 37\%$, purchased from VWR Chemicals), and titanium isopropoxide $\text{Ti}(\text{OPr}^i)_4$ (purity $\approx 99.999\%$, purchased from Sigma Aldrich). All solutions were magnetically stirred for 2 hours before impregnation. The compositions and main parameters of these solutions are summarized in Table II. 1, for Si(HIPE)s with a 0.07 g.mL^{-1} density. Then, compositions were adapted to Si(HIPE) density. All weighing was performed on an analytical balance with a precision of 0.05 mg (Mettler Toledo XPE 204).

Table II. 1: Overview of the product quantities weighed for solutions preparation to impregnate 0.07 g.mL^{-1} dense Si(HIPE)s, the main parameters values, and the theoretical TiO_2 contents

Solution category	Slurry	Precursor solution		
	$\text{TiO}_2(\text{P25})@\text{Si}(\text{HIPE})$	$\text{TiO}_2@\text{Si}(\text{HIPE})\text{s}$		
Water (g)	50	31.06	25.18	56.29
HNO_3	few drops	-	-	-
HCl (g)	-	17.25	13.98	20.97
$[\text{iPrOH}] (\text{M})$	0	6	5	0
TiOPr^i (g)	-	8.30	24.90	24.90
P25 (g)	0.716	-	-	-
$[\text{H}_2\text{O}]/[\text{Ti}]$	-	59.09	15.97	35.69
$[\text{H}^+]/[\text{Ti}]$	-	5.99	1.62	2.43
pH	2.2	<0.5	<0.5	<0.5
Expected TiO_2 content per imp. (% wt)	17	25	50	50
Number of impregnation steps	3	2	1	1
Expected final TiO_2 content (%wt)	38	40	50	50

b. Impregnation stage

Once the solutions were formulated, the Si(HIPE)s were added and the whole was placed in a desiccator with tap, connected to a vacuum pump (Büchi V-700). The vacuum was then carried out by steps between 150 and 30 mbar, to operate the air extraction gently. At each step, the effervescence was expected to stop (about 15 minutes) before pushing the vacuum again. At 30 mbar, the vacuum was broken, and the denser silica matrices fell to the bottom of the solution. Vacuum cycles were then operated until the Si(HIPE)s remained at the bottom of the solution, even under vacuum (indicator of the total air extraction). Once this dynamic vacuum stage was completed, the valve was closed, and the desiccator was left under static vacuum at 30 mbar for approximately 16 hours.

When impregnation was done in two or more steps, a drying time was necessary between the impregnations, to release the porosity of solvent. This was done by placing the materials between two sheets of paper under a fume hood for 1 or 2 weeks, depending on the size of the material. For one-step impregnation, the drying step was also necessary before proceeding with the heat treatment.

c. Heat treatment

At this stage, the materials were mixed materials with a silica matrix, with a porosity of about 90%, and amorphous or P25 TiO₂ particles.

Once dry, the monoliths were ready to undergo a crystallization step, with the objective of removing impregnation residues and crystallize TiO₂ particles for monoliths impregnated with TiO₂ precursor solution. The corresponding heat treatments (in the Nabertherm L3 furnace) were a first rise in temperature, operated at 2°C.min⁻¹, to reach 120°C. A step of two hours was then carried out, in order to ensure the total extraction of the remaining water adsorbed within the material. Then, a new rise at a rate of 2°C.min⁻¹ took place until reaching 300°C (for TiO₂(P25)@Si(HIPE)) and 400°C (for TiO₂@Si(HIPE)), where a step of 5 hours is established. Finally, the temperature was lowered by inertia of the furnace, until it returned to room temperature. The temperature rise ramps can be modified and adapted to the shape of the material. Indeed, the larger the dimension of the material, the more insulating the silica is.

2 Characterizations

The main objective of these characterizations is to obtain, at all scales, knowledge of the material properties. Photocatalytic behaviors can then be related or discussed compared to the structure and texture of TiO₂@Si(HIPE)s.

1) Structural and morphological characterizations

a. Macroscopic length scale

First, the terms used in the designation of the parts of the monoliths, as well as the different possible monolithic shapes, will be described. Then, the different characterization techniques used on a macroscopic scale will be detailed, in particular their application to these innovative materials TiO₂@Si(HIPE)s. The internal visualization of the materials textures was obtained by Scanning Electron Microscopy (SEM). The Electron Probe Micro Analysis (EPMA) technique allows visualizing the distribution of TiO₂ embedded in the monolith, on a macroscopic scale. Finally, mercury porosimetry makes it possible to obtain the pore size distribution among other quantities characteristic of the materials porosity.

Photographs and designations

Before use in photocatalytic test, the synthesized monoliths were obtained in the form of cylinder with a diameter of about 3.2 cm and a height of 5 (Figure II. 2), or 10 mm. They therefore had two flat surfaces (compared to the curved lateral surface). The surface denominated as the top surface in this manuscript was the one with a slight curvature derivate from the meniscus of the sol. This surface has been sanded down to a nearly perfect flat surface and will be the so-called irradiated surface thereafter. The surface denominated as the bottom surface has been sanded down in order to smooth any inhomogeneity and paying attention to keep the two surfaces parallel. This surface will be brought into contact with the reactor. The lateral surface has been retained as was and will be called edge in the following text.

It is important to note here that the shape of the monoliths depends closely on the shape of the container in which the sol is poured. It is thus possible to obtain a wide variety of shapes.

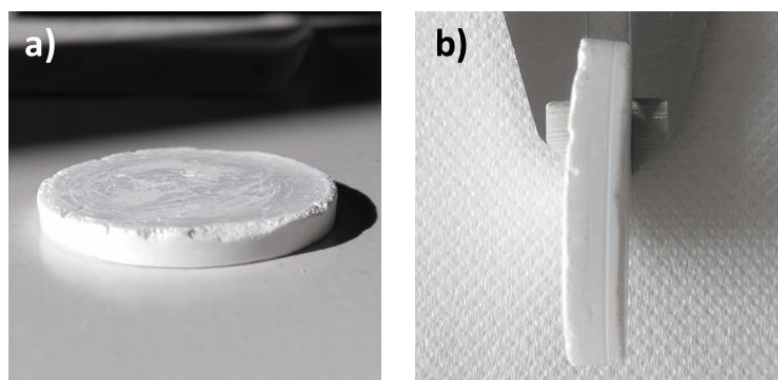


Figure II. 2: Photographs of a cylindrical 5 mm-thick synthesized monolith a) global and b) sidewise

Scanning Electron Microscopy (SEM)

Scanning Electron Microscopy (SEM) is a technique commonly used for local textural and chemical characterization of massive materials. It is based on the interaction of these materials with a focused electron beam, which typically has an energy ranging from 0.2 to 30 keV. The different radiations emitted by matter (secondary electrons, backscattered electrons and X-rays), in response to the incident electron beam, are used to form representative images of the material properties (topography, compositional heterogeneities and local elemental composition respectively). During the project, measurements were performed using FEI NOVA NANO SEM 450 microscope, under low vacuum mode. This mode is recommended for materials such as glass, ceramics or other non-conductive materials. With conventional SEM analysis operated under high vacuum, this kind of insulating samples require prior coating with carbon or gold in order to prevent an electrical charge from accumulating on the sample.

In low vacuum mode, the sample chamber contains water vapor. Its ionization by the primary beam limits the charge effects, thus preventing electrical charge accumulation. Moreover, the secondary

electron signal is also enhanced by cascade amplification by the gas (Figure II. 3). For backscattered electron imaging, a typical pressure of 50 Pa is taken, and a Gaseous Analytical Detector (GAD detector) is used (Figure II. 4).

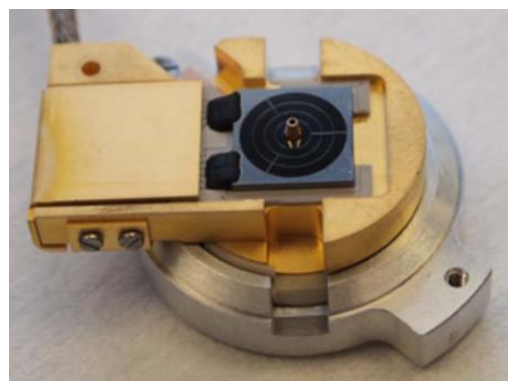
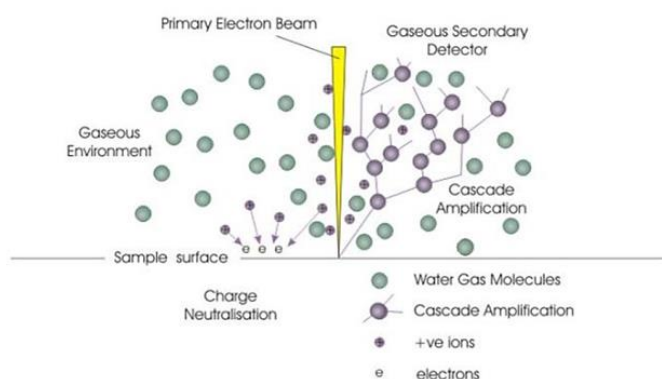


Figure II. 3: Principle of detector in low vacuum ⁵

Figure II. 4: Picture of Gaseous Analytical Detector ⁶

Backscattered electrons (BSE) consist of high-energy electrons originating in the electron beam that are reflected or back-scattered out of the specimen interaction volume by elastic scattering interactions with specimen atoms. Since heavy elements (high atomic number) backscatter electrons more strongly than light elements (low atomic number), and thus appear brighter in the image, BSE are used to detect contrast between areas with different chemical compositions ($Z(\text{Ti}) = 22$, $Z(\text{Si}) = 14$). To modulate this contrast, the electron's landing energy was varied from 5 to 15 kV. However, the volume of interaction increases with the electron's landing energy. Thus, TiO_2 particles appear brighter, but also those hidden behind or in the core of a silica hollow sphere can be visualized (Figure II. 5).

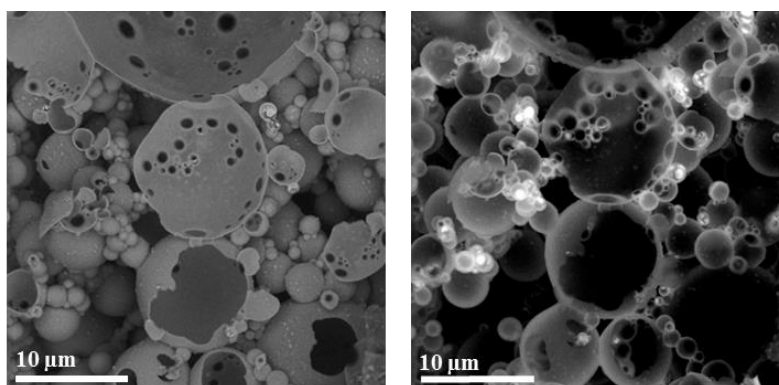


Figure II. 5: (left) SEM images of typical $\text{TiO}_2@Si(\text{HIPE})$ topology at 5 kV, and (right) chemical contrast at 15 kV

Characteristic X-rays that are produced by the interaction of electrons with the sample may also be detected in an SEM equipped for Energy-Dispersive X-ray Spectroscopy (EDS) or Wavelength Dispersive X-ray Spectroscopy (WDS). Analysis of the X-ray signals may be used to map the

distribution (Figure II. 6) and estimate the abundance of elements in the sample (Figure A 1 and Figure A 2 annex). The microanalyses performed by EDS during the study use an EDS SDD detector (Silicon Drift Detector).

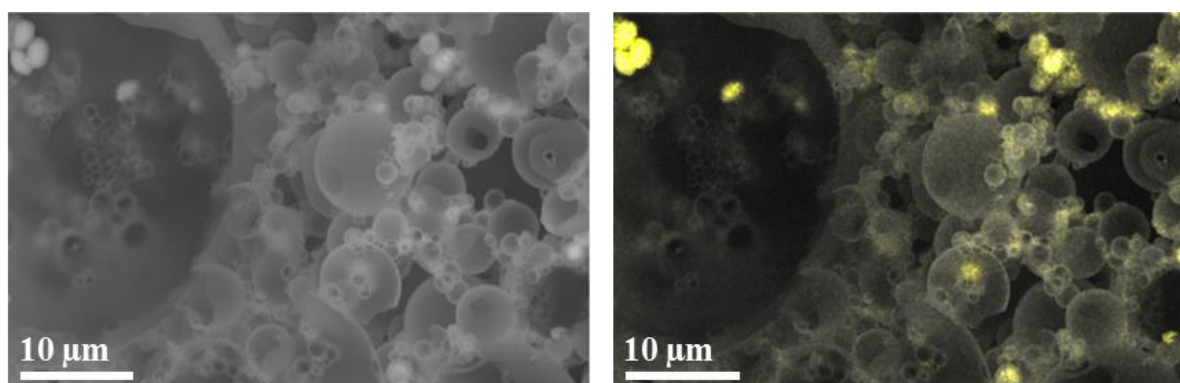


Figure II. 6: (left) SEM-EDS image and (right) the distribution of Ti element, highlighted in yellow

Electron Probe Micro Analysis (EPMA)

EPMA is implemented on catalyst mainly to control the deposit homogeneity of the active phase at the grain scale (bead or extruded). This technique works by bombarding a micro-volume of a sample with a focused electron beam (typical energy = 5-30 keV) and collecting the X-ray photons thereby emitted by the various elemental species ⁷. The recorded WDS spectra allow identifying the elements, characterized by the wavelength of the emitted X-rays, and quantify their content, related to peak intensity. The fundamentals of electronic probe microanalysis have been laid by Castaing at the same time as the apparatus development the which, in French, carries its name (“microsonde de Castaing”). During the project, measurements were performed using JEOL JXA 8100 microprobe, including five WDS spectrometers.

The following information is extracted from procedures manual of electronic microscopy and microanalysis operated in IFPEN.

The implementation of the X microanalysis can be schematically broken down into six steps: i) the excitement of a core level of the elements ($E_{\text{electron beam}} > E_{\text{ionization}}$), ii) the emission of X-photons, iii) the detection of X-photons by WDS detectors, iv) the photon counting, v) the subtraction of the background intensity to the intensity of the characteristic peaks, and vi) the establishment of intensity-concentration relationship.

This relationship requires the sample to be perfectly flat. The samples are placed in cylindrical patterns of 2.5 cm in external diameter and 2.3 cm in internal diameter by 1 cm in height then embedded in a resin. The studs are then polished so that the grains have a cross section. The samples being electrically insulating, a thin layer of 20 to 30 nm of carbon is deposited under vacuum. The circumference of the stud is covered with silver lacquer to facilitate electrical contact with the sample holder of the microprobe. However, the viscosity of the resin induced impregnation difficulties within the porosity of

the monoliths. Due to the high porosity of the monoliths and their poor impregnation (Figure II. 7), only qualitative profiles could be produced.

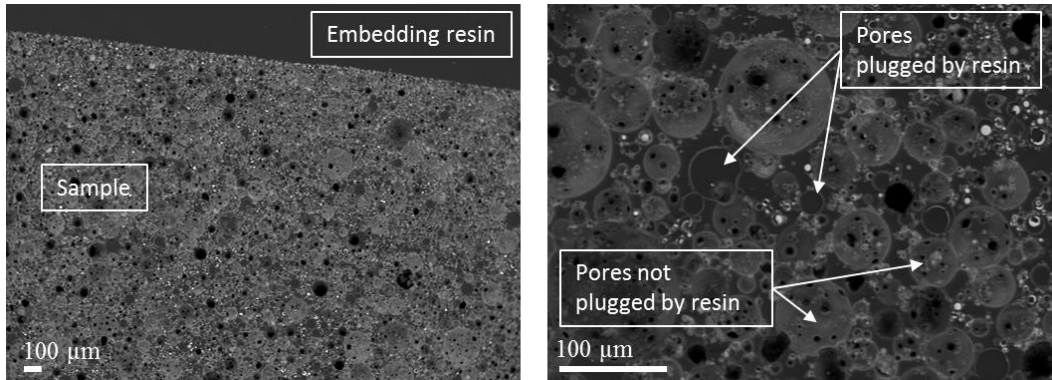


Figure II. 7: SEM images of monolith fracture sampling for EPMA

Mercury intrusion porosimetry

Mercury intrusion porosimetry is an extremely useful characterization technique for shaped porous materials. This technique provides a wide range of information, e.g. the pore size distribution, the total pore volume or porosity, the skeletal and apparent density, and the specific surface area of a sample. However, all these values do not take into account microporosity, since pores between about 500 μm and 3.5 nm can only be investigated ⁸.

The technique of mercury intrusion is based on the behavior of “non-wetting” liquids capillary. A non-wetting agent ($\gamma > 90^\circ$) cannot be spontaneously absorbed by the pores itself, because of surface tension. However, the mercury intrusion is possible under the action of an external force, the pressure. Thus, the theory is based on the Washburn equation (Eqn II. 1).

$$\Delta P = \frac{2 \gamma \cos \theta}{r_{pore}} \quad \text{Eqn II. 1}$$

This equation shows an inverse proportionality relationship between the pressure difference (ΔP) applied to mercury and the pore size (r_{pore}). Obviously, it considers the surface tension of mercury (γ) and the contact angle (θ) between the solid and mercury. During the project, measurements were performed on an Autopore IV Micromeritics porosimeter with the following parameters: 130° contact angle, 485 dyn-cm-1 mercury surface tension and 124 MPa maximum intrusion pressure.

Among its limitations, the Washburn equation applies only to uniformly cylindrical or slit pores. The shape of the pores will therefore be very simplified and often not representative of a real solid.

Besides, this technique is sensitive to edge effects. Especially, monoliths provide a surface textural heterogeneity (Figure II. 8) resulting from surface tensions (sol/air, sol/plastic), which can constrain mercury intrusion (Figure II. 9). To limit this effect as much as possible, monolith sampling was carried out at the center of the monoliths (i.e. circumference excluded). However, the top and

bottom surfaces remained a source of distortion. The results must therefore be exploited with a critical sense.

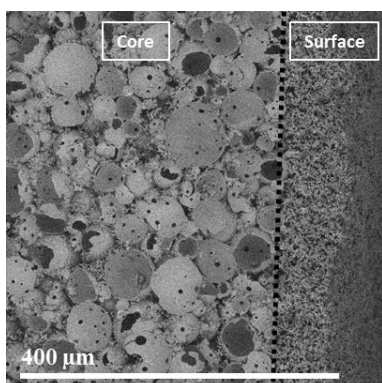


Figure II. 8: SEM image of $\text{TiO}_2@\text{Si}(\text{HIPE})$, exhibiting the surface overconcentration of TiO_2

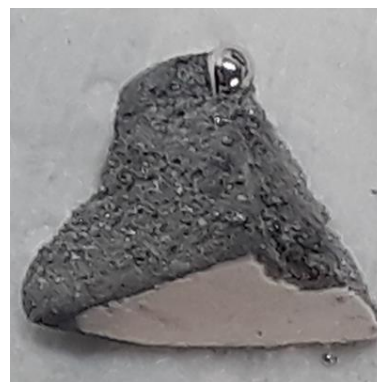


Figure II. 9: Photograph of a piece of monolith after mercury porosimetry measurement

Due to the low density of the materials, the volume of the monolith pieces necessary for the analysis to be as representative as possible is significant. A primary experimental condition is therefore to use a 10 mL penetrometer for this kind of material.

b. Meso- and microscopic length scale

The different characterization techniques used on a meso- and microscopic scale will be detailed, in particular their application to these innovative materials $\text{TiO}_2@\text{Si}(\text{HIPE})$ s. Evaluation of TiO_2 effective content embedded in $\text{Si}(\text{HIPE})$ s was realized with two techniques: XRF and ICP. Then, the nitrogen physisorption makes it possible to obtain the meso and micro surface area among other quantities characteristic of the meso- and micro-porosity of materials. Finally, the texture and structure of TiO_2 particles were visualized and characterized with TEM and XRD analyses.

Elemental analysis

The elemental analysis was used in order to determine the effective content of TiO_2 impregnated in the silica matrices, compared to the nominal content. It was assumed during synthesis that one mole of TiO_2 precursor gives one mole of TiO_2 . To evaluate the intrinsic activities of materials (formula §3.2.a), it was then necessary to have the effective TiO_2 content.

X-Ray Fluorescence (XRF) semi-quantitative analysis

Chemical analysis by this technique is based on the interaction properties of matter with X-rays. When matter is bombarded with X-rays, matter re-emits energy in the form of X-rays: this is X-ray fluorescence. The X-ray spectrum emitted by the material is characteristic of the composition of the sample. By analysing this spectrum, the elementary composition can be deduced, i.e. the mass

concentrations of elements. Primary X-rays interact with the atoms in the sample to ionize these atoms. They pass from the fundamental state to the excited state by ejecting one or more electrons from the lowest occupied electronic layers. Then, these atoms return to their stable state by filling their gap with an electron from the upper layers. The XRF phenomenon is due to the rearrangement of the electronic cloud. The atom returns to its fundamental state by emitting a photon. The energy of the emitted photon is equal to the difference in energy of the 2 orbital layers concerned. The energies of the electronic levels being characteristic of atoms, the energy of the emitted photon is also characteristic. Each line of each element has different ionization energies and therefore, according to Planck's law, a wavelength of its own.

From a practical point of view, semi-quantitative XRF analysis was chosen for two reasons. The first was the non-destructive nature of the analysis: the residual powder can be used for another analysis. The second was the feasibility of measurements on small quantities of material. Unfortunately, this last point is also a limitation of the analysis. The small quantity induces a fine thickness of the powder bed analysed. Not being in the optimal conditions of measurement (infinite thickness), the values obtained present an uncertainty of the order of 20%.

During the project, measurements were performed on PERFORM'X Sequential X-Ray Fluorescence Spectrometer, from Thermo Fisher Scientific.

Inductively Coupled Plasma – Optical Emission Spectroscopy (ICP-OES)

To obtain more precise values, another technique of elemental analysis, the ICP-OES, was used. The liquid sample is introduced into the nebulizer using a peristaltic pump. The nebulizer and nebulization chamber assembly form an aerosol consisting of fine sample droplets dispersed in argon. The spray chamber sorts the aerosol to keep only the finest droplets below 10 μm and limits the solvent charge in the plasma (pop up). This fine mist is then introduced by the injector into the plasma core. The energy released by the argon plasma allows the destruction of chemical forms, atomization, ionization and excitation of the elements present in the sample. By returning to a more stable state, the atom emits a photon of energy characteristic of the electronic transition. The number of photons emitted is proportional to the element concentration in the sample. The emitted photon is then collected through a detector near the plasma. The photon of the wavelength corresponding to the element and the type of emission (atomic or ionic) passes through a series of optics and diffraction system. The Rowland circle is thus used to separate the emitted photons according to their wavelengths and then sent them on CCD sensors.

From a practical point of view, to prepare the liquid sample, the powder sample was mixed with an acid solution based on H_2SO_4 and HF in volume proportions (1:4), and the whole was heated until complete mineralization. Then, without acid evaporation, water was added so as to obtain a dilution per 1000.

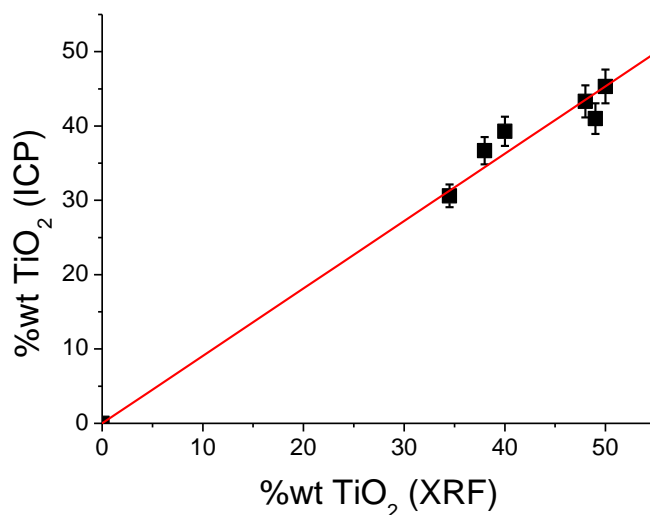


Figure II. 10: Correlation between the two elemental analysis methods for six samples. Trend curve equation: $y = 0.907x$, and correlation coefficient $R^2 = 0.982$.

The destructive and risky (HF) nature of this technique has limited its use. However, it has a good accuracy of the measured quantities of Ti (about 5% errors). Several samples were then analyzed to determine a correction factor for the XRF technique (Figure II. 10). Note that the amount of Si cannot be evaluated by this technique. Silicon dioxide and fluoridic acid could react and form SiF_4 which is a volatile compound.

During the project, measurements were performed on SPECTRO ARCOS ICP-OES analyzer.

Isothermal sorption

Nitrogen physisorption is an essential analytical technique to describe the micro and meso-structural characteristics of porous materials. By analyzing sorption isotherms (e.g. Brunauer-Emmett-Teller (BET), Barrett-Joyner-Halenda (BJH), and t-plot methods), quantities such as specific surface area or size distribution of meso- and micro-pores can be determined. The principle of sorption isotherms is based on the fact that when nitrogen gas is in contact with a solid at 77K, a specific number of gas molecules will be attracted to the surface of the solid by van der Waals forces. The number of physisorbed molecules depends on the relative pressure (P/P_0) of the N_2 gas in equilibrium with it. At low pressures ($P/P_0 < 0.2$), micropores are filled with N_2 , then with pressure increase mesopores are filled, and finally, from ca. $P/P_0 = 0.96$, macropores are filled. Differences in adsorption and desorption mechanisms constitute the basis for the interpretation of isotherms in terms of porosity and pore structure⁹.

In the 1985 IUPAC recommendation physisorption isotherms were grouped into six types¹⁰. This classification of physisorption isotherms is currently updated into eight types (I(a), I(b), II, III, IV(a), IV(b), V and, VI), and hysteresis loops into six types (H1, H2(a), H2(b), H3, H4, H5)¹¹. According to the typical shape of isotherms for a Si(HIPE) obtained using the non-continuous

volumetric technique (Figure II. 11), they seem to match with a mix of Type I (gradual increase in the amount adsorbed, at low pressure) and IV (presence of a slight hysteresis, at higher pressure). The hysteresis loop can be associated to the H4 one, like activated carbon ^{11, 12} (Figure II. 12). In addition, the difference between desorption and adsorption curve for relative pressures below 0.47 is due to a kinetic problem related to the presence of micropores. The materials could be then described as significantly microporous, and slightly mesoporous (more details in Chapter 3).

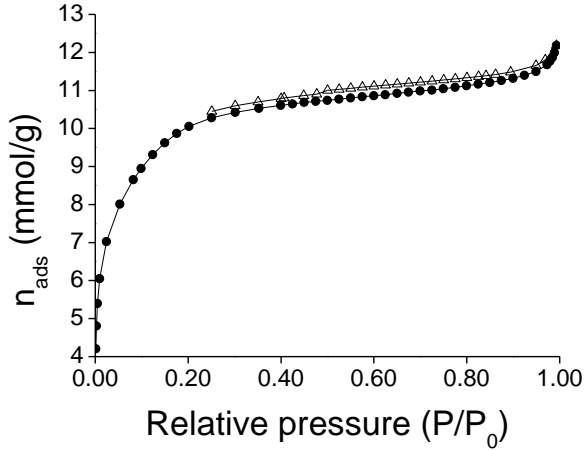


Figure II. 11: Nitrogen adsorption isotherms at 77K obtained for a typical Si(HIPE)

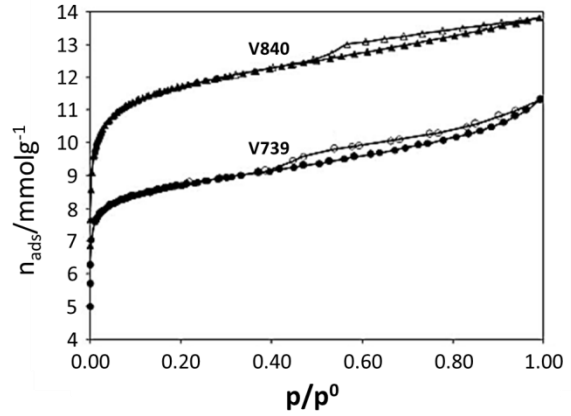


Figure II. 12: Nitrogen adsorption isotherms at 77 K obtained for two activated carbons (V739 and V840) ¹³

The Brunauer-Emmett-Teller (BET) method is widely used to determine the specific surface area (a_s) of the material, extracted from the following Eqn II. 2 ¹¹:

$$a_s = \frac{n_m \cdot L \cdot \sigma_m}{m} \quad \text{Eqn II. 2}$$

Where, n_m is the monolayer capacity defined as the amount of adsorbate enough to cover the surface with a complete monolayer of molecules, L is the Avogadro constant, σ_m is the molecular cross-sectional area and m the mass of the adsorbent. Then, the t-plot method is used to determine the microporous volume, V_μ , and surface, S_μ . Analytically, the adsorbed volume is plotted as a function of the thickness t of the adsorbed nitrogen film. This thickness is calculated from the following Harkins and Jura's expression (Eqn II. 3) ¹⁴:

$$t = \left[\frac{13.99}{0.034 - \log(P/P_0)} \right]^{1/2} \quad \text{Eqn II. 3}$$

Then, the asymptote at the plateau is plotted to extract the y-intercept and slope corresponding to the volume and the microporous surface respectively. Currently, this asymptote is applied over the range 0.35 - 0.50 nm. However, due to micropores polydisperse character, the linear domain of multilayer adsorption begins for thicker adsorbed nitrogen film. Therefore, the asymptote application

range should be moved from 0.50 to 0.80 nm. Moreover, according to the BJH method, the description of the mesoporosity is based on a discrete analysis of the desorption branch of the isotherm. Relative pressure intervals are defined, and it is assumed that, at each relative pressure point, the desorbed gas comes, on the one hand from the desorption of the condensed gas in a certain pore size range, and on the other hand from the thinning of the adsorbed layer in the larger pores previously emptied of their condensed gas. Thus, the size distribution of micro and mesopores can be obtained. However, for micropores, this distribution is not the most relevant, due to nitrogen diffusion kinetics at low pressures. Indeed, argon adsorption isotherms are more adapted to the description of micropores, because this one allows describing small pore sizes at higher pressures than nitrogen.

During the project, measurements were performed on an ASAP 2010 Micromeritics porosimeter.

Transmission Electron Microscopy (TEM)

TEM analyses are widely used to obtain topological (bright field TEM or dark field STEM) and/or chemical information (EDS-STEM) at the micro/nanoscale (HR-TEM, Figure II. 13).

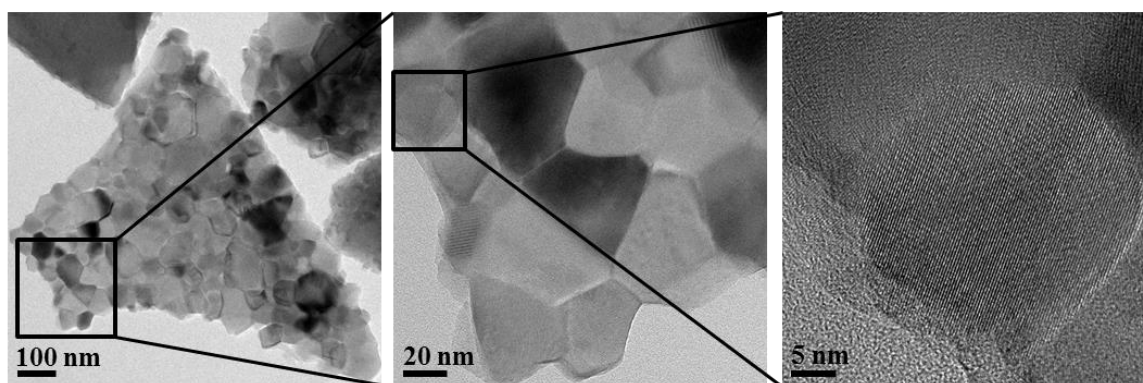


Figure II. 13: HR-MET images of TiO_2 crystals in a $\text{TiO}_2@Si(\text{HIPE})$

To form image, the electrons transmitted through a sample are collected, after interacting with it. Obviously, the sample is often an ultrathin section less than 100 nm thick, which is a constraint in monolith sampling. Although the walls thickness of silica hollow spheres is relatively small (≈ 100 nm), the large size (few μm) of these spheres requires significant fragmentation of the sample during its preparation (commonly, sonication of grinded monolith dispersed in ethanol, and deposit on a copper grid coated with a Formvar/carbon membrane). This implies that it is sometimes difficult to distinguish the area from the monolithic structure observed (especially inside or outside a sphere). The more relevant preparation used to observe a thin sample of monolith preserving structure, is a PIPS (Precision Ion Polishing System) preparation (Figure II. 14). For the ion milling process, a pellet of grinded monolith was stuck on a nickel grid, mechanically sanded, and then slied with the Gatan 691 PIPS. In this machine, two focused Ar ion beams mill the dimple-ground sample in such a way that a hole results

at the desired position. The edges of the hole then have a gradual thickness, which provides areas thin enough for imaging.

Furthermore, EDS analyses were carried out to compare the Ti content in the silica walls on two samples from different impregnation methods. For this, about ten qualitative EDS analyses per sample were carried out on the silica support without visible TiO₂ clusters, by post-treatment of the mappings. The ratio of Ti and Si intensities was then calculated and averaged over the number of measurements per sample. The results are presented and discussed in Chapter III 2 1) b.

Moreover, the chemical contrast between TiO₂ and silica makes it possible to distinguish them on a TEM image. During the project, measurements were performed using two microscopes: i) a Jeol JEM 2100F with a field emission gun (FEG), an acceleration voltage of 200 kV, and equipped with a HAADF detector for STEM acquisitions, ii) a Jeol JEM 2200FS with a field emission gun (FEG, high resolution), an acceleration voltage of 200 kV, and equipped with a BF (Bright Field) detector for STEM acquisitions.

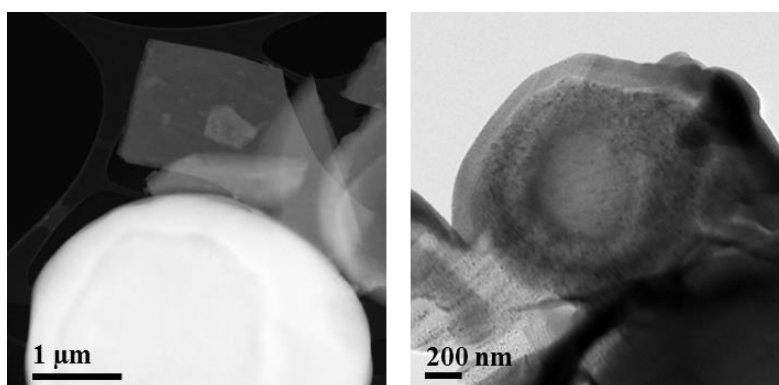


Figure II. 14: (left) STEM image of a TiO₂ cluster without the surrounding structure, commonly prepared and (right) TEM image of a TiO₂ cluster anchored inside a silica hollow sphere, from PIPS preparation

X-ray diffraction (XRD)

X-ray powder diffraction is most widely used for the identification of unknown crystalline materials. More precisely, in this project, the objective of this analysis was to identify the allotropic phase(s) of TiO₂ (anatase and/or rutile), and the size of the crystallites (from the Scherrer equation, Eqn II. 4). Moreover, if crystallized TiO₂ particles provide a mix of phases, XRD is used to determine the phase proportion.

$$\tau = \frac{K * \lambda}{\beta * \cos(\theta)} \quad \text{Eqn 4}$$

Where, τ is the average size of the crystallites, K is a shape factor (usually 0.9), λ is the wavelength of the copper ray $K\alpha$ (which is 1.5418 Å), β is the full width at half maximum (FWHM), and θ the Bragg angle.

X-ray diffraction is based on constructive interference of monochromatic X-rays and a crystalline sample. These X-rays are generated by a cathode ray tube, filtered to produce monochromatic radiation, collimated to concentrate, and directed toward the sample. The interaction of the incident rays with the sample produces constructive interference and a diffracted ray, when conditions satisfy Bragg's Law : $n\lambda = 2d \cdot \sin \theta$. This law relates the wavelength of electromagnetic radiation, λ (modulo diffraction order n), to the diffraction angle, θ , and the lattice spacing, d , in a crystalline sample. These diffracted X-rays are then detected, processed, counted, and associated to d-spacings. As each mineral has a unique set of spaces-d, XRD is an essential mineral identification method ¹⁵.

A method for estimating the crystallinity rate was implemented using XRD patterns. For this purpose, 5 mechanical mixtures of P25 TiO₂ and silica from the grinding of a so-called reference Si(HIPE) were made for the following weight proportions P25/silica: 10/90, 20/80, 30/70, 50/50, 100/0. P25 TiO₂ has an anatase/rutile ratio of 80/20. The theoretical anatase weight percentage was calculated by weighting the theoretical TiO₂ weight percentage by the anatase proportion. Then, the 48°2θ ray net area was measured due to the low impact of the amorphous signal on the baseline. An abacus could then be made and is presented in Figure II. 15. The mass percentage in anatase of a sample obtained by the abacus can then be compared with the theoretical one: the ratio delivers the crystallinity rate. The theoretical anatase weight percentage of a sample is obtained by multiplying the anatase percentage (XRD analysis) and the TiO₂ weight percentage (XRF analysis). A strong hypothesis of this method is that the TiO₂/silica system responds in the same way whatever the silica origin. To overcome this problem, a standard must be added to each sample to correct the pattern if necessary. However, due to lack of time this could not be achieved. This method will therefore only be used to qualitatively compare the four impregnation methods.

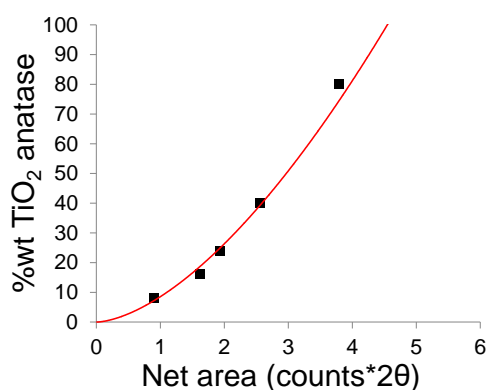


Figure II. 15: Abacus connecting the theoretical mass percentage of anatase and the 48°2θ ray net area of the mechanical mixtures. Trend curve equation: $y = 8.547 \cdot x^{1.624}$, and correlation coefficient $R^2 = 0.972$.

During the project, measurements were performed on a PANalytical X'Pert PRO MPD diffractometer, with a copper X-ray source. The scattered radiation was collected on two detectors: a punctual one and an X'Celerator rapid detector. Both are preceded by a secondary graphite crystal monochromator.

2) Electronic characterization: diffuse reflectance UV-Visible spectroscopy

In photocatalysis, diffuse reflectance UV/Vis spectroscopy is routinely used to determine the bandgap energy of semiconductors (active phase). In the case of opaque samples such as solids, the transmission is zero and it is then adapted to analyze them in diffuse reflection. Diffuse reflection occurs when light (from 200 to 900 nm) is reflected in many directions, unlike specular reflection, which reflects radiation in a single direction. Then, the relative change in the amount of light reflected from a surface (compared to Spectralon reference) is measured and plotted as a function of wavelength for sketching the spectrum.

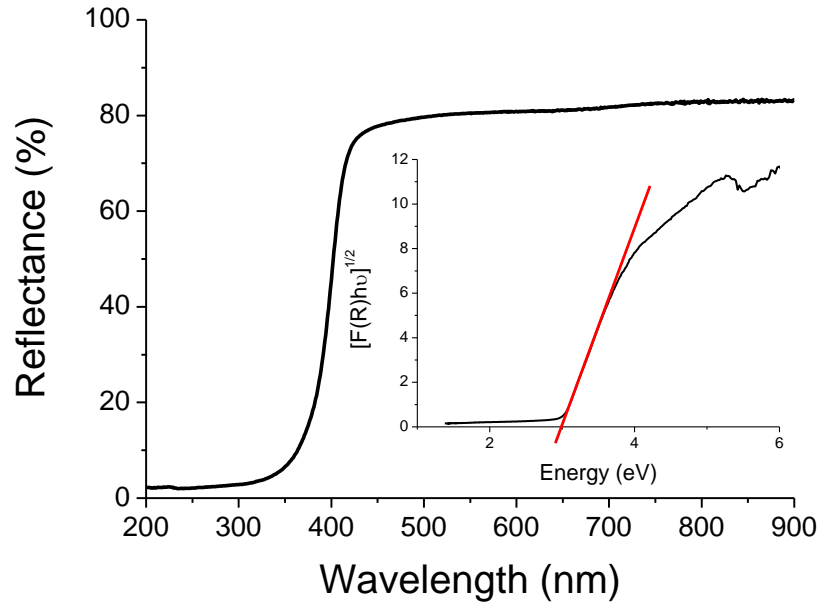


Figure II. 16: UV-Visible diffuse reflectance spectrum for a typical $\text{TiO}_2@\text{Si}(\text{HIPE})$. Insert: plot of transformed KM function $[F(R)hv]^{1/2}$ vs. hv for a typical $\text{TiO}_2@\text{Si}(\text{HIPE})$

The Kubelka-Munk (KM) function is used to describe the diffuse reflection of light if the following four assumptions are met: i) the incident light diffuses through the particles, ii) there is no reflection at the interfaces, iii) the particles are randomly dispersed, and iv) particle size is less than sample thickness. In this case, the relative diffuse reflectance (R) is related to absorption (k) and scattering (s) coefficient according the Kubelka-Munk (K-M) function ($F(R)$, Eqn II.5):

$$F(R) = \frac{(1 - R)^2}{2R} = \frac{k}{s} \quad \text{Eqn II. 5}$$

Then, the bandgap energy can be obtained from the plots of $[F(R)hv]^{1/2}$ as a function of hv photons energy, as the intercept of the extrapolated linear part of the plot at $[F(R)hv]^{1/2} = 0$ (e.g. Figure II. 16).

During the project, measurements were performed on Agilent CARY 60 UV-Visible spectrometer, and the reference (infinitely reflective compound) used is a Spectralon plate. All $TiO_2@Si(HIPE)s$ samples showed a band gap energy of 3 eV.

3) Light diffusion characterization

The interest sought in the use of monoliths is to perform photoreduction reactions of CO_2 through a volume, and no longer over a surface of thin film photocatalytic systems. The light penetration does not exceed 400 nm depths in TiO_2 bulk for a wavelength of 320 nm¹⁶. Thus, it is important to determine the penetration depth of photons in the tested materials. For this purpose, two techniques were applied. The first one provided a visual indication of this penetration, while the second was based on physical measurements.

a. Gold salt impregnation method

A gold salt solution of 10^{-2} M concentration was prepared from $KAuCl_4$ powder (purity = 99.995%, Sigma-Aldrich), in 2-propanol solvent. Monoliths were then impregnated under vacuum in a desiccator, as mentioned above in §1.2.b). They were finally air-dried, between two sheets of absorbent paper. Chloroaurate ions were reduced into gold nanoparticles under UV radiation. The irradiation was performed for 1 hour using a metal halide lamp ($P_{280-395\text{ nm}} = 24\text{ W.cm}^{-2}$), located 5 mm from the monolith surface. Due to their size, gold nanoparticles provided violet color which acted as a visual indicator of photons penetration.

b. Pulsed laser method

To characterize the optical diffusion properties of the various samples, the times of flights of individual photons travelling across the sample relative to the incident pulse was recorded, owing to a simultaneous spatial and time-resolved setup. This last one is consisting of a streak camera (HAMAMATSU Streak Scope C10627). The excitation light was the frequency doubled output of the $\lambda = 1030\text{ nm}$ wavelength, 10 MHz repetition rate, 300 fs line width pulses delivered by a diode-pumped Ytterbium femtosecond oscillator from Amplitude systems (t-Pulse 200). The beam was very slightly focused to a 1 mW, 1 mm (Figure II. 17).

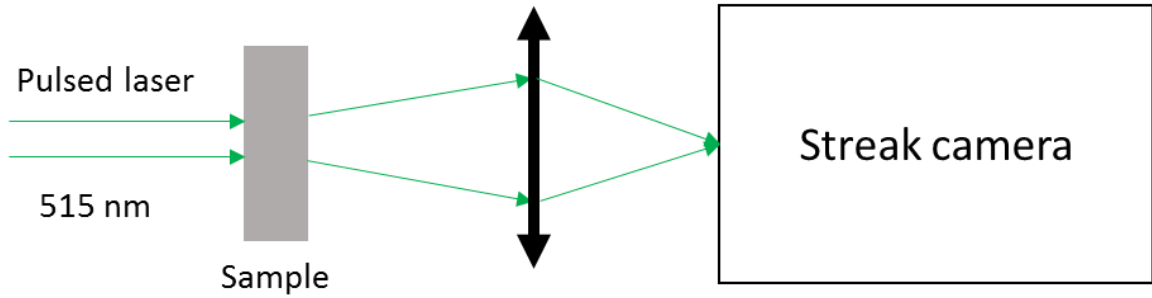


Figure II. 17: Overview of simultaneous spatial and time-resolved setup

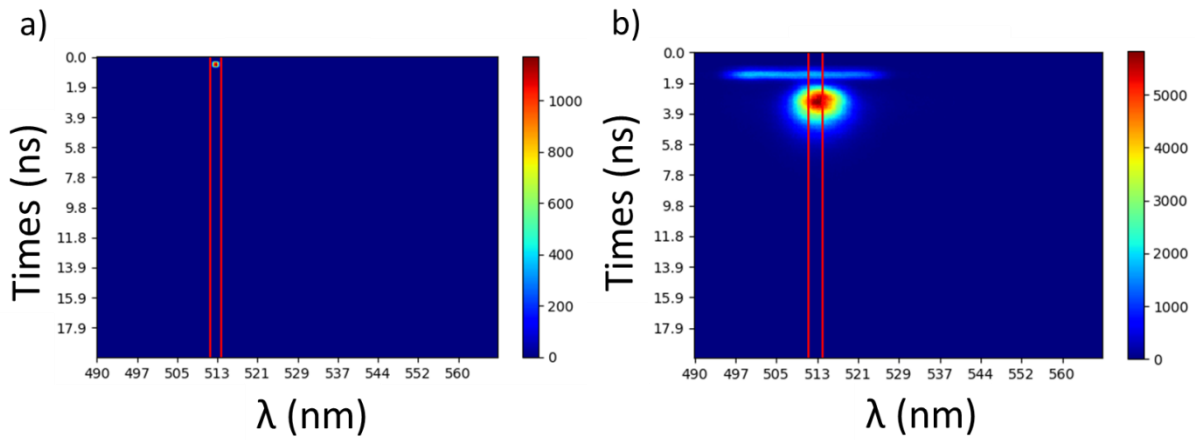


Figure II. 18: Imaging of light pulse propagation through **a)** no sample and **b)** diffuse sample

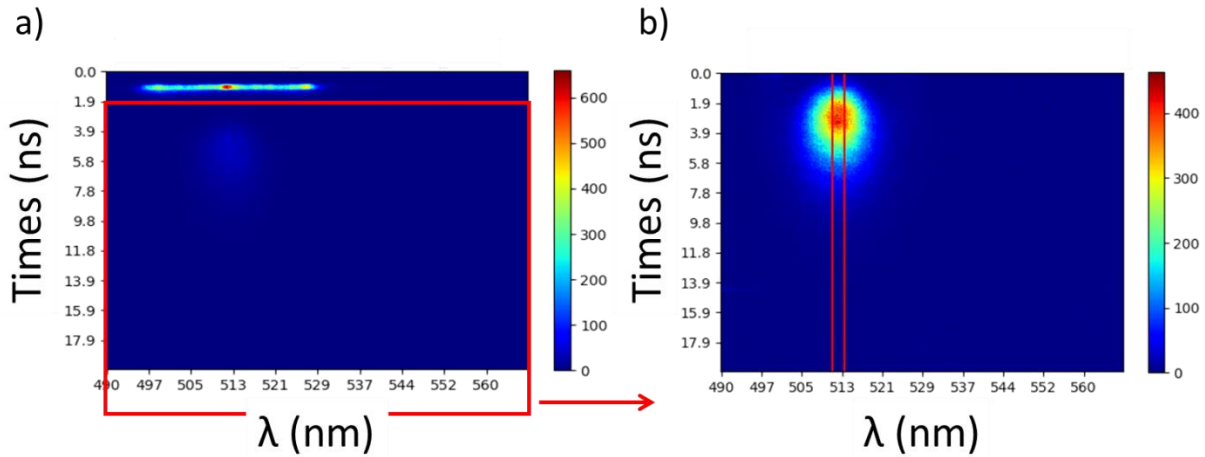


Figure II. 19: Imaging of light pulse propagation through sample with cracks **a)** original and **b)** with time shift

The light pulse propagation through no sample provide a small stain (Figure II. 18 a), while through a diffuse sample, the stain is prolonged in time and coarse in space (Figure II. 18 b). The shiny line above the stain in Figure II. 18 b is explained by the presence of cracks in the sample; some of the

light passes through the cracks and exits the material earlier than that which is diffused. In order not to disturb the collection of photons by this phenomenon, which is not representative of the diffuse character of the sample, a time shift is operated as shown in Figure II. 19. The two red lines delimit the integration zone in order to obtain the temporal profile. Each sample is measured in three positions for reproducibility. The temporal profile is obtained by integrating signal into the area defined by spot width without sample. In Figure II. 20, the three profiles shown correspond to the 3 positions. Then, the temporal profiles and the full solution of the diffusion equation described in Chapter 1 are fitted to extract the characteristic values, as the transport mean free path (l_t).

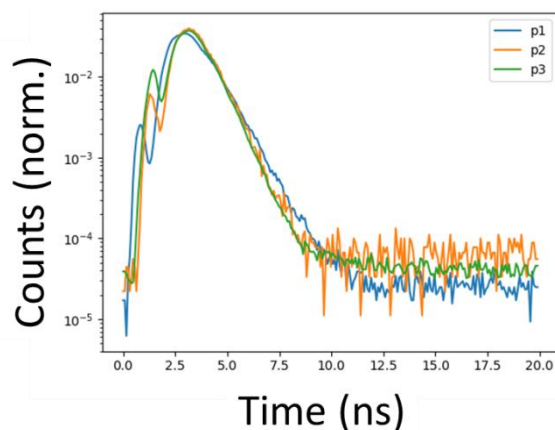


Figure II. 20: Temporal profiles for three positions on the sample

3 Photocatalytic tests

The objective of the photocatalytic tests is to evaluate the behavior of the active phase, TiO_2 , within a hierarchically porous structure, Si(HIPE), about the CO_2 photocatalytic reduction in the presence of water.

1) Set up

A modular unit was set up at IFPEN during Dina Lofficial's PhD¹⁷ to carry out tests in liquid phase or gas phase configuration. Throughout the project, the set up was used in the gas phase configuration and continuous mode. The different elements of this unit, the operating modes used as well as the results obtained are presented in the following sections.

a. Reactor

The stainless-steel cylindrical reactor used ($\varnothing_{\text{ext}} = 7$ cm) provided two parts with different internal diameters ($\varnothing_{\text{int, upper}} = 3.7$ cm and $\varnothing_{\text{int, lower}} = 5$ cm). The gas inlet is operated in the upper part of the reactor, and the outlet in the lower one. At the junction between these both parts, a Teflon ring was

placed and locked by a clamping ring. Then, prior to insert the monolith in the reactor, it is slightly sanded to homogenize and flatten the surface that will be irradiated. The contact between the Teflon ring and the monolith is achieved by a vacuum grease edging (Figure II. 21). The whole is hermetically closed by an O-ring and a clamping ring, fixing at the top a quartz optical window (Figure II. 22) and at the bottom a stainless-steel plate.

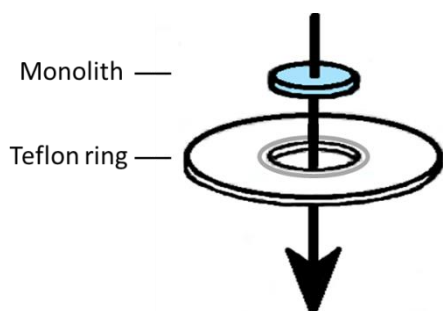


Figure II. 21: Representation of the monolith - Teflon ring assembly

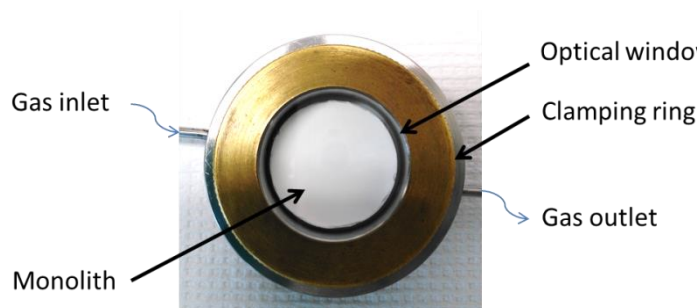


Figure II. 22: Top view of the monolith-Teflon ring assembly inside the reactor

The reactor configuration involves a bed-through reaction. Two types of materials were tested: cylindrical monoliths and powders. The monoliths provided a diameter of 3.2 cm. The powders were arranged within the volume left by the 2.6 cm diameter and 1 mm height Teflon ring (a support membrane was then added under the Teflon ring).

b. Devices

Photocatalysis experiments were carried out in a reactor as mentioned above operating at atmospheric pressure and ambient temperature and irradiated by a xenon lamp Max303 Asahi Spectra (irradiance spectra Figure II. 23).

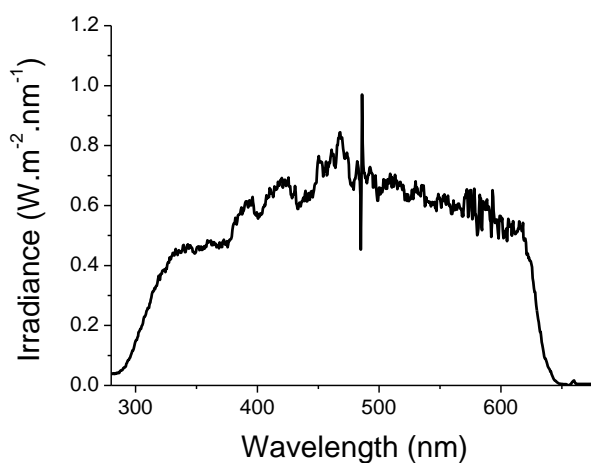


Figure II. 23: Irradiance spectra of Max303 Asahi Xenon lamp

Products were analyzed on-line by a gas TCD sensor micro chromatograph Lan3000 (SRA Instruments, $\mu\text{GC-TCD}$). Gas phase analyses were performed every 10 minutes. The analytical parameters selected for optimal gas separation under our conditions are presented in Table A 4, in annex. The micro-chromatograph was calibrated for all gases from different gas cylinders with controlled contents. The retention times, in seconds, of the gases analyzed by the first three columns of the chromatograph are listed in Table A 5, annex. No species produced has been detected on the fourth; retention times will not be itemized.

c. Procedure

First, a system purging step was performed to avoid the presence of oxygen from the air during the reaction (anaerobic conditions). This step consisted in performing the vacuum a first time up to less than 200 mbar, then rising to atmospheric pressure by injection of argon at $30 \text{ mL}\cdot\text{min}^{-1}$. A second vacuum was performed, and then a mix flow of argon at $30 \text{ mL}\cdot\text{min}^{-1}$ and CO_2 at $3.0 \text{ mL}\cdot\text{min}^{-1}$ was injected into the reactor. Once atmospheric pressure was reached, the argon flow was stopped while CO_2 flow was maintained. CO_2 source was B20 gas cylinder (purity > 99%, Air Liquide), and argon source was gas distribution network (purity > 99.999%, Air Liquide). The set-up is illustrated in Figure II. 24.

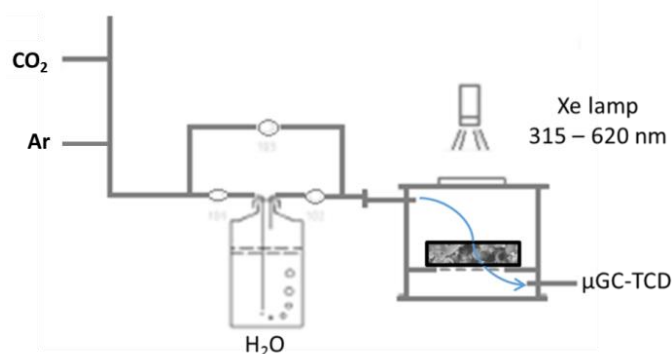


Figure II. 24: Schematic representation of photocatalytic experiment set up

A water saturator was placed upstream of the reactor, inside which CO_2 bubbled. The quantity of water was estimated at ca. 3% by volume, which corresponds to a molar ratio CO_2 over H_2O equal to around 30. Once the CO_2 concentration stabilized (controlled by gas chromatograph analysis), its flux was reduced to $0.3 \text{ mL}\cdot\text{min}^{-1}$ (except special mention). The system was then irradiated for 20h (except special mention). For visualization convenience, an example of classical photocatalytic test is shown in Figure II. 25, with instantaneous rates of H_2 , CO , CH_4 , and C_2H_6 production versus time on stream. Note that the test start increase does not correspond to a material activation time, but to the set-up lines filling time.

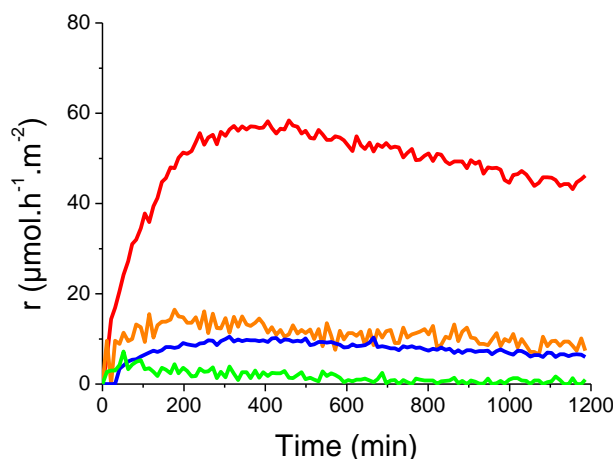


Figure II. 25: Productions of all detected products are drawn: H_2 (red), CO (orange), CH_4 (blue) and C_2H_6 (green) for a TiO_2 powder sample

2) Evaluation of photocatalytic performances

According to the reaction equation (Eqn II. 6, not balanced for clarity reasons), a couple of products could be produced, only those written were detected during the project. The product formation is initiated by the generation of electron-hole pairs according to the following reaction: $h\nu \rightarrow e_{BC}^{SC} + h_{BV}^+$. The half reaction equations corresponding to the products, normalized for one mole of product, are summarized in Table II. 2.

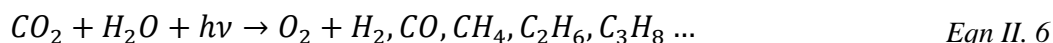


Table II. 2: The half reaction equations involved in the photocatalytic process of water splitting and CO_2 photoreduction

Reaction type	Reaction
Oxidation	$H_2O + 2h^+ \rightarrow \frac{1}{2} O_2 + 2H^+$
	$2e^- + 2H^+ \rightarrow H_2$
	$CO_2 + 2H^+ + 2e^- \rightarrow CO + H_2O$
Reduction	$CO_2 + 8H^+ + 8e^- \rightarrow CH_4 + 2H_2O$
	$2CO_2 + 14H^+ + 14e^- \rightarrow C_2H_6 + 4H_2O$
	$3CO_2 + 20H^+ + 20e^- \rightarrow C_3H_8 + 6H_2O$

To evaluate the photocatalytic properties of materials, intrinsic and global activities as well as selectivity are studied quantities. The first one provides information on the intrinsic performances of the catalyst, closely related to the crystalline structure of this catalyst, and the second one takes into account the material shaping, especially its textural structure (e.g. pore size distribution). In addition, the

selectivity evaluates the overall orientation of the reactions towards the formation of desired products compared to the (undesired) dihydrogen, resulting from the recombination of the protons generated by water oxidation. The presence of water as sacrificial agent in the CO₂ photoreduction implies that water splitting process occurs as side reaction.

a. Photocatalytic activities

Global activity per mass

These activities are expressed per mass of TiO₂ and distinguished into two categories: one by product and the other over all products. The first one compares independently the behavior of catalysts for each product, while the second globalize the contributions giving access to an overall activity.

- *To represent the performance of catalyst by product i formed, two quantities were chosen: the instantaneous production rate of product i at a given time (r_m^i , Eqn II. 7) and the total production of product i at the end of the test time t (P_m^i , Eqn II. 8) corresponding to the area under the curve of the previous quantity.*

$$r_m^i = \frac{[i] * Q_{tot}}{V_m^{25^\circ C} * m_{cat}} * 60 * 10^6 \quad \text{Eqn II. 7}$$

$$P_m^i = \int_0^t \frac{[i](x) * Q_{tot}}{V_m^{25^\circ C} * m_{cat}} * 60 * 10^6 dx \quad \text{Eqn II. 8}$$

With:

- ✓ r_m^i the production rate of product i per catalyst mass unit, $\mu\text{mol} \cdot \text{h}^{-1} \cdot \text{g}^{-1}$
 - ✓ $[i]$ the concentration of product i over time, ppmVol
 - ✓ Q_{tot} the flow of CO₂ and H₂O injected, i.e. $3 \cdot 10^{-4} \text{ L} \cdot \text{min}^{-1}$
 - ✓ $V_m^{20^\circ C}$ the molar volume of a gas at 25°C, i.e. $24,5 \text{ L} \cdot \text{mol}^{-1}$
 - ✓ m_{cat} the catalyst mass (TiO₂), g
 - ✓ $60 * 10^6$ homogenizes the units in $\mu\text{mol} \cdot \text{h}^{-1}$
 - ✓ P_m^i total production of product i at the end of the test time t per unit mass of catalyst, $\mu\text{mol} \cdot \text{g}^{-1}$
 - ✓ t the time, min
- *To represent the catalyst performance over all products, the electron consumption associated with each product must be considered. Indeed, one mole of hydrogen valorizes two moles of photons ($1 \text{ hv} = 1 \text{ e}^-$), while one mole of methane valorizes 8 moles of photons. The two quantities chosen are therefore: the instantaneous electron consumption rate at a given time ($r_m^{e^-}$, Eqn II. 9) and the total electron consumption at the end of the test time t ($C_m^{e^-}$, Eqn II. 10) corresponding to the area under the curve of the previous quantity.*

$$r_m^{e^-} = \sum_i \frac{n_i^{e^-} * [i] * Q_{tot}}{V_m^{25^\circ C} * m_{cat}} * 60 * 10^6 \quad \text{Eqn II. 9}$$

$$C_m^{e^-} = \int_0^t \sum_i \frac{n_i^{e^-} * [i] * Q_{tot}}{V_m^{25^\circ C} * m_{cat}} * 60 * 10^6 dx \quad \text{Eqn II. 10}$$

With:

- ✓ $r_m^{e^-}$ the electron consumption rate per catalyst mass unit, $\mu\text{mole} \cdot \text{h}^{-1} \cdot \text{g}^{-1}$
- ✓ $C_m^{e^-}$ the total electron consumption at the end of the test time t, $\mu\text{mole} \cdot \text{g}^{-1}$
- ✓ $n_i^{e^-}$ the stoichiometric coefficient of the electrons consumed per mole of product i

Global activity per surface

These activities are normalized by the irradiated geometric surface of the material. The distinction between an evaluation by product and another over all products is also done in the following expressions: the instantaneous production rate of product i at a given time (r_S^i , Eqn II. 11) and the total production of product i after the test time t (P_S^i , Eqn II. 12); and the instantaneous electron consumption rate at a given time ($r_S^{e^-}$, Eqn II. 13) and the total electron consumption after the test time t ($C_S^{e^-}$, Eqn II. 14).

$$r_S^i = \frac{[i] * Q_{tot}}{V_m^{25^\circ C} * S_{irr}} * 60 * 10^6 \quad \text{Eqn II. 11}$$

$$P_S^i = \int_0^t \frac{[i](x) * Q_{tot}}{V_m^{25^\circ C} * S_{irr}} * 60 * 10^6 dx \quad \text{Eqn II. 12}$$

$$r_S^{e^-} = \sum_i \frac{n_i^{e^-} * [i] * Q_{tot}}{V_m^{25^\circ C} * S_{irr}} * 60 * 10^6 \quad \text{Eqn II. 13}$$

$$C_S^{e^-} = \int_0^t \sum_i \frac{n_i^{e^-} * [i] * Q_{tot}}{V_m^{25^\circ C} * S_{irr}} * 60 * 10^6 dx \quad \text{Eqn II. 14}$$

With:

- ✓ r_S^i the production rate of product i per unit area irradiated, $\mu\text{mol} \cdot \text{h}^{-1} \cdot \text{m}^{-2}$
- ✓ S_{irr} the surface of the irradiated material, soit $8,04 \cdot 10^{-4} \text{ m}^2$ for a monolith and $5,3 \cdot 10^{-4} \text{ m}^2$ for P25 TiO₂ powder
- ✓ P_S^i the total production of product i at the end of the test time t per irradiated area, $\mu\text{mol} \cdot \text{m}^{-2}$
- ✓ $r_S^{e^-}$ the electron consumption rate per unit area, $\mu\text{mole} \cdot \text{h}^{-1} \cdot \text{m}^{-2}$
- ✓ $C_S^{e^-}$ the total electron consumption at the end of the test time t, $\mu\text{mole} \cdot \text{m}^{-2}$

To compare the photocatalytic performance of the materials tested, it was chosen to use the average electron consumption rates ($\mu\text{mole} \cdot \text{h}^{-1} \cdot \text{m}^{-2}$), normalized by catalyst mass or by unit area, and defined as follows:

$$\overline{r_{\{m\}}^{e-}} = \frac{1}{TOS} \int_0^{TOS} \sum_i \frac{n_i^{e-} * [i] * Q_{tot}}{V_m^{25^{\circ}C} * \left\{ \frac{S_{irr}}{m_{cat}} \right\}} * 60 * 10^6 dx \quad \text{Eqn II. 15}$$

Where TOS is the Time Of Set, corresponding to the duration of the test.

b. Selectivity

Electron selectivity is defined as the percentage of electrons brought by the oxidation of water and consumed by product i at a given time (S_i^{e-} , Eqn II. 16). To simplify the comparison between selectivities, the average quantity (over the number of analyses) is used ($\overline{S_i^{e-}}$, Eqn II. 17).

$$S_i^{e-} = \frac{n_i^{e-} * [i]}{\sum_j n_j^{e-} * [j]} \quad \text{Eqn II. 16}$$

With:

- ✓ S_i^{e-} the instantaneous selectivity of electrons towards the formation of product i, %
- ✓ $\overline{S_i^{e-}}$ the average selectivity of electrons towards product formation i, %

4 Conclusion

Our study focuses on the use of monolithic materials to intensify the photocatalysis process. The integrative chemistry principle made it possible to structure these materials at all scales. The silica skeleton bearing the microporosity was formed by a sol-gel route. The silica precursor (TEOS) undergone hydrolysis-condensation steps in acid catalysis to form the three-dimensional network. The surfactant (TTAB) had a dual role of stabilizing the direct concentrated emulsion (dodecane as dispersed phase), which was the macroporosity precursor, and of mesostructuring due to its liquid crystal arrangement. This first step formulated the silica support bearing the hierarchical porosity, Si(HIPE). The TiO₂ active phase incorporation was carried out by impregnation with colloidal solutions and crystallization by heat treatment, to form the material TiO₂@Si(HIPE). These solutions were produced by the hydrolysis-condensation mechanism in acid catalysis of the precursor TTIP or P25 TiO₂ particle dispersion in an acidic aqueous phase. The routine synthesis protocol and the four impregnation methods have been detailed in the first part.

To understand the behavior of these materials about CO₂ photoreduction, and to relate the performance achieved to their physicochemical properties, a multi-length scale characterization set was applied. Macropores make it possible to considerably lower the pressure gradients within the structure, thus ensuring the material integrity when fluids flow through it¹⁸. This property is essential when impregnating TiO₂. Thus, these macropores were visualized and characterized by SEM and mercury intrusion porosimetry, as well as the TiO₂ distribution throughout the silica matrix was evaluated by

EPMA. The micro and meso structures are the place where adsorption, desorption and reactions occur. It is therefore important to know the material structure at these scales. For this purpose, the XRF/ICP, TEM, XRD and diffuse reflectance UV-Visible spectroscopy analyses quantified and characterized the active phase, while nitrogen physisorption made it possible to determine the specific surface area developed. The material hierarchical porosity plays a key role in the multiple scattering of light, as does the refractive index of the scatters. Thus, the transport mean free path of photons was evaluated by a pulsed laser method. All these characterization techniques were described in this chapter, and notably their application to these porous monolithic materials. The material physicochemical characteristics will be discussed in Chapter III as a function of synthetic parameters.

The behavior evaluation of synthesized materials and commercial P25 TiO₂ powder with regard to CO₂ photoreduction was performed on the set-up and under the conditions detailed in this chapter. The key parameters to keep in mind are that photocatalytic tests were performed at ambient temperature, atmospheric pressure and anaerobic conditions were sought. Besides, CO₂ flow rate was maintained at 0.3 cc.min⁻¹, the molar ratio of CO₂ over H₂O was about 30, and the irradiation power has always been adjusted to be as close as possible to 80 W.m⁻². The main quantities used in the photocatalytic performance evaluation were the average electron consumption rate normalized per unit mass or surface and the average selectivity. Their values will be discussed in Chapter IV as function of material physicochemical properties.

5 References

- (1) Silverstein, M. S. Emulsion-Templated Porous Polymers: A Retrospective Perspective. *Polymer* **2014**, 55 (1), 304–320.
- (2) Gaikwad, P.; Bachelard, N.; Sebbah, P.; Backov, R.; Vallée, R. A. L. Competition and Coexistence of Raman and Random Lasing in Silica-/Titania-Based Solid Foams. *Advanced Optical Materials* **2015**, 3 (11), 1640–1651.
- (3) Carn, F. Intégration Entre Chimie Douce et Fluides Complexes Pour La Genèse d'architectures Poreuses Hiérarchisées: Synthèses, Caractérisations et Application, Université de Bordeaux 1, 2006.
- (4) Carbonell, E.; Ramiro-Manzano, F.; Rodríguez, I.; Corma, A.; Meseguer, F.; García, H. Enhancement of TiO₂ Photocatalytic Activity by Structuring the Photocatalyst Film as Photonic Sponge. *Photochem. Photobiol. Sci.* **2008**, 7 (8), 931–935.
- (5) University of Glasgow - Schools - School of Geographical & Earth Sciences - Research and Impact - Research Facilities - ISAAC : Imaging Spectroscopy and Analysis Centre - Services - Scanning Electron Microscopy - Imaging - LowVacuum
<https://www.gla.ac.uk/schools/ges/researchandimpact/researchfacilities/isaac/services/scanningelectronmicroscopy/imaging/lowvacuum/> (accessed Oct 14, 2018).
- (6) Dufek, M. User Operation Manual
https://siliconpr0n.org/media/fei/nova_nanosem/online_doc.pdf.
- (7) Introduction to Electron Probe Microanalysis (EPMA)
<http://www.cameca.com/products/epma/technique> (accessed Oct 14, 2018).
- (8) Giesche, H. Mercury Porosimetry: A General (Practical) Overview. *Particle & Particle Systems Characterization* **2006**, 23 (1), 9–19.

- (9) Bertier, P.; Schweinar, K.; Stanjek, H.; Ghanizadeh, A.; Clarkson, C. R.; Busch, A.; Kampman, N.; Prinz, D.; Amann-Hildebrand, A.; Krooss, B. M.; et al. On the Use and Abuse of N₂ Physisorption for the Characterization of the Pore Structure of Shales; 2016; pp 151–161.
- (10) Sing, K. S. W. Reporting Physisorption Data for Gas/Solid Systems with Special Reference to the Determination of Surface Area and Porosity (Recommendations 1984). *Pure Appl. Chem.* **1985**, 57 (4), 603–619.
- (11) Thommes, M.; Kaneko, K.; Neimark, A. V.; Olivier, J. P.; Rodriguez-Reinoso, F.; Rouquerol, J.; Sing, K. S. W. Physisorption of Gases, with Special Reference to the Evaluation of Surface Area and Pore Size Distribution (IUPAC Technical Report). *Pure and Applied Chemistry* **2015**, 87 (9–10), 1051–1069.
- (12) Sing, K. S. W.; Williams, R. T. Physisorption Hysteresis Loops and the Characterization of Nanoporous Materials. *Adsorption Science & Technology* **2004**, 22 (10), 773–782.
- (13) Nabais, J.; Laginhas, C.; Carrott, P.; Ribeiro Carrott, M. M. Thermal Conversion of a Novel Biomass Agricultural Residue (Vine Shoots) into Activated Carbon Using Activation with CO₂. *Journal of Analytical and Applied Pyrolysis* **2010**, 87, 8–13.
- (14) Lynch, J. *Physico-Chemical Analysis of Industrial Catalysts: A Practical Guide to Characterisation*; Editions TECHNIP, 2003.
- (15) X-ray Powder Diffraction (XRD)
https://serc.carleton.edu/research_education/geochemsheets/techniques/XRD.html (accessed Oct 14, 2018).
- (16) Hagfeldt, A.; Grätzel, M. Light-Induced Redox Reactions in Nanocrystalline Systems. *Chem. Rev.* **1995**, 95, 49–68.
- (17) Lofficial, D. Photosynthèse Artificielle: Élaboration de Matériaux Composites Pour La Valorisation de CO₂ Par Photocatalyse, Université de Lyon, 2015.
- (18) Brun, N. Chimie Intégrative Pour La Conception de Matériaux Poreux Fonctionnels Avancés et Applications, Université de Bordeaux, 2010.

Chapter III

TiO₂@Si(HIPE) physicochemical characteristics

This chapter consists in three parts dedicated to the physicochemical characteristics of materials: morphologies, structures and light diffusion. The first part describes the synthesized material morphology at all scales: at first, the porous silica matrix, and the latter after TiO₂ impregnation. Reproducibility and repeatability considerations are studied to the characteristic quantities to determine their relevance. The second part establishes the synthetic parameter influence on TiO₂ structure and crystallinity, and the silica matrix morphology. Variables of interest can then be identified to discuss their influence on photocatalytic performance (Chapter IV). The last part describes the light diffusion in materials through the transport mean free path of photons as a function of morphological properties.

TABLE OF CONTENTS

1	<u>MORPHOLOGICAL DESCRIPTIONS.....</u>	<u>83</u>
1)	Si(HIPE): SILICA MATRIX.....	83
A.	MACROSCOPIC LENGTH SCALE	83
B.	MESO- AND MICROSCOPIC LENGTH SCALE.....	85
C.	REPRODUCIBILITY AND REPEATABILITY	87
2)	TiO ₂ @Si(HIPE)	88
A.	MACROSCOPIC LENGTH SCALE	88
B.	MESO- AND MICROSCOPIC LENGTH SCALE.....	91
C.	REPRODUCIBILITY AND REPEATABILITY	93
3)	CONCLUSION	94
2	<u>INFLUENCE OF SPECIFIC PARAMETERS</u>	<u>94</u>
1)	TiO ₂ STRUCTURE AND PARTICLE MORPHOLOGY	94
A.	IMPREGNATION METHODS OVER PARTICLE MORPHOLOGY	95
	P25 slurry impregnation (<i>P25</i>)	96
	TiO ₂ precursor solution: impregnation in two steps, with alcohol (<i>Ila</i>)	96
	TiO ₂ precursor solution: impregnation in one step, with alcohol (<i>Ia</i>)	98
	TiO ₂ precursor solution: impregnation in one step, without alcohol (<i>I</i>)	98
B.	CALCINATION TREATMENT OVER TiO ₂ STRUCTURE	100
	In-situ (<i>Ia impregnation method</i>)	101
	Ex-situ (<i>Ila impregnation method</i>)	102
C.	IMPREGNATION METHODS OVER TiO ₂ STRUCTURE	103
2)	MORPHOLOGICAL Si(HIPE) MODIFICATIONS	105
A.	OIL VOLUME FRACTION (ϵ).....	105
B.	OIL CHAIN LENGTH (C_x)	107
C.	CALCINATION TREATMENT (T)	109
D.	LOCAL SHEAR (v)	111
E.	THICKNESS (t).....	113
3)	CONCLUSION	114
3	<u>LIGHT DIFFUSION.....</u>	<u>114</u>
4	<u>CONCLUSION.....</u>	<u>117</u>

5 REFERENCES 118

1 Morphological descriptions

Using the characterization methods detailed in Chapter II, the description of the material morphological properties has been drawn and is detailed hereafter.

1) Si(HIPE): silica matrix

In a first step, the silica matrices are studied as catalyst support and porosity bearer of the final material. All measurements presented below are based on the analysis of a single solid from the routine synthesis. From a global point of view, all the samples are shaped in cylindrical monolithic form, with a diameter of about 3.2 cm and a variable height (photographs Chapter II).

a. Macroscopic length scale

The porosity visualization by Scanning Electron Microscopy (SEM) allows accounting for the hierarchical structure. Notably, the very large macropores, resulting from the condensation of the silica precursor at the interface of the sol and the oil droplets used as macroscopic templates, present macropores ranging from a dozen to a hundred of microns (Figure III. 1). Macroscale connecting windows, induced by the shrinkage of the monoliths, are located in the thin films that separate two adjacent droplets (Figure III. 1 b-d), and they range from a few hundred nanometers to several microns.

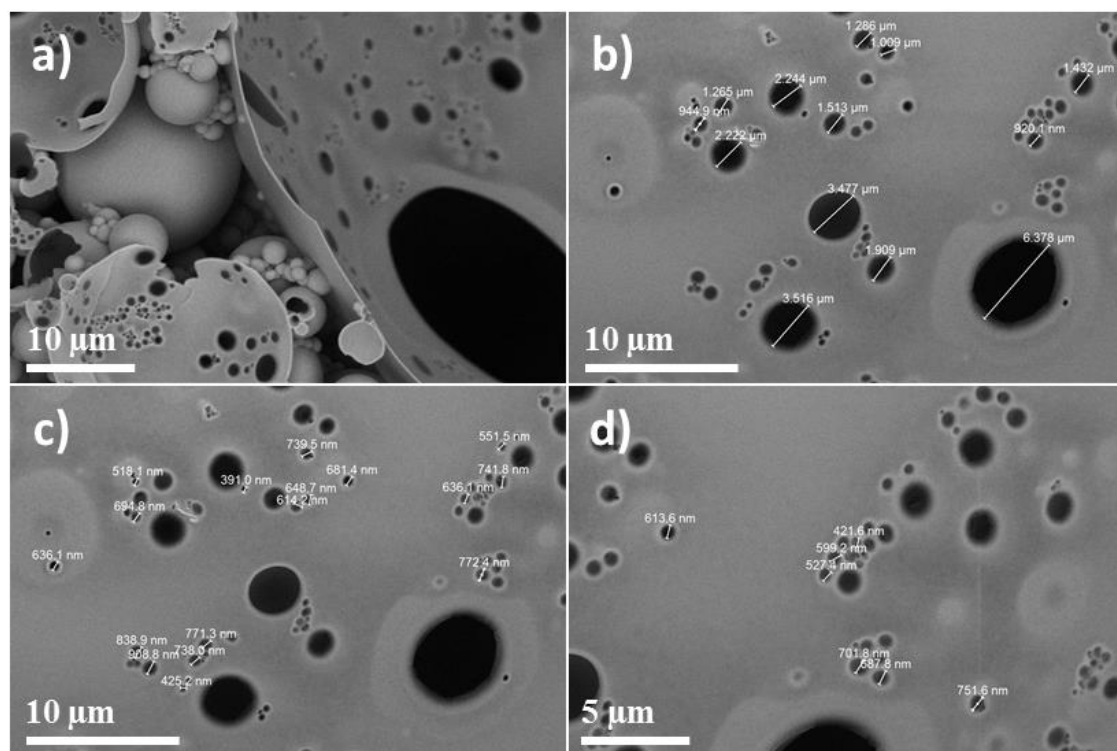


Figure III. 1: SEM images of macroscopic cell windows of a typical Si(HIPE) at magnifications 2.5k a), 3.5k b) and c), and 5k d), with window size measurements

Based on mercury intrusion porosity measurements, the macroscopic cell window distribution was obtained. This technique only measures pore diameters that minimize mercury infiltration. Thus, the pore size distributions correspond to the interconnections between pores, not to the droplet mode silica spheres. These interconnections are called cell windows. Figure III. 2 shows a polydisperse and bimodal distribution. The polydisperse character is related to the window size distribution which spreads from 10 nm up to 5 μm . The bimodal character is explained by the material structure in aggregated hollow spheres which results in both internal and external junctions/windows. The peak centered on 3.1 μm corresponds to the interstices formed at the junction of three (or more) hollow silica spheres; these are the so-called "external" windows (Figure III. 3). The shoulder at this peak corresponds to the "internal" windows formed by the junction between two walls of adjacent hollow spheres.

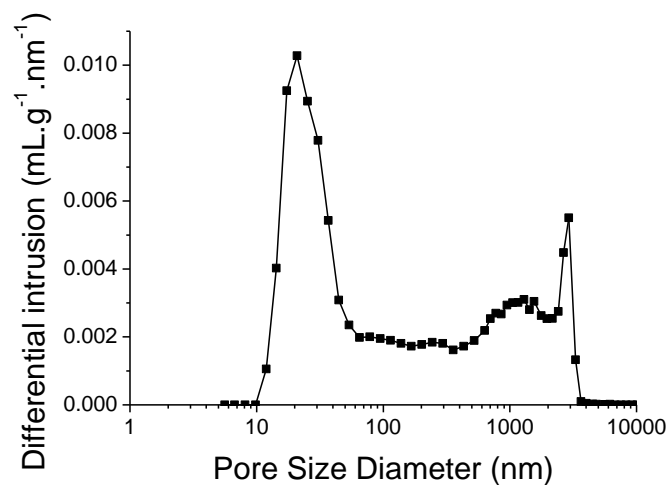


Figure III. 2: Pore size distribution for a typical Si(HIPE) as measured by mercury intrusion porosimetry

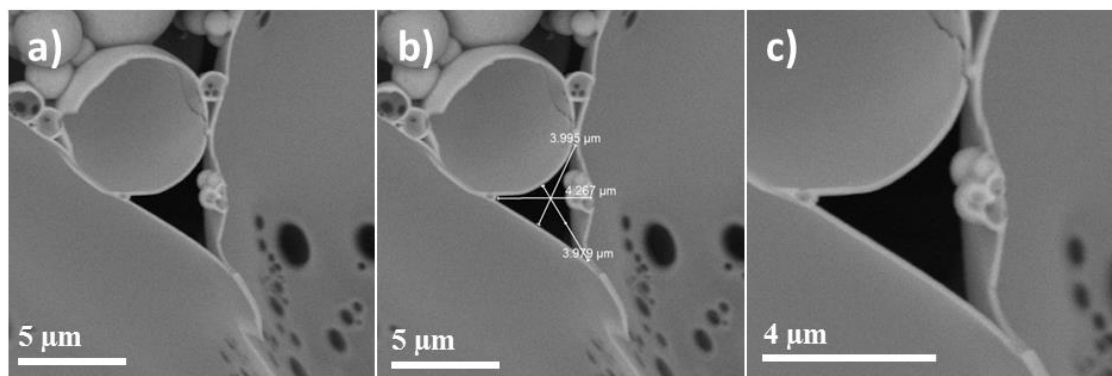


Figure III. 3: SEM images of external cell window of a typical Si(HIPE) at magnification 5k **a**) with window size measurements **b**), and a zoom at magnification 10k **c**)

The peak centered at 20 nm can be assimilated to an internal window population for very small hollow silica spheres. Unfortunately, this pore size is not visible to SEM.

According to these measurements (summarized in Table III. 2), this silica monolith provides a porosity of 92%, corresponding to an apparent density of 0.06 g.mL⁻¹ and a skeletal density of 0.8 g.mL⁻¹. Note that the skeletal density resulting from mercury porosimetry does not take into account microporosity, unlike that obtained by helium pycnometry.

b. Meso- and microscopic length scale

To characterize Si(HIPE)s at meso- and microscale, nitrogen adsorption, TEM and XRD analyses were carried out. It is necessary to recall that the cationic surfactant, used for the genesis of hybrid monoliths, stabilizes not only the oil/water interface of the concentrated direct emulsion, but also induces a supramolecular assembly of micelles. Therefore, after intensive heat treatment or washing, these macrocellular materials reveal a mesostructured more or less ordered at the mesoscopic length scale. Wall cells observed by TEM show vermicular type morphology (Figure III. 4 a))

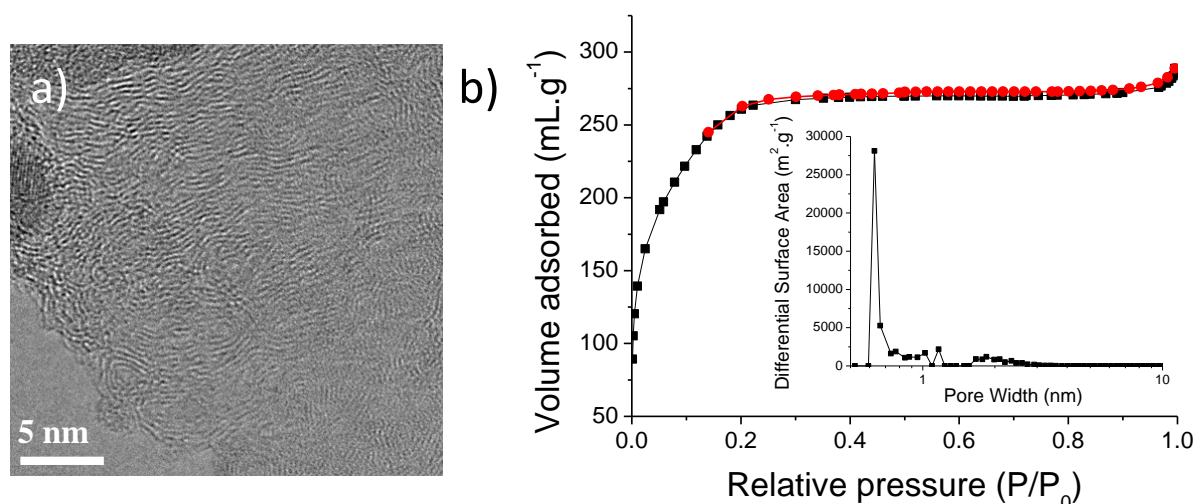


Figure III. 4: **a)** HR-TEM image of the worm-like structure of a silica zone of a TiO₂@Si(HIPE) sample, and **b)** Nitrogen adsorption and desorption isotherms of a typical Si(HIPE). (●) desorption curve, (■) adsorption curve. Insert: corresponding pore size distribution by Horvath-Kawazoe and DFT calculations.

As described in the Chapter II, nitrogen isotherms provide a type I – IV with a narrow H4 hysteresis (Figure III. 4 b)), testifying to a highly microscopic and weakly mesoscopic porosity. Microporosity, intrinsic to the amorphous structure of silica, represents 90% of the porous volume probed by nitrogen (according to the volume values: $V_{\text{porous}} = 0.447 \text{ mL.g}^{-1}$ and $V_{\mu} = 0.402 \text{ mL.g}^{-1}$). Moreover, the specific surface area of this silica monolith sampled is determined using the BET method and is 938 m².g⁻¹. From a general point of view, the specific surface area of a silica monolith can be retained as being of the order of 1000 m².g⁻¹ (brought essentially by the microporosity).

Contrary to a typically microporous material, the adsorption branch shows a curve over a large relative pressure range ($0.01 < P/P_0 < 0.2$), before the linear domain (corresponding to the adsorption of

nitrogen in the multilayer form). This rounding can be explained by a micropores polydisperse character, with most of the size less than 1 nm (as represented in the insert of Figure III. 4 b)). The pore size distribution was calculated by Horvath-Kawazoe model and density functional theory (DFT) model. The Horvath-Kawazoe method is a semi-empirical analytic model of adsorption in micropores that is commonly used for determining the pore size distributions of microporous materials^{1,2}. However, to confirm this hypothesis, a description of micropores by new characterizations such as argon adsorption must be considered.

Due to the very low proportion of mesopores compared to micropores, the hysteresis is very narrow and the description of mesopore sizes by the BJH method is very approximate. On the Figure III. 5, the left graph seems to exhibit a population of mesopores around 3-4 nm. This population is the result of the surfactant (TTAB) mesostructuring nature as described by F. Carn in his PhD work³. The graph on the right confirms the presence of mesopore around 20 nm and the low volume it represents.

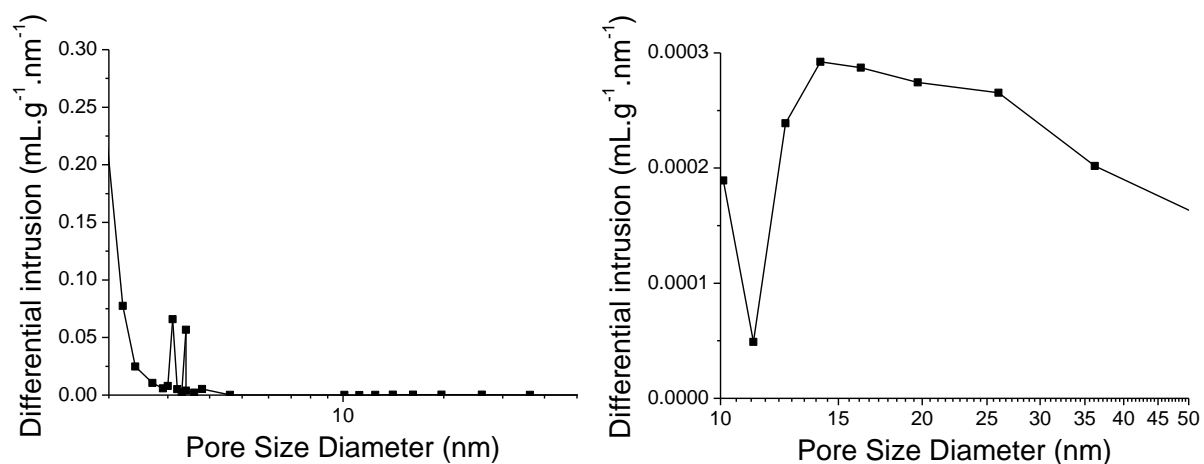


Figure III. 5: Pore size distribution from 2 to 50 nm (**left**) and a zoom on the 10-50 nm region (**right**), from BJH method

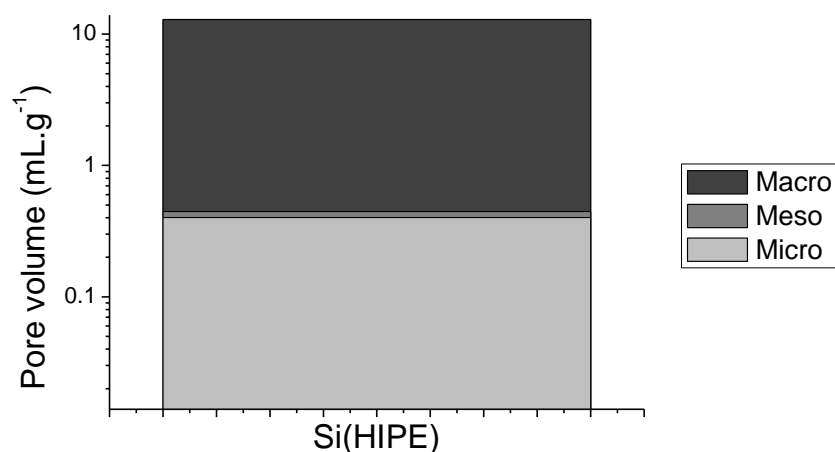


Figure III. 6: Representation of the volumes taken by the macro-, meso- and microporosity within a silica monolith

The Figure III. 6 shows the volume distribution within a silica monolith and points out the low part of mesopores compared to macro- and micropores. For this representation, it was chosen to take the values of the microporous volume resulting from the t-plot and that of the mesoporous volume resulting from the BJH method, i.e. according to the nitrogen isotherms. For macroporous volume, mercury porosimetry is the most suitable technique. The macroporous volume is therefore extracted from this measurement.

c. Reproducibility and repeatability

In order to increase knowledge on the silica matrix synthesis process, some materials were compared with regard to the reproducibility and repeatability of this method. Their concepts can be defined as follows ⁴:

- Reproducibility: close agreement between individual results obtained with the same method on an identical material under different conditions (e.g. with different operators or different laboratories)
- Repeatability: close agreement between successive results obtained with the same method on an identical material under the same conditions (e.g. same operator, same measuring instrument, same laboratory, short time repetitions)

Generally, statistics are based on a large data set (minimum 10 samples) evaluation to increase representativeness. The low mass of a solid limits its sampling. Only three or four values could be obtained per quantity. It is therefore important to note that only orders of ideas are expressed here. Indeed, the accuracy of the measurements applied to Si(HIPE)s could not be statistically evaluated. However, the accuracy of the measurements inherent to the measuring instruments is known and specified in the summary tables.

As a reminder, a batch is associated with a sol, and this sol is divided into several materials (from 2 to 5). Repeatability can therefore be assessed in two ways: inter and intra-batch. The first way accounts for the reproducibility of the sol itself, while the second rather reflects the homogeneity of the sol and the condensation conditions.

From a repeatability point of view, a first inter-batch comparison was carried out on three batches (Batches 1, 2 and 3) synthesized under the same conditions, over a short period (1 day). The pore size distribution shows for all three batches the same bimodal character corresponding to the peak centered above 1 μm with the shoulder towards smaller sizes, and another peak centered around 20 nm (Figure A 3 in annex). Then, nitrogen isotherms show the same type I-IV branches and type H4 hysteresis (Figure A 4 in annex). Regarding the observable values (Table A 6 and Table A 7 in annex), the majority provide mean deviation of less than 10%, except for the BJH surface (22%). This seems to indicate either a fluctuating mesoporosity depending on the batches, or a difficulty in characterizing it.

Experimentally, this can be explained by a variation in shear from one sol to another. From a characterization point of view, as described in paragraph §11)b, the strong microporosity can disturb the mesoporosity probing. And finally, this can also be due to the low mesoporosity value.

In a second step, three solids from the same batch (Batch 4) were compared. Visually, curves appear to overlap for the three solids (Figure A 6 and Figure A 7 in annex). Regarding the observable values (Table A 8 and Table A 9, in annex), the majority provide mean deviation of less than 10%, except for three of them. BJH surface, median pore aperture and skeletal density provide mean deviation of more than 10%. This could be explained by a sol inhomogeneity. A sol is poured into different containers, and then the monolith from each container can be different from the others. This may be an indicator of an inhomogeneous oil incorporation.

The observed trends seem to show that a risk of sol inhomogeneity exists. This indicates that by characterizing a single solid in a batch (minimal destruction of materials), it is possible to obtain a morphological order of idea (mean deviation < 20%) of solids from this batch. However, to ensure the morphology of a given material, the complete characterization of said material is necessary.

From a reproducibility point of view, by comparing for example Batch 1 (operator 1) and Batch 4 (operator 2), an operator effect can be observed. Indeed, for example, the median pore aperture varies by around 3 μm between these two batches. This can be explained by a different agitation speed between batches. Indeed, it has been seen that the higher the shear rate the smaller the oil drops, and therefore the interconnection windows⁵. In this case, a larger pore population may therefore result from a lower shear rate. The synthesis being manual, it seems obvious that an operator effect is visible. Furthermore, other causes can affect the material morphology. For example, more or less extraction of the fume hood can evaporate more or less dodecane, or the raw material used and so on. For all these reasons, the impact of TiO₂ impregnation on the material morphology is discussed by comparing the TiO₂@Si(HIPE) with its starting Si(HIPE) as much as possible.

2) TiO₂@Si(HIPE)

As explained above, TiO₂ impregnation impact is extracted from the TiO₂@Si(HIPE) and starting Si(HIPE) (before impregnation) comparison. Note that following descriptions are based on the characterizations of TiO₂@Si(HIPE)s synthesized by the two-step impregnation method.

a. Macroscopic length scale

The SEM images Figure III. 7 a, b and c, (top, bottom and edge of the monolith respectively), show surface heterogeneity. Indeed, when TEOS condenses into silica, the sol is in contact with the air at the top surface (Figure III. 7 a). Thus, the air bubbles incorporated during the emulsion of the dodecane rise to this surface, creating this heterogeneity of structure. At the edges, initially the sol is in contact with the walls of the Petri dish. Since materials shrink, the gel moves away from the walls and

contact is made with air. The cracks in Figure III. 7 c may be due to TiO₂ precursor condensation which applies stresses to the surface, or simply to a brittleness resulting from the contraction of the material. Conversely, the bottom surface is in contact throughout the synthesis with the bottom of the Petri dish (Figure III. 7 c). Silica hollow spheres (red arrow) form leaving gaps between them open to impregnation and condensation of TiO₂ (white arrow). Figure III. 7 d is a snapshot of the inside of the material, which shows the desired hierarchical porosity.

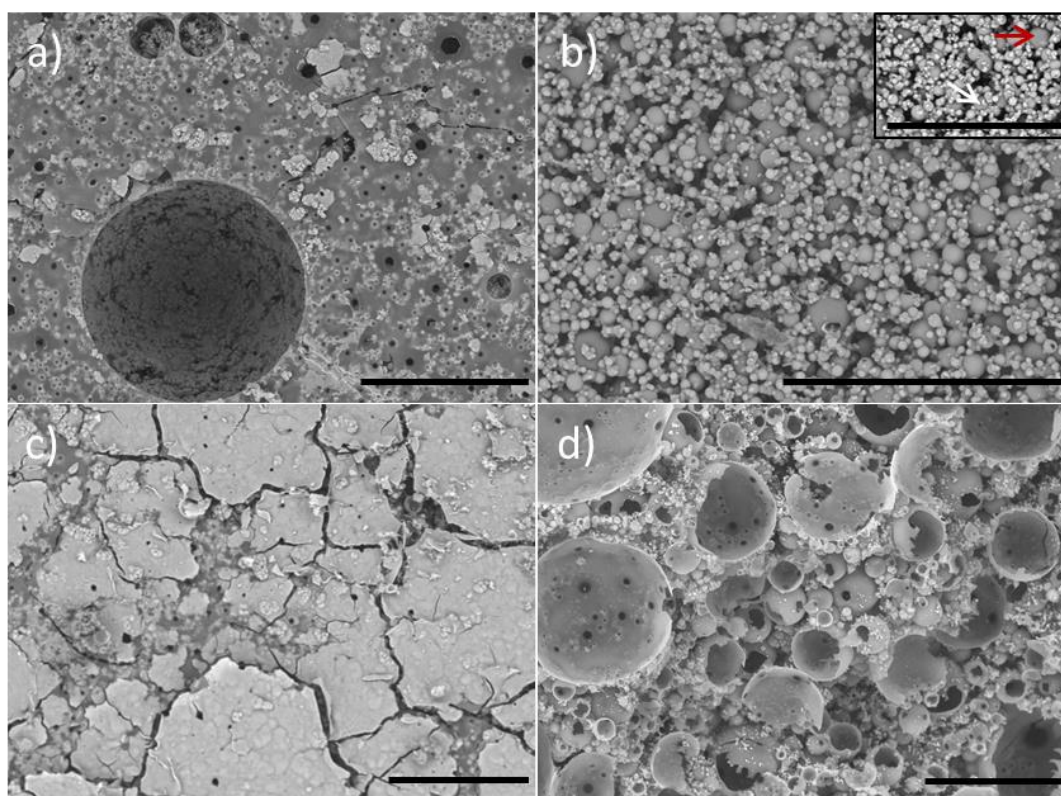


*Figure III. 7: Scanning Electron Microscopy Images of top surface **a**), bottom surface **b**) (red arrow = silica shell, white arrow = TiO₂ particle), edge **c**) and inside **d**) of a typical monolith TiO₂@Si(HIPE). Scale bars : 100 μ m*

To ensure a homogeneous distribution of TiO₂ in the entire volume of the silica matrix, EPMA (Electron Probe Micro Analysis) measurements were carried out on one TiO₂@Si(HIPE) slice, in two directions (5 profiles per direction): according to thickness and length (Figure III. 8). The average profiles show homogeneity of TiO₂ distribution throughout the material. This is confirmed by the distribution coefficients, summarized in Table III. 1. The closer this coefficient is to 1, the more homogeneous the distribution. Only the edge, and the top and bottom faces appear to show a slight deviation from the surface mean. The reason of this deviation was previously explained (analysis of the SEM images).

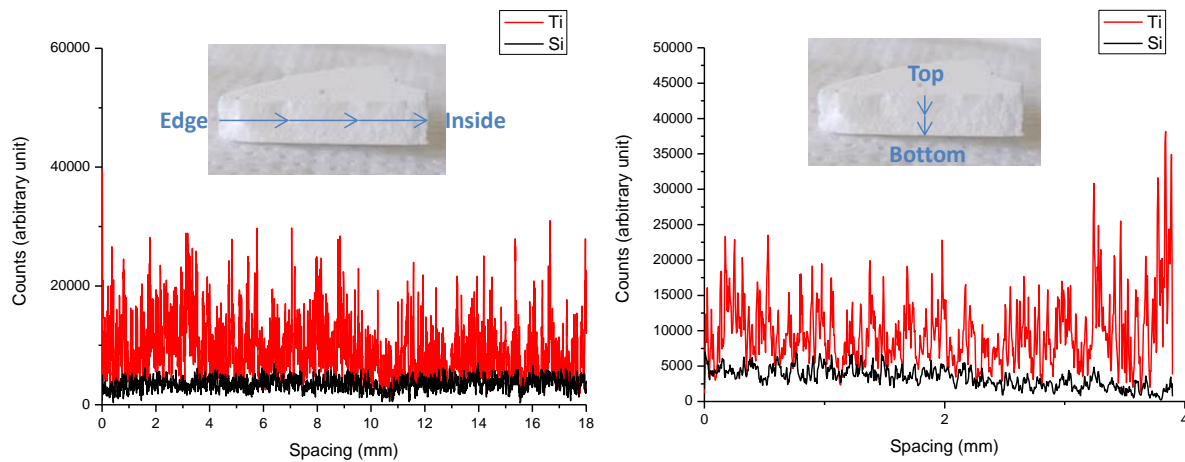


Figure III. 8: Average profiles of Ti and Si distributions measured by EPMA over the length (*left*) and thickness (*right*) of a TiO₂@Si(HIPE)-type monolith

Table III. 1: Ti and Si distribution coefficients values for both profiles

Element	Length profile	Thickness profile
Si	1.00	1.06
Ti	0.99	0.89

The pore size distributions obtained by mercury intrusion porosimetry before and after impregnation are shown in Figure III. 9 b. The volume of mercury intrusion decreases over all the pore size range. This decrease is consistent with a blocking effect of the porosity by TiO₂ particles. Mesopores and/or micropores may be the preferred nucleation sites for TiO₂. Once blocked, mercury access to macropores is reduced. Besides, TiO₂ particles also aggregate at the center of hollow silica spheres reducing their available volume (Figure III. 9 a). These pore size distributions are represented here for impregnation with TiO₂ precursor solution, in two times. However, similar conclusions are drawn for the other impregnation modes. Their difference lies in the structure developed by the TiO₂ particles and their distribution. This point is detailed in §2.1).

Despite the decrease in introduced mercury volume, a high porous percentage is retained after impregnation (Table III. 2). The increase in bulk density shows an effective addition of TiO₂ to the silica matrix. Based on these values, the TiO₂ incorporated can be estimated at around 45% wt. In addition, skeletal density seems increasing with introduction of dense elements ($d_{\text{TiO}_2} = 4.23 \text{ g.mL}^{-1}$). Moreover, TiO₂ impregnation does apparently not modify the median pore aperture (volume). A slight shift towards larger pore sizes is understandable by the loss of a certain volume of macro- and mesopores. However, no destruction of the silica structure is to be noted.

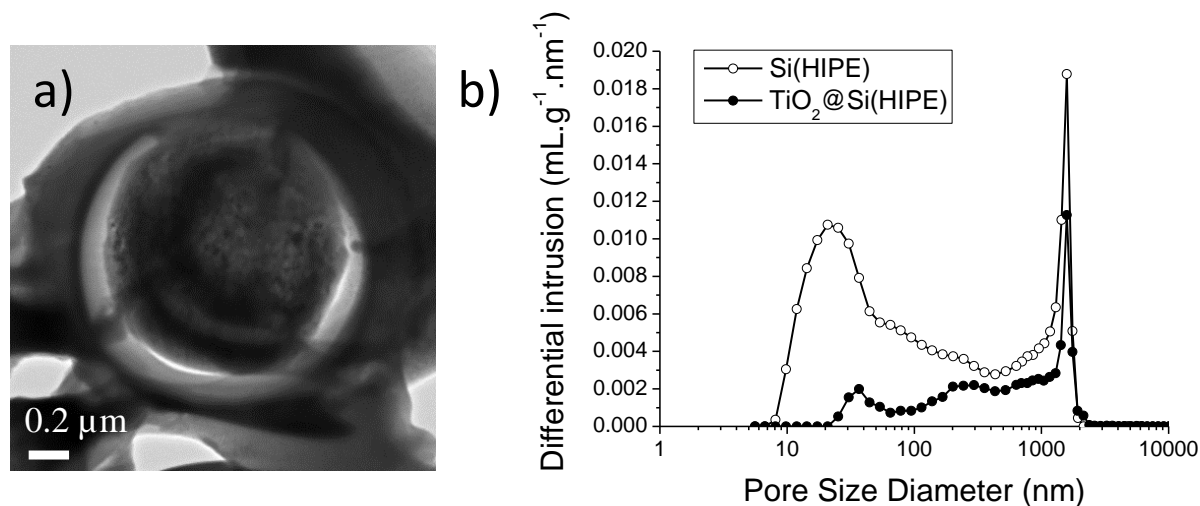


Figure III. 9: **a)** HR-TEM image of aggregated TiO₂ particles into a sphere with a diameter of approximately 1.18 μm in the core of a hollow silica sphere; **b)** Pore size distributions as measured by mercury intrusion porosimetry for monoliths before (○) and after impregnation (●) by a TiO₂ precursor solution in two steps.

Table III. 2: Summary of characteristic values obtained by mercury porosimetry before (Si(HIPE)) and after (TiO₂@Si(HIPE)) impregnation

Materials	Si(HIPE)	TiO ₂ @Si(HIPE)
Intrusion volume (mL.g ⁻¹)	14.49	8.34
Porosity (%)	92	91
Bulk density (g.mL ⁻¹)	0.06	0.11
Skeletal density (g.mL ⁻¹) – Hg	0.78	0.94
Median pore aperture (nm)	1453	1535

b. Meso- and microscopic length scale

Measurements by nitrogen isotherms confirm the part loss of mesopores, and also show a decrease in microporous volume (Figure III. 10). The part loss microporosity can be explained by the insertion of TiO₂ precursor molecules in the heart of the silica network. During impregnation, these infiltrate into the silica walls and can remain blocked when the monoliths dry. Moreover, the density increases with the TiO₂ incorporation. Thus, the specific surface area (standardized per gram of material) is inevitably reduced. The TiO₂ incorporation implies a halving of the BET surface: $S_{\text{BET}} \text{ Si(HIPE)} = 1023 \text{ m}^2.\text{g}^{-1}$, and $S_{\text{BET}} \text{ TiO}_2@\text{Si(HIPE)} = 539 \text{ m}^2.\text{g}^{-1}$.

The STEM analysis coupled with an EDS mapping of a TiO₂@Si(HIPE) monolith impregnated in two steps allows to account for the dispersion of TiO₂ (Figure III. 11). On the one hand, there are aggregates of TiO₂ particles, more or less geometric in shape, displaying high green intensity on the

mapping. Some particles aggregate in the form of a grain bed of about 25 nm thick. This bed seems to line the pore walls (Figure III. 11 c). On the other hand, the mostly orange part thus seems to constitute a piece of silica wall. This one presents, in a diffuse but certain way, green points. There are therefore ultra-dispersed Ti atoms within the silica walls. This is characteristic of a homogeneous nucleation followed by heterogeneous growth of TiO₂ particles (more details on TiO₂ structure in §2.1).

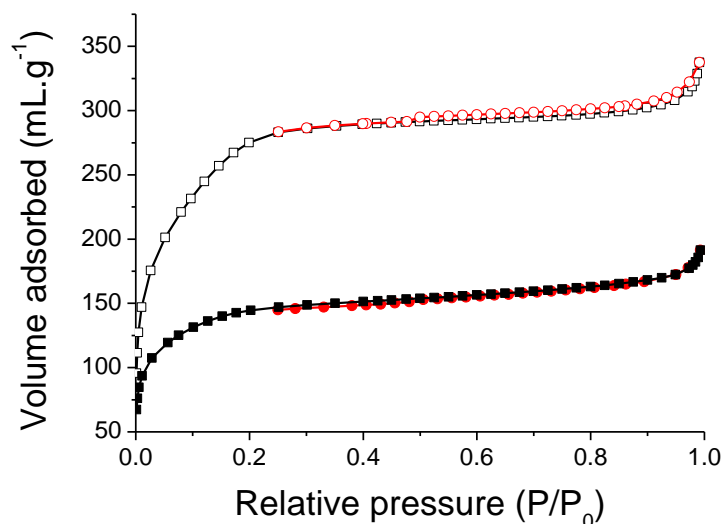


Figure III. 10: Nitrogen adsorption and desorption isotherms of a typical Si(HIPE) before (\square) adsorption curve, (\circ), desorption curve, and after impregnation in two steps (\blacksquare) adsorption curve, (\bullet) desorption curve.

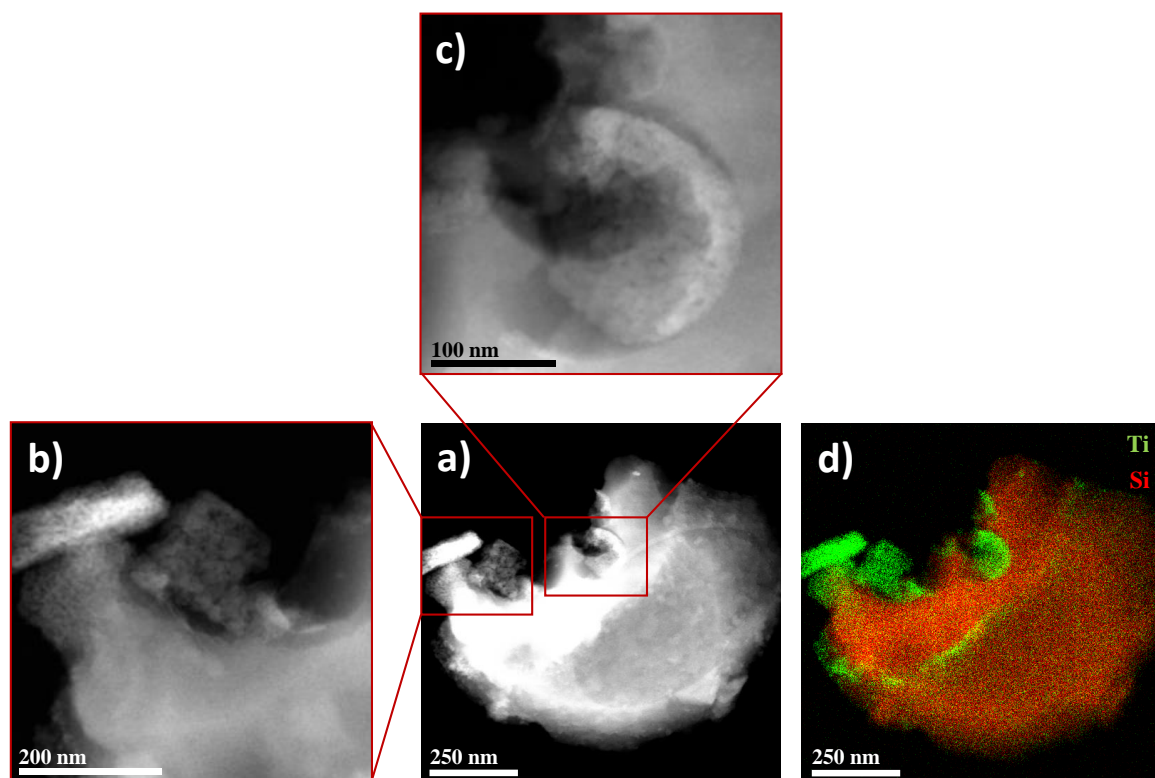


Figure III. 11: STEM images of a piece TiO₂@Si(HIPE) at magnification 120k a), an area zoom at 250k b), another at 500k c), and a mapping d) of the a) image.

As described in Chapter II, the TiO₂ content is determined by XRF analysis and corrected by a factor 0.9. This factor is extracted from the ICP/XRF correlation. Due to the impregnation method influence, this point is discussed in §2.1).

c. Reproducibility and repeatability

On the same principle as in §1.1)c, repeatability has been roughly assessed in two ways: inter and intra-batch. No material set meets the reproducibility study conditions, so it will not be addressed for TiO₂@Si(HIPE). For same reasons than previously, only orders of ideas are expressed here.

From a repeatability point of view, a first inter-batch comparison was carried out on three batches (Batches 5, 6 and 7) synthesized under the same conditions, over a short period (1 day). Note that these batches are the result of the impregnation in two steps of Batches 1, 2 and 3, Si(HIPE)s. The pore size distribution shows for all three batches the same polydisperse and bimodal character (Figure A 7), representative of the porous structure provided by the Si(HIPE) support. Then, nitrogen isotherms also show the same type I-IV branches and type H4 hysteresis (Figure A 8). Regarding the observable values (Table A 10 and Table A 11, in annex), skeletal density (18%) and BJH surface (29%) still provide high mean deviation. The BJH surface mean deviation could be explained with the large slice of microporosity, as previously. Even if the microporous volume probed by nitrogen (e.g. $V_{\mu} = 0.211 \text{ mL.g}^{-1}$, Batch 5) is less than for Si(HIPE)s, this one still constitutes an important part (70%) compared to the mesoporosity in TiO₂@Si(HIPE)s. Skeletal density measured by mercury intrusion porosimetry does not account for microporosity which can create discrepancies between batches. Furthermore, mercury intrusion porosimetry and nitrogen isotherms sampling represents only 5% of the material. This point makes sense regarding the intrusion volume (12%) and bulk density (11%) mean deviation values. Despite these values, the pore size distributions (Figure A 7, in annex) clearly show the strong similarity of the morphology.

In a second step, three solids from the same batch (Batch 8) were compared. Visually, pore size distribution curves appear to overlap for the three solids (Figure A 9, in annex). The adsorption branches of the Figure A 10 in annex show a similarity between the three solids for relative pressures below c.a. 0.4. This translates into reliable BET surface and microporous volume mean deviation values, 3.2% and 3.8% respectively (Table A 12, in annex). Hysteresis however shows significant differences. Desorption branch of solid 3 reveals a measuring instrument deviation. This is reflected by a very large error on BJH surface of 76% (Table A 13, in annex).

TiO₂ content provides reliable inter- and intra-batch mean deviation values, 4.72% and 2.17% respectively. However, the difference between the means of these two sets (32% wt vs. 41% wt of TiO₂, respectively) is of 10 percent points. Thus, from a reproducibility point of view, TiO₂ content is not reliable. Due to the several differences between these sets (Si(HIPE) morphology, raw materials, synthesis period), no origin of this discrepancy can be determined.

Based on these considerations, it was decided to dedicate one monolith per batch to the characterization. This one being then considered as representative of the batch made possible to obtain the morphological characteristics of the monoliths resulting from the same batch. This strategy has optimized analysis time and minimized material loss during characterization. Indeed, one material provides enough material to perform mercury intrusion porosimetry, nitrogen isotherms, XRF, XRD and SEM images in parallel. Each of these analyses being destructive of the monolithic structure, the sacrifice of one material allowed to keep the others of the same batch for photocatalytic tests.

3) Conclusion

Si(HIPE)s and TiO₂@Si(HIPE)s provide a greater proportion of micro- and macropores than mesopores. The TiO₂ impregnation implies micropore lock induced by TiO₂ nucleation on mesopores and/or micropores, and a halving of the BET surface. The pore size distribution is defined by the sol formulation and coherent for monoliths resulting from the same batch. TiO₂ content repeatability is reliable enough to assign the value obtained for a monolith to the whole batch.

Mercury intrusion porosimetry and nitrogen isotherms sampling represents only 5% of the material. Then, the BJH surface and the skeletal density seem to promote a greater error (> 10%) than on the other quantities evaluated. These values will therefore not be considered later in discussions.

As far as possible, sols were made under the same condition procedures and Si(HIPE) batches were characterized before impregnation. One monolith (Si(HIPE) and/or TiO₂@Si(HIPE)) per batch was dedicated to undergoing the characterizations representative of each batch. Moreover, each batch is considered as single due to no reproducibility study performed on TiO₂@Si(HIPE).

2 Influence of specific parameters

The influence of the synthetic parameters on TiO₂ morphology and structure will be detailed in the first part of this paragraph. Then, the influence of synthetic parameters on the matrix morphology will be discussed.

1) TiO₂ structure and particle morphology

To identify the influence of the impregnation method on the TiO₂ embedded structure and content, four different solutions (detailed in Chapter II) were used. Materials are labelled as follow: TiO₂(P25)@Si(HIPE), TiO₂(IIa)@Si(HIPE), TiO₂(Ia)@Si(HIPE) and TiO₂(I)@Si(HIPE), where P25 corresponds to P25 slurry impregnation, IIa to two impregnation steps with alcohol in solution, Ia to one impregnation step with alcohol in solution, and I to one step impregnation without alcohol in solution. As reminder, the alcohol added to the solution is isopropanol, ⁱPrOH. The physicochemical characteristics of these materials are summarized in Table A 14 and Table A 15, in annex.

It is recalled here that the heat treatment applied to the materials is identical (and detailed in Chapter II), except that the calcination temperature is limited to 300°C for TiO₂(P25)@Si(HIPE) to avoid the modification of the original crystal structure of P25 nanoparticles.

a. Impregnation methods over particle morphology

The first method involves the suspension of already crystallized TiO₂ P25 particles. The other three involve the impregnation of a titania alkoxide precursor, Ti(OPrⁱ)₄. These are characterized by external parameters, which are their Ti(OPrⁱ)₄ concentration, the presence and concentration of alcohol (iPrOH) and their pH. The first and last parameters are translated by the ratios [H₂O]/[Ti] and [H⁺]/[Ti] (values in Table II. 1, Chapter II). According to the literature, these three parameters can influence the TiO₂ particles morphology. The ratio $h = [\text{H}_2\text{O}]/[\text{Ti}]$ is the hydrolysis ratio ⁶. Depending on its value, hydrolysis-condensation process differs ($h < 1$, $1 < h < z$, and $z < h$, where z is the oxidation state of the metal and equal to 4 here). The three solutions provide a ratio h above z , meaning that a large excess of water is added to the alkoxide. In this domain, cross-linked polymers, particulate gels or precipitates can be obtained, by fast condensation rate. Moreover, all three solutions provide an acidic pH, or an acid catalysis. Then, hydrolysis rates are greatly improved ⁶. Furthermore, the presence of alcohol in the solution implies alcohol interchange. Hydrolysis and condensation rates depend on the nature of the alkyl group. Sanchez *et al.* ⁷ depicted a useful guide providing the relative hydrolysis and condensation rates and different products which can be obtained. They especially found that Ti(OPrⁱ)₄/iPrOH solution provide fast hydrolysis and condensation rates, leading to colloidal gel or gelatinous precipitate. About the TiO₂ particles morphology and more particularly the particle diameter, Vorkapic *et al.* ⁸ showed in particular the effect of pH and alcohol. It appears that smallest particles are formed at $[\text{H}^+]/[\text{Ti}] \approx 0.5$. Below, particles size provides a strong dependence of pH, whereas above (present condition), a weak pH influence is observed. Besides, a time-stability is shown over 24 hours, but instability for 5-days ageing. In present case, impregnation stage occurred over around a 24-hours duration. Moreover, they found that particles are larger in the presence of alcohol and that the size increases as the amounts of alcohol increase. Furthermore, they compared the particle diameter evolution over time with and without alcohol. They found that alcohol presence slows down the peptization reaction. In our study, the method labelled *Ia* provide 6M, the *Ia* method 5M, and 0M of (added) alcohol for the *I* last method. Thus, at iso-ratio h , TiO₂@Si(HIPE) samples should provide larger particle diameter in the order: $I < Ia < IIa$.

To qualitatively account for the distribution of TiO₂ particles in materials, SEM and TEM images are discussed below. It is recalled here that the microscopy images are unfortunately not representative of the entire material. The most relevant ones were chosen to bear witness to the predominantly observed distribution for each impregnation method.

P25 slurry impregnation (P25)

In the case of impregnation with a suspension of P25 TiO₂ particles, the Figure III. 12 shows the particle distribution at different magnification. According to the image a), particles seem to be heterogeneously dropped off on walls of large silica hollow spheres. Images b), c) and f) show that particles aggregate and collapse pore apertures from 4 to around 15 μm. However, all these pore apertures are not collapsed. This could depend on the size of silica hollow sphere behind the aperture. Particles can also line the walls forming a film, as displayed by images d) and e).

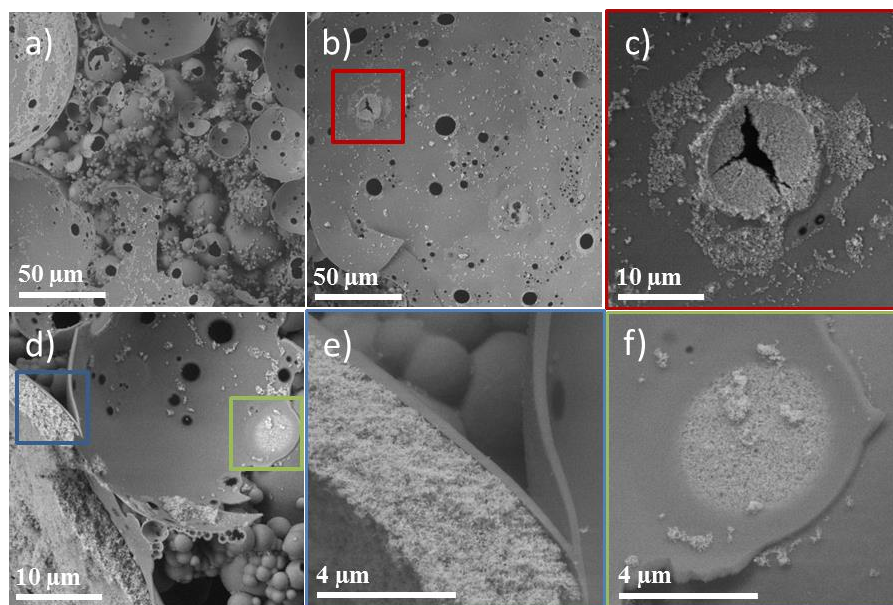


Figure III. 12: SEM images of a typical TiO₂(P25)@Si(HIPE) **a)** and **b)** at magnification 500, **c)** and **d)** at 2.5k, where **c)** is a zoom on red square of **b)**, **e)** and **f)** at 10k, which are zooms on blue and green squares of **d)**, respectively

TiO₂ precursor solution: impregnation in two steps, with alcohol (IIa)

According to the Figure III. 13, the distribution of TiO₂ particles seems largely different in the case of *IIa* impregnation method than previously. Images a) and b) show only few aggregates of TiO₂ particles on walls of large silica hollow spheres. Higher voltage is applied on image c) to penetrate deeper, visualized behind silica walls and improve the contrast. Then, TiO₂ seems to fill small silica hollow spheres ($\varnothing < 10 \mu\text{m}$). According to images e) and f), the filling can be in film or porous ball form. Thanks to the PIPS type preparation (described in Chapter II), TEM images, preserving the HIPE structure, were recorded and are displayed in Figure III. 14. The image a) shows a silica hollow sphere filled with TiO₂. A zoom (Figure III. 14 b)) at the contact area between TiO₂ and silica was done. This area provides three distinct domains, for which SAED patterns are displayed in Figure III. 14 d), e) and f). The domain I seems to be simply the amorphous silica wall of the hollow sphere. The domain II provides polynanocrystalline zones with a few crystals, whereas domain III counts a huge number of crystals, with the appearance of a reticular plane. TEM-EDS mapping Figure III. 14 c) shows that Ti is

also present in domain I. All these considerations point towards pseudo-epitaxial TiO₂ growth. In other words, the first layer of TiO₂ present in the vicinity of the silica walls remains amorphous even after the thermal treatment, while the TiO₂ domains crystallinity is increasing when going farther from the silica-titania interface. This implies that Si-O-Ti bonds exist and are not easily cleaved to afford discretized SiO₂ and TiO₂ phases during thermal treatment (contrary to Sosnov *et al.*⁹), and then amorphous silica network can hinder the TiO₂ crystallization upon thermal treatment.

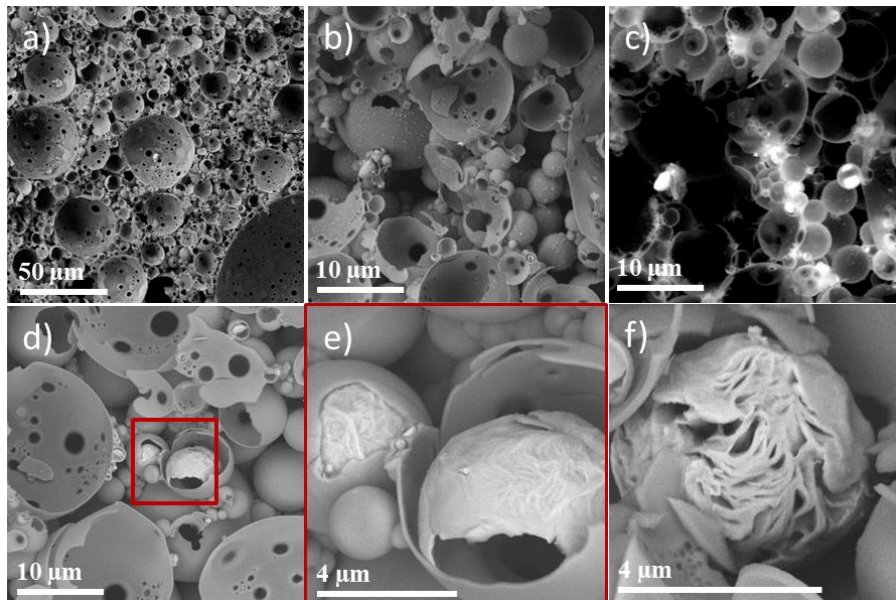


Figure III. 13: SEM images of a typical TiO₂(IIa)@Si(HIPE) **a**) at magnification 500, **b**), **c**) and **d**) at 2.5k, where **c**) is a 15kV image of **b**), **e**) and **f**) at 10k, where **e**) is a zoom on red square of **d**)

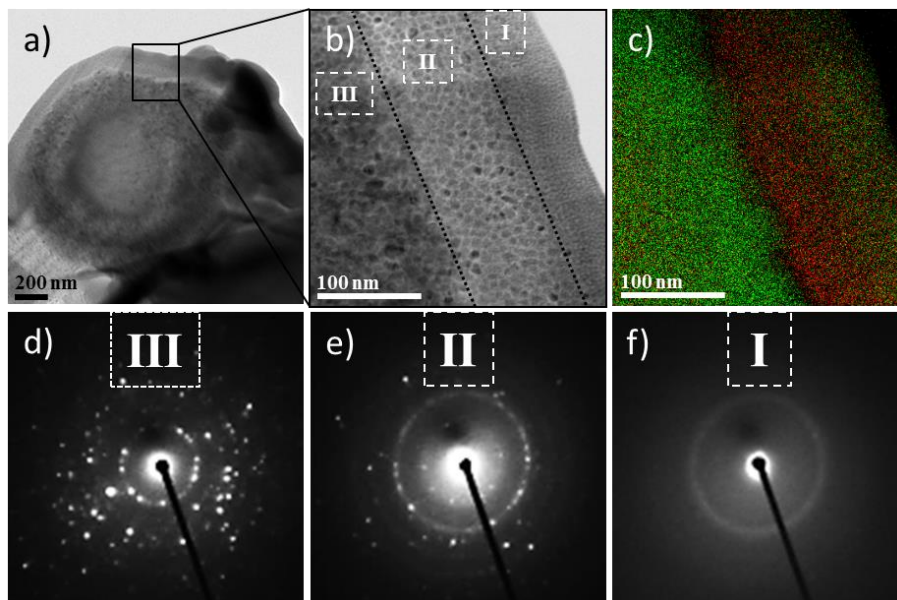


Figure III. 14: TEM images in bright field of a typical TiO₂(IIa)@Si(HIPE) **a**) and **b**) where **b**) is a zoom on black rectangle of **a**), providing three domains, **c**) an EDS mapping of **b**) with Ti and Si elements in green and red respectively, **d**), **e**) and **f**) SAED patterns of the III, II and I domains of **b**) respectively

TiO₂ precursor solution: impregnation in one step, with alcohol (Ia)

According to Figure III. 15 a), only few particles seem to be aggregated as previously. However, at higher magnification (images b) and c)), large spherical aggregates are clearly visible but smaller ones are also present and diffusely dispersed. More visible on image d), these small spots of TiO₂ are also present on the external surface of silica hollow spheres. This observation supports the hypothesis of a mixture of large unpeptized TiO₂ particles and smaller TiO₂ clusters in the impregnation solution.

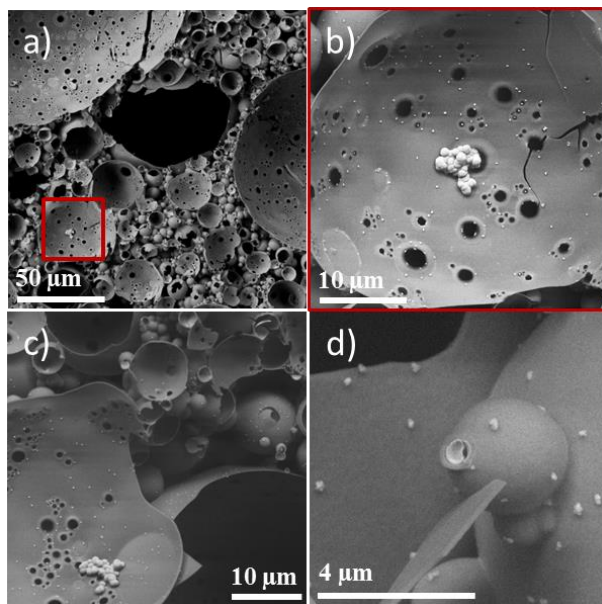


Figure III. 15: SEM images of a typical TiO₂(Ia)@Si(HIPE) **a)** at magnification 500, **b)** and **c)** at 2.5k, where **b)** is a zoom on red square of **a)**, **d)** at 10k

TiO₂ precursor solution: impregnation in one step, without alcohol (I)

With this last impregnation method, resulting materials provide the most diverse TiO₂ particles distribution. On Figure III. 16 a), some patch-like aggregates are visible, dropped off on walls of large silica hollow sphere. They are dispersed similarly to the previous one. However, the image b) shows a new type of TiO₂ deposition. Actually, on the external surface, a large part of external silica hollow spheres joints is covered by a TiO₂ particle aggregate film. On image c), some small silica hollow spheres seem also filled with TiO₂, as described for the *Ia* method; and patch-like aggregates, zoomed and displayed in image d).

These three types of TiO₂ deposition (in film form inside and outside silica hollow spheres and patch-like on walls of large silica hollow sphere) were observed by TEM (Figure III. 17). On the first row, 1 μm-large silica hollow spheres with TiO₂ film covering the joints are visible on the left, at higher magnification on the middle, and an EDS mapping is showed on the right. The second row provides the same type of images focused on the 20-nm thick film of TiO₂ particles lining the silica wall. The last one deals with patch-like aggregates. Surprisingly, this aggregate is not composed of spherical TiO₂ particles, but an assembly of them. This assembly looks like a rice grain and seems to provide porosity. Another important point is the Ti element content in silica walls, which appears lower than in the sample

for *Ia* method. To check this, different areas were analyzed in EDS on both sample (TiO₂(*I*)@Si(HIPE) and TiO₂(*IIa*)@Si(HIPE)). The method is described in Chapter II, and results are displayed in this Chapter, §2.1)c, in Table III. 3.

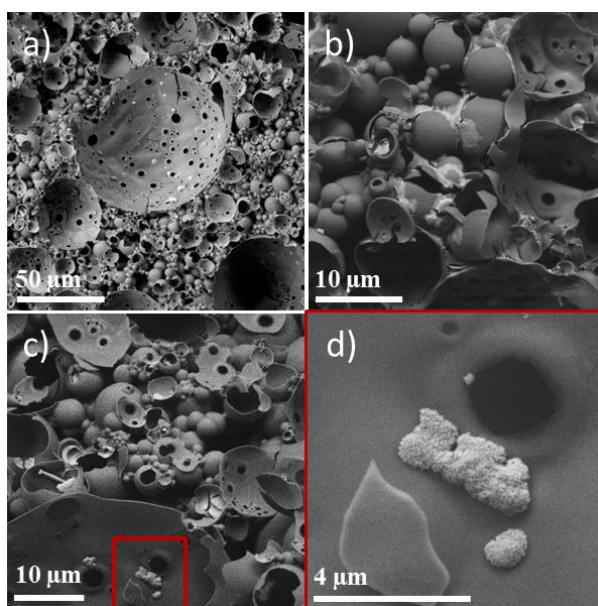


Figure III. 16: SEM images of a typical TiO₂(*I*)@Si(HIPE) **a**) at magnification 500, **b**) and **c**) at 2.5k, **d**) at 10k which is a zoom on red square of **c**)

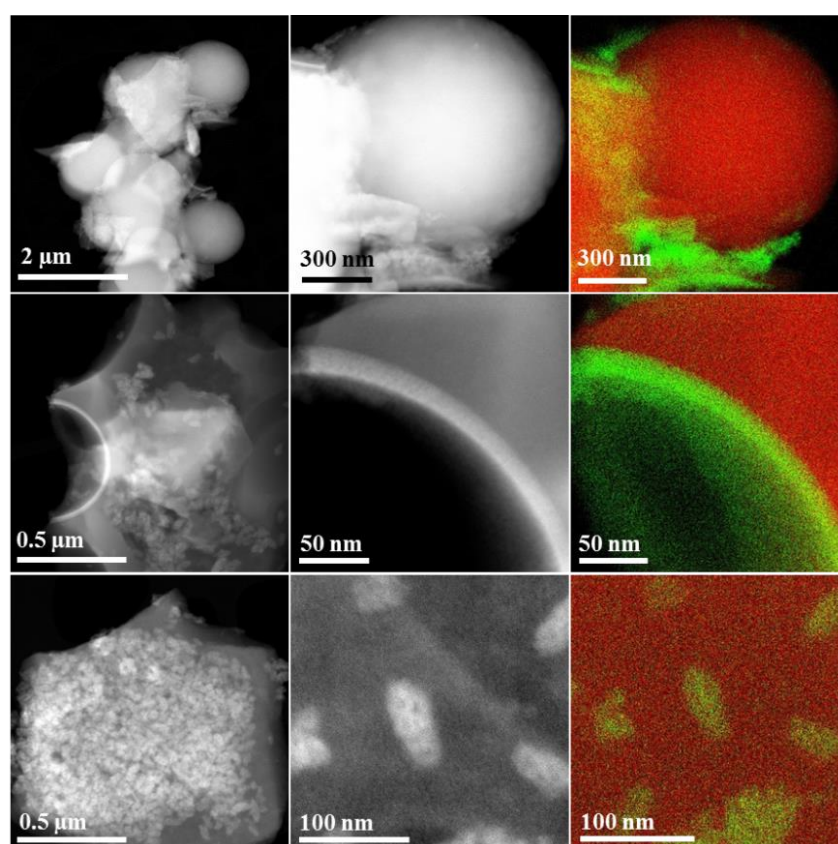


Figure III. 17: TEM images in dark field of a typical TiO₂(*I*)@Si(HIPE) (**left**), with zooms (**middle**) and EDS mappings (**right**) of Ti and Si elements in green and red, respectively

b. Calcination treatment over TiO₂ structure

As described above, the parameters of titania alkoxide precursor solutions influence the TiO₂ particle morphologies, but also the anatase-to-rutile phase transformation temperature¹⁰. Anatase-to-rutile transition mechanisms are closely dependent on particle size and number in a certain volume. Zhang and Banfield¹¹ consider three mechanisms: i) Interface Nucleation (IN), ii) Surface Nucleation (SN), and iii) Bulk Nucleation (BN). Then, they proposed three models, the predominance of each of which is dependent on the temperature (Figure III. 18). In the present study, calcination temperatures are considered as low, so interface nucleation mechanism seems to be predominant. This implies that materials, providing the largest number of small particles, i.e. with nanoparticles of large specific surface area, will promote anatase-to-rutile transition.

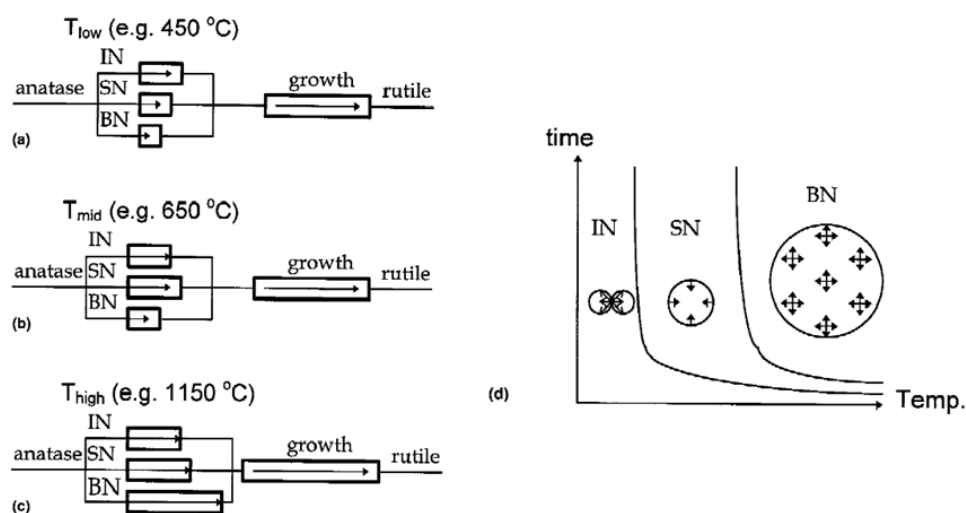


Figure III. 18: **a)** At lower temperatures, interface nucleation predominates the transformation; **b)** at intermediate temperatures, surface nucleation predominates; and **c)** at very high temperatures, bulk nucleation predominates. Diagram **d)** shows the time and temperature dependence of the three dominant regions¹¹

To estimate the allotropic phases in presence and crystallite size as a function of the thermal treatment, two abacuses were made: *in-situ* and *ex-situ*. During her thesis project, Céline Perego¹² observed a deviation between *in-situ* and *ex-situ* calcination, due to the intrinsic calcination conditions of the devices (real temperature profile, air flow, etc...). The first abacus was carried out *in-situ* for nominal TiO₂ loading rates from 15 to 60 % wt, by the *Ia* impregnation method. Thus, the influence of TiO₂ loading rate and calcination temperature on the crystalline phases obtained could be determined. The second one was performed *ex-situ* on *Ila* impregnated materials. Thus, the influence of temperature and calcination time was evaluated.

In-situ (Ia impregnation method)

The measurements were made on a Panalytical X'pert MPD diffractometer with Bragg-Brentano geometry θ - θ , equipped with a rear graphite monochromator Anton-Paar HTK16, with a temperature rise of $2^\circ \cdot \text{min}^{-1}$ carried out *in-situ* over a total duration of 2 hours 46 for each sample. Measurements are made every 100°C , with a waiting time of 30 minutes before each measure to ensure temperature stabilization. The radiation used is Cu K α , with an average wavelength of 1.5418 Å, and generated with a working voltage of 40 kV and a working current of 50 mA.

Regarding the Figure III. 19, three regimes can be distinguished as a function of the calcination temperature: i) $T < 500^\circ\text{C}$, ii) $600^\circ\text{C} < T < 800^\circ\text{C}$ and iii) $900^\circ\text{C} < T$. The regime i) provides only anatase crystalline phase for TiO₂ loading rate ranging from 15 to 40 %wt, and a mix of anatase and rutile for 50 and 60 %wt. These observations are in agreement with the Zhang and Banfield model ¹¹ which considers that in this temperature range, rutile nucleation is dependent on the number of anatase/anatase contact zones in a certain volume. At higher temperatures (regime ii), the movements of titanium and oxygen atoms become sufficiently important that the nucleation of the rutile on the surface free of any contact of anatase (surface nucleation) becomes possible ¹¹. Then, rutile appears for lower TiO₂ content. Finally, core nucleation predominates at the highest temperatures (regime iii)), when the amount of core atoms is much larger than the amount of surface atoms ¹². The predominance of nucleation modes is also time-dependent, which may explain the absence of rutile for 15%wt of TiO₂.

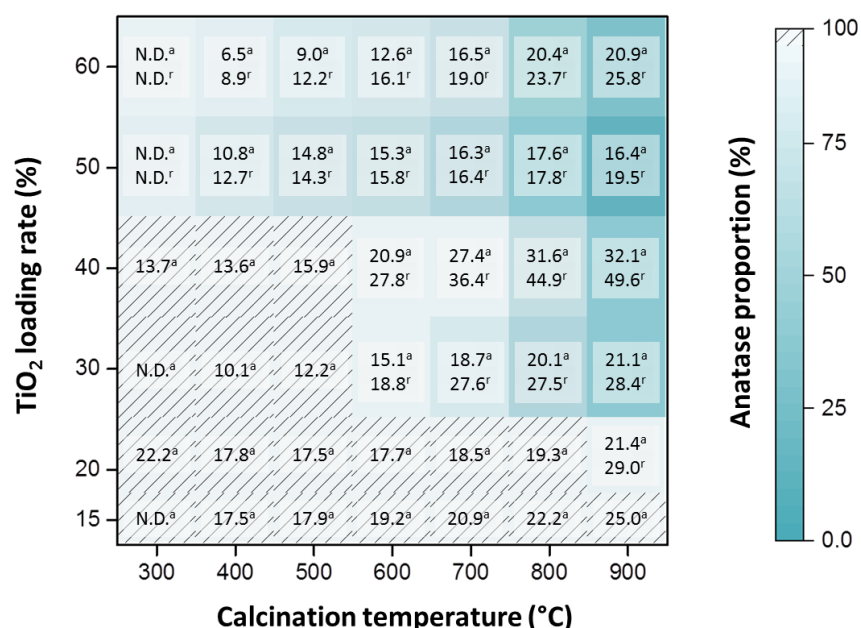


Figure III. 19: Overview of crystal structures and crystal size %anatase (a) / %rutile (r) as a function of TiO₂ loading rate and calcination temperature

Ex-situ (IIa impregnation method)

Calcination treatment was performed with a muffle furnace (Nabertherm, L3). All temperature rises were of 2°.min⁻¹, whereas calcination temperature and plateau duration were modified. Moreover, all materials provide around 30%wt of TiO₂ content (resulting from XRF analysis). The temperature range studied is between 500 and 900°C, and that of time is between 1 and 4 hours.

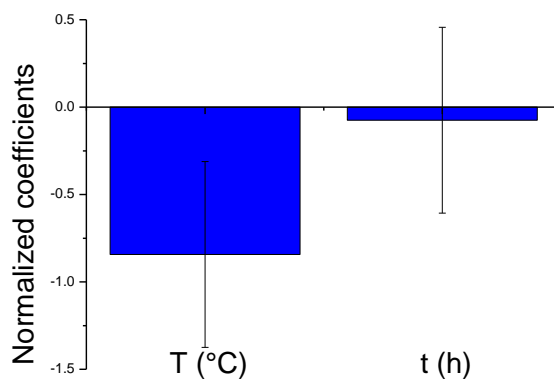


Figure III. 20: Normalized coefficients of both variables with 95% confidence intervals

To assess the influence of these two variables (temperature and calcination time) in the process to obtain a given percentage of anatase, linear regression was applied to the data. The data of trials and parameters of the statistical study are summarized in Table A 16 and Table A 17, in annex. Because of the small amount of material, tendency can be expressed here by a limited number of tests carried out. Models to determine the proportion of anatase (F) as a function of temperature and calcination time were obtained using these analyses. The Figure III. 20 shows the normalized coefficients obtained by linear regression model for the two variables, which reflect the influence of the studied variables on the crystal phase percentage (F). The higher the absolute value of a coefficient, the greater is the influence of the variable on the result (F). When the confidence interval around the normalized coefficients includes the value 0, the influence of a variable in the model is not significant¹³. According to this analysis, it was found that in the range studied of anatase (F), the influence of calcination time is not significant to provide crystal phases, whereas temperature has the main influence.

As examples, the evolution of the crystal structure as a function of the calcination temperature (at iso- plateau duration, 4 hours) is shown in Figure III. 21, and the evolution of the crystal structure as a function of the plateau duration (at iso- calcination temperature, 700 °C) is shown in Figure III. 22.

This figure shows that a TiO₂(IIa)@Si(HIPE) containing 30% wt of TiO₂ and *ex-situ* calcinated at 700 °C provides only anatase phase no matter how long the plateau. According to the *in-situ* results, a TiO₂(Ia)@Si(HIPE) containing 30%wt of TiO₂ should provide an anatase/rutile mixed phase, at 700 °C calcination temperature. This difference in crystalline phase can therefore come either from the calcination mode (*ex-situ* vs. *in-situ*) or from the impregnation method (IIa vs. Ia). However, a TiO₂(Ia)@Si(HIPE) containing 30% wt of TiO₂ and *ex-situ* calcinated at 700 °C provides a 90/10

anatase/rutile mixed phase (XRD pattern in Figure A 11, in annex). The difference origin is then due to impregnation method. It was seen that the *Ila* impregnation method might result in a certain content of TiO₂ locked in amorphous form at the silica walls. This means less “crystallizable” TiO₂. In other words, if 10% of TiO₂ remain locked in the silica walls, only 20% TiO₂ can crystallize. According to Figure III. 19 (*in-situ*), at 20%wt of TiO₂ and 700 °C calcination, TiO₂ then only provides anatase crystalline phase.

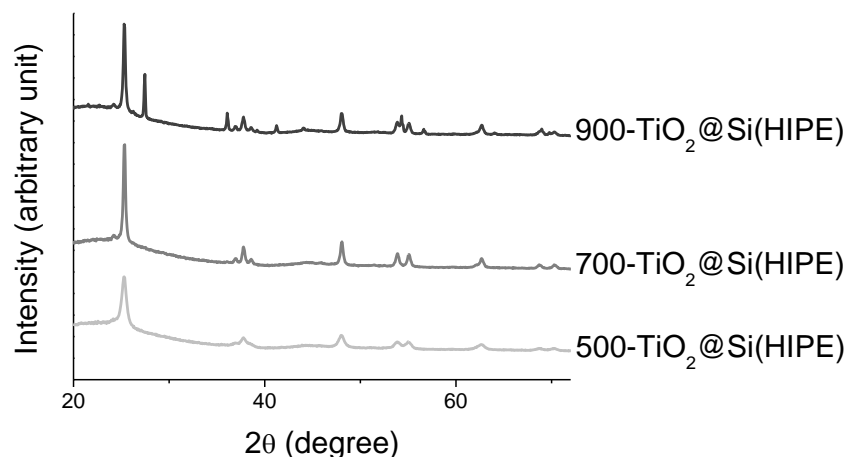


Figure III. 21: XRD patterns of TiO₂(*Ila*)@Si(HIPE)s in function of calcination temperature, for 4-hours dwell time

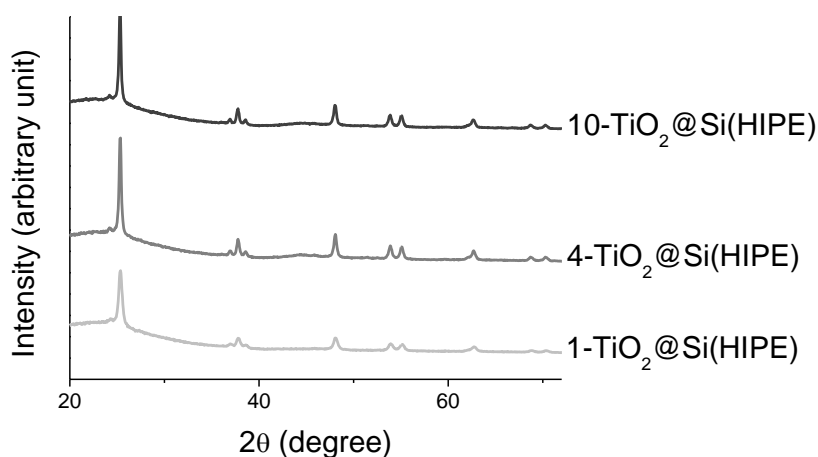


Figure III. 22: XRD patterns of TiO₂(*Ila*)@Si(HIPE)s in function of plateau duration, for 700 °C

c. Impregnation methods over TiO₂ structure

A notable difference in the four impregnation processes is the number of impregnations performed. As a reminder, a TiO₂(P25)@Si(HIPE) sample has undergone three impregnations, a *Ila* sample two impregnations, then *Ia* and *I* samples have undergone only one impregnation. It is clearly visible in Table III. 3 that the more impregnation steps there are, the further the effective TiO₂ content is from the expected one. This can be explained by a decrease in the pore accessibility as impregnations. The direct consequence is a TiO₂ particle dilution in the Si(HIPE) volume, and thus interfaces, which

limits the (IN) anatase-rutile transition mechanism. Then, TiO₂(IIa)@Si(HIPE) samples provide crystallized TiO₂ only as anatase. Although the TiO₂(P25)@Si(HIPE) sample has only a low effective TiO₂ content, it is recalled that in this case the impregnated TiO₂ particles are already crystallized at 80% anatase and 20% rutile.

Table III. 3: Summary of characteristic values regarding TiO₂ content and structure, embedded in Si(HIPE)s by four methods

	TiO ₂ (P25)@Si(HIPE)	TiO ₂ (IIa)@Si(HIPE)	TiO ₂ (Ia)@Si(HIPE)	TiO ₂ (I)@Si(HIPE)
Expected TiO ₂ content (%wt)	38	40	50	50
Effective TiO ₂ content (%wt)	18	24	43	44
Crystallinity (%)	97	33	54	44
Ti/Si-silica walls	-	0.13	-	0.04
Anatase/Rutile ratio	90/10	100/0	90/10	90/10
Anatase crystallite size (nm)	21	21	12	12
Rutile crystallite size (nm)	33	-	13	8

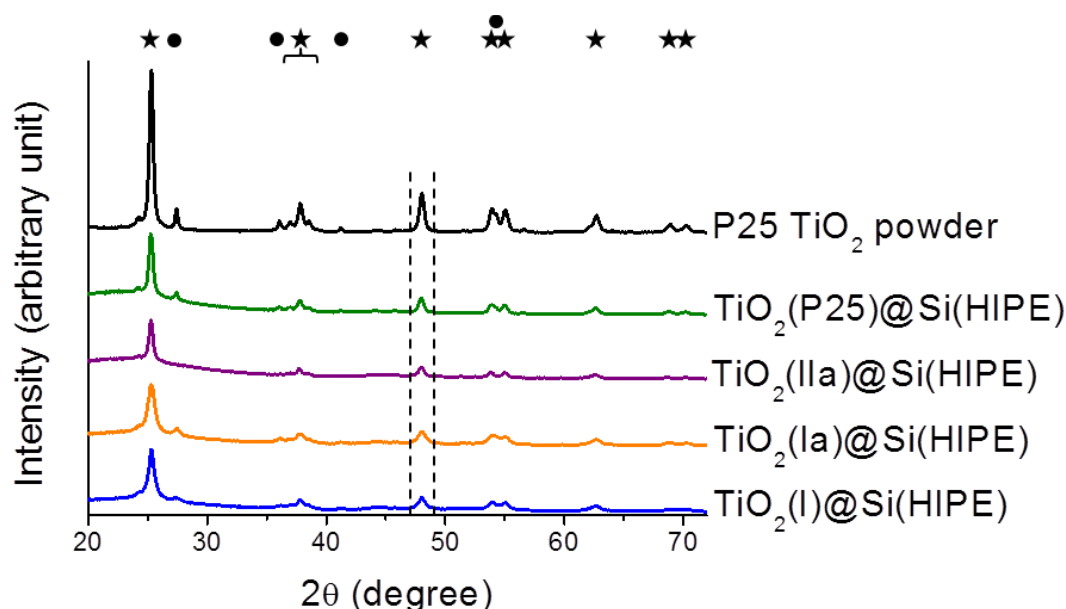


Figure III. 23: XRD patterns of the photocatalytic reference (P25 TiO₂) and the TiO₂@Si(HIPE)s materials from the four impregnation methods, providing anatase (★) and/or rutile (●) phases. The dashed lines delimit the bounds applied in the areas measurement, for the crystallinity rate calculation.

In order to determine the impregnation method influence on the crystallization of TiO₂, crystallinity rates were calculated for the four impregnation methods and the ratio Ti over Si in silica walls for two methods. According to the abacus made and described in Chapter II, the TiO₂(P25)@Si(HIPE) sample is 97% crystallized (Table III. 3). This value makes the method more reliable, since it is very close to reality. The area measured for the crystallinity rate calculation is shown between the two dashed lines in Figure III. 23. The samples from a one-step impregnation show a better

crystallinity rate than those from a two-step impregnation. Furthermore, by comparing the relative Ti contents in the silica walls of the TiO₂(IIa)@Si(HIPE) and TiO₂(I)@Si(HIPE) samples, it appears that the two-step impregnation seems to promote the TiO₂ incorporation into the silica walls. These considerations could be related to Ti-O-Si bonds which block TiO₂ crystallization, and thus active phase formation.

Furthermore, all materials of the next section were impregnated by the two-step method. Note that TiO₂ content varies from 20 to 45% wt. They present TiO₂ only as anatase phase. Then, at iso-TiO₂ content (ca. 45% wt of TiO₂), the impregnation method in one-step provide anatase/rutile mixed phase at calcination temperature of 450°C, contrary to the two-step one. The main reason is most probably the Ti-O-Si bonds promoted by the two-step impregnation method, which limits the number of anatase/anatase contact in a given volume during heat treatment, and then rutile nucleation.

2) Morphological Si(HIPE) modifications

As a reminder, one of the objectives of the project is to evaluate the influence of porosity on photon penetration and therefore on photocatalytic performances. To vary the porosity of Si(HIPE) supports, several synthetic parameters were modified to determine their influence on morphological properties. This parametric study is detailed in this paragraph.

It has been seen that the TiO₂ impregnation reduces the porous volume without changing the macropore size distribution. Thus, pore size distributions obtained by mercury intrusion porosimetry and nitrogen isotherms will be graphically represented only for Si(HIPE)s. However, the characteristic values of morphology will be detailed for all materials in the appendix. Moreover, in this study only two-step impregnations were carried out, then materials should be labelled X-TiO₂(IIa)@Si(HIPE)s, where X is the modified parameter. To simplify their designation, materials will be noted X-TiO₂@Si(HIPE)s. Their XRD patterns are shown in the annex whereas the relevant structural parameters are put in tables in the main text.

a. Oil volume fraction (ϵ)

As already seen in literature⁵, oil volume fraction has an impact on the morphological properties and especially on the pore size distribution. Although the conclusions drawn from this study are similar to those of Florent Carn³, this point is detailed in order to provide precise characteristics of the synthesized materials and comments adapted to the context of the study.

According to the routine protocol of Si(HIPE) synthesis, all parameters were retained except the oil volume. Thus, the influence of the volume fraction in oil could be evaluated. First, the SEM images make it possible to account for the evolution of the materials morphology (Figure III. 24). As the oil volume fraction increases, the large macropores size decreases (first and second rows of Figure III. 24); so are the wall thicknesses (last row of Figure III. 24). Indeed, by means of the measurements made on

the images, wall thicknesses obtained in increasing order of volume fractions are: 200, 140, 148, 90 and 39 nm (no measure for $\varepsilon = 0.73$). The pore size distributions shown in Figure III. 25 have the bimodal character seen above. It is interesting to note that two regimes seem to be emerging. The first for fractions less than or equal to 0.67 involves a progressive decrease in the size of the macropore population. Then, a sudden break (also visible on the images Figure III. 24) of the pore size distribution seems to tend towards a monomodal character. This break is also shown in Table A 18 in the annex, given the characteristic values derived from mercury intrusion porosimetry, except for porosity which fluctuates between 70 and 95 % no matter the oil volume fraction. The sharp decrease in the size of the macropore population has induced an increase in the mesopore population, visible on the isotherms Figure III. 26. The characteristic values derived from nitrogen physisorption are given in Table A 19 in annex. As an indication, mesoporous volume percentages are given so as to better reflect the increase in the mesopore share. Conversely, the BET surface is constant around 1000 m².g⁻¹ no matter the oil volume fraction. In short, the variation in the oil volume fraction has a strong impact on the size distribution of macro- and meso-pores, while porosity and BET surface appear to be unaffected. Thus, it is clearly shown that the increase in the overall viscosity of the emulsion *via* the increase of the oil fraction volume beyond the compact random stacking allows to reduce the diameter of the drops and to tighten their size distribution.

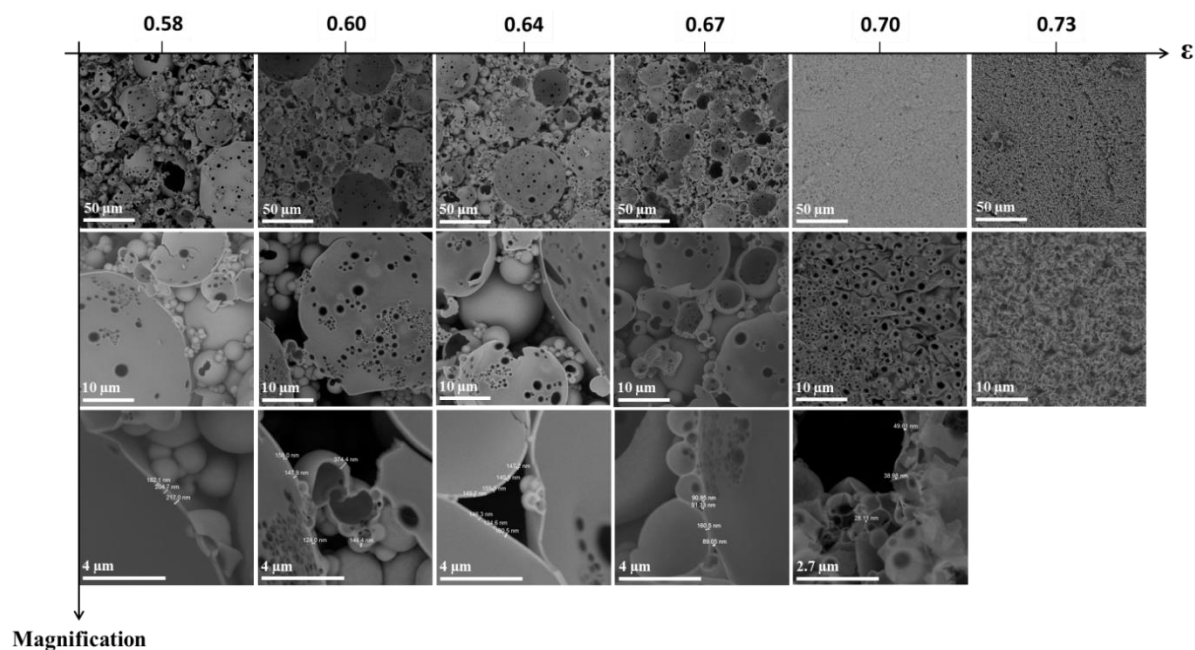


Figure III. 24: SEM images of samples, prepared with oil volume fractions increasing from 0.58 to 0.73. The top line corresponds to the low magnification and the line below to the strong magnification. The thickness of the silica walls is measured on this last line and specified in the text for the sake of clarity.

Note that the materials for the volume fractions 0.70 and 0.73 underwent such a strong shrinkage that they became too small to be positioned in the reactor, and thus tested. They were therefore not impregnated with TiO₂. According to Table A 20 in annex, after impregnation of TiO₂, the 0.58-

TiO₂@Si(HIPE) sample retains a median pore diameter around 2000 nm, while the others have pores of 1700 ± 30 nm in diameter. Table A 21 in the annex of the nitrogen physisorption values shows, not surprisingly, a halving of the BET surface area and an average value of $440 \text{ m}^2 \cdot \text{g}^{-1}$. Despite a similar impregnation method for the ϵ -TiO₂@Si(HIPE)s batches, they provide different TiO₂ content, probably derived from a synthesis period difference (0.60 and 0.67 samples impregnated the same day). Moreover, all these materials present anatase phase of crystallized TiO₂ (XRD patterns in Figure A 12, in annex). However, crystallite sizes range from 13 to 23 nm. For ϵ -TiO₂@Si(HIPE)s, crystallite sizes and TiO₂ content are both fluctuating parameters. A quantity taking both parameters into account should therefore be introduced in order to evaluate their influence in photo-activity: the TiO₂ specific surface area (Chapter IV).

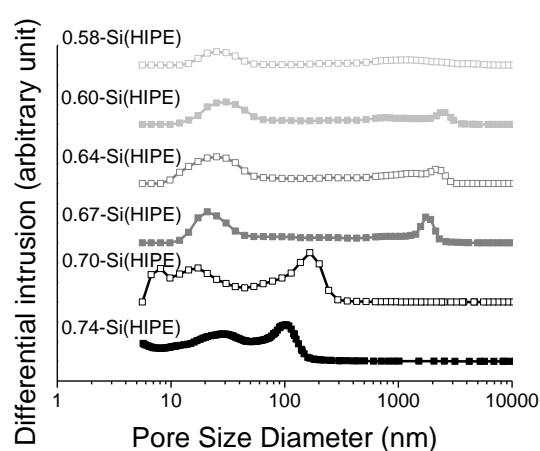


Figure III. 25: Pore size distributions of ϵ -Si(HIPE)s, where ϵ is the oil volume fraction

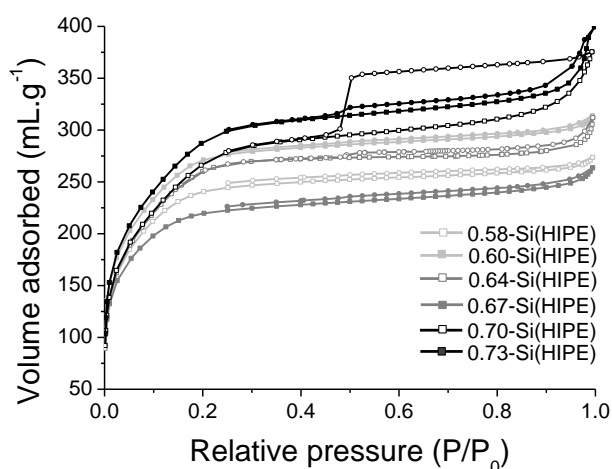


Figure III. 26: Nitrogen adsorption (\square) and desorption (\circ) isotherms of ϵ -Si(HIPE)s, where ϵ is the oil volume fraction

Table III. 4: Summary of TiO₂ characteristic values of ϵ -TiO₂@Si(HIPE)s, where ϵ is the oil volume fraction

	ϵ -TiO ₂ @Si(HIPE)			
	0.58-TiO ₂ @Si(HIPE)	0.60-TiO ₂ @Si(HIPE)	0.64-TiO ₂ @Si(HIPE)	0.67-TiO ₂ @Si(HIPE)
%wt TiO ₂ content (%)	29	43	24	45
Anatase/Rutile ratio	100/0	100/0	100/0	100/0
Anatase crystallite size (nm)	22.8	15.8	20.6	13.1
Rutile crystallite size (nm)	-	-	-	-

b. Oil chain length (C_x)

Another parameter that can influence the Si(HIPE) morphology is the oil chain length. The viscosity of the oil used is then changed. According to Tadros¹⁴, the viscosity of the dispersed phase

plays an important role in the breakup of droplets; the higher the viscosity, the longer it will take to deform a drop.

According to the routine protocol of Si(HIPE) synthesis, all parameters were retained except the oil chain length. Thus, this influence is obtained with use of nonane, dodecane and pentadecane as oil. First, the SEM images make it possible to account for the evolution of the materials morphology (Figure III. 27). The only notable difference in morphology is the appearance of the silica walls for C₉-Si(HIPE) sample. Some kind of islets are formed. This may be due to the more volatile nature of short chain oils. By forming gas bubbles, blocked by the continuous phase, the silica condensation follows the shape of these bubbles. Figure III. 28 shows an increase in macropore population size with chain length. In addition, for C₁₅-Si(HIPE) sample, the loss of mesopores is visible. This is consistent with the increase in viscosity of the dispersed phase and thus the delay in the breakup of droplets. The nitrogen isotherms (Figure III. 29) show that the chain length does not influence the microporosity of the materials. Characteristic values from mercury intrusion porosimetry and nitrogen physisorption are presented in Table A 22 and Table A 23 in annex, respectively.

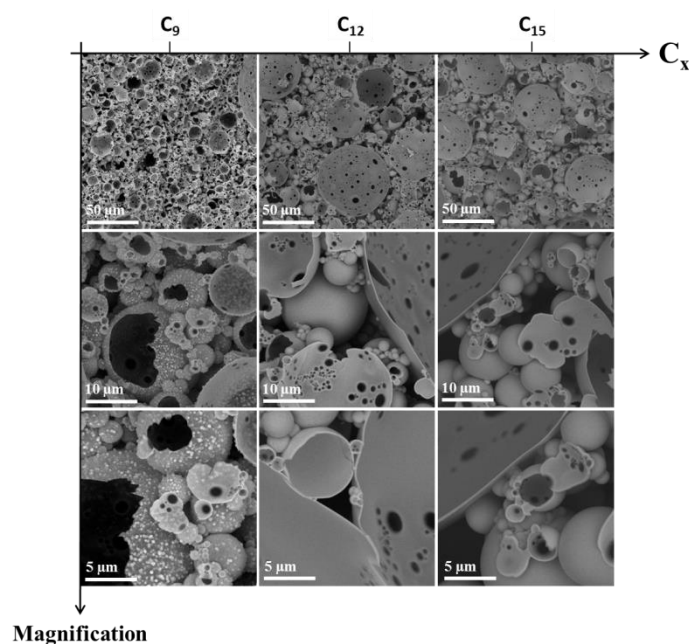


Figure III. 27: SEM images of samples, prepared with an oil having a chain length increasing from 9 to 15. The top line corresponds to the low magnification and the line below to the strong magnification.

After TiO₂ impregnation, the gap between the median pore diameters is reduced, while keeping a difference of 150 nm between each material. However, this difference represents only 10% of the median pore diameter, which is not significant regarding mean standard deviation. The other characteristic values derived from mercury intrusion porosimetry and nitrogen physisorption (Table A 24 and Table A 25 in annex) are almost identical. Moreover, the TiO₂ structural characteristics, presented in Table III. 5, are considered identical for all C_x-TiO₂@Si(HIPE)s: 100% anatase and

crystallite sizes around 21.4 nm (XRD patterns in Figure A 13, in annex). The only significant difference is the TiO₂ content of the C₁₅ sample. Then, this material set is not of interest to be discussed from a photocatalytic point of view.

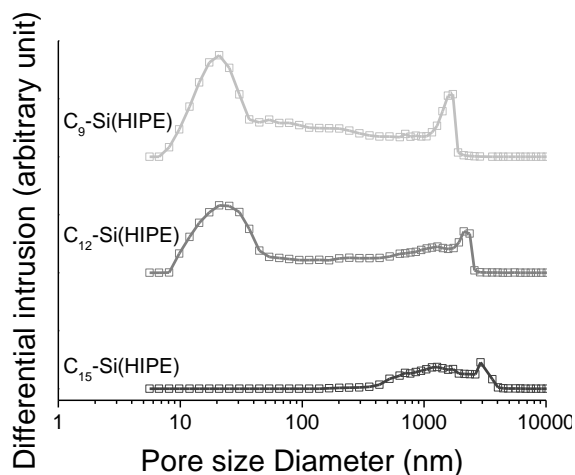


Figure III. 28: Pore size distributions of C_x-Si(HIPE)s, where x is the oil carbon number

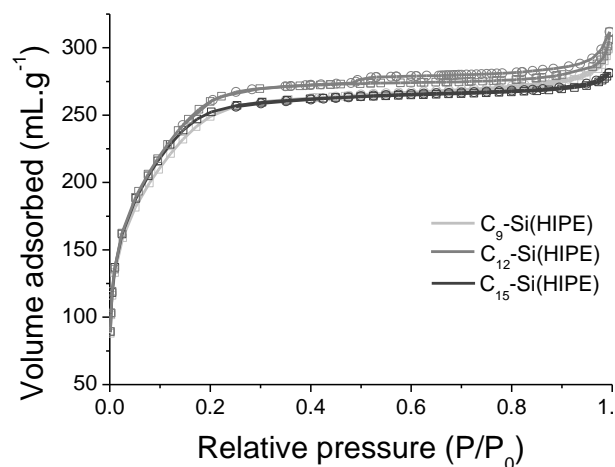


Figure III. 29: Nitrogen adsorption (□) and desorption (○) isotherms of C_x-Si(HIPE)s, where x is the oil carbon number

Table III. 5: Summary of TiO₂ characteristic values of C_x-TiO₂@Si(HIPE)s, where x is the oil chain length

	C _x -TiO ₂ @Si(HIPE)		
	C ₉ -TiO ₂ @Si(HIPE)	C ₁₂ -TiO ₂ @Si(HIPE)	C ₁₅ -TiO ₂ @Si(HIPE)
%wt TiO ₂ content (%)	24	24	19
Anatase/Rutile ratio	100/0	100/0	100/0
Anatase crystallite size (nm)	22.3	20.6	21.3
Rutile crystallite size (nm)	-	-	-

c. Calcination treatment (T)

The silica calcination temperature of the silica is also a parameter influencing the materials porosity. Indeed, according to the Zhuravlev model¹⁵, the presence and quantity of silanols vary according to the applied temperature. The modification of the silica structure can influence the contraction phenomenon and therefore the porosity.

According to the routine protocol of Si(HIPE) synthesis, all parameters were retained except the calcination temperature of the last plateau, varying from 550 to 850 °C. First of all, the SEM images make it possible to account for the evolution of the materials morphology (Figure III. 30). The materials batch calcined at 750°C was inhomogeneous. Only one monolith provided a common shape (top and bottom surfaces almost parallel). This one was kept for impregnation and photocatalytic testing. Therefore, the starting silica matrix morphology could not be analyzed. At 550 and 850 °C, the large

macropores size seems smaller than that of 650-Si(HIPE) (first and second rows of Figure III. 30), so are the wall thicknesses (last row of Figure III. 30). Indeed, by means of the image-based-direct-measurements, wall thicknesses obtained in increasing order of calcination temperature are: 77, 140, 70 nm (no measure for T = 750 °C). These values do not appear to follow any particular trend with the calcination temperature evolution. Note that the 650-Si(HIPE) sample was not synthesized on the same day as the others. The manual shear rate could therefore vary, explaining the similarity between the 550- and 850-Si(HIPE)s samples. The pore size distributions in Figure III. 31 also show a bimodal character with slight difference on the mesopore population. The 550- and 850-Si(HIPE)s samples provide median pore diameters around 1000 nm (Table A 26 in annex), 600 nm less than the 650-Si(HIPE) sample. If the variations at the macro and mesoscopic length scales seem more due to a variation in shear rate, it appears in Figure III. 32 that the calcination temperature very strongly influences the microporosity. Indeed, the 850-Si(HIPE) sample provides 64% microporosity by volume compared to the total volume probed by nitrogen, instead of 86% for the others. This decrease in microporous volume appears consistent with the Zhuravlev model, and the gradual loss of internal silanols in silica with increasing temperature. Characteristic values from mercury intrusion porosimetry and nitrogen physisorption are presented in Table A 26 and Table A 27 in annex, respectively.

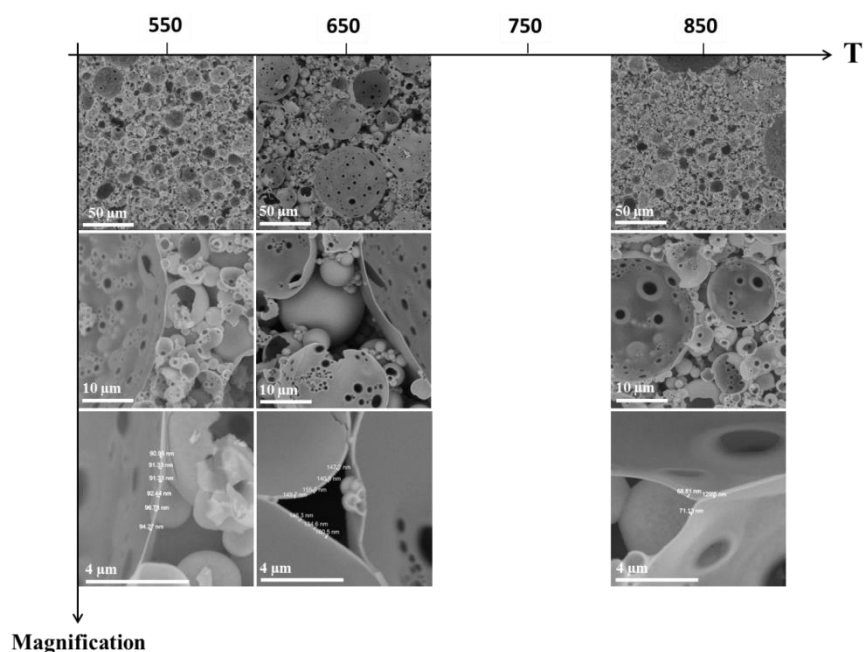


Figure III. 30: SEM images of sample, prepared with calcination temperature increasing from 550 to 850 °C. The top line corresponds to the low magnification and the line below to the strong magnification. The thickness of the silica walls is measured on this last line and specified in the text for the sake of clarity.

After TiO₂ impregnation, 550-Si(HIPE) expressed a low mechanical strength. As such, measurement carried out by mercury intrusion porosimetry was not considering, and photocatalytic testing could not be performed. Considering the characteristic values derived from mercury intrusion

porosimetry (Table A 28 in annex) samples are almost identical, except the median pore diameter of 650-Si(HIPE). The characteristic values derived from nitrogen physisorption (Table A 29 in annex) depict strong influence of calcination temperature over microporosity. Moreover, the TiO₂ structural characteristics, presented in Table III. 6, show that all T-TiO₂@Si(HIPE)s are composed of 100% anatase, crystallite sizes vary from 15.4 to 20.6 nm and TiO₂ contents vary from 24 to 44%. In short, from a morphological point of view, the main fluctuating parameter is BET surface. This one could be studied and compared with the TiO₂ specific surface area.

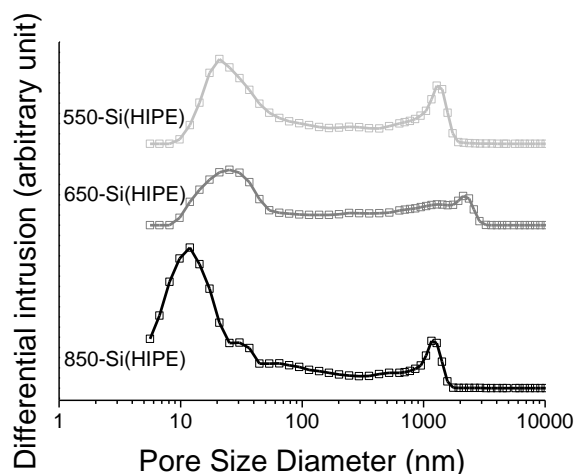


Figure III. 31: Pore size distributions of T-Si(HIPE)s, where T is the calcination temperature in °C

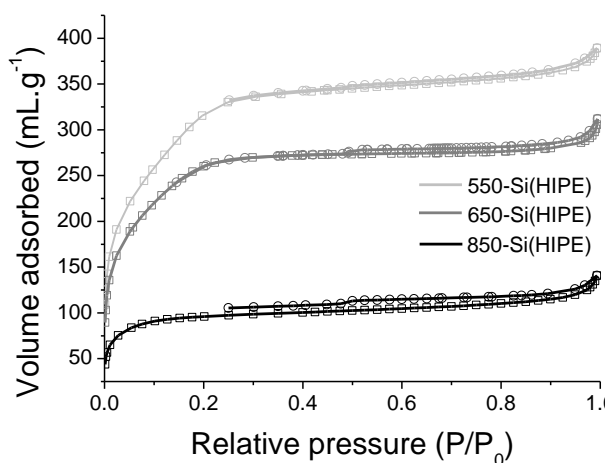


Figure III. 32: Nitrogen adsorption (□) and desorption (○) isotherms of T-Si(HIPE)s, where T is the calcination temperature in °C

Table III. 6: Summary of TiO₂ characteristic values of T-TiO₂@Si(HIPE)s, where T is the calcination temperature in °C

	T-TiO ₂ @Si(HIPE)			
	550-TiO ₂ @Si(HIPE)	650-TiO ₂ @Si(HIPE)	750-TiO ₂ @Si(HIPE)	850-TiO ₂ @Si(HIPE)
%wt TiO ₂ content (%)	44	24	34	36
Anatase/Rutile ratio	100/0	100/0	100/0	100/0
Anatase crystallite size (nm)	17.4	20.6	18.5	15.4
Rutile crystallite size (nm)	-	-	-	-

d. Local shear (v)

To determine the influence of this parameter, an automatic shearing system was operated, with a mechanical stirrer (emulsification) and a syringe pump (incorporation of dodecane). Note that the 200-Si(HIPE) sample has undergone impregnation before being characterized, so only the pore size distribution of this sample will be compared to the other Si(HIPE)s.

According to the routine protocol of Si(HIPE) synthesis, all parameters were retained except the imposed shearing, varying from 150 to 250 rpm. First, the SEM images make it possible to account for

the morphology evolution of materials (Figure III. 33). At low local shear, Si(HIPE) provides less compacted hollow sphere than usually, and a population of kind small silica balls. At high local shear, the structure appears to be the result of a combination of emulsion and foam, with very large macropores (ex-air bubbles). From pore size distribution in Figure III. 34 (characteristic values from mercury intrusion porosimetry are summarized in Table A 30 in annex), macropores decrease in size with increasing induced-shear rate (the decrease is symbolized by the blue arrow Figure III. 34), due to viscosity increase³. It appears once again that when macropores decrease in size the mesopore population increases. Despite the different isothermal nitrogen appearance, the characteristic values obtained and summarized in Table A 31 in annex show only a slight difference in the BET surface and microporous volume.

After TiO₂ impregnation, v-TiO₂@Si(HIPE)s retain a strong morphology difference, especially the median pore diameters. In the order of increasing local shear, the pore diameters of v-TiO₂@Si(HIPE)s are 3038, 881 and 269 nm. However, microporosity is almost the same for these materials. All the characteristic values from mercury intrusion porosimetry and nitrogen physisorption are summarized in Table A 28 and Table A 29 in annex, respectively. Moreover, the TiO₂ structural characteristics, presented in Table III. 7, show that all T-TiO₂@Si(HIPE)s are composed of 100% anatase, crystallite sizes vary from 11.4 to 21.3 nm and TiO₂ contents vary from 20 to 30% (XRD patterns in annex Figure A 15). In short, from a morphological point of view, the main fluctuating parameter is median pore diameter. This one could be studied and compared with the TiO₂ specific surface area.

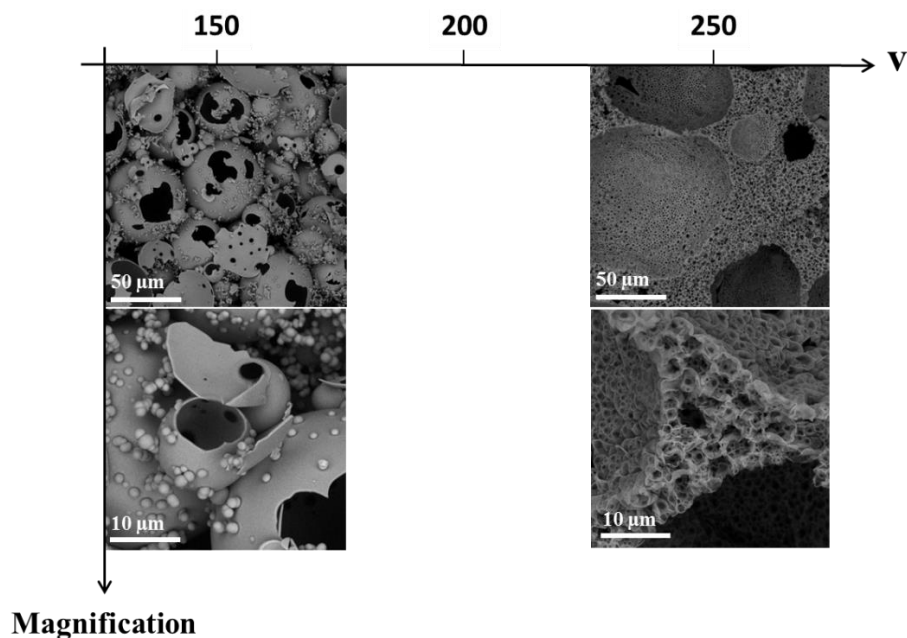


Figure III. 33: SEM images of samples prepared with local shear increasing from 150 to 250 rpm. The top line corresponds to the low magnification and the line below to the strong magnification. The thickness of the silica walls is measured on this last line and specified in the text for the sake of clarity.

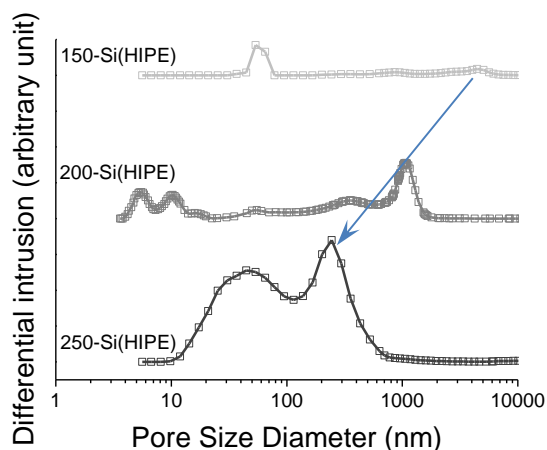


Figure III. 34: Pore size distributions of v -Si(HIPE)s, where v is the local shear in rpm

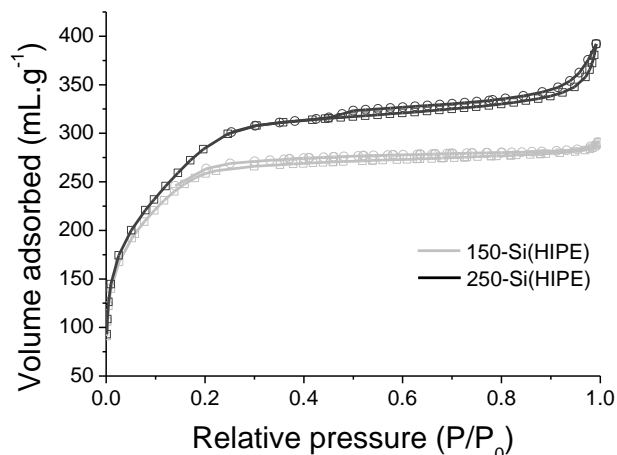


Figure III. 35: Nitrogen adsorption (\square) and desorption (\circ) isotherms of v -Si(HIPE)s, where v is the local shear in rpm

Table III. 7: Summary of TiO₂ characteristic values of v -TiO₂@Si(HIPE)s, where v is the local shear in rpm

	v -TiO ₂ @Si(HIPE)		
	150-TiO ₂ @Si(HIPE)	200-TiO ₂ @Si(HIPE)	250-TiO ₂ @Si(HIPE)
%wt TiO ₂ content (%)	24	30	20
Anatase/Rutile ratio	100/0	99/1	100/0
Anatase crystallite size (nm)	21.3	11.4	20
Rutile crystallite size (nm)	-	-	-

e. Thickness (t)

It was shown in Chapter II that monoliths with different thicknesses were synthesized. The objective here is to determine the influence of the sol thickness over morphology. The pore size distributions and nitrogen isotherms of batches 25, 26 and 27 are represented in Figure A 16, Figure A 17, Figure A 18, Figure A 19, Figure A 20 and Figure A 21, in annex respectively. Considering the characteristic values in Table III. 8, the sol origin appears to have more influence than the sol thickness. The relative difference between Batch 27 materials is about 15%, which does not seem significant regarding the error bars. Moreover, nitrogen physisorption data in Table III. 9 do not show noticeable difference. Note that these materials have been impregnated and used for the study of *ex-situ* calcination treatment on the structure of TiO₂. Their morphology after TiO₂ impregnation will therefore not be discussed.

Table III. 8: Summary of *t*-Si(HIPE)s morphological characteristics, where *t* is the poured sol thickness in mm, obtained by *mercury intrusion porosimetry* measurements

Batch y	t-Si(HIPE) _y					
	25		26		27	
	5	10	10	15	5	15
Intrusion volume (mL.g ⁻¹)	14.39	14.49	13.11	13.74	13.98	15.07
Porosity (%)	94	94	92	93	93	94
Bulk density (g.mL ⁻¹)	0.07	0.07	0.07	0.07	0.07	0.06
Median pore aperture (nm)	1492	1583	2128	2137	1650	1952

Table III. 9: Summary of *t*-Si(HIPE)s morphological characteristics, where *t* is the poured sol thickness in mm, obtained by *nitrogen physisorption* measurements

Batch y	t-Si(HIPE) _y					
	25		26		27	
	5	10	10	15	5	15
BET surface (m ² .g ⁻¹)	1011	980	938	1012	942	1004
Microporous volume (mL.g ⁻¹)	0.437	0.429	0.402	0.435	0.416	0.439

3) Conclusion

The impregnation methods have a strong impact (*I* vs. *II*) on the TiO₂ crystalline phases. The main reason is most probably the Ti-O-Si bonds promoted by the two-step impregnation method, which influence crystallization. No matter the Si(HIPE) porosity, the TiO₂ crystalline phase remains constant at 100% anatase. Only crystallite sizes vary from about 10 to 25 nm. The TiO₂ structure therefore seems to depend only on the impregnation method in this study (the calcination treatment has not been modified).

The parameters, that most influence the final material morphology, are the calcination temperature of silica, and the shear rate during emulsification. In perspective, the quantity of surfactants (mesostructuring) is a parameter that should be studied.

From X-TiO₂@Si(HIPE)s samples, the influence of TiO₂ specific surface area (i.e. crystallite size and % wt TiO₂), BET surface, and the median pore diameter could be studied.

3 Light diffusion

It is recalled here that one objective of the project is to determine the impact of porosity (especially pore size distribution) on the photocatalytic act (detailed in Chapter IV), and notably on photon penetration. This point will be discussed through physical measures, in this part. Initially, a monolith

and a powder bed are compared, due to the high contrast of porosity between the two photocatalytic systems. In a second stage, several monoliths with different median aperture diameters will be compared.

In order to characterize the optical diffusion properties of the various samples, the times of flights of individual photons travelling across the sample relative to the incident pulse were recorded, owing to a simultaneous spatial and time-resolved setup. Figure III. 36 shows the recorded two-dimensional streak plots for a $L = 8.5$ mm thick TiO₂(IIa)@Si(HIPE) and a $L = 2.0$ mm thick TiO₂ powder. Samples clearly exhibit a strongly multi-diffusive character, with photons being significantly delayed in the sample in both cases. The packing of the grains in the TiO₂ powder results in a mean exit time of light longer than in TiO₂(IIa)@Si(HIPE). A small crack is evidenced in the latter, causing a part of the excitation pulse to exit early, as observed by the line at about 0.8 ns. In order to quantitatively characterize the samples and obtain the light diffusion parameters as the transport mean free path l_t and the inelastic absorption length l_i , the temporal profiles of light transmitted by the samples in the forwards direction were firstly extracted, as shown by the horizontal lines drawn in the streak plots (Figure III. 36, a) and b)). They were then fitted with the full solution of the diffusion equation (Chapter II), valid for $\lambda \ll l_t \ll L$ at all times for a δ -function light source¹⁶.

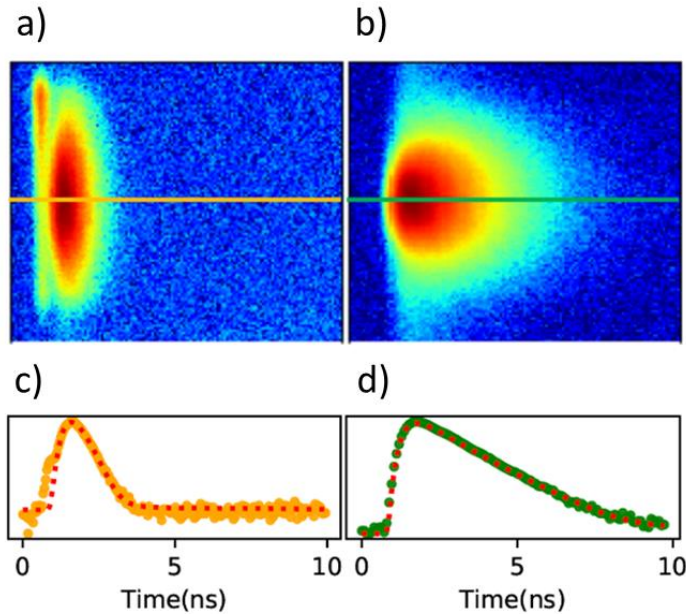


Figure III. 36: Streak (semi log) plots **a)** for a $L = 8.5$ mm thick TiO₂(IIa)@Si(HIPE) and **b)** for a $L = 2.0$ mm thick TiO₂ powder (horizontal axis: time delay on a logarithmic scale, vertical axis: spatial diffusion on a linear scale). **c)** and **d)** Respective (semi log) temporal decay profiles extracted at the maximum intensities (orange and green horizontal lines in (a) and (b), respectively) and fitted by the full solution of the diffusion equation (red dashed lines).

These profiles and their corresponding fits are shown on a semi-logarithmic plot in Figure III. 36, c) and d). The extrapolation length (z_e) is the position where the diffusive mode nulls. The penetration

length (z_p) is the position of the effective source for the source equation. It thus also signals the position of maximum intensity in the sample. These two lengths are generally set identical and match $z_0 = \frac{2}{3} l_t \left(\frac{1+R}{1-R} \right)$ in the case of no absorption. The proper reflectivities R are set at the boundaries¹⁷. Owing to this simple model of light diffusion through a slab geometry, the temporal profiles obtained experimentally could be appropriately fitted (Figure III. 36, c) and d)). The extracted values for the transport mean free paths are $l_t = 20.1 \pm 1.3 \mu\text{m}$ and $l_t = 3.1 \pm 0.3 \mu\text{m}$ for TiO₂(IIa)@Si(HIPE) and the TiO₂ powder, respectively. On the other side, the inelastic absorption length proved to be a rather insensitive parameter of the fit, revealing a very weak absorption of the samples at the chosen excitation wavelength ($\lambda = 515 \text{ nm}$), as it was already observed and reported in previous experiments on similar materials^{18,19,20}. Based on these results, the light penetration length for which the maximum intensity will be observed in the samples is $z_p = z_0 \cong \frac{2l_t}{3}$. As such, the light penetration depths are expected to be slightly less than one order of magnitude larger in TiO₂(IIa)@Si(HIPE) with $z_p \cong 13 \mu\text{m}$ to compare with $z_p \cong 2 \mu\text{m}$ for the powdered sample. The photocatalytic activity of TiO₂(IIa)@Si(HIPE)s can thus be expected, on purely photonic basis, to occur more in the bulk of the system than what has been usually observed for powders (even if the precise values of z_p just reported will not be strictly transferrable in the excitation conditions of the photocatalytic experiments). Experimentally, light penetration visualization was performed by UV-reduction of gold salt embedded in TiO₂@Si(HIPE). It is visible in Figure III. 37, that a photon penetration of several millimeters can be achieved.

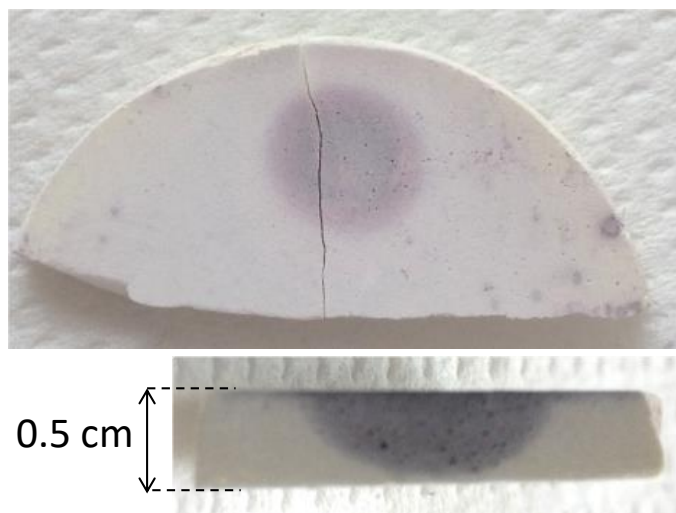


Figure III. 37: Top and side view of an Au/TiO₂@Si(HIPE) monolith irradiated by a UV lamp for 1 hour.

Furthermore, to intuit monolith behavior, two other TiO₂(IIa)@Si(HIPE)s providing different median pore aperture diameter were analyzed. All measurements are summarized in the Table A 34, in annex.

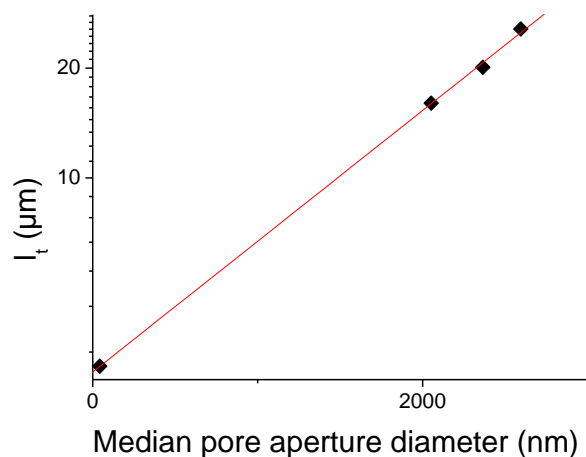


Figure III. 38: Transport mean free path (l_t) values as compared to median pore aperture diameter (D) for the bed powder and TiO₂@Si(HIPE)s. A strong exponential correlation between the two parameters is clearly observed ($R^2 = 0.9995$).

As illustrated in Figure III. 38, an exponential correlation between transport mean free paths and mean pore aperture diameter of materials is observed (which corresponds to the diameter of connecting windows between adjacent hollow spheres). This leads to the conclusion that a reduction of the bouncing frequency induced by increasing the distance between cell walls is favorable to enhance the photon transport mean free path. Light transport within these porous materials could be intuited strongly dependent on this diameter and can be tuned regarding the material morphology and porosity.

4 Conclusion

Si(HIPE)s and TiO₂@Si(HIPE)s provide high porosity (from 70 to 90%), bearing a huge proportion of micro- and macropores. The first ones provide polydisperse pore size, mainly less than 1 nm. The last ones are described by polydisperse and bimodal characters, with pore size spreading from about 10 nm to few microns. Pores are connected by internal cell windows of hundreds of nanometers, and the silica hollow sphere aggregation forms external cell windows of few microns. Moreover, the vermicular-like silica structure was induced by the mesoscopic population arrangement. The TiO₂ impregnation implies micropore lock induced by TiO₂ nucleation on mesopores and/or micropores, and a halving of the BET surface (from ca. 1000 to 500 m².g⁻¹). According to reproducibility and repeatability considerations, one monolith (Si(HIPE) and/or TiO₂@Si(HIPE)) per batch was dedicated to undergoing the characterizations representative of each batch.

The impregnation methods have a strong impact (I vs. II) on the TiO₂ crystalline phases. The main reason is most probably the Ti-O-Si bonds promoted by the two-step impregnation method, which influence crystallization. No matter the Si(HIPE) porosity, the TiO₂ crystalline phase remains constant at 100% anatase from the two-step impregnation method. Only crystallite sizes vary from about 10 to

25 nm. The parameters X that most influence the final material morphology are the calcination temperature of silica and the shear rate during emulsification. From X-TiO₂@Si(HIPE)s samples, the influence of TiO₂ specific surface area, BET surface; and the median pore diameter could be studied over the photocatalytic performances. Furthermore, light diffusion experiments highlight the contrast in photon penetration within a powder bed or a monolith. The larger the median pore aperture diameter, the greater the transport mean free path of photon, and therefore the photon penetration. This supports the importance of linking morphological and structural characteristics to the photocatalysis principle. Thus, the following chapter is describing photocatalytic performances as a function of HIPE properties/characteristics.

5 References

- (1) Lastoskie, C. M. A Modified Horvath-Kawazoe Method for Micropore Size Analysis. In *Studies in Surface Science and Catalysis*; Unger, K. K., Kreysa, G., Baselt, J. P., Eds.; Characterisation of Porous Solids V; Elsevier, 2000; Vol. 128, pp 475–484.
- (2) Horváth, G.; Kawazoe, K. Method for the calculation of effective pore size distribution in molecular sieve carbon. *Journal of Chemical Engineering of Japan* **1983**, *16* (6), 470–475.
- (3) Carn, F. Intégration Entre Chimie Douce et Fluides Complexes Pour La Genèse d'architectures Poreuses Hiérarchisées: Synthèses, Caractérisations et Application, Université de Bordeaux 1, 2006.
- (4) Arnal, F. Répétabilité & reproductibilité d'une méthode <http://flarnal.e-monsite.com/medias/files/revet-1.pdf>.
- (5) Carn, F.; Colin, A.; Achard, M.-F.; Deleuze, H.; Sellier, E.; Birot, M.; Backov, R. Inorganic Monoliths Hierarchically Textured via Concentrated Direct Emulsion and Micellar Templates. *J. Mater. Chem.* **2004**, *14* (9), 1370–1376.
- (6) Livage, J.; Henry, M.; Sanchez, C. Sol-Gel Chemistry of Transition Metal Oxides. *Progress in Solid State Chemistry* **1988**, *18* (4), 259–341.
- (7) Sanchez, C.; Livage, J.; Henry, M.; Babonneau, F. Chemical Modification of Alkoxide Precursors. *Journal of Non-Crystalline Solids* **1988**, *100* (1), 65–76.
- (8) Vorkapic, D.; Matsoukas, T. Effect of Temperature and Alcohols in the Preparation of Titania Nanoparticles from Alkoxides. *Journal of the American Ceramic Society* **1998**, *81* (11), 2815–2820.
- (9) Sosnov, E. A.; Malkov, A. A.; Malygin, A. A. Hydrolytic Stability of the Si–O–Ti Bonds in the Chemical Assembly of Titania Nanostructures on Silica Surfaces. *Russ. Chem. Rev.* **2010**, *79* (10), 907.
- (10) Ding, X.-Z.; Qi, Z.-Z.; He, Y.-Z. Effect of Hydrolysis Water on the Preparation of Nano-Crystalline Titania Powders via a Sol-Gel Process. *Journal of Materials Science Letters* **1995**, *14* (1), 21–22.
- (11) Zhang, H.; Banfield, J. F. Phase Transformation of Nanocrystalline Anatase-to-Rutile via Combined Interface and Surface Nucleation. *Journal of Materials Research* **2000**, *15* (2), 437–448.
- (12) Perego, C. De La Maîtrise Morphologique de Nanoparticules de TiO₂ Au Contrôle Du Frittage, Université Claude Bernard Lyon 1, 2009.
- (13) Analyse de la variance ou ANOVA <https://www.xlstat.com/fr/solutions/fonctionnalites/analyse-de-la-variance-ou-anova> (accessed Oct 14, 2018).
- (14) Tadros, T. F. Emulsion Formation, Stability, and Rheology. In *Emulsion Formation and Stability*; Wiley-Blackwell, 2013; pp 1–75.

- (15) Zhuravlev, L. T. The Surface Chemistry of Amorphous Silica. Zhuravlev Model. *Colloids and Surfaces A: Physicochemical and Engineering Aspects* **2000**, 173 (1–3), 1–38.
- (16) Wiersma, D. S.; Muzzi, A.; Colocci, M.; Righini, R. Time-Resolved Experiments on Light Diffusion in Anisotropic Random Media. *Phys. Rev. E* **2000**, 62 (5), 6681–6687.
- (17) Zhu, J. X.; Pine, D. J.; Weitz, D. A. Internal Reflection of Diffusive Light in Random Media. *Phys. Rev. A* **1991**, 44 (6), 3948–3959.
- (18) Gaikwad, P.; Ungureanu, S.; Backov, R.; Vynck, K.; Vallée, R. a. L. Photon Transport in Cylindrically-Shaped Disordered Meso-Macroporous Materials. *Opt. Express* **2014**, 22 (7), 7503–7513.
- (19) Bachelard, N.; Gaikwad, P.; Backov, R.; Sebbah, P.; Vallée, R. A. L. Disorder as a Playground for the Coexistence of Optical Nonlinear Effects: Competition between Random Lasing and Stimulated Raman Scattering in Complex Porous Materials. *ACS Photonics* **2014**, 1 (11), 1206–1211.
- (20) Gaikwad, P.; Bachelard, N.; Sebbah, P.; Backov, R.; Vallée, R. A. L. Competition and Coexistence of Raman and Random Lasing in Silica-/Titania-Based Solid Foams. *Advanced Optical Materials* **2015**, 3 (11), 1640–1651.

Chapter IV

CO₂ photoreduction performances

This chapter consists in two parts dedicated to the photocatalysts behavior understanding, under our CO₂ photoreduction conditions. The first part deals with proof of concept establishment. Firstly, the influence of specific parameters is described over P25 TiO₂ powder photocatalytic performance. Secondly, CO₂ photoreduction process evidences through TiO₂@Si(HIPE)s are provided, and their performances are compared to those of P25 powder bed as function of photocatalytic bed thickness. The second part describes the model hypotheses and defines the quantities used, and then the model is confronted with experimental results, leading to the descriptor definition of the material behaviors. The last part deals with the extracted trends from modeled photogeneration charge carrier kinetic values (k₀) as function of specific parameters).

TABLE OF CONTENTS

<u>1</u>	<u>PROOF OF CONCEPT AND EXPERIMENTAL LIMITATION</u>	125
1)	PRELIMINARY TESTING	125
A.	POWDER VS. MONOLITH	125
B.	CRITICAL PARAMETERS	127
	Irradiance	127
	Dilution	128
	Oxygen	129
2)	TiO ₂ @Si(HIPE) BEHAVIOR	132
A.	CO ₂ PHOTOREDUCTION PROCESS THROUGH TiO ₂ @Si(HIPE)	132
B.	CO ₂ PHOTOREDUCTION ENHANCEMENT THROUGH TiO ₂ @Si(HIPE)	134
	Behavior over bed thickness	134
	Residence time influence	136
<u>2</u>	<u>KINETIC MODELLING</u>	137
1)	MODEL DESCRIPTION	137
A.	HYPOTHESES	138
B.	PHOTON QUANTITY DESCRIPTION	138
C.	ACTIVE SITE DESCRIPTION	139
D.	GLOBAL EQUATION RATE	140
2)	CONFRONTATIONS WITH EXPERIMENTAL RESULTS	141
A.	MATERIAL DESCRIPTION	141
B.	PARAMETER FITTING	142
C.	K COEFFICIENT CORRELATION	144
D.	LIGHT ATTENUATION COEFFICIENT CORRELATIONS	145
<u>3</u>	<u>TiO₂@Si(HIPE) BEHAVIOR UNDERSTANDING</u>	146
1)	TiO ₂ SPECIFIC SURFACE AREA	147
2)	TiO ₂ SSA CONTRIBUTION	148
3)	MEDIAN PORE DIAMETER	150
4)	SYNTHESIZED AND COMMERCIAL TiO ₂ : INFLUENCE OF TiO ₂ ORIGIN	150
<u>4</u>	<u>CONCLUSION</u>	151

5 REFERENCES 154

1 Proof of concept and experimental limitation

This section is dedicated to confirming the project interest while describing the framework in which the materials are studied. In a first step, a P25 TiO₂ performance comparison is established between powder and monolith (TiO₂(P25)@Si(HIPE)) photocatalytic bed. Then, hypotheses are proposed and discussed using a study over P25 TiO₂ powder. In a second step, CO₂ photoreduction process improvement through TiO₂@Si(HIPE)s evidences are given and confirmed by complementary studies.

1) Preliminary testing

As the reference photocatalyst, P25 TiO₂ is used in this part to discuss the improvement that Si(HIPE) support can bring, as well as the phenomena involved in the CO₂ photoreduction process.

a. Powder vs. monolith

To concretely visualize the influence of supporting active phase with Si(HIPE), a photocatalytic performance comparison of P25 TiO₂ powder and this last embedded inside Si(HIPE) is carried out at iso-TiO₂ mass. As presented in Table A 35 in annex, both systems provide 0.063 ± 0.003 g of TiO₂ and similar crystalline structure. It should be noted that the difference in anatase/rutile proportions between the two systems can be induced by the measurement error and the amorphous signal intervention in the TiO₂(P25)@Si(HIPE) system. As the difference is not significant and the TiO₂ origin is identical in both systems, this difference is not considered to have an impact in the comparison of photocatalytic performance. P25 TiO₂ powder and TiO₂(P25)@Si(HIPE) systems differ mainly by the bed thickness (0.36 and 3.6 mm, respectively), the irradiated surface (5.31 cm² and 9.08 cm², respectively) and the TiO₂ particles dilution in Si(HIPE). Production rates of each detected products are displayed in Figure A 22 in annex. Then, the average electron consumption rates normalized by photocatalyst mass and irradiated area were calculated to take into account all these products and quantify the photocatalytic performances.

Table IV. 1: Photocatalytic performances of P25 TiO₂ powder and TiO₂(P25)@Si(HIPE)

	P25 TiO ₂ powder	TiO ₂ (P25)@Si(HIPE)
r_e (μmole·h ⁻¹ ·g ⁻¹)	2.7	4.5
r_e (μmole·h ⁻¹ ·m ⁻²)	314	327

According to Table IV. 1, the average electron consumption rates normalized by TiO₂ mass show better performance for TiO₂(P25)@Si(HIPE). This implies that TiO₂ particles embedded in Si(HIPE) provide better efficiency than particles in powder bed shape. Knowing that the active phase has the same structure and is present in the same quantity in both systems, this improvement in global activity per unit mass may be explained as follows. Firstly, pulsed laser experiments (Chapter 3) proved that light penetration is deeper in TiO₂@Si(HIPE) than in powder due to multiple scattering in macroporous disordered media. Then activated TiO₂ particles quantity could be higher than in powder bed. In other words, if the TiO₂ mass contained in both systems is identical, the TiO₂ efficient mass can vary between both. Secondly, particles dilution could limit oxygen coverage onto TiO₂ particles, thus decreasing back reaction rates.

Furthermore, according to selectivities presented in Figure IV. 1, it clearly appears that main products are hydrogen and methane, but proportions differ from one system to the other. More generally, TiO₂(P25)@Si(HIPE) favors products emerging from multi(>2)-electronic reactions to the detriment of those resulting from bi-electronic reactions. As a reminder, hydrogen and carbon monoxide need 2e⁻ to be produced, while methane needs 8 and ethane 14. Only 26% of TiO₂(P25)@Si(HIPE) products result from bi-electronic reactions contrary to 57% for P25 TiO₂ powder. As a direct consequence and because of the same active phase, the average electron consumption rate is highest for TiO₂(P25)@Si(HIPE). Since the active phase has not undergone any modification (such as doping or addition of co-catalysts) from one system to another, no improvement in charge separation is expected, although this could have explained the selectivities. This preferential orientation towards methane and ethane can result from following phenomena: the local photon flux is improved in the porous structure so that a larger electron quantity is generated per active site, or incomplete reverse reactions (leading to CO formation for example) are limited.

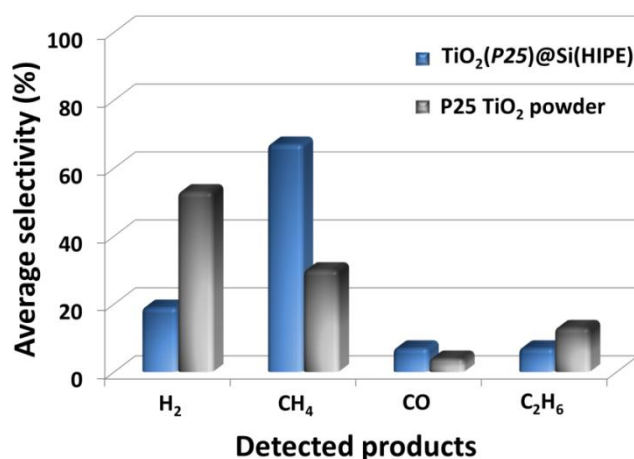


Figure IV. 1: Average selectivity towards detected products for TiO₂(P25)@Si(HIPE) (blue) and P25 TiO₂ powder (black)

Moreover, the average electron consumption rates normalized by irradiated surface show similar performances for both systems. Due to the difference in TiO₂ loading rate (118 g.m⁻² for powder and 70 g.m⁻² for monolith), the monolith activity would be expected to be 40% lower than that of the powder. However, the improvement in TiO₂ efficiency makes it possible to maintain a global activity per unit area equivalent to that of powder.

With these first results, a real interest in the use of Si(HIPE)s as active phase bearer has been raised. Then, to discuss the assumptions made above, a detailed study focused on P25 TiO₂ powder is presented hereafter.

b. Critical parameters

Three effects that may govern the observed photocatalytic performance have been highlighted above: photon penetration, TiO₂ particle dilution and reverse reactions. Note that a control chart is being constructed to assess the error made on the evaluation of photocatalytic activities. First points roughly give a standard deviation of 15%.

Irradiance

The photon flux density is hardly measurable at the material heart, then the lamp irradiance influence was studied on a 60 mg bed of P25 TiO₂ powder. The irradiated surface is always the same and equal to 5.31 cm².

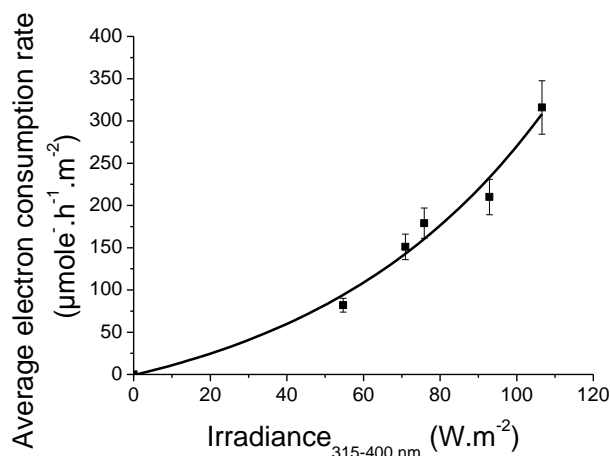


Figure IV. 2: Photocatalytic performances of P25 TiO₂ powder as a function of the irradiance for wavelengths ranging from 315 to 400 nm

Contrary to linear proportionality observed by Hermann *et al.*¹ for photo-oxidation of organics, Figure IV. 2 shows a 2nd order polynomial relation between global activity per area and irradiance. This indicates that a strong radiant flux influence is to take into account and confirms the photo-induced nature of the catalytic process activation. This notably show that (in present conditions) photon supplying seems to be the rate determination step, which confirms the stake of improving photon

harvesting. Note that highest average electron consumption rate is obtained for highest irradiance (in the studied range). However, for lamp lifetime reason, its irradiance has been fixed at 80 W.m⁻².

Dilution

The hypothesis of a strong impact of TiO₂ particle dilution in the silica matrix has been previously proposed. To evaluate this effect, a comparison of the photocatalytic performance profiles of the P25 TiO₂ with and without dilution as a function of the involved TiO₂ mass was carried out. P25 TiO₂ dilution was operated by mechanical mixing of P25 TiO₂ with an equal amount of silica powder (Davisil Grade 710, purchased from Sigma Aldrich).

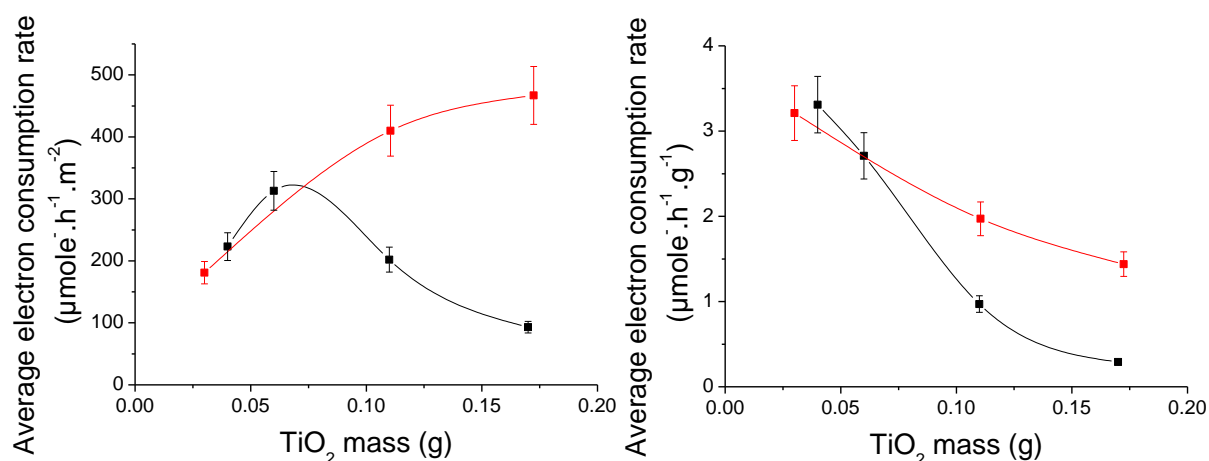


Figure IV. 3: Photocatalytic performance comparison of P25 TiO₂ powder (black curve) and 50/50-TiO₂/SiO₂ mixed powder (red curve), normalized by irradiated area (left) and TiO₂ mass (right)

Concerning global activities per irradiated area (Figure IV. 3 left), it appears that two radically different profiles are drawn. TiO₂ diluted in silica (red curve) seems to provide the expected behavior described by Herrmann¹. This firstly consists in a linear increase of the activity, corresponding to the increase of active phase involved, until a given mass. After this mass, a plateau seems to be emerging and might correspond to a screening effect. Herrmann assigned this effect to a light penetration limit, implying that at this given mass, the maximum amount of TiO₂ in which all particles are totally illuminated is achieved. In other words, all the added TiO₂ mass is inefficient. This can be correlated with the corresponding global activity per mass behavior (Figure IV. 3 right, red curve). This decrease with TiO₂ mass causes TiO₂ mass (denominator) increases faster than the activity. Focusing now on P25 TiO₂ without dilution (black curves), it appears that no plateau is achieved for the global activity per surface (Figure IV. 3 left). This could be induced by back reactions. They were not taken into account by Herrmann, because his assumption was for VOCs mineralization in oxidative medium (no back reaction workable). Mass increase induced bed thickness increase. Assuming an O₂ coverage increase along the catalytic bed, the active phase density could favor back reactions. Indeed, in diluted TiO₂ particle system, the encounter probability between products (hydrocarbons), oxygen and irradiated particles is lower, due to potential adsorption on silica (not active). Similarly, this may be correlated

with a more abrupt decrease of global activity per mass compared to that provided by the diluted system (Figure IV. 3 right).

Moreover, regarding selectivities (Figure IV. 4), it appears that diluted systems favor selectivity toward products from multi(>2)-electronic reactions. The difference between both systems is even greater as the TiO₂ mass (the catalytic bed thickness) increases. This implies that in diluted systems, electron density is locally higher than in no-diluted systems.

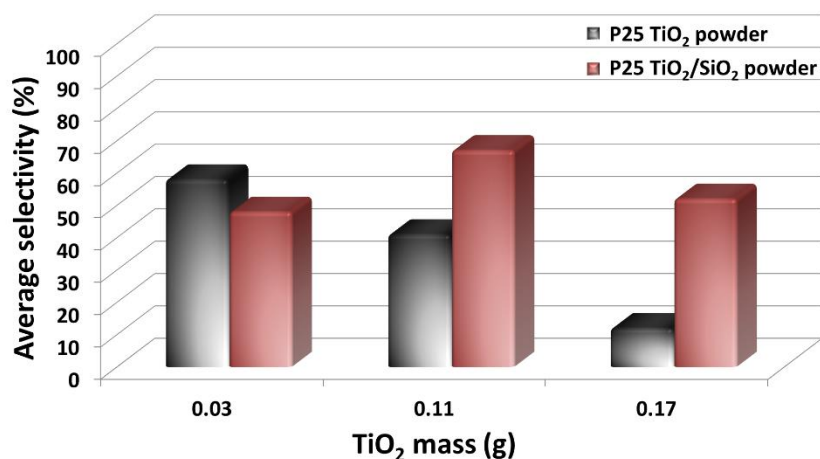


Figure IV. 4: Selectivities towards products from multi(>2)-electronic reactions as function of TiO₂ mass, of P25 TiO₂ powder (black) and P25 TiO₂/SiO₂ (50/50) powder (red)

Oxygen

Oxygen is an essential element in the CO₂ photoreduction process. Indeed, oxygen is a reaction product. This implies in particular that the more oxygen there is, the more reverse reactions may be favored (by equilibrium displacement). Then, its presence and influence are going to be discussed.

Theoretically, according to reaction equations given below and the products amount, the dioxygen amount is calculable and equal to the measured amount. The reaction equations displayed in Figure IV. 5 are considered to be those relevant to the detected products and involving oxygen formation.

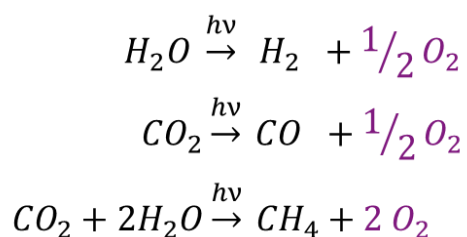


Figure IV. 5: Reaction equations associated to the detected products and involving oxygen formation

To assess the evolution of oxygen during a test, the oxygen concentration was monitored during purging time, then after turning on the light during a long test (44h), and finally, after turning off the light for 24h (Figure IV. 6). Firstly, during the purging time, O₂ concentration has been decreased and

stabilized at about 30 ppm and no product was detected. When the light was switched on, O₂ concentration dropped drastically to 10 ppm, while H₂, CO and CH₄ products were formed. Then O₂ concentration gradually increased during the test, while product concentrations decreased. However, according to the reaction equations, O₂ concentration should follow the same reaction profile than products. Moreover, assuming that all O₂ amount above 30 ppm (starting amount) was produced from reactions, produced O₂ quantity was around 0.08 μmol (purple region). The theoretical amount was about 0.28 μmol. Then, it may be intuitive that a certain oxygen amount is adsorbed by the photocatalyst. Indeed, UV irradiation implies oxygen vacancies with whom dioxygen could react to produce a stoichiometric surface ², or with H₂O co-adsorption could form bridging hydroxyls ³. When light was turned off, the products (H₂, CH₄ and CO) immediately stopped being produced, and the oxygen desorbed.

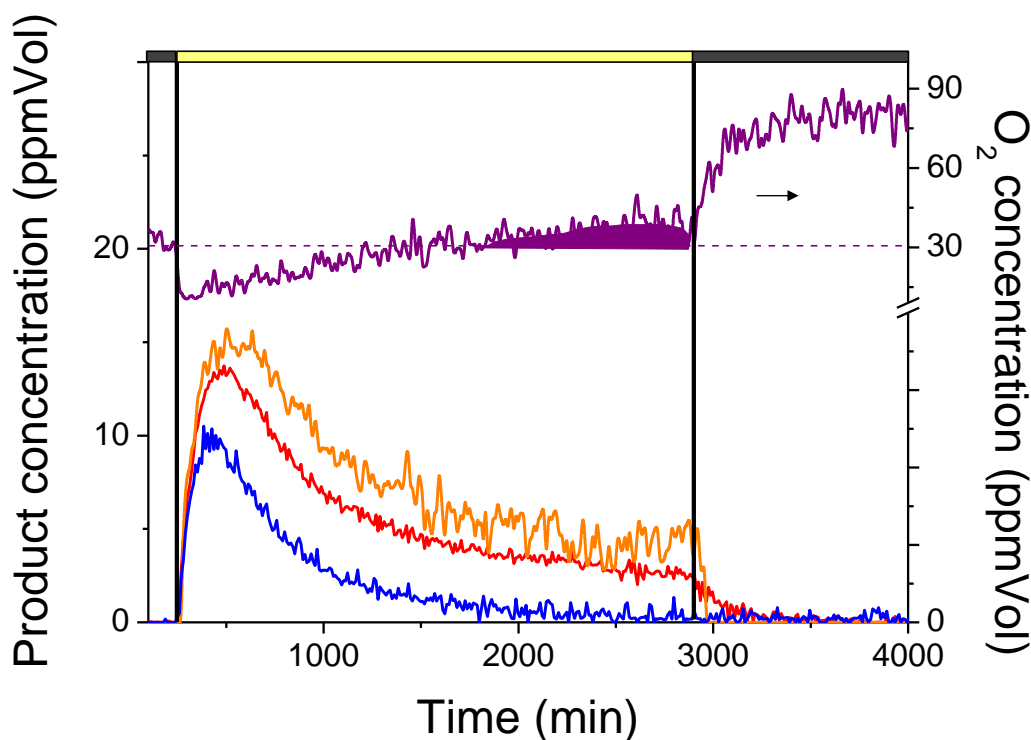


Figure IV. 6: Photocatalytic test monitored at first without light, then with light over 44 hours, and finally without light over 24 hours. Photocatalyst: 0.15g of P25 TiO₂ powder. Species: H₂ (red), CO (orange), CH₄ (blue) and O₂ (purple)

Due to strong oxygen reactivity exhibited here, oxygen could significantly influence the photocatalytic process. The more oxygen adsorbed on the surface, the greater the probability of products (hydrocarbons) adsorption in the vicinity. This can then promote reverse reactions. To estimate this influence, photocatalytic performances are compared between almost anaerobic conditions and with non-negligible O₂ amount.

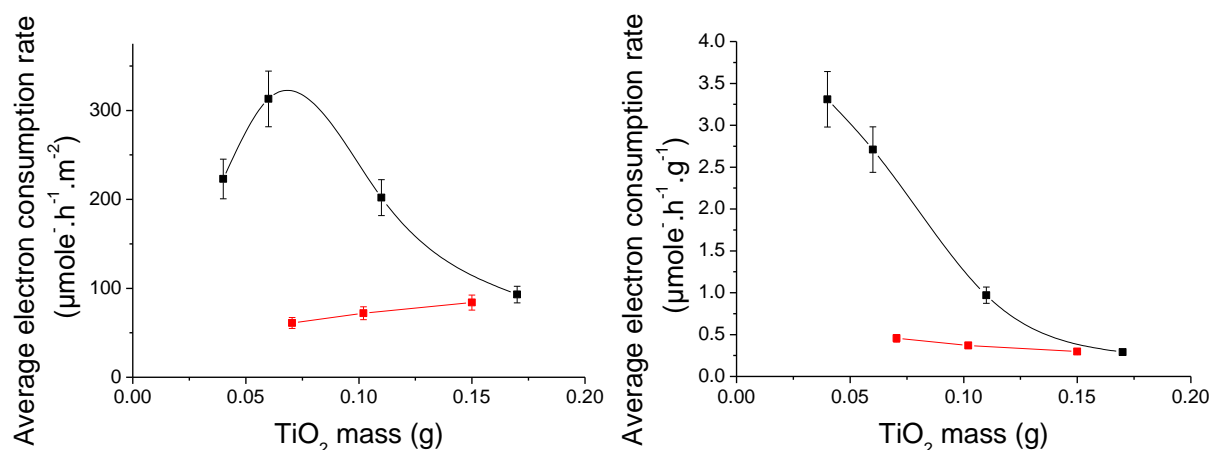


Figure IV. 7: Photocatalytic performance comparison of P25 TiO₂ powder “without” O₂ (black curve) or “with” O₂ (red curve), normalized by irradiated surface (left) and TiO₂ mass (right)

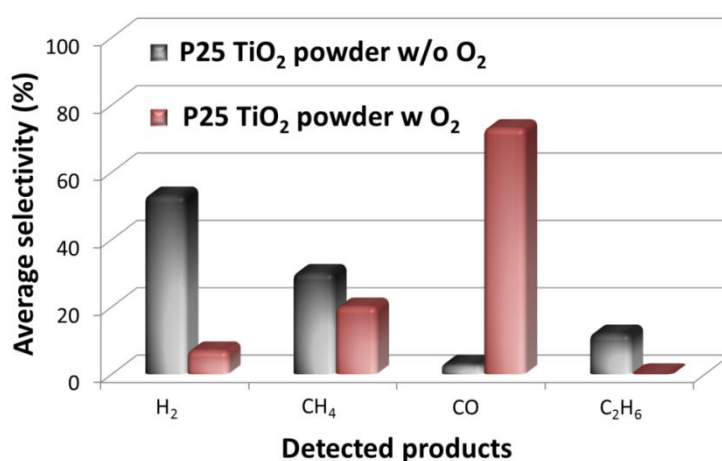


Figure IV. 8: Selectivities of 0.0607 g P25 TiO₂ powder “without” O₂ (black) and 0.0705g P25 TiO₂ powder “with” O₂ (red)

More precisely, almost anaerobic conditions (system “without” oxygen) are considered to have been met when O₂ concentration is maintained below 20 ppm during the test, under illumination. When the system is considered to contain a significant O₂ amount (“with” oxygen), its concentration increases during the test to 80 ppm or more. According to Figure IV. 7, it appears that O₂ presence drastically reduces the photocatalytic performances. The average electron consumption rates normalized by irradiated surface provide a slight increase with TiO₂ mass compared to the decrease observed for P25 TiO₂ powder system “without” oxygen. The average electron consumption rates normalized by TiO₂ mass is coherent with the behavior normalized by irradiated surface. Furthermore, considering selectivities, it clearly appears Figure IV. 8 that O₂ presence strongly influences selectivities towards CO formation compared to system without O₂. As a reminder photoreduction of CO₂ to CH₄, for example, is a multistep reaction. CO can be an intermediate product^{4,5,6}, and then could be the back-reaction product.

It has been seen in this section that photocatalytic performances are closely dependent on irradiance. In other words, the effective photon supply can be considered as the limiting reactant. In addition, the active phase dilution in a silica matrix limits reverse reactions. And finally, the oxygen presence drastically reduces the TiO₂ performance, and directs reactions towards the CO and CO₂ production. With these elements established, the TiO₂@Si(HIPE) synthesized materials behavior can be discussed.

2) TiO₂@Si(HIPE) behavior

A blank photocatalytic test set is first described to confirm that CO₂ photoreduction process occurs through synthesized TiO₂@Si(HIPE). Then, to assess the 3D process, monolith and powder bed are confronted as function of thickness.

a. CO₂ photoreduction process through TiO₂@Si(HIPE)

First, to confirm that the CO₂ photoreduction process for fuel production effectively occurs through our synthesized materials and under our set-up conditions, a set of blank photocatalytic reactions was carried out (Figure IV. 9). The blank reactions were performed under following conditions: (i) without light source with TiO₂ active phase and both reactant feed, (ii) without TiO₂ photocatalyst, under reactant feed flow and light irradiation, and (iii) without CO₂ flow under Ar/H₂O flow in the presence of photocatalyst and light source. In all experiments, no or weak hydrocarbons product formation was observed and derived from background signal, compared to the average electron consumption rate with these three elements: the presence of photocatalyst, light irradiation, and CO₂ feed. This proves that the detected products are effectively derived from the CO₂ conversion by activating TiO₂ under UV irradiation and using water as a sacrificial agent. Note that blank reaction without H₂O was not performed due to intrinsic water presence into TiO₂@Si(HIPE)s.

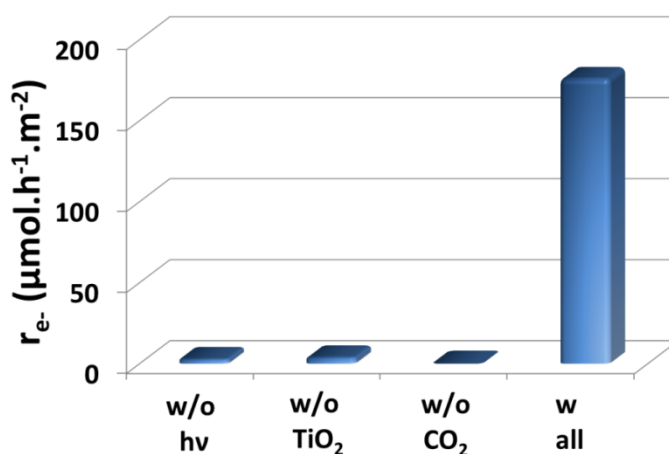


Figure IV. 9: Blank photocatalytic tests operated through TiO₂@Si(HIPE)s

During the CO₂-free experiment, H₂O presence was maintained. Thus, due to water splitting process, hydrogen production was expected to occur. It is interesting to note that only hydrogen was

produced, but in a very small proportion. Performance levels similar to those achieved for CO₂ reduction could have been expected. The origin of this low hydrogen production has not yet been elucidated, but an experimental limitation must be specified here. To be as close as possible to the test conditions, the argon flow setpoint has been set at 0.3 cc.min⁻¹. However, the flow meter used in this experiment was calibrated for CO₂. Thus, the argon flow rate could not be precisely controlled and was higher than the setpoint. The faster the flow rate, the less time the reactants must adsorb, limiting reactivity. Additional analyses were therefore carried out to prove that the hydrocarbons were indeed produced from the CO₂ injected into the reactor: a NMR solid analysis with ¹³CO₂ and a TGA/MS.

NMR analysis of the solid was initially planned to identify intermediate reaction species adsorbed within the material. Thus, after a few hours of testing, the reactor is hermetically sealed and placed in a glove box to perform the sampling for analysis. Figure IV. 10 shows the sample (red) and the empty rotor (blue) signals. These signals appear identical. While the low quantities of hydrocarbons produced may explain the signal absence (device sensitivity), the feed stream contains nearly 100% ¹³CO₂. Thus, without irradiation (Figure A 23 in annex), CO₂ does not adsorb. Carbon dioxide interacts only weakly with the clean rutile (110) surface^{7,8,9}. Henderson⁸ found that after vacuum annealing TiO₂ (110), its surface contains oxygen vacancies which bind CO₂ only slightly more strongly than do the five-coordinate Ti⁴⁺ sites typical of the nearly perfect TiO₂ (110) surface. It can therefore be envisaged that no carbonate-type pollutants will adsorb either.

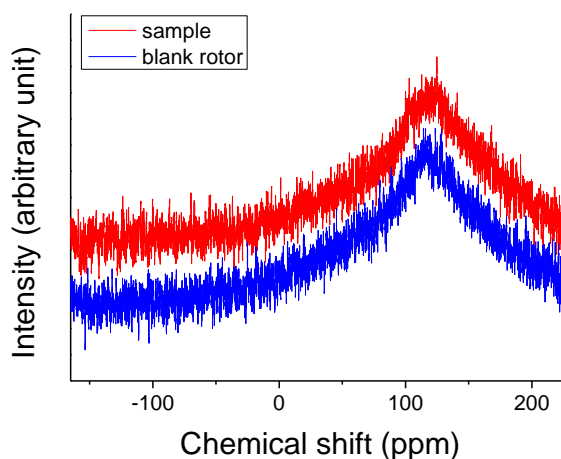


Figure IV. 10: NMR analysis of TiO₂@Si(HIPE) tested (red) and empty rotor (blue)

To address the issue more generally, a TGA/MS analysis was performed on a TiO₂@Si(HIPE) sample that had not been tested and stored in air. This is to determine the residues present on the surface of the synthesized materials before any use. Table IV. 2 summarizing the mass losses relating to the record presented in the annex (Figure A 24) is presented below. For a heat treatment ranging from 30 to 900°C, only a loss of about 15% of water was detected. Finally, no pollutant could be responsible for this increase in photocatalytic performance with monolith thickness.

Table IV. 2: Summary of mass losses and their associated MS analyses results

	RT → 30°C	30 → 750°C	750 → 900°C	Total (%)
%wt variation	9.3	4.6	1.4	15.3
Derivative DTG	30°C	50°C	Shoulder at 880°C	-
Effluent analysis by MS	H ₂ O	H ₂ O	H ₂ O	H ₂ O

b. CO₂ photoreduction enhancement through TiO₂@Si(HIPE)

It has just been demonstrated that the products result from the CO₂ photoconversion. To go further, the photocatalytic performances are evaluated in this section regarding the catalytic bed thickness, as well as the reactants residence time influence through the thickness variation.

Behavior over bed thickness

With a twofold objective of comparing the P25 TiO₂ powder with the TiO₂@Si(HIPE) and better understanding the TiO₂@Si(HIPE) behavior, it was chosen to study their photocatalytic performance as a function of bed thickness. Note that during the bed thickness study, CO could not be measured due to a technical problem during some tests. Thus, to properly compare the systems regarding average electron consumption rates, the CO was removed for all tests.

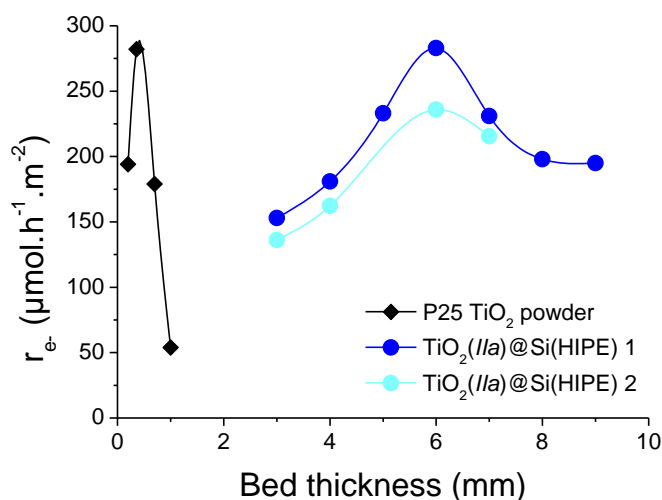


Figure IV. 11: Average electron consumption rates of P25 TiO₂ powder bed (black) vs. two TiO₂(IIa)@Si(HIPE)s (blue) as function of bed thickness

Figure IV. 11 shows the same trend for P25 TiO₂ powder activity as function of catalytic bed thickness, compare to that as function of TiO₂ mass. An optimum is found for about 360 μm bed thickness after which a continuous decrease is observed. This phenomenon was previously attributed to oxygen coverage gradient within the catalytic bed thickness, favoring thus the back-oxidation reaction

of the products (H₂, CO, CH₄) by O₂, until photon concentration falls short leading to a plateau in activity. With TiO₂@Si(HIPE), the behavior seems to be significantly shifted to thicker photocatalytic bed as maximum activity is reached for a 6 mm-bed thickness. Those results lead us to the conclusion that TiO₂@Si(HIPE) allows enhanced photon penetration as already suggested by optical diffusion properties characterization, and furthermore greatly limits back-reactions, probably due to the TiO₂ dilution in the silica matrix. Actually, the drop-in activity after the maximum is significantly less abrupt, than in powder bed. Then, for thickness larger than 8 mm (TiO₂(IIa)@Si(HIPE) 1), a plateau could be distinguished, owing to screening effect¹. A bulk photo-driven scenario seems to be emerging rather than commonly observed surfaced ones, where up to 6 mm thicker becomes better. In other words, if fundamental phenomena described for the P25 TiO₂ powder bed are also found for monoliths, the efficiency range is wider for monoliths than for powder beds.

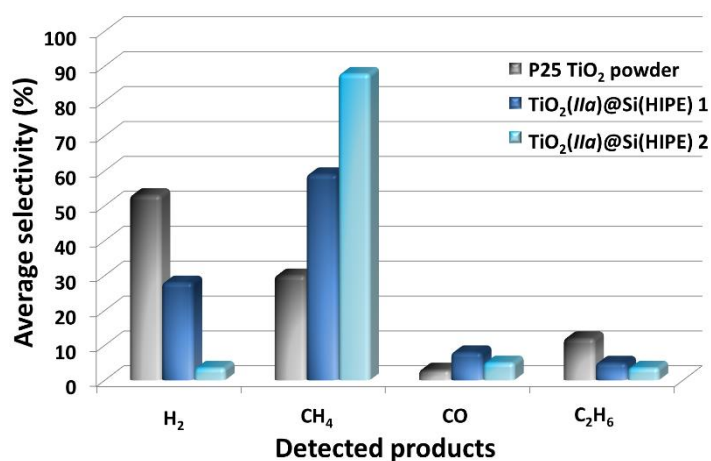


Figure IV. 12: Average selectivities of P25 TiO₂ powder (black) and TiO₂(IIa)@Si(HIPE)s: 1 (dark blue) and 2 (light blue), at their respective optimal thickness (360 μm for P25 TiO₂ powder, and 6 mm for TiO₂(IIa)@Si(HIPE)s)

To discuss selectivities, CO must be taken into account. For this purpose, the tests for which the CO peak integration has been effective are selected. Thus, TiO₂(IIa)@Si(HIPE)s (1 and 2) and P25 TiO₂ powder selectivities, at their respective optimal thickness, are displayed in Figure IV. 12. This figure then suggests that TiO₂@Si(HIPE)s favor methane production which requires 8 electrons, whereas H₂ is the main product for TiO₂ as powder which requires only two electrons. This enhanced selectivity might be related with the fact that photons concentration is higher within the thickness of TiO₂@Si(HIPE), leading to enhanced electron density onto the TiO₂ particles surface. It should be noted that the difference in selectivity between the two TiO₂(IIa)@Si(HIPE)s may be related to the oxygen presence in the TiO₂(IIa)@Si(HIPE) 1 tests. The methane production then decreases in favor of products resulting from bi-electronic reactions (H₂ or O₂).

Residence time influence

The tests presented in the previous comparisons were performed according to the routine protocol, i.e. with a CO₂ flow rate of 0.3 cc.min⁻¹. However, since the thickness varies from one test to another, the reactants residence time also varies. As the residence time influence chemical reactions, it is essential to verify that the increase in photocatalytic performance as a function of the monolith thickness ($h < 6$ mm) is not only due to the reactants contact time.

To check this, a series of iso-residence time tests were performed (varied flow rate) and compared to the trend of iso-flow tests. Note that due to flowmeter technical limitations, iso-residence time tests could not be carried out routinely, particularly for thick monoliths ($h > 5$ mm). According to Figure IV. 13, it appears that at iso-residence time (full circle), the global activity per irradiated surface unit increases. This implies that there is indeed an increase in the number of active irradiated sites deeper in the catalyst bed. Thus, this curve validates the character "thicker is better" and implies the use of the entire monolith volume. In other words, the penetration of photons up to 5 mm is undeniable. At iso-volume, a moderate performance difference is visible (black arrow). This reflects the fact that a shorter residence time barely reduces the performance level. Indeed, a low contact time limits the reaction.

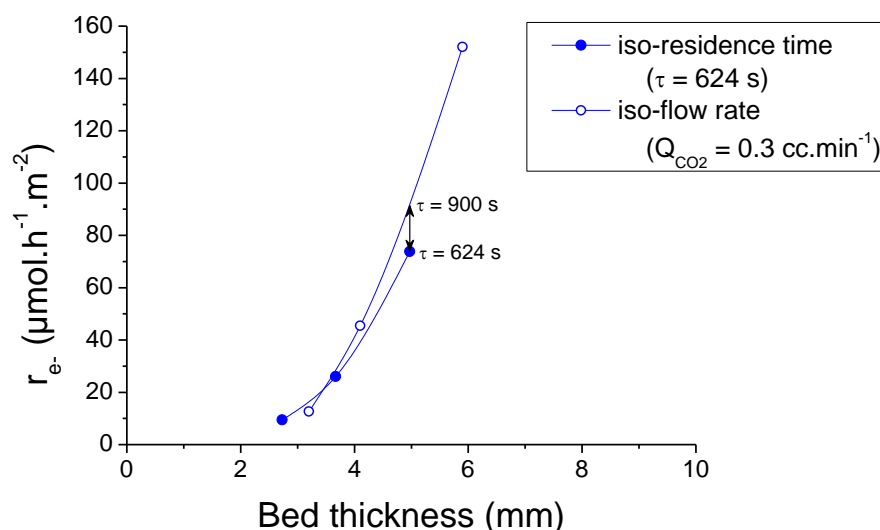


Figure IV. 13: Residence time influence over the bed thickness behavior of TiO₂(IIa)@Si(HIPE)

According to this study, the increase in photocatalytic performance as a function of thickness is not induced solely by the increase in residence time. To complete the proof of concept, a study on the pollutant presence such as carbonates or VOCs has been carried out. Indeed, their adsorption prior to the test can increase hydrocarbon yields.

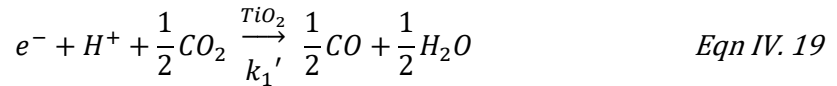
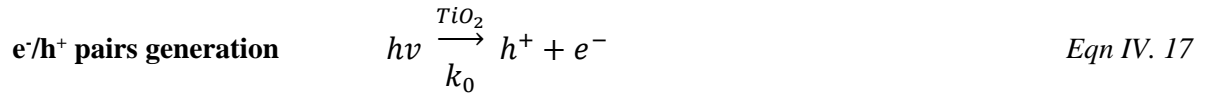
In this section, different parameters involved in the CO₂ photoreduction process through TiO₂@Si(HIPE) have been identified: the dilution effect, the photon penetration depth and the oxygen presence. The aim now is to link these parameters to the material physicochemical characteristics. For this purpose, a kinetic model has been implemented and is described in the following section.

2 Kinetic modelling

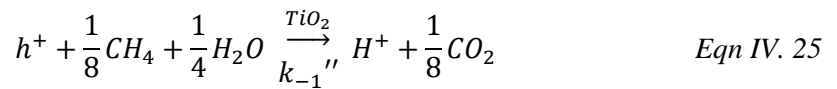
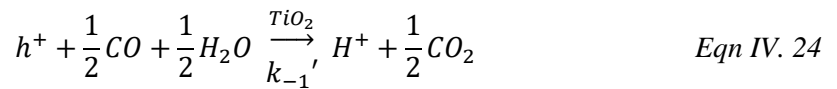
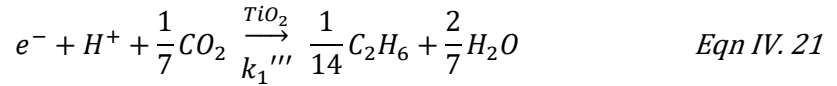
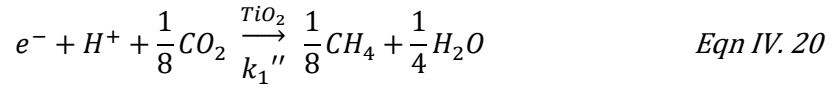
In this section, the kinetic model implementation is detailed. Then, its confrontation with the experimental results is treated through the identification of the descriptive parameters and their meaning.

1) Model description

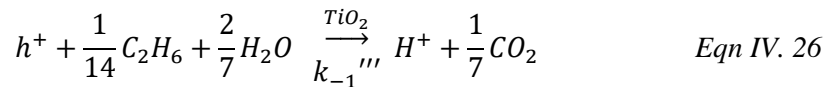
The first step in establishing the model is to define the half reactions considered. Then, the main ones involving on the one hand photo-generated electrons and holes, and on the other hand all the gas phase compounds measured during experimentation (meaning H₂O, CO₂, H₂, CO, CH₄, C₂H₆ and O₂) are detailed below. All selected reactions are those considered most probable and normalized with respect to the electron or hole.



Main half reactions of water splitting and CO₂ reduction



Main reverse half reactions





a. Hypotheses

Thus, rate equations involving electron consumption or generation can be written considering the following assumptions: i) surface reactions are the limiting step (compared to adsorption), ii) a Langmuir-Hinshelwood formalism is applied; except for photons because they are mostly supposed to be absorbed in the bulk of TiO₂ nanoparticles (Eley-Rideal formalism), and iii) stoichiometric coefficients are equal to the partial orders, as each reaction is bethought as elementary step; except for CO₂ and H₂O, for which a 0 order is assumed due to their concentration that not significantly change in and out of the reactor (large excess):

$$r_{e^-}^{hv}(h) = k_0 \cdot E(h) \cdot C_s^{irr}(h) \quad Eqn IV. 28$$

$$r_{e^-}^{H_2}(h) = k_1 \cdot n_{H^+}^{surf1} \cdot n_{e^-}^{surf1} = K_1 \cdot \theta_{H^+} \cdot \theta_{e^-} \cdot C_s^{irr}(h)^2 \quad Eqn IV. 29$$

$$r_{e^-}^{CO}(h) = k_1' \cdot n_{H^+}^{surf1} \cdot n_{e^-}^{surf1} \cdot n_{CO_2}^{surf0} = K_1' \cdot \theta_{H^+} \cdot \theta_{e^-} \cdot C_s^{irr}(h)^2 \quad Eqn IV. 30$$

$$r_{e^-}^{CH_4}(h) = k_1'' \cdot n_{H^+}^{surf1} \cdot n_{e^-}^{surf1} \cdot n_{CO_2}^{surf0} = K_1'' \cdot \theta_{H^+} \cdot \theta_{e^-} \cdot C_s^{irr}(h)^2 \quad Eqn IV. 31$$

$$r_{e^-}^{C_2H_6}(h) = k_1''' \cdot n_{H^+}^{surf1} \cdot n_{e^-}^{surf1} \cdot n_{CO_2}^{surf0} = K_1''' \cdot \theta_{H^+} \cdot \theta_{e^-} \cdot C_s^{irr}(h)^2 \quad Eqn IV. 32$$

$$r_{e^-}^{O_2}(h) = k_{-2} \cdot n_{H^+}^{surf1} \cdot n_{e^-}^{surf1} \cdot n_{O_2}^{surf1/4} = k_{-2} \cdot \theta_{H^+} \cdot \theta_{e^-} \cdot \theta_{O_2}^{1/4} \cdot C_s^{irr}(h)^{9/4} \quad Eqn IV. 33$$

Where, $r_{e^-}^{hv}(h)$ is the rate of electron generation from photon absorption by TiO₂. $r_{e^-}^{H_2}(h)$, $r_{e^-}^{CO}(h)$, $r_{e^-}^{CH_4}(h)$, $r_{e^-}^{C_2H_6}(h)$ are the rates of electrons consumption for H₂, CO, CH₄ and C₂H₆ production respectively. $r_{e^-}^{O_2}(h)$ is the rate of electrons consumption for O₂ back-reduction. All rates are expressed in (mol.h⁻¹) and reported as a function of h , being the photocatalytic bed thickness in (m). K_1 , K_1' , K_1'' and K_1''' are apparent kinetic constants in (mol⁻¹.h⁻¹). k_0 and k_{-2} are kinetic constants in (mol⁻¹.h⁻¹) and (mol^{-5/4}.h⁻¹) respectively. $n_X^{surf m}$ is the amount of X species onto the TiO₂ surface in (mol^m) at the partial order m, and θ_X is the surface coverage onto TiO₂ nanoparticles for each species X. $E(h)$ and $C_s^{irr}(h)$ are the molar quantities of absorbable photons and irradiated TiO₂ surface sites respectively. These two quantities are defined below.

b. Photon quantity description

$E(h)$ is defined as the molar quantity in (mol) of absorbable photons (315-400 nm, corresponding to a bandgap of 3.1 eV) within the bed thickness h , expressed as below considering light scattering is following Beer-Lambert law:

$$E(h) = E^0 \times \int_0^h e^{-\alpha \cdot z} \cdot dz = E^0 \times \frac{(1 - e^{-\alpha h})}{\alpha} \quad \text{Eqn IV. 34}$$

Where α is an attenuation coefficient related to the Beer-Lambert law in (m⁻¹), z is the position between 0 and h in the depth axis of photocatalyst bed, and E^0 is the molar quantity in absorbable photons (315-400 nm) per unit of depth without attenuation (mol.m⁻¹), and expressed as followed:

$$E^0 = \frac{PFD \cdot S^{irr}}{v} \quad \text{Eqn IV. 35}$$

Where PFD is the Photon Flux Density and set at 2.62.10⁻⁴ mol.s⁻¹.m⁻² for each experiment, S^{irr} is the geometric irradiated section of the material (m²), and v is the velocity of light in the photocatalytic bed in (m.s⁻¹) and expressed as followed:

$$v = \frac{\varepsilon \cdot c}{n_{air}} + \frac{(1 - \varepsilon) \cdot \%_{TiO_2}^m \cdot c}{n_{TiO_2} \cdot \left(\%_{TiO_2}^m + \%_{SiO_2}^m \times \frac{d_{TiO_2}}{d_{SiO_2}} \right)} + \frac{(1 - \varepsilon) \cdot \%_{SiO_2}^m \cdot c}{n_{SiO_2} \cdot \left(\%_{SiO_2}^m + \%_{TiO_2}^m \times \frac{d_{SiO_2}}{d_{TiO_2}} \right)}$$

Eqn IV. 36

Where ε is the void rate of the bed or monolith, c is the speed of light in vacuum (299 792 458 m.s⁻¹), n_{air} is the refractive index of air (1.0003), n_{TiO_2} is the refractive index of TiO₂ (2.61), n_{SiO_2} is the refractive index of SiO₂ (1.45), $\%_{TiO_2}^m$ is the mass percentage of TiO₂ in the sample, $\%_{SiO_2}^m$ is the mass percentage of SiO₂ in the sample, d_{TiO_2} is the density of TiO₂ (4.23 kg.L⁻¹), and d_{SiO_2} is the density of SiO₂ (2.65 kg.L⁻¹).

c. Active site description

$C_s^{irr}(h)$ is defined by the molar quantity of irradiated TiO₂ surface sites and can be expressed as followed:

$$C_s^{irr}(h) = C_s \times \int_0^h e^{-\alpha \cdot z} \cdot dz = C_s \times \frac{(1 - e^{-\alpha h})}{\alpha} \quad \text{Eqn IV. 37}$$

Where C_s is the molar quantity of TiO₂ surface sites per unit of depth (mol.m⁻¹), and expressed as followed:

$$C_s = \frac{d_{sample} \cdot S^{irr} \cdot 10^6 \cdot \%_{TiO_2}^m \cdot D_{TiO_2}}{M_{TiO_2}} \quad \text{Eqn IV. 38}$$

Where d_{sample} is the bulk density of powder bed or TiO₂@Si(HIPE) in (g.mL⁻¹), M_{TiO_2} is the TiO₂ molar mass (80 g.mol⁻¹), and D_{TiO_2} is the dispersion of tetrahedral TiO₂ cluster assuming a spherical model. D_{TiO_2} is expressed as followed:

$$D_{TiO_2} = \frac{6 \cdot V_{TiO_2}}{S_{TiO_2} \cdot d_{cryst}} \quad \text{Eqn IV. 39}$$

Where V_{TiO_2} is the volume of equivalent sphere for tetrahedral TiO₂ cluster (0.034205 nm³), and S_{TiO_2} is the section of equivalent sphere for tetrahedral TiO₂ cluster (0.127394 nm²). V_{TiO_2} and S_{TiO_2} are calculated using crystallographic data for anatase TiO₂ given in Material Studio 7.0 software by Accelrys[®]. d_{cryst} is the TiO₂ crystallite mean diameter in (nm), given by XRD analysis using Scherrer equation.

d. Global equation rate

Having defined each terms or equation rate, and considering electron as a very reactive intermediate, the steady state approximation is applied to this species, meaning:

$$\frac{d\theta_{e^-}}{dt} = 0 = r_{e^-}^{hv}(h) - r_{e^-}^{H_2}(h) - r_{e^-}^{CO}(h) - r_{e^-}^{CH_4}(h) - r_{e^-}^{C_2H_6}(h) - r_{e^-}^{O_2}(h) \quad \text{Eqn IV. 40}$$

Thus:

$$0 = k_0 \cdot E(h) \cdot C_s^{irr}(h) - K_1 \cdot \theta_{H^+} \cdot \theta_{e^-} \cdot C_s^{irr}(h)^2 - K_1' \cdot \theta_{H^+} \cdot \theta_{e^-} \cdot C_s^{irr}(h)^2 - K_1'' \cdot \theta_{H^+} \cdot \theta_{e^-} \cdot C_s^{irr}(h)^2 - K_1''' \cdot \theta_{H^+} \cdot \theta_{e^-} \cdot C_s^{irr}(h)^2 - k_{-2} \cdot \theta_{H^+} \cdot \theta_{e^-} \cdot \theta_{O_2}^{1/4} \cdot C_s^{irr}(h)^{9/4}$$

Eqn IV. 41

And:

$$\theta_{e^-} = \frac{k_0 \cdot E(h) \cdot C_s^{irr}(h)}{K_1 \cdot \theta_{H^+} \cdot C_s^{irr}(h)^2 + K_1' \cdot \theta_{H^+} \cdot C_s^{irr}(h)^2 + K_1'' \cdot \theta_{H^+} \cdot C_s^{irr}(h)^2 + K_1''' \cdot \theta_{H^+} \cdot C_s^{irr}(h)^2 + k_{-2} \cdot \theta_{H^+} \cdot \theta_{O_2}^{1/4} \cdot C_s^{irr}(h)^{9/4}}$$

Eqn IV. 42

The global reaction rate is defined as the sum of electron consumption for H₂, CO, CH₄ and C₂H₆ production (Eqn IV. 27). According to the equation Eqn IV. 24, the following equality can be written (Eqn IV. 28), and finally the global reaction rate $r_{e^-}(h)$ in (mol.h⁻¹) is expressed as in Eqn IV. 29:

$$r_{e^-}(h) = r_{e^-}^{H_2}(h) + r_{e^-}^{CO}(h) + r_{e^-}^{CH_4}(h) + r_{e^-}^{C_2H_6}(h) \quad \text{Eqn IV. 43}$$

$$r_{e^-}^{H_2}(h) + r_{e^-}^{CO}(h) + r_{e^-}^{CH_4}(h) + r_{e^-}^{C_2H_6}(h) = r_{e^-}^{hv}(h) - r_{e^-}^{O_2}(h) \quad \text{Eqn IV. 44}$$

$$r_{e^-}(h) = r_{e^-}^{hv}(h) - r_{e^-}^{O_2}(h) \quad \text{Eqn IV. 45}$$

Thus:

$$r_{e^-}(h) = k_0 \cdot E(h) \cdot C_s^{irr}(h) - k_{-2} \cdot \theta_{H^+} \cdot \theta_{e^-} \cdot \theta_{O_2}^{1/4} \cdot C_s^{irr}(h)^{9/4} \quad \text{Eqn IV. 46}$$

By introducing θ_{e^-} equality given by steady state approximation (Eqn IV. 26), the global reaction rate becomes:

$$r_{e-}(h) = k_0 \cdot E(h) \cdot C_s^{irr}(h) \times \frac{(K_1 + K_1' + K_1'' + K_1''')}{(K_1 + K_1' + K_1'' + K_1''') + k_{-2} \cdot \theta_{O_2}^{1/4} \cdot C_s^{irr}(h)^{1/4}} \quad \text{Eqn IV. 47}$$

This equation is then only depending on three parameters: $E(h)$ and $C_s^{irr}(h)$ which are measurable parameters depending on α , and θ_{O_2} for which it is much more difficult to find relevant description. Nevertheless, a strong dependence between θ_{O_2} and $E(h)$ is assumed as O₂ is the common co-product of all H⁺ and CO₂ photoreduction, then a n order relationship between θ_{O_2} and $E(h)$ is proposed as follow:

$$\theta_{O_2} = K_{O_2} \times \frac{E(h)^n}{C_s^{irr}(h)} \quad \text{Eqn IV. 48}$$

Where K_{O_2} is an apparent constant in (mol^{1/n-1}). This assumption allows us to simplify the global rate equation expressed in mol.h⁻¹ (Eqn IV. 33) or in mol.h⁻¹.m⁻² (Eqn IV. 34):

$$\bar{r}_{e-}(h) = k_0 \cdot E(h) \cdot C_s^{irr}(h) \times \frac{K}{K + E(h)^{n/4}} \quad \text{Eqn IV. 49}$$

$$\bar{r}_s^{e-}(h) = \frac{k_0 \cdot E(h) \cdot C_s^{irr}(h)}{S^{irr}} \times \frac{K}{K + E(h)^{n/4}} \quad \text{Eqn IV. 50}$$

With:

$$K = \frac{(K_1 + K_1' + K_1'' + K_1''')}{k_{-2} \cdot K_{O_2}^{1/4}} \quad \text{Eqn IV. 51}$$

This global reaction rate may then be fitted with the experimental r_{e-} in mol.h⁻¹.m⁻² defined in Chapter II (Eqn II. 15), and reminded here:

$$\bar{r}_s^{e-} = \frac{1}{T.O.S.} \int_0^{T.O.S.} \sum_i \frac{n_i^{e-} * [i](t) * Q_{tot}}{V_m^{25^\circ C} * S^{irr}} * 60 * dt$$

2) Confrontations with experimental results

The model was applied to four materials to assess their behavior towards CO₂ photoreduction (involving water as a sacrificial agent) through the adjustment parameters. First, the material physicochemical properties are briefly described. Then, the model fit parameter values are discussed. Finally, particular attention is paid to the K constant and the light attenuation coefficients.

a. Material description

The four materials compared are three Si(HIPE)s impregnated with TiO₂ following the steps described in Table A 36 (in annex) and labeled TiO₂@Si(HIPE) I, II, and III, and P25 TiO₂ powder. Diffuse reflectance UV/Visible spectroscopy, XRF and XRD data (and patterns) presented in annexed

Table A 37 (and Figure A 25) show that all materials provide bandgap energy of 3.1 eV. TiO₂ contents of TiO₂@Si(HIPE) I and II are higher than III's, due to TTIP concentration in impregnation solutions. Among TiO₂@Si(HIPE) materials, only TiO₂@Si(HIPE) II has an anatase/rutile mixed phase. The 2nd impregnation step was done with an aged solution. Peptized TiO₂ particles were impregnated, which limits Ti-O-Si bonds and favors anatase/anatase interfaces and then mixed phase crystallization. As well known, P25 TiO₂ powder contains 80% anatase and 20% rutile. Their respective crystallite sizes are also indicated. Despite the weak accuracy of the method generalization described in Chapter II §2.1)b, the crystallinity rates of the different materials are given in Table A 37 in annex. They will be used in the calculation of the TiO₂ specific surface area (SSA) contribution, described below in this paragraph.

The characteristic quantity values of the material morphology are summarized in Table A 38 and Table A 39, in annex. TiO₂@Si(HIPE)s provide similar porosity varying around 74.6%. P25 TiO₂ powder bed presents higher porosity of about 92%, which is calculated according to the equation Eqn I. 21, in Chapter I. Two bed densities are distinguished. The first one is extracted from mercury intrusion porosimetry and identical for the three TiO₂@Si(HIPE)s (0.12 g.mL⁻¹). Since the powder bed density cannot be measured by mercury intrusion porosimetry, a second bed density is used. This is calculated from the weighted mass and measured geometrical volume of materials. The four materials provide different median pore aperture, especially for P25 TiO₂ powder. This one corresponds to the intergrain mesoporosity and is calculated from cubic close packing approximation. Considering the set of four materials, BET surfaces and TiO₂ contents are strongly different. Then, TiO₂ SSA contribution quantity is introduced. This one corresponds to the ratio between specific surface area of TiO₂ and that of material, so S_{BET} extracted from nitrogen physisorption. To estimate the TiO₂ SSA, a spherical model is used by associating crystallite size (from XRD data) to the diameter of an equivalent particle, according to the following equation:

$$SSA = S_{part} * nb_{part} = 4\pi * r_{part}^2 * \frac{\%m_{TiO_2}}{\sum_i(\%nb_{part\ i} * m_{part\ i})} \quad Eqn\ IV.\ 52$$

Where S_{part} and nb_{part} are respectively the developed surface by a r_{part} -radius particle and the particle number. This one is estimated by the ratio of the TiO₂ mass percentage in the material and the sum of the number-weighted masses of r_i -radius particles. Thus, r_{part} is the average radius of r_i -radius particles.

Considering that only crystallized TiO₂ particles are active in photocatalysis, this TiO₂ SSA could be weighted by the crystallinity rate associated to the considered material.

b. Parameter fitting

Using least-squares method to fit k_0 , K , α and n , it was possible to best fit model and experimental data for the four samples by minimizing the sum of squared residuals:

$$S = \sum_{i=1}^n r_i^2 = \sum_{i=1}^n (y_i^{experimental} - y_i^{model})^2 \quad \text{Eqn IV. 53}$$

Experimental data are provided in the Table A 40, in annex. It has been found a unique n order value being 16, and other best fitted parameters are provided in the Table IV. 3.

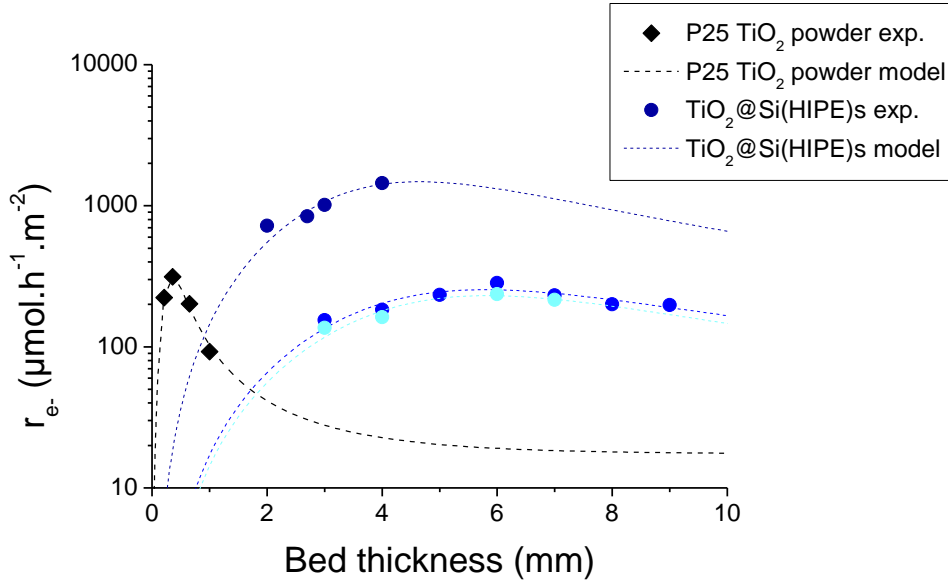


Figure IV. 14: Modeling “ r_e ” (average electron consumption rate normalized by time and surface) as compared to bed thickness for photocatalytic gas phase CO₂ reduction with H₂O as sacrificial agent. Experimental data are given as diamond for TiO₂ powder and circle of blue, from the darkest to the lightest for TiO₂@Si(HIPE)s I, II and III, respectively.

As illustrated in Figure IV. 14 activity plots as a function of bed thickness for TiO₂ powder bed and the set of prepared TiO₂@Si(HIPE)s I, II and III revealing diverse activities (partially related to crystallinities, TiO₂ loadings and particle sizes) were used to fit modeling to experimental data. By adjusting k_0 , K and α for each material, a very good agreement between model and experiments was achieved, highlighting the strong dependence of photocatalytic reaction rates with bed thickness, making relevant our previous hypothesis on deeper photon penetration within TiO₂@Si(HIPE)s and crucial role on oxidation back-reactions. k_0 value is found higher for TiO₂ P25, meaning that the well-known commercial powder is intrinsically more efficient to create reactive electron-hole pairs at TiO₂ surface slab by photon absorption than the *in-situ* generated TiO₂ phases during TiO₂@Si(HIPE) synthesis. Nevertheless, it is shown that HIPE carriers allow deeper light penetration (α is significantly reduced, Table IV. 3) then higher quantity of efficient photons compared to the whole bed volume (Figure A 26, in annex) and constant activity per gram as the mass of photocatalyst is increased until deeper catalytic bed (Figure A 27, in annex).

Table IV. 3: Model best parameters k_0 , K and α fitted with experimental data, taking into account a unique value for n of 16.

Materials	k_0 (mol ⁻¹ .h ⁻¹)	K (mol ⁴)	α (m ⁻¹)
P25 TiO ₂ powder	4.27E+16	5.62E-76	522
TiO ₂ @Si(HIPE)			
I	2.15E+15	9.35E-71	16
II	1.80E+14	3.34E-70	26
III	4.59E+14	2.77E-70	12

c. K coefficient correlation

Furthermore, because of TiO₂@Si(HIPE) use, a great decrease of reverse reaction by O₂ reduction and H₂ and/or C_xH_y oxidation is observed. This is probably linked with the TiO₂ active phase dilution within the macroporous silica matrix leading to lower surface coverage onto TiO₂ nanoparticles for O₂ species θ_{O_2} . Indeed, a trend is observed between the constant K derived from the kinetic model and the relative contribution of specific surface area for TiO₂ nanoparticles Figure IV. 15. The higher K , the more we can assume that the reverse reaction rate is low.

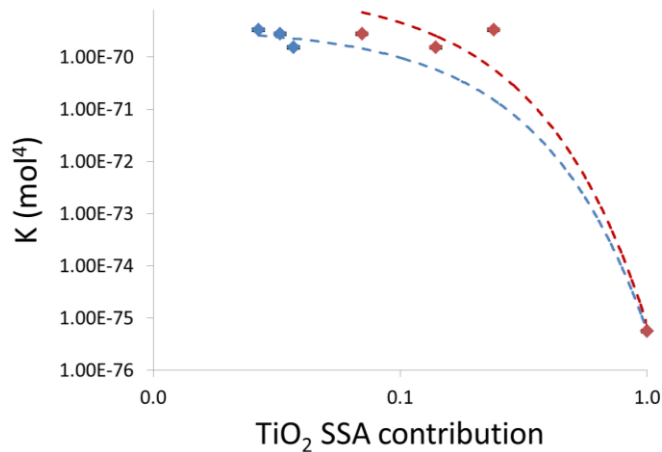


Figure IV. 15: Observed trend between constant K from kinetic model and the TiO₂ SSA contribution. This contribution is weighted by crystallinity rate (blue) or not (red). The contribution for P25 TiO₂ is 1, meaning that all the specific surface is due to TiO₂ nanoparticles. An exponential correlation is observed with correlation coefficients: respectively $R^2 = 0.9982$ for blue curve and $R^2 = 0.9664$ for red curve

This parameter appears to be related to the TiO₂ SSA contribution as shown in Figure IV. 15 (blue curve). This was obtained by applying a TiO₂ crystallinity rate to the three materials studied in the model. However, it was notified that due to a lack of rigor in the crystallinity rate calculation method presented in Chapter II, it was not applied to all studied materials. Thus, to extract the K value (in the following section) consistently, it was chosen to also plot the K values as a function of the TiO₂ SSA contribution without applying crystallinity rates (red curve). Note that the K error bars are unknown.

d. Light attenuation coefficient correlations

As highlighted above, light penetration seems to be described in the model by the light attenuation coefficient α . Besides, it has been seen in Chapter III that photon mean free path l_t and median pore aperture diameter are linked (Figure III. 38, §3). To correlate the model with these photonics experiments, light attenuation coefficient values obtained by the model are compared with photon mean free path values obtained by laser pulsed experiments and median pore aperture diameter values from mercury intrusion porosimetry (Figure IV. 16). Both present a strong correlation, meaning that photocatalyst performances are indeed highly predictable by knowing bed porosity and/or by measuring photon transport within material. TiO₂@Si(HIPE)s seem to act as very efficient “photonic sponge” thanks to its internal architecture. This term was earlier suggested by Carbonell *et al.*¹⁰ for hard templated porous thin films of TiO₂, demonstrating no thickness advantages according to attenuation coefficient α dependence revealed by this work.

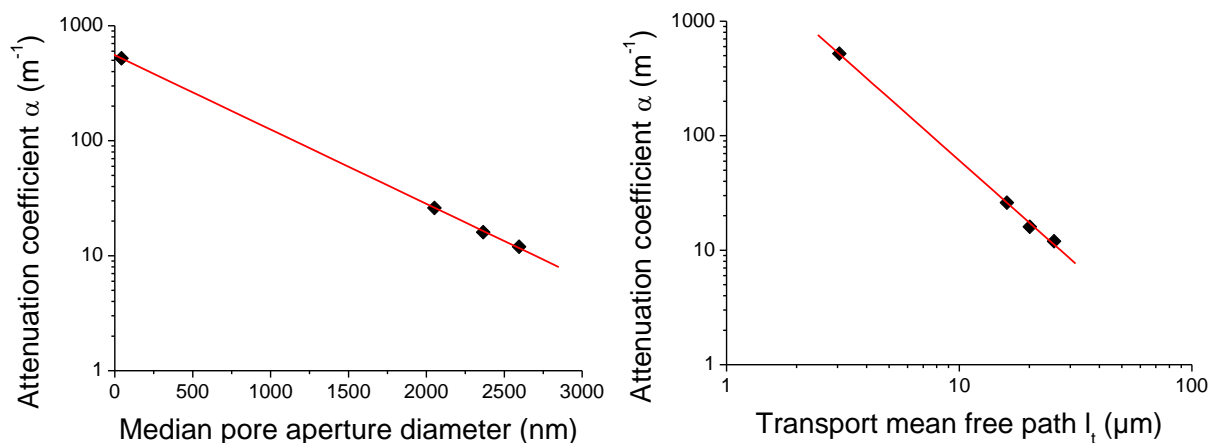


Figure IV. 16: Beer-Lambert attenuation coefficient α extracted from kinetic modeling reported as a function of **left**) median pore aperture diameter given by Hg porosimetry for TiO₂@Si(HIPE)s and by geometric model for TiO₂ powder and **right**) transport mean free paths l_t obtained from photonic characterization, with correlation coefficient: respectively $R^2 = 0,9988$ for a) and $R^2 = 0.9988$ for b).

3 TiO₂@Si(HIPE) behavior understanding

One objective of the model implementation is to extract quantities allowing the comparison of materials in a series (X-TiO₂@Si(HIPE), where X = ε, T, and v), even if they have different physicochemical characteristics. Indeed, the modifications applied to the material synthesis presented in Chapter III have shown that it is difficult to obtain a coherent series with a single varying parameter. In addition, the monolith shaping for the test, i. e. two flat and parallel surfaces, often implies a variation in thickness between two materials. And, it has been seen that photocatalytic performances do not change linearly over the entire thickness range.

Thus, to compare the material performances in the same series and between the series, the k_0 values were calculated from the equation established for the kinetic model (Eqn IV. 33). K values were estimated by the correlation between K and the TiO₂ specific surface area contribution (without crystallinity rates taken into account), and α values by the correlation between α and the median pore aperture diameter. It is recalled here that the k_0 represents the apparent kinetics of electron-hole pair generation, since it is difficult to discriminate effective charge carriers from all generated electron-hole pairs.

$$k_0 = \frac{\overline{r_{e^-}}(h)_{exp}}{E(h) \cdot C_s^{irr}(h)} \times \frac{K + E(h)^4}{K} \quad \text{Eqn IV. 54}$$

The objective of this section is to identify the influencing parameters and understand how they act on the electron-hole pair generation (k_0), with respect to the fluctuating parameters identified in Chapter 3: the TiO₂ specific surface area (TiO₂ SSA), the BET surface area (S_{BET}), as well as the median pore diameter. A spotlight will be placed on the origin of TiO₂ (synthesis methods: *P25*, *Ila*, *Ia* and *I*) regarding selectivities. The characteristic and calculated values are presented in the annexed Table A 41, Table A 42 and Table A 43, and the global graphs in Figure A 28, Figure A 29 and Figure A 30. Note that C_x-TiO₂@Si(HIPE) materials (described in Chapter III) provide identical k_0 values (5.40E+14, 5.03E+14, and 5.53E+14 mol⁻¹.h⁻¹ for C₉-, C₁₂-, and C₁₅-TiO₂@Si(HIPE) respectively), which is consistent with similar physicochemical characteristics.

The data are represented on the graphs with an estimated y-axis error bars of 40% (rounded up to the nearest ten) for k_0 , estimated from four reference tests and displayed in Table IV. 4. The x-axis error bar values are displayed as a function of fluctuating parameters in Table IV. 5. A precise uncertainty calculation would be a gain in the description of trends.

Table IV. 4: k_0 values of reference tests (tests used to build the control chart) and associated mean, standard deviation and mean-relative deviation values. Photocatalyst: 0.1 g of P25 TiO₂ powder.

	REF1	REF2	REF3	REF4
k_0 (mol ⁻¹ .g ⁻¹) (*E+42)	4.42	3.33	1.52	3.44
Mean (*E+42)		3.18		
Standard deviation (*E+42)		1.21		
Mean deviation (%)		38		

Table IV. 5: Estimated errors of fluctuating parameters

	Error (%)	Source
TiO ₂ content (%wt)	20	XRF measurement error
Crystallite size (nm)	10	XRD measurement error
TiO ₂ SSA (m ² .g ⁻¹)	40	$\frac{\Delta TiO_2 SSA}{TiO_2 SSA} = \frac{2\Delta r_{cryst}}{\bar{r}_{cryst}} + \frac{\Delta \%_{TiO_2}^m}{\%_{TiO_2}^m}$
S _{BET} (m ² .g ⁻¹)	10	N ₂ physisorption measurement error + mean deviation from TiO ₂ @Si(HIPE) repeatability
TiO ₂ SSA contribution	50	$\frac{\Delta TiO_2 SSA cont}{TiO_2 SSA cont} = \frac{\Delta TiO_2 SSA}{TiO_2 SSA} + \frac{\Delta S_{BET}}{S_{BET}}$
Median pore size diameter (nm)	10	mean deviation from TiO ₂ @Si(HIPE) repeatability rounded up to the nearest ten

1) TiO₂ specific surface area

The ε-, T-, and v-TiO₂@Si(HIPE) series showed variations in physicochemical characteristics such as crystallite size and TiO₂ content. The influence of these two parameters on the electron-hole pair generation kinetics will be discussed first. However, since they are not independent of each other, the TiO₂ specific surface area has been introduced to take these two parameters into account, and its influence will be studied in a second step.

Series are presented independently in Figure A 28, in annex. By pooling the three series, it appears in Figure IV. 17 (left) that the kinetics of electron-hole pair generation seems to decrease exponentially as a function of TiO₂ content. This trend can be related to the fact that the higher the TiO₂ content, the greater the defect number. Since defects are privileged sites for charge recombination, they may reduce the photogenerated charges quantity. Similar considerations can be expressed about crystallite size Figure IV. 17 (right). Actually, the smaller the crystallites are, the more defects there are¹¹, and therefore

the more potential charge recombination sites. Figure IV. 18 groups these considerations together through the TiO₂ specific surface area influence. The translation of the displayed decrease is that the kinetics of electron-hole pair generation is favored by a small number of large crystallites and disadvantaged by a multitude of small crystallites. In other words, the lower the defect density, the higher the quantity of photogenerated charges.

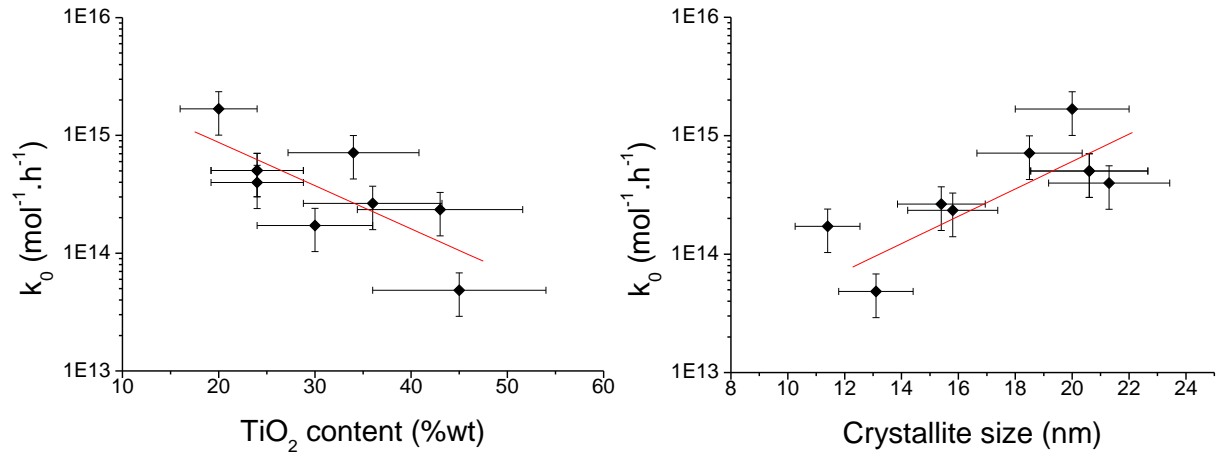


Figure IV. 17: TiO₂ content (**left**) and anatase crystallite size (**right**) influence over electron-hole pair generation kinetics evolution

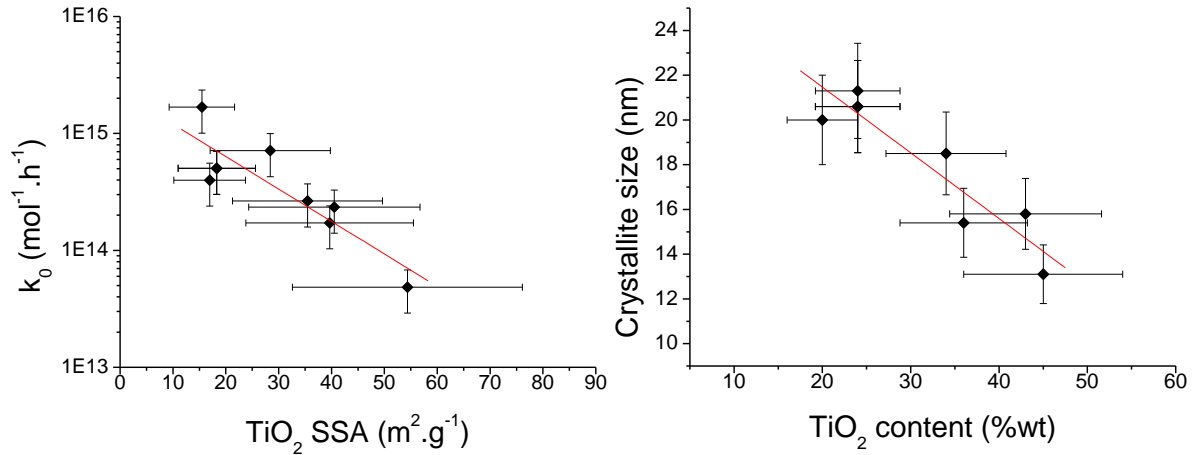


Figure IV. 18: **left**) TiO₂ specific surface area influence over electron-hole pair generation kinetics evolution and **right**) crystallite size evolution as function of TiO₂ content (one aberrant point has been removed)

2) TiO₂ SSA contribution

The T-TiO₂@Si(HIPE) series is not discussed here because the S_{BET} variation is implied by removal of silanols constituting the silica wall. In other words, this variation also includes changes in surface chemistry. Indeed, the higher the calcination temperature, the less surface silanols there are¹². Moreover, during TiO₂ impregnation, the bonds between TiO₂ and silica are also modified. This point is a limitation of the model due to the surface chemistry (silanols density), or the intimacy between TiO₂ and silica that

are not taken into account. Furthermore, when calculating the k_0 values, the $\frac{K+E(h)^4}{K}$ term (Eqn IV. 38) is representative of the back reactions impact over photocatalytic performances. It has been seen in the model confrontations with the experimental results that these reverse reactions have a low impact for less than 4 mm-thick monolith. This is verified by a $\frac{K+E(h)^4}{K}$ term value close to 1. All the data processed, the tables given in the annex, confirmed this point, except for the 850-TiO₂@Si(HIPE) sample. It provides a value of 1.5, for a thickness of 3.25 mm. This difference ($1.5 \neq 1$) is in line with the surface chemistry influence. A potential explanation is related to the oxygen surface coverage. Indeed, when an oxygen molecule is formed and still bridged at the surface, it can desorb, migrate and adsorb further along the catalytic bed; or only migrate on the surface. The hydroxyl groups absence on the silica surface can limit the O₂ migration out of TiO₂, and thus increase the O₂ surface coverage onto TiO₂ surface. In this sense, the back reactions would then be favorable. Another potential explanation is related to the interaction of the H₂O molecules with the active sites onto TiO₂ surface which could be either facilitated by a high concentration of surface OH groups¹³, or limited in their absence. Thus, H₂O reactant becomes a limiting one.

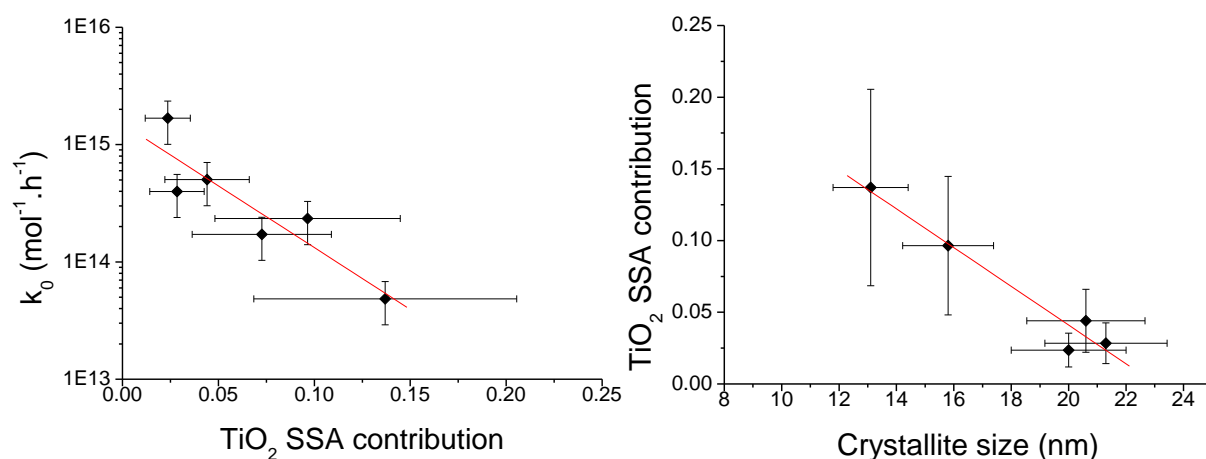


Figure IV. 19: **left**) TiO_2 SSA contribution influence over electron-hole pair generation kinetics evolution and **right**) TiO_2 SSA contribution evolution as function of crystallite size (one aberrant point has been removed)

In addition, the S_{BET} surface analyzed by nitrogen adsorption does not discriminate between the surface developed by silica and that developed by TiO₂. To take into account this BET surface it was decided to introduce the descriptor: TiO₂ Specific Surface Area (SSA) contribution. As reminder, this is defined as the ratio between the TiO₂ specific surface area and the BET surface area. This quantity reflects the distribution/dilution of TiO₂ within Si(HIPE): a value of 1 meaning that all the specific surface is due to TiO₂ nanoparticle. Figure IV. 19 left) depicts the trend observed for TiO₂@Si(HIPE). Against all expectations, the electron-hole pair generation kinetics decreases with the dispersion of TiO₂. From Figure IV. 19 right), it appears that in these material series, the TiO_2 SSA contribution decreases

with the crystallite size. This consideration seems to confirm that crystallite size is a highly influential parameter: large crystallite sizes favor electron-hole pair generation more than TiO₂ dispersion.

3) Median pore diameter

The parameters having an impact on k_0 are the descriptors relating to the TiO₂ structural characteristics, as confirmed by the TiO₂ SSA contribution influence. To determine any influence of the median pore diameter, it is therefore necessary to have a coherent series whose TiO₂ structure (crystallite size, TiO₂ content, crystalline phase...) is identical for each material. The materials synthesized during the project do not have these characteristics. Thus, it is not possible to discuss here the influence of median pore diameter over the charge carriers photogeneration. However, this point is a way of improvement to be considered in understanding the phenomena involved in TiO₂@Si(HIPE) monoliths.

4) Synthesized and commercial TiO₂: influence of TiO₂ origin

Due to mismatch between the densities (obtained by weighing) of TiO₂(*Ia*)@Si(HIPE) and TiO₂(*I*)@Si(HIPE), the TiO₂(*M*)@Si(HIPE) series could not be studied via the calculation of k_0 (structural characterizations are displayed in Table III. 3, Chapter III). It is therefore important to highlight here the differences in selectivity according to the impregnation methods. It has been seen that in terms of photocatalytic intrinsic performance P25 TiO₂ is better than most synthesized materials. However, with regard to selectivity, it favors products resulting from reactions involving two electrons. As shown in Figure IV. 20, TiO₂ from the precursor hydrolysis-condensation significantly limits the hydrogen and carbon monoxide production, in favor of methane and ethane. To go further, for the TiO₂(*I*)@Si(HIPE) sample, products resulting from so-called multi(>2)-electronic reactions represent more than 90% of the products. Besides alkanes, especially C₂₊, deliver much more energy liberated by combustion than hydrogen and CO (the High Calorific Value (HCV) of hydrogen is of 286 kJ.mol⁻¹, HCV(CO) = 283 kJ.mol⁻¹, HCV(CH₄) = 889 kJ.mol⁻¹, and HCV(C₂H₆) = 1 560 kJ.mol⁻¹).

The promotion of multi-electronic reactions implies a higher electron density on active sites. This can be induced by a better charge carrier separation. Indeed, the P25 excellent photocatalytic activity is particularly associated with the anatase/rutile mixed phase¹⁴. The authors attribute to the rutile an antenna role due to its lower bandgap energy, and an aid in the charge carrier separation by electron transfer. They highlight the importance of the intimate contact between rutile and anatase to enhancing the catalytic activity. TiO₂(*Ia*)@Si(HIPE) and TiO₂(*I*)@Si(HIPE) have an anatase/rutile mixed phase. Their crystalline structure varies due to the rutile crystallite size (13 nm and 8 nm, respectively). TiO₂(*I*)@Si(HIPE) shows an average electron consumption rate higher than TiO₂(*Ia*)@Si(HIPE) (682 μmol.h⁻¹.m⁻² and 163 μmol.h⁻¹.m⁻², respectively), and a higher orientation towards methane and ethane (Figure IV. 21). It would therefore seem that a size effect of rutile crystallites (for an equivalent TiO₂ content) is significant¹⁵. However, the TiO₂(*Ia*)@Si(HIPE) sample

only shows the anatase phase, and still shows a preferential orientation towards products resulting from multi(>2)-electronic reactions. It therefore appears that another consideration must be taken into account, which may be linked to the crystallite orientations^{16,17}. Further study on crystallite arrangement on the particle surface would therefore be of interest in our conditions.

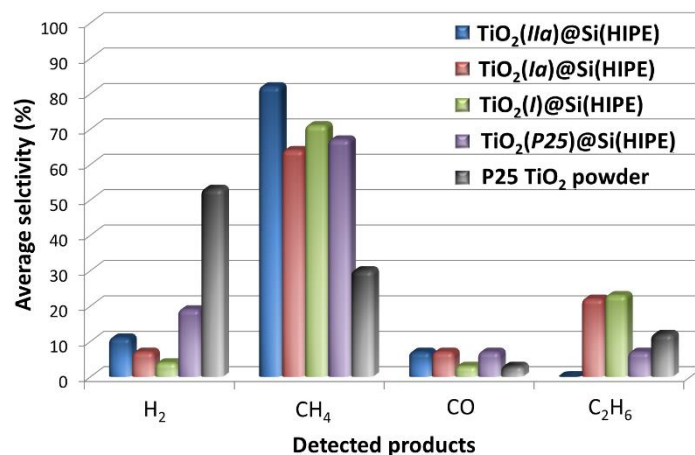


Figure IV. 20: Average selectivities towards each product for materials obtained by the four impregnation methods, and for P25 TiO₂ powder

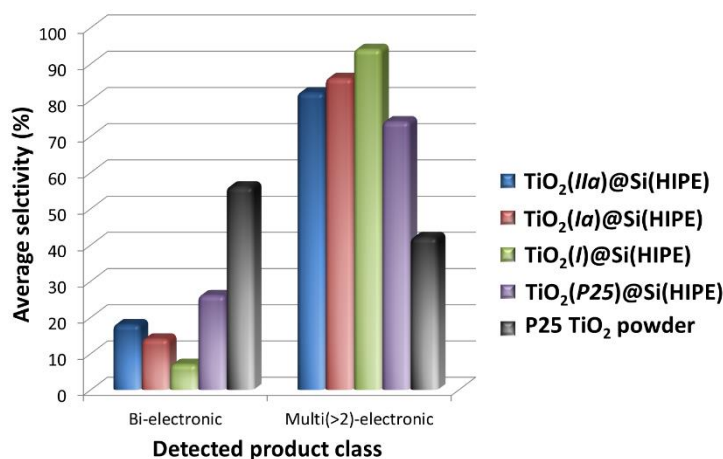


Figure IV. 21: Average selectivities towards products grouped by reaction class from which they are derived for materials obtained by the four impregnation methods and for P25 TiO₂ powder

4 Conclusion

Through the study of parameters influencing the commercial TiO₂ powder (P25 TiO₂) photocatalytic performance, it was possible to highlight the key behaviours of materials about CO₂ photoreduction. The photon supply is the limiting step in our conditions. In addition, dilution within a silica matrix limits the back-reaction impact. Besides, the oxygen presence drastically reduces the TiO₂ performance, and directs reactions towards the CO and CO₂ production. Furthermore, blank photocatalytic tests and

additional analyses (¹³C NMR and TG/MS) confirmed that hydrocarbon production was indeed derived from the CO₂ photoreduction process involving water.

To compare the materials tested at different thicknesses, a kinetic model based on Langmuir-Hinshelwood and Eley-Rideal formalisms was implemented. It considers photons as reactants in the same way as CO₂ and H₂O. By fitting the model with four materials studied as a function of the catalytic bed thickness, the descriptors k_0 , K , and α could be evaluated. The constant k_0 describes the photogeneration rate of electron-hole pairs and has shown that TiO₂ P25 has the best intrinsic photocatalytic performance. The constant K describes the reverse reaction impact on performance. The higher K , the more we can assume that the reverse reaction rate is low. Besides, this constant seems to be related in particular to the TiO₂ specific surface area contribution. Then, the attenuation coefficient α is significantly reduced using porous monoliths and seems to be related in particular to the median pore aperture diameters and the transport mean free path of photons.

Using the correlations established during model implementation, the k_0 constants were calculated for each material of the X-TiO₂@Si(HIPE) series. Their study showed that the photogeneration rate of electron-hole pairs is higher when there are few large crystallites than when there are many small ones. This behavior could be related to defect density. In addition, this rate counter-intuitively decreases as the TiO₂ SSA contribution increases. In addition, the TiO₂ impregnation method in Si(HIPE)s strongly influences selectivity. Indeed, when TiO₂ particles are derived from the TiO₂ precursor impregnation, they preferentially direct the products towards methane and ethane. The TiO₂/TiO₂ and TiO₂/SiO₂ contact intimacy would deserve to be studied.

Synthesized materials have several advantages. Among these, the soft chemistry use can be mentioned, implying low energy expenditure during synthesis. In addition, the porous silica structure with good mechanical resistance makes the materials manageable (compared to a more or less powdery material) and also the active phase impregnation. It should be noted that the impregnation was only carried out with titanium oxide during the project. However, this preparation method can be generalized to any active phase capable of being added as colloidal suspension.

To go further, material regeneration tests have been carried out as shown in Table IV. 6. The first test corresponds to a photocatalytic test performed on the material after its synthesis. Then, the regeneration conditions are applied to the material, and it is tested again under the same conditions as the first test. It appears that a venting or argon flush over a few hours/days did not allow to recover the photocatalytic performances achieved during the first test. However, a heat treatment at a temperature lower than the calcination temperature applied for the TiO₂ crystallization showed that the material was performing closer to its initial level than other regeneration conditions. A more precise study of the optimal regeneration conditions is to be expected, as well as an evaluation after several regeneration cycles.

Table IV. 6: Regeneration tests applied on a TiO₂(I)@Si(HIPE) sample and associated photocatalytic performances for 15.43h-irradiation time

	Test n°1	Test n°2	Test n°3	Test n°4	Test n°5
		After test n°1	After test n°2	After test n°3	After test n°4
Regeneration conditions	-	1h Ar flush	1h open-air	2 days open-air	350°C, 2h calcination
r_e (μmol.h⁻¹.m⁻²)	894	390	387	285	650

Among the various materials synthesized, one material has shown extremely interesting performance levels towards the CO₂ photoreduction, whose physicochemical characteristics are presented in the annexed Table A 37. Indeed, the maximum average electron consumption rate (normalized per unit of irradiated surface area) was obtained for a 4 mm thickness, and reaches a value 5 times higher than that obtained by the optimal P25 TiO₂ powder bed (Figure IV. 22). Moreover, the selectivities of this material do not derogate from the rule expressed above, which implies a preferential formation of hydrocarbons with a high energy value: methane and ethane (Figure IV. 23).

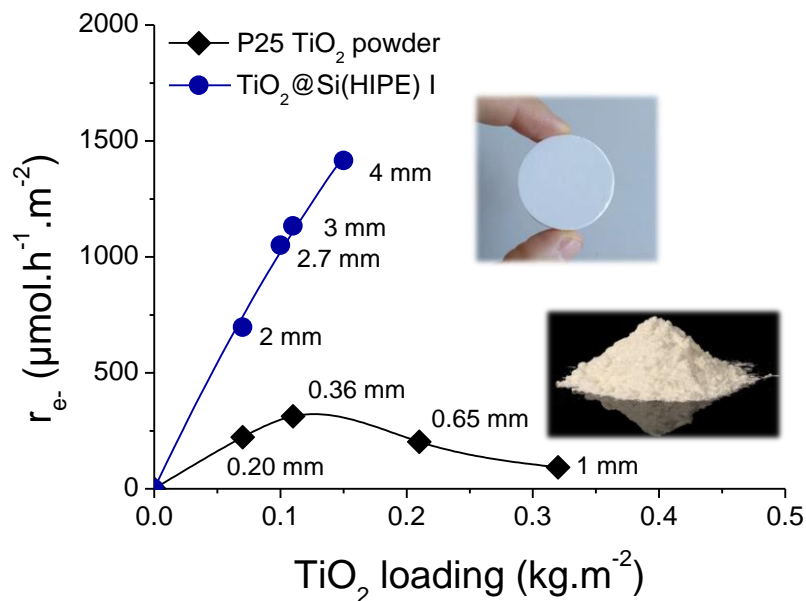


Figure IV. 22: Photocatalytic performance comparison of TiO₂@Si(HIPE)I and P25 TiO₂ powder, as function of TiO₂ loading

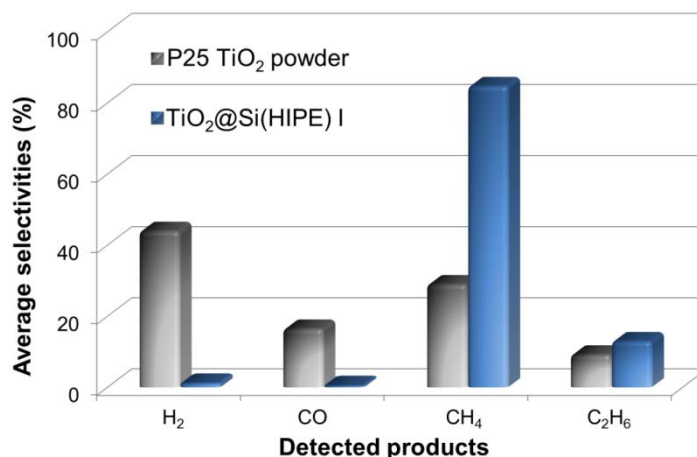


Figure IV. 23: Selectivities of TiO₂@Si(HIPE) I and P25 TiO₂ powder, at their respective optimal thickness

Despite the strengths highlighted, there are still areas for improvement. First, the material synthesis takes about two months, mainly due to the drying time. Further development work must therefore be carried out using faster drying techniques that maintain the material integrity, such as supercritical drying. Secondly, the material batches showed differences in terms of physicochemical characteristics that should be smoothed. To this end, an automated synthesis could make it possible to eliminate the operator-dependent character induced by manual emulsification. During the project, an assembly including the use of mechanical agitation *via* a blade and the dodecane incorporation using a syringe pump was used. A more detailed study of the blade design and rotational speed should be considered to make this process viable. In addition, the anatase/rutile ratio influence could not be analyzed due to the lack of a coherent series. To rigorously compare anatase/rutile proportions, those must be the only parameter to vary. Synthesized materials with varying anatase/rutile proportions exhibited either different crystallite sizes or different shaping (powder vs. monolith). A synthesis method controlling both phase proportions and crystallite sizes would then allow this parameter to be studied. Furthermore, the kinetic model requires testing on a larger number of materials, with different behaviors, to refine the descriptors. In addition, mechanistic considerations are to be considered to better understand and therefore predict via the model the physicochemical characteristics necessary for selectivity in high value-added hydrocarbons.

5 References

- (1) Herrmann, J.-M. Heterogeneous Photocatalysis: Fundamentals and Application to the Removal of Various Types of Aqueous Pollutants. *Catalysis Today* **1999**, *53*, 115–129.
- (2) Epling, W. S.; Peden, C. H. F.; Henderson, M. A.; Diebold, U. Evidence for Oxygen Adatoms on TiO₂(110) Resulting from O₂ Dissociation at Vacancy Sites. *Surface Science* **1998**, *412–413*, 333–343.

- (3) Fujishima, A.; Zhang, X.; Tryk, D. TiO₂ Photocatalysis and Related Surface Phenomena. *Surface Science Reports* **2008**, *63*, 515–582.
- (4) Ji, Y.; Luo, Y. Theoretical Study on the Mechanism of Photoreduction of CO₂ to CH₄ on the Anatase TiO₂(101) Surface. *ACS Catal.* **2016**, *6* (3), 2018–2025.
- (5) Ji, Y.; Luo, Y. New Mechanism for Photocatalytic Reduction of CO₂ on the Anatase TiO₂(101) Surface: The Essential Role of Oxygen Vacancy. *J. Am. Chem. Soc.* **2016**, *138* (49), 15896–15902.
- (6) Li, K.; Peng, B.; Peng, T. Recent Advances in Heterogeneous Photocatalytic CO₂ Conversion to Solar Fuels. *ACS Catal.* **2016**, *6* (11), 7485–7527.
- (7) Göpel, W.; Rocker, G.; Feierabend, R. Intrinsic Defects of TiO₂(110): Interaction with Chemisorbed O₂, H₂, CO, and CO₂. *Physical Review B* **1983**, *28*, 3427–3438.
- (8) Henderson, M. A. Evidence for Bicarbonate Formation on Vacuum Annealed TiO₂(110) Resulting from a Precursor-Mediated Interaction between CO₂ and H₂O. *Surface Science* **1998**, *400* (1), 203–219.
- (9) Civiš, S.; Ferus, M.; Zukalová, M.; Zukal, A.; Kavan, L.; Jordan, K. D.; Sorescu, D. C. Oxygen Atom Exchange between Gaseous CO₂ and TiO₂ Nanoclusters. *J. Phys. Chem. C* **2015**, *119* (7), 3605–3612.
- (10) Carbonell, E.; Ramiro-Manzano, F.; Rodríguez, I.; Corma, A.; Meseguer, F.; García, H. Enhancement of TiO₂ Photocatalytic Activity by Structuring the Photocatalyst Film as Photonic Sponge. *Photochem. Photobiol. Sci.* **2008**, *7* (8), 931–935.
- (11) Diebold, U. The Surface Science of Titanium Dioxide. *Surface Science Reports* **2003**, *48* (5), 53–229.
- (12) Zhuravlev, L. T. The Surface Chemistry of Amorphous Silica. Zhuravlev Model. *Colloids and Surfaces A: Physicochemical and Engineering Aspects* **2000**, *173* (1–3), 1–38.
- (13) Kou, J.; Lu, C.; Wang, J.; Chen, Y.; Xu, Z.; Varma, R. S. Selectivity Enhancement in Heterogeneous Photocatalytic Transformations. *Chem. Rev.* **2017**, *117* (3), 1445–1514.
- (14) Hurum, D. C.; Agrios, A. G.; Gray, K. A.; Rajh, T.; Thurnauer, M. C. Explaining the Enhanced Photocatalytic Activity of Degussa P25 Mixed-Phase TiO₂ Using EPR. *J. Phys. Chem. B* **2003**, *107* (19), 4545–4549.
- (15) Thompson, W. A.; Perier, C.; Maroto-Valer, M. M. Systematic Study of Sol-Gel Parameters on TiO₂ Coating for CO₂ Photoreduction. *Applied Catalysis B: Environmental* **2018**, *238*, 136–146.
- (16) Cao, Y.; Li, Q.; Li, C.; Li, J.; Yang, J. Surface Heterojunction between (001) and (101) Facets of Ultrafine Anatase TiO₂ Nanocrystals for Highly Efficient Photoreduction CO₂ to CH₄. *Applied Catalysis B: Environmental* **2016**, *198*, 378–388.
- (17) Chang, X.; Wang, T.; Gong, J. CO₂ Photo-Reduction: Insights into CO₂ Activation and Reaction on Surfaces of Photocatalysts. *Energy Environ. Sci.* **2016**, *9* (7), 2177–2196.

Conclusion and *perspectives*

The subject of this thesis work was the photocatalytic conversion of carbon dioxide involving water. Since solar energy is an abundant source of energy on our time scale, solar-driven-fuel-production by exploiting anthropogenic CO₂ emissions appears to be a solution with great potential, which can simultaneously contribute to solve the climate change issues and produce large quantities of carbon-neutral energy.

According to the literature review, CO₂ has been successfully converted using sunlight into high value-added hydrocarbons. However, reaction rates and selectivity in desired products such as methane and C₂₊ are still too low to consider industrial applications. Main drawbacks are arising from the photocatalytic process itself, *i.e.* light trapping and harvesting, charge separation-recombination and transportation, surface and backward reactions, and they need to be optimized. Main research topics deal with: the modification of the intrinsic properties of semiconductors, the discovery of new architectures or composite structures developing optimized heterojunctions and the use of new molecular complexes as dyes for sensitized solar cells and photocatalysts. To develop effective photo-induced processes, equal importance must be given to the photocatalysis fundamental processes, photoreactor design and catalyst synthesis. It is therefore necessary to increase the surface/volume ratio of the photo-active materials in use, addressing thus a severe foot-print penalty.

In this project, the synthesis of self-standing solid foams bearing a hierarchically organized porosity and embedding TiO₂ particles (TiO₂@Si(HIPE)s) has been proposed to achieve a three-dimensional CO₂ photoconversion.

The physicochemical characteristics of these materials have shown that they provided a high porosity (about 90%) structured at all length scales. The major part was constituted by micro and macroporosity. This high porosity had several advantages: i) the improved convection of the liquids allowed homogeneous impregnation throughout the entire volume of the monoliths (evidenced by Electron Probe Micro Analysis), ii) the low pressure drop made it possible to perform the tests in continuous flow mode, and iii) the photon penetration was increased by an order of magnitude compared to a conventional shaping (powder bed). Four impregnation methods were performed, showing variations in the distribution and morphology of TiO₂ particles. The two-step impregnation revealed the formation of Ti-O-Si bonds blocking TiO₂ in amorphous form in the vicinity and inducing a pseudo-epitaxial phenomenon of crystallization. A mixed anatase/rutile phase with a heat treatment of 450°C was obtained by the one-step impregnation methods. Monolithic material series with modulable silica matrix physicochemical characteristics have been synthesized by modifying parameters such as oil volume fraction, calcination temperature and rotational speed during emulsification. Despite the same impregnation method for all materials in these series, the TiO₂ content and its crystalline structure fluctuated. Thus, to compare the photocatalytic performances of these materials while taking into account their physicochemical properties, a kinetic model based on a mixed Langmuir-Hinshelwood and Eley-Rideal formalism was implemented. To identify the descriptors, an understanding of the

parameters/phenomena influencing photocatalytic performance was necessary. Thus, it has been shown that i) the TiO₂ activity was highly dependent on photon supply, ii) the TiO₂ particles dilution within a silica matrix (structured or unstructured) limited reverse reactions and iii) the oxygen presence promoted reverse reactions and directed selectivity towards CO production. In addition, the TiO₂@Si(HIPE)s use has shown similar behavior to TiO₂ P25 powder beds but more broadly over the catalytic bed thickness range. The maximum photocatalytic performance for TiO₂@Si(HIPE) has been obtained for thicknesses in the range of 5-6 mm (and 360 μm for the powder bed). It has been shown that the reactant residence time played a minor role. To describe the monoliths behavior, parameters k_0 (electron-hole pair formation kinetics constant), K (apparent kinetics constant related to reverse reactions) and α (light attenuation coefficient) were therefore implemented in the model. Using the correlations established during model implementation for K and α , the k_0 constants were calculated for each material of the TiO₂@Si(HIPE) series. Their study highlighted that defect density and, TiO₂/TiO₂ and TiO₂/SiO₂ contact intimacy could play a significant role over the photocatalytic performances. Finally, among the various materials synthesized, a TiO₂@Si(HIPE) has shown performance levels such that a reduction in the material footprint by a factor of 5 would be possible compared to a powder bed.

During the CO₂ photoreduction project, additional air purification tests were carried out at IPREM-Pau by Mickael Le Behec and Sylvie Lacombe. Adsorption and mineralization measurements on acetone and toluene were very promising. On the one hand the adsorption values of acetone and toluene showed that TiO₂@Si(HIPE)s can reach significantly higher levels even compared to materials known to be very capacitive such as activated carbons or Quartzel. On the other hand, the mineralization rates of toluene and acetone were at least as good as those obtained by the known state-of-the-art implementations. In addition, TiO₂@Si(HIPE) allowed very stable photocatalytic activities to be obtained, unlike the use of Quartzel. With Quartzel material, there was a rapid material deactivation, which was characterized by a decrease in carbon dioxide production and a significant yellowing of the material during the irradiation test phase.

Nevertheless, different work perspectives should be explored. In the continuity of an improvement in photon penetration and therefore in the realization of photocatalytic processes in volume, it can be considered to play on the Mie diffusion. Indeed, anisotropic diffraction induced by scattering objects intensifies the photon propagation in the incident direction. The characteristic size of these scatterers must be of the same order of magnitude as the incident beam wavelength. In order to synthesize such objects, the hard template synthesize is an integrative chemistry tool which can be used. Indeed, by synthesizing latex beads of tailored and monodisperse size, they can be incorporated into the Si(HIPE) starting sol. After sintering, the TiO₂@Si(HIPE) silica walls would then have pores of about 380 nm, monodisperse in size, acting as scatterers and directing UV photons in depth. According to this thesis work, the light attenuation coefficient α decreases with the median pore aperture diameter. Thus, to go further in the material structuring, the increase in pore size would then be beneficial to photon

penetration. For this purpose, a tailored decrease in the rotation speed during emulsification and/or a reduction in the oil volume fraction would increase the oil droplet size and therefore the pore size after sintering. In addition, it has been seen in the literature that a heterojunction between two semiconductors improves photon absorption and charge carrier separation (e. g. the heterojunction between anatase and rutile). It can then be imagined to chemically modify the silica support to make it a semiconductor that will then be in contact with the impregnated TiO_2 while preserving the hierarchical porosity. For this purpose, a transition metal salt such as FeCl_2 or CuCl_2 would be incorporated into the starting Si(HIPE) sol to form a colored meta-silicate after heat treatment, which therefore absorbs visible light. At the application level, if these materials have proven their worth for air photopurification, good performance can also be expected for water photopurification.



université
de BORDEAUX



Annexes

Table A 1: CO₂ photoreduction systems containing TiO₂ or TiO₂-based photocatalysts

light source	photocatalyst	co-catalyst	experimental condition	main products and highest yield
1000 W Xe-lamp (AM 1.5)	TiO ₂ (P25)	Au/Cu (2:1)	1.25 cm ² catalyst film (0.6 mg), CO ₂ and H ₂ O vapor	286 (H ₂)/2200 ± 300 (CH ₄) μmol g ⁻¹ h ⁻¹
300 W Xe-lamp (λ = 420–780 nm)	anatase TiO ₂	Pt ⁰ /Pt ²⁺	100 mg of catalyst, CO ₂ bubbled 60 min	~22.3 (H ₂)/~0.3 (CO)/ 1.98 (CH ₄) μmol h ⁻¹
0.3 mW cm ⁻² LED (λ = 365 nm)	brookite TiO ₂ nanorod	0.05 wt % Au or 0.4 wt %Ag	5 mg of catalyst, 5 mL of CO ₂ -saturated 0.2 M KHCO ₃	~0.50 μmol CH ₃ OH (Au); >2.50 μmol CH ₃ OH (Ag)
300 W Hg-lamp	VN-co-doped anatase TiO ₂ nanotube arrays		4 cm ² nanotube film in CO ₂ -saturated 0.1 M KHCO ₃	64.5 (CH ₄) μmol h ⁻¹ cm ⁻²
300 W Hg-lamp	anatase TiO ₂ nanotubes	Pt and 0.1 mol % MgO	8 cm ² nanotubes film in CO ₂ saturated with 0.1 M KHCO ₃	100.2 (CH ₄)/10.4 (CO) ppm h ⁻¹ cm ⁻²
300 W Xe-lamp	mesoporous anatase TiO ₂ nanofibers		100 mg of catalyst, CO ₂ and H ₂ O vapor	1.95 (CH ₄) μmol h ⁻¹
300 W Xe-lamp	anatase TiO ₂ nanosheet		40 mg of catalyst, CO ₂ and H ₂ O vapor	0.23 (CH ₄) ppm h ⁻¹
40 W Hg-lamp (λ = 254 nm)	anatase TiO ₂ hierarchical microspheres	0.6 wt %Pt	200 mg of catalyst, 100 μL of H ₂ O and 50 ps CO ₂	~0.74 (CH ₄)/~3.70 (CO)/~44.6 (H ₂) μmol h ⁻¹
300 W Xe-lamp	ordered mesoporous TiO ₂		100 mg of catalyst, CO ₂ and H ₂ O vapor	0.019 (CH ₄)/0.014 (CO) μmol h ⁻¹
300 W Xe-lamp	3.0 wt % NaOH modified anatase TiO ₂		80 mg of catalyst, CO ₂ and H ₂ O vapor	~0.88 (CH ₄)/~0.8 (H ₂) μmol h ⁻¹
halogen lamp	TiO ₂ /Cu(II) phthalocyanine		50 mg of catalyst in water (pH 3.00), CO ₂ bubbled 30 min	10.42 (HCOOH) μmol in 8 h
300 W Xe-lamp	3D hierarchically porous TiO ₂	1.7 wt %Cu, 0.9 wt %Pt	100 mg of catalyst, CO ₂ and H ₂ O vapor	1.20 (CH ₄) μmol h ⁻¹
20 W LED (λ > 400 nm)	TiO ₂ @SiO ₂ @Fe ₃ O ₄ [Ru (bpy) ₃ phenene-NH ₂](PF ₆) ₂ CoPc		100 mg of catalyst in H ₂ O/TEA (4:1), CO ₂ bubbled 30 min	257.01 (CH ₃ OH) μmol in 24 h
300 W Xe-lamp	anatase TiO ₂	1.0 wt %Pt	100 mg of catalyst, CO ₂ and H ₂ O vapor	0.12 (CH ₄) (Pt at (010) facet); 0.26 (CH ₄) (Pt at (001) facet) μmol h ⁻¹
300 W Xe-lamp	anatase TiO ₂ with exposed special facets		100 mg of catalyst, CO ₂ and H ₂ O vapor	0.17 (CH ₄) (010); 0.07 (CH ₄) (101); 0.02 (CH ₄) (001) μmol h ⁻¹
300 W Xe-lamp	anatase TiO ₂ nanoplates with coexposed (101) and (001) facets		100 mg of catalyst, CO ₂ and H ₂ O vapor	0.14 (CH ₄) μmol h ⁻¹
300 W Xe-lamp	cubic anatase TiO ₂		50 mg of catalyst, CO ₂ and H ₂ O vapor	0.23 (CH ₄)/0.07 (CH ₃ OH) μmol h ⁻¹
300 W Xe-lamp (λ > 420 nm)	mixed-phase TiO ₂ , Zn(II) porphyrin		60 mg of catalyst, CO ₂ and H ₂ O vapor	0.06 (CH ₄)/0.48 (CO) μmol h ⁻¹
300 W Xe-lamp	brookite TiO ₂	0.5 wt %Ag	150 mg of catalyst, CO ₂ and H ₂ O vapor	11.5 (CH ₄)/128.8 (CO) ppm h ⁻¹
solar simulator (λ = 200–1000 nm)	bicrystalline TiO ₂ with anatase–rutile	1.0 wt %Cu	50 mg of catalyst, 20 mL min ⁻¹ CO ₂ and H ₂ O vapor	0.034 (CH ₄)/0.19 (CO) μmol h ⁻¹ (H ₂ pretreated)
solar simulator (λ = 200–1000 nm)	bicrystalline TiO ₂ with anatase–brookite		100 mg of catalyst, CO ₂ and H ₂ O vapor	<0.005 (CH ₄)/0.21 (CO) μmol h ⁻¹ (anatase: brookite = 3:1)
solar simulator (λ = 200–900 nm)	bicrystalline TiO ₂ microspheres with anatase–brookite	Ag ⁰	30 mg of catalyst, CO ₂ /H ₂ O/CH ₃ OH ratio of 97.1/2.3/0.6	0.15 (CH ₄)/4.35 (CO) /46.8 (H ₂) μmol h ⁻¹
500 W Xe-lamp (AM 1.5G)	hydrogenerated TiO ₂ (H-TiO ₂)		90 mg of catalyst, CO ₂ and H ₂ O vapor	1.95 (CH ₄)/1.27 (CO) nmol h ⁻¹
300 W Xe-lamp (AM 1.5G)	mixed-phase TiO ₂	0.2 wt % Mg	150 mg of catalyst, CO ₂ and H ₂ O vapor	0.15 (CH ₄)/0.015 (CO) /0.045 (H ₂) μmol h ⁻¹
1.5 W energy-saving bulbs	oxygen-rich TiO ₂ (P25)		100 mg of catalyst, 5 mL min ⁻¹ of CO ₂ saturated with H ₂ O vapor	0.012 (CH ₄) μmol h ⁻¹

Table A 2: continued

light source	photocatalyst	co-catalyst	experimental condition	main products and highest yield
Xe-lamp	monoethanolamine functionalized TiO ₂		20 mg of catalyst, CO ₂ and H ₂ O vapor	666.75 (CO)/861 (CH ₄) ppm h ⁻¹
300 W visible light sources (UV < 5%)	N-doped rutile TiO ₂ nanorod arrays		100 mg of catalyst in water solution, 50 mL min ⁻¹ CO ₂ bubbled 30 min	10.4 (CH ₄)/31.2 (CO) ppm h ⁻¹ (by NH ₄); 8.45 (CH ₄)/2535 (CO) ppm h ⁻¹ (by NH ₃)
125 W Hg-lamp (λ = 365 nm)	3.0 wt % Ce-doped anatase TiO ₂		25 mg of catalyst in 25 mL of solution, CO ₂ pressure 1.4 bar	0.008 (CH ₄)/0.008 (CO) μmol h ⁻¹ (solution); 0.007 (CO)/0.64 (HCOOH)/5.2 (H ₂) μmol h ⁻¹ (N ₂ S)
200 W Hg-lamp or 500 W halogen lamp	0.5 wt % Ce-doped anatase TiO ₂		catalyst-coated ceramic honeycomb monoliths with 177 channels with CO ₂ inlet	~13 (H ₂)/4 (CH ₃ OH)/3 (C ₂ H ₅ OH)/3 (CH ₃ CHO) μmol g ⁻¹ h ⁻¹ (UVA); ~3.8 (H ₂)/~0.2 (CH ₃ OH) /~0.2 (C ₂ H ₅ OH) /~0.2 (CH ₃ CHO) μmol g ⁻¹ h ⁻¹ (vis)
6 W cm ⁻² Hg-lamp (λ = 365 nm)	TiO ₂ /5.0 wt % Ce-doped TiO ₂ films		44 mm ² catalyst film under CO ₂ /He with CO ₂ /H ₂ O = 1.2	~20 (CH ₄) μmol g ⁻¹ h ⁻¹
6 W cm ⁻² Hg-lamp (λ = 365 nm)	TiO ₂ /1.0 wt % Fe-doped TiO ₂ films		40 mm ² catalyst film under CO ₂ /He with CO ₂ /H ₂ O = 1.2	~95 (CH ₄) μmol g ⁻¹ h ⁻¹
300 W Xe-lamp (λ > 420 nm)	co-doped order mesoporous anatase TiO ₂		100 mg of catalyst, CO ₂ and H ₂ O vapor	0.005 (CH ₄)/0.079 (CO) /0.19 (H ₂)/0.012 (O ₂) μmol h ⁻¹
500 W halogen lamp (λ = 380–1100 nm)	1.5 wt % V-doped, 0.5 wt % Ce-doped, or 1 wt % Co-doped anatase TiO ₂		200 mg of catalyst, CO ₂ and H ₂ O vapor	3.70 (CH ₄)/9.58 (H ₂) (V-doped); 5.62 (CH ₃ OH)/2.34 (H ₂) (Ce-doped); 5.22 (CH ₃ OH)/5.38 (H ₂) (Co-doped) μmol h ⁻¹
18 W cm ⁻² UV-lamp (λ = 365 nm)	0.1 wt % Ni-doped anatase TiO ₂		500 mg of catalyst in 1 L of CO ₂ -saturated water	7.0 (CH ₄) μmol h ⁻¹
9 W Hg-lamp (λ = 365 nm)	1.0 wt % Ce-doped anatase TiO ₂		500 mg of catalyst, CO ₂ -saturated 0.2 M NaOH	0.55 (CH ₄)/11.75 (CH ₃ OH)/52 (HCHO) μmol h ⁻¹
8 W Hg-lamp (λ = 254 nm)	0.28 mol % Ce-doped anatase TiO ₂		100 mg of catalyst, 0.1 L of CO ₂ -saturated 0.2 M NaOH	~0.089 (CH ₄)/~4.17 (H ₂) μmol h ⁻¹
8 W UVA lamp (λ = 365 nm)	3 wt % Mn-doped anatase TiO ₂ nanotubes		100 mg of catalyst, 0.2 M MEA solution, CO ₂ bubbled 1 h	0.17 (CH ₄)/0.009 (CO) μmol h ⁻¹
500 W Hg-lamp (λ = 365 nm)	10 wt % In-doped anatase TiO ₂		250 mg of catalyst, 1.2 bar CO ₂ , 2 bar He and H ₂ O vapor	20.25 (CH ₄)/61 (CO)/0.015 (C ₂ H ₄)/0.70 (C ₂ H ₆)/0.005 (C ₃ H ₈)/0.005 (C ₃ H ₆) μmol h ⁻¹
300 W Xe-lamp (λ > 400 nm)	Ti ³⁺ -self-doped rutile TiO ₂	1.0 wt % Cu ^I /Pd	100 mg of catalyst, 1.0 atm water-saturated CO ₂	0.13 (CH ₄) μmol h ⁻¹
100 W Xe-lamp (λ = 320–780 nm)	TiO ₂ (P25)	0.5 wt % Pt and 1 wt % MgO	20 mg of catalyst, CO ₂ and H ₂ O vapor	0.44 (H ₂)/0.44 (CH ₄)/0.0006 (CO) μmol g ⁻¹ h ⁻¹
500 W Xe-lamp	anatase TiO ₂	1.0 wt % Pt	20 mg of catalyst, 4 bar CO ₂ and H ₂ O vapor	358.4 (H ₂)/258.4 (CH ₄) /~12 (C ₂ H ₆) ppm
125 W Hg-lamp (λ = 254–364 nm)	TiO ₂ (anatase or rutile)	0.1 wt % Au	500 mg of catalyst in CO ₂ -saturated water, N ₂ SO ₃ as hole scavenger	4.25 (CH ₄)/1.25 (H ₂)/23.5 (liquid phase) μmol h ⁻¹ (anatase)
30 W white light LED (λ > 400 nm)	anatase TiO ₂	1.0 wt % Au	100 mg of catalyst, CO ₂ and H ₂ O vapor (7.25:1)	0.017 (CH ₄)/0.002 (CO) /0.017 (H ₂) μmol h ⁻¹
16 W Hg-lamp and 300 W Xe-lamp	Ti foil-based anatase TiO ₂ nanowire film	0.7 wt % Ag	882 mm ⁻² catalyst film in CO ₂ -saturated water	3 (CH ₃ OH) μmol cm ⁻² h ⁻¹ (λ > 420 nm); 8.3 (CH ₃ OH) μmol cm ⁻² h ⁻¹ (UV-vis)
300 W Xe-lamp (λ > 420 nm)	anatase TiO ₂ hollow spheres	Ag	100 mg of catalyst, CO ₂ and H ₂ O vapor	0.75 (CH ₄)/0.15 (O ₂) μmol h ⁻¹
500 W Xe-lamp (λ > 400 nm)	anatase TiO ₂	2.5 wt % Ag	400 mg of catalyst in 400 mL of water, CO ₂ bubbled 0.5 h before irradiation	11.96 (CH ₃ OH) μmol h ⁻¹
Two 90 mW cm ⁻² UV-LED (λ = 365 ± 38 nm)	anatase TiO ₂	1.0 wt % Pd	2.2 g of catalyst under He flow, containing 1 vol % CO ₂ and 4 vol % H ₂ O, heating at 140 °C	140.8 (CH ₄) μmol h ⁻¹
16 W Hg-lamp and 300 W Xe-lamp	anatase TiO ₂ microflower film	0.5 wt % Cu (Cu ^I)	882 mm ⁻² catalyst film in CO ₂ -saturated water	1.8 (CH ₃ OH) μmol cm ⁻² h ⁻¹
20 W Hg-lamp (λ = 254 nm)	anatase TiO ₂ hollow sphere	3 wt % CuO	10 mg of catalyst in 0.2 mL of H ₂ O under 50 psi CO ₂	0.021 (CH ₄)/0.14 (CO) / 0.028 (H ₂) μmol h ⁻¹
500 W Xe-lamp	anatase TiO ₂ nanofibers	0.05 mol % Au, 0.16 mol % Pt	5 mg of catalyst, CO ₂ and H ₂ O vapor	0.57 (CH ₄)/~0.10 (CO) μmol h ⁻¹

Table A 3: continued

light source	photocatalyst	co-catalyst	experimental condition	main products and highest yield
300 W Xe-lamp	Au@TiO ₂ yolk-shell hollow spheres		10 mg of catalyst, CO ₂ and H ₂ O vapor	0.025 (CH ₄)/0.017 (C ₂ H ₆) $\mu\text{mol h}^{-1}$
300 W Xe-lamp	anatase TiO ₂	0.5 wt % Pt/1 wt % MgO	20 mg of catalyst, 2 MPa CO ₂ and 1 mL of H ₂ O	0.0006 (H ₂)/0.22 (CH ₄) $\mu\text{mol h}^{-1}$
400 W Xe-lamp	anatase/rutile TiO ₂	5 wt % MgO	30 mg of catalyst, CO ₂ and H ₂ O vapor, 150 °C	0.6 (CO) $\mu\text{mol h}^{-1}$
100 W Hg-lamp ($\lambda < 390 \text{ nm}$)	Mg-Al LDO/TiO ₂		50 mg of catalyst, CO ₂ and H ₂ O vapor, 200 °C	produced 15.3% CO
450 W Xe-lamp ($\lambda > 400 \text{ nm}$)	Mg-Al LDO/TiO ₂		100 mg of catalyst, CO ₂ and H ₂ O vapor (150 °C)	0.40 (CO) $\mu\text{mol h}^{-1}$ (90 wt % TiO ₂)
450 W Xe-lamp ($\lambda > 420 \text{ nm}$)	TiO ₂ , 5'-(4-[bis(4-methoxy-methylphenyl)amino]phenyl-2,2'-dithiophen-5-yl)cyclopropane carboxylic acid		10 mg of catalyst with 0.1 μmol RePH and 1.5 μmol MOD in 3 mL of DMF solution containing 0.1 M BiH, CO ₂ bubbled 30 min before irradiation	TON _{CO} \geq 570 in 30 h
Fluorescent bulbs ($\lambda = 400 - 800 \text{ nm}$)	N-TiO ₂ , 0.5% chlorophyll		250 mg of catalyst in 250 mL of water, 10 mL min ⁻¹ CO ₂	0.12 (CH ₄)/0.03 (C ₂ H ₄) /0.04(C ₂ H ₆)/36.25 (H ₂) μmol in 6 h
125 W Hg-lamp	TiO ₂ , Cu(II) phthalocyanine		catalyst in CO ₂ /CH ₄ /He mix gas (40 psi)	18% (CH ₄) and 14% (CO ₂) conversion rate
20 W LED ($\lambda > 400 \text{ nm}$)	TiO ₂ , Ru(bpy) ₃ Cl ₂		100 mg of catalyst in H ₂ O/TEA/DMF (1:1:3), CO ₂ bubbled 30 min	187.6 (CH ₃ OH)/236.4 (O ₂) μmol in 24 h
20 W LED ($\lambda > 400 \text{ nm}$)	TiO ₂ , K ₄ [Fe ₆ (CN) ₆]	Cu(OH) ₂ cluster	100 mg of catalyst in H ₂ O/TEA/DMF (2:1:7), CO ₂ bubbled 30 min	149 (CH ₃ OH) μmol in 24 h
100 W Xe-lamp	anatase TiO ₂ nanotube arrays		4 cm ² nanotubes film in CO ₂ -saturated water	10 (CH ₃ OH) /9 (C ₂ H ₅ OH) $\text{nmol h}^{-1} \text{ cm}^{-2}$
300 W Xe-lamp ($\lambda > 400 \text{ nm}$)	TiO ₂ yolk-shell hierarchical microspheres		100 mg of catalyst, CO ₂ and H ₂ O vapor	0.21 (CH ₃ OH) $\mu\text{mol h}^{-1}$
300 W UV lamp	mesoporous anatase TiO ₂		500 mg of catalyst, CO ₂ and H ₂ O vapor	1.32 (CH ₄)/3.44 (CO) /2.74 (CH ₃ OH)/2.88 (H ₂) $\mu\text{mol h}^{-1}$
200 W Hg-lamp	10 wt % montmorillonite loaded TiO ₂		continuous monolith reactor, 20 mL min ⁻¹ CO ₂ /CH ₄ (1:1) gas	237.5 (CO)/55.7 (C ₂ H ₆) /0.557 (CH ₃ OH) $\mu\text{mol g}^{-1} \text{ h}^{-1}$
200 W Xe/Hg-lamp	TiO ₂ -SBA-15	Au	catalyst in 1.5 bar 6000 ppm of CO ₂ and H ₂ O vapor	1.13 $\times 10^{-3}\%$ (AQY)
14 W UV-lamp ($\lambda = 254 \text{ nm}$)	Cu-TiO ₂ -ZSM-5		500 mg of catalyst in 500 mL of CO ₂ -saturated 0.1 M NaHCO ₃	25.0 (CH ₃ OH) $\mu\text{mol h}^{-1}$
300 W UV lamp	20 wt % TiO ₂ -KIT 6		200 mg of catalyst, 50 mL min ⁻¹ flow of 20% CO ₂ in He and H ₂ O vapor	1.78 (CH ₄)/4.82 (CO) / 0.04 (CH ₃ OH)/0.36 (H ₂) $\mu\text{mol h}^{-1}$

Table A 4: μ GC-TCD analysis parameters for CO_2 valorization test monitoring

Parameters	Column A	Column B	Column C	Column D
Detectable gases	H_2 , O_2 , N_2 , CH_4 , CO	Air, N_2 , CH_4 , CO	CH_4 , CO_2 , C_2H_4 , C_2H_6 , C_3H_6 , C_3H_8 , C_3H_4	C_3H_6 , C_3H_8 , C_3H_4 , C_4H_{10} , C_4H_6 , C_5H_{12}
Column type	MS5A	MS5A	PLOTQ	OV1
Dimensions	10 m x 0.32 mm	10 m x 0.32 mm	10 m x 0.32 mm	14 m x 0.32 mm
Injection temperature (°C)	50	50	70	50
Column temperature (°C)	50	70	60	40
Injection time (ms)	100	100	50	50
Backflush time (s)	4	4	-	-
Column pressure (psi)	28	28	25	25
Carrier gas	Argon	Helium	Helium	Helium

Table A 5: Retention time of quantified gases for the first three columns

Column	A			B	C				
	H_2	O_2	N_2	CO	CH_4	CO_2	Ethane	H_2O	Propane
Retention times (s)	39.4	50.5	64.8	118.7	23.6	25.1	40.0	96.1	138.1

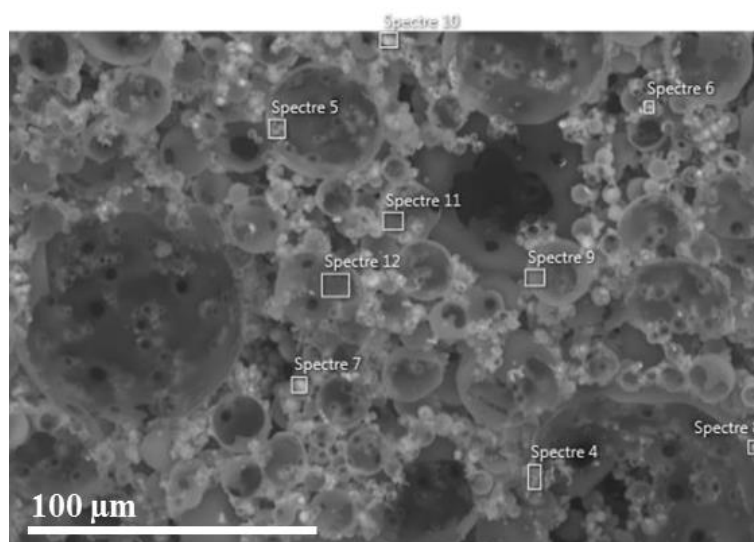


Figure A 1: SEM-EDS image with analysed areas (results in Figure A 2 in annex)

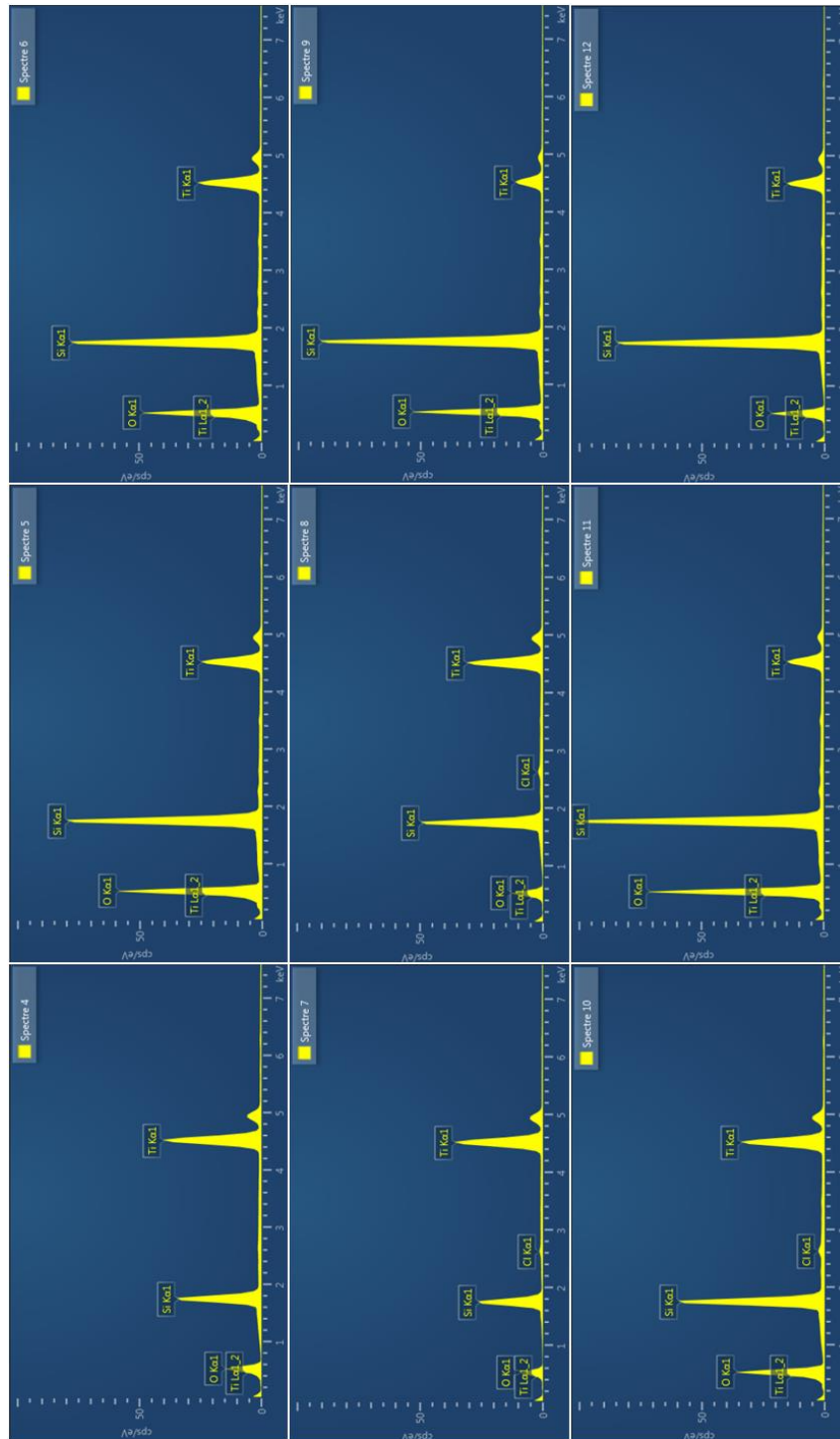


Figure A 2: EDS spectra associated with the Figure A 1 in annex

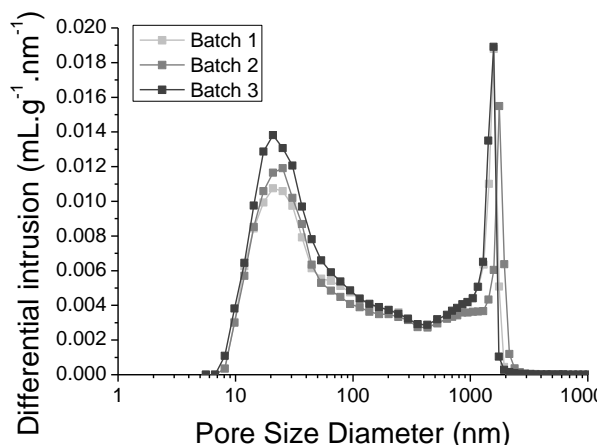


Figure A 3: Pore size distributions of silica matrices from three different batches

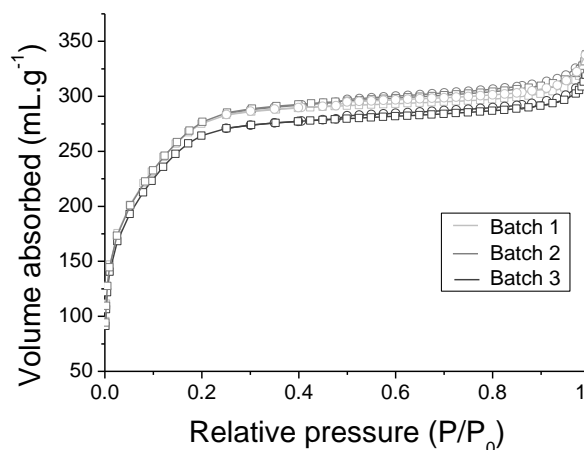


Figure A 4: Nitrogen adsorption (\square) and desorption (\circ) isotherms of silica matrices from three different batches

Table A 6: Summary of morphological characteristics of Si(HIPE)s from three different batches, obtained by **mercury intrusion porosimetry** measurements; and of the mean, standard deviation and mean-relative deviation values associated with each quantity

	Batches			Mean	Standard deviation	Mean deviation (%)
	1	2	3			
Intrusion volume (mL.g⁻¹) (+/- 2%)	14.49	14.58	14.13	14.4	0.238	1.7
Porosity (%) (+/- 5%)	92	93	92	92.3	0.577	0.6
Bulk density (g.mL⁻¹) (+/- 10%)	0.06	0.07	0.07	0.067	0.006	8.7
Skeletal density (g.mL⁻¹) (+/- 10%)	0.78	0.94	0.86	0.86	0.080	9.3
Median pore aperture (nm)	1453	1416	1619	1496	108	7.2

Table A 7: Summary of morphological characteristics of Si(HIPE)s from three different batches, obtained by **nitrogen physisorption** measurements; and of the mean, standard deviation and mean-relative deviation values associated with each quantity

	Batches			Mean	Standard deviation	Mean deviation (%)
	1	2	3			
BET surface (m².g⁻¹) (+/- 5%)	1023	1026	989	1013	20.6	2.0
Microporous volume (mL.g⁻¹) (+/- 10%)	0.438	0.437	0.414	0.430	0.014	3.2
BJH surface (m².g⁻¹)-desorption curve (+/- 10%)	43	28	34	35	7.55	22

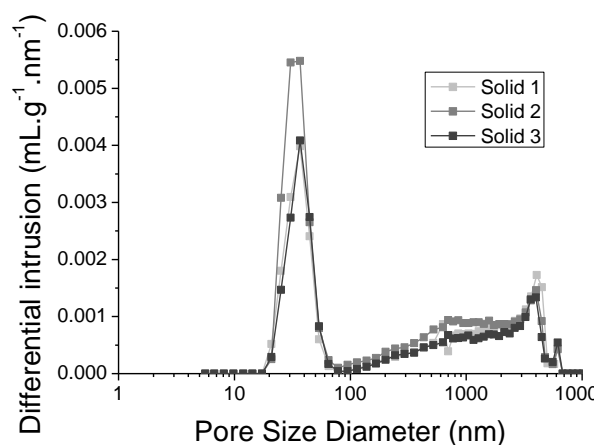


Figure A 5: Pore size distributions of three silica matrices from one batch (Batch 4)

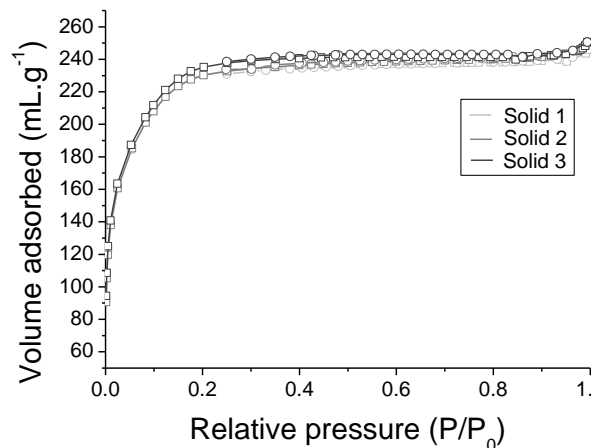


Figure A 6: Nitrogen adsorption (□) and desorption (○) isotherms of three silica matrices from one batch (Batch 4)

Table A 8: Summary of morphological characteristics of **three Si(HIPE)s from one batch (Batch 4)**, obtained by **mercury intrusion porosimetry** measurements; and of the mean, standard deviation and mean-relative deviation values associated with each quantity

	Batch.Solid			Mean	Standard deviation	Mean deviation (%)
	4.1	4.2	4.3			
Intrusion volume (mL.g⁻¹) (+/- 2%)	10.19	9.28	10.13	9.87	0.509	5.2
Porosity (%) (+/- 5%)	82	76	79	79	3.00	3.8
Bulk density (g.mL⁻¹) (+/- 10%)	0.11	0.11	0.12	0.113	0.006	5.1
Skeletal density (g.mL⁻¹) (+/- 10%)	0.44	0.35	0.36	0.38	0.049	13
Median pore aperture (nm)	4568	4179	6415	5054	1194	24

Table A 9: Summary of morphological characteristics of **three Si(HIPE)s from one batch (Batch 4)**, obtained by **nitrogen physisorption** measurements; and of the mean, standard deviation and mean-relative deviation values associated with each quantity

	Batch.Solid			Mean	Standard deviation	Mean deviation (%)
	4.1	4.2	4.3			
BET surface ($\text{m}^2\cdot\text{g}^{-1}$) (+/- 5%)	879	880	898	885	10.7	1.2
Microporous volume ($\text{mL}\cdot\text{g}^{-1}$) (+/- 10%)	0.349	0.352	0.360	0.137	0.006	1.6
BJH surface ($\text{m}^2\cdot\text{g}^{-1}$)-desorption curve (+/- 10%)	28	25	20	24.3	4.04	17

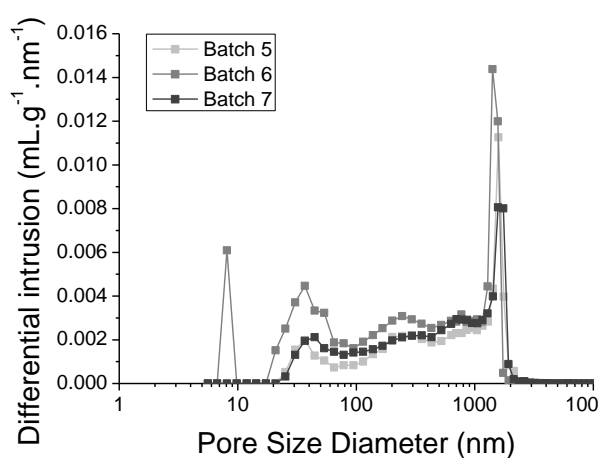


Figure A 7: Pore size distributions of $\text{TiO}_2@\text{Si}(\text{HIPE})\text{s}$ from three different batches

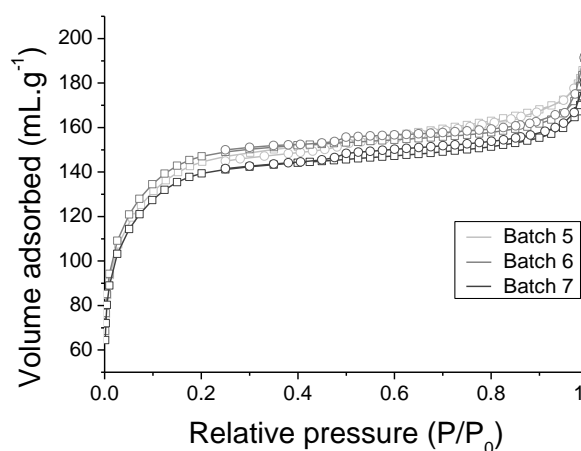


Figure A 8: Nitrogen adsorption (\square) and desorption (\circ) isotherms of $\text{TiO}_2@\text{Si}(\text{HIPE})\text{s}$ from three different batches

Table A 10: Summary of morphological characteristics of $\text{TiO}_2@\text{Si}(\text{HIPE})\text{s}$ from three different batches, obtained by mercury intrusion porosimetry measurements; and of the mean, standard deviation and mean-relative deviation values associated with each quantity

	Batches			Mean	Standard deviation	Mean deviation (%)
	5	6	7			
Intrusion volume (mL.g^{-1}) (+/- 2%)	8.34	10.37	8.85	9.19	1.06	12
Porosity (%) (+/- 5%)	91	94	94	93	1.73	1.9
Bulk density (g.mL^{-1}) (+/- 10%)	0.11	0.09	0.11	0.103	0.012	11
Skeletal density (g.mL^{-1}) (+/- 10%)	1.19	1.59	1.7	1.49	0.268	18
Median pore aperture (nm)	1535	1432	1483	1483	51.5	3.5

Table A 11: Summary of morphological characteristics of $\text{TiO}_2@\text{Si}(\text{HIPE})\text{s}$ from three different batches, obtained by nitrogen physisorption measurements; and of the mean, standard deviation and mean-relative deviation values associated with each quantity

	Batches			Mean	Standard deviation	Mean deviation (%)
	5	6	7			
BET surface ($\text{m}^2.\text{g}^{-1}$) (+/- 5%)	539	552	524	538	14.0	2.6
Microporous volume (mL.g^{-1}) (+/- 10%)	0.211	0.221	0.206	0.213	0.008	3.6
BJH surface ($\text{m}^2.\text{g}^{-1}$)-desorption curve (+/- 10%)	42	24	29	31.7	9.29	29

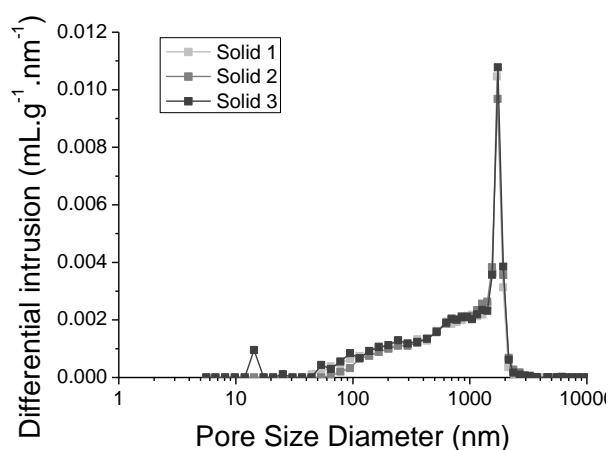


Figure A 9: Pore size distributions of three $\text{TiO}_2@\text{Si}(\text{HIPE})\text{s}$ from one batch (Batch 8)

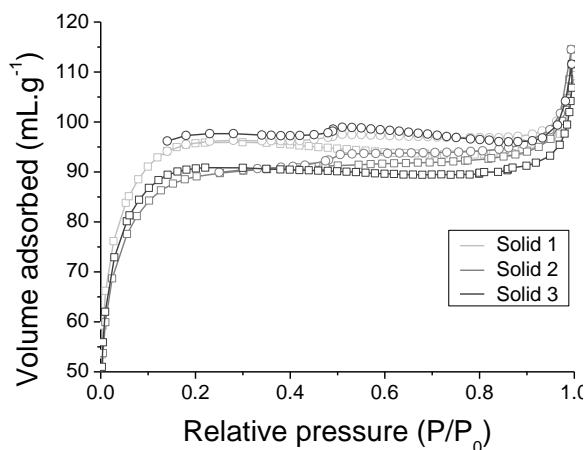


Figure A 10: Nitrogen adsorption (\square) and desorption (\circ) isotherms of three $\text{TiO}_2@\text{Si}(\text{HIPE})\text{s}$ from one batch (Batch 8)

Table A 12: Summary of morphological characteristics of **three TiO₂@Si(HIPE)s** from one batch (Batch 8), obtained by **mercury intrusion porosimetry** measurements; and of the mean, standard deviation and mean-relative deviation values associated with each quantity

	Batch.Solid			Mean	Standard deviation	Mean deviation (%)
	8.1	8.2	8.3			
Intrusion volume (mL.g⁻¹) (+/- 2%)	7.85	8.01	8.08	7.98	0.118	1.5
Porosity (%) (+/- 5%)	93	91	94	92.7	1.53	1.6
Bulk density (g.mL⁻¹) (+/- 10%)	0.12	0.12	0.12	0.12	0.000	0.0
Skeletal density (g.mL⁻¹) (+/- 10%)	1.78	1.28	1.82	1.63	0.301	19
Median pore aperture (nm)	1720	1721	1746	1729	14.7	0.9

Table A 13: Summary of morphological characteristics of **three TiO₂@Si(HIPE)s** from one batch (Batch 8), obtained by **nitrogen physisorption** measurements; and of the mean, standard deviation and mean-relative deviation values associated with each quantity

	Batch.Solid			Mean	Standard deviation	Mean deviation (%)
	8.1	8.2	8.3			
BET surface (m².g⁻¹) (+/- 5%)	355	334	339	343	11.0	3.2
Microporous volume (mL.g⁻¹) (+/- 10%)	0.143	0.134	0.134	0.137	0.005	3.8
BJH surface (m².g⁻¹)-desorption curve (+/- 10%)	2	11	5	6	4.58	76

Table A 14: Summary of **TiO₂(M)Si(HIPE)s** morphological characteristics, where *M* is the impregnation method, obtained by **mercury intrusion porosimetry** measurements

Materials	TiO ₂ (P25)@Si(HIPE)	TiO ₂ (IIa)@Si(HIPE)	TiO ₂ (Ia)@Si(HIPE)	TiO ₂ (I)@Si(HIPE)
Intrusion volume (mL.g⁻¹)	5.85	7.75	7.41	6.69
Porosity (%)	70	89	91	90
Bulk density (g.mL⁻¹)	0.16	0.12	0.13	0.14
Median pore aperture (nm)	4164	1655	2000	1941

Table A 15: Summary of **TiO₂(M)Si(HIPE)s** morphological characteristics, where *M* is the impregnation method, obtained by **nitrogen physisorption** measurements

Materials	TiO ₂ (P25)@Si(HIPE)	TiO ₂ (IIa)@Si(HIPE)	TiO ₂ (Ia)@Si(HIPE)	TiO ₂ (I)@Si(HIPE)
BET surface (m².g⁻¹)	500	415	426	288
Microporous volume (mL.g⁻¹)	0.202	0.172	0.161	0.130

Table A 16: Summary of trials performed for linear regression, with the input variables and the analysed output (F)

N° trial	Input		Output
	T _{cal} (°C)	t _{cal} (h)	% _{anatase}
1	500	1	100
2	500	4	100
3	500	10	100
4	700	1	100
5	700	4	100
6	700	10	100
7	900	1	45
8	900	4	60
9	900	10	35

Table A 17: Adjustment coefficients corresponding to regression model adjustment statistics

	Meaning	Value
Observations	The number of observations taken into account in the calculations	9
Weight sum	The sum of the weights of the observations taken into account in the calculations	9
DOF	The number of Degrees Of Freedom is the number of independent variables. The higher the number, the higher the level of confidence in the influence of variables.	6
R²	The model determination coefficient. R ² is interpreted as the proportion of the variability of the dependent variable explained by the model. The closer the R ² is to 1, the better the model.	0.716
RMSE	The mean-square error (MSE) represents the error variance. The error is the difference between experimental and modeling values. The variance of a random variable characterizes the dispersion of its values around its mathematical expectation. The root-mean-square error (RMSE) represents standard deviation. The smaller the standard deviation, the more discrimination can be made between the means of two different variables.	17

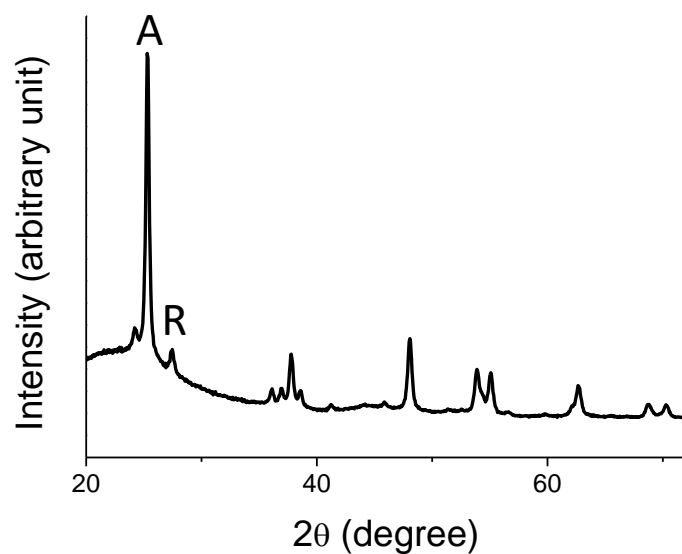


Figure A 11: XRD pattern of a $\text{TiO}_2(1a)@Si(\text{HIPE})$ sample containing 30%wt of TiO_2 and ex-situ calcinated at 700°C . A = anatase, R = rutile

Table A 18: Summary of $\epsilon\text{-Si}(\text{HIPE})$ s morphological characteristics, where ϵ is the oil volume fraction, obtained by **mercury intrusion porosimetry** measurements

	$\epsilon\text{-Si}(\text{HIPE})$					
	0.58-Si(HIPE)	0.60-Si(HIPE)	0.64-Si(HIPE)	0.67-Si(HIPE)	0.70-Si(HIPE)	0.74-Si(HIPE)
Intrusion volume (mL.g^{-1})	7.94	11.99	13.98	13.48	4.15	2.07
Porosity (%)	70	93	93	95	82	73
Bulk density (g.mL^{-1})	0.09	0.08	0.07	0.07	0.20	0.36
Median pore aperture (nm)	1950	2052	1651	1767	158	91

Table A 19: Summary of $\epsilon\text{-Si}(\text{HIPE})$ s morphological characteristics, where ϵ is the oil volume fraction, obtained by **nitrogen physisorption** measurements

	$\epsilon\text{-Si}(\text{HIPE})$					
	0.58-Si(HIPE)	0.60-Si(HIPE)	0.64-Si(HIPE)	0.67-Si(HIPE)	0.70-Si(HIPE)	0.74-Si(HIPE)
BET surface ($\text{m}^2.\text{g}^{-1}$)	912	1014	942	834	976	1054
Microporous volume (mL.g^{-1})	0.383	0.429	0.416	0.343	0.424	0.462
%vol. mesoporous (%)	10	12	14	16	27	25

Table A 20: Summary of ϵ -TiO₂@Si(HIPE)s morphological characteristics, where ϵ is the oil volume fraction, obtained by *mercury intrusion porosimetry* measurements

	ϵ -TiO ₂ @Si(HIPE)			
	0.58-TiO ₂ @Si(HIPE)	0.60-TiO ₂ @Si(HIPE)	0.64-TiO ₂ @Si(HIPE)	0.67-TiO ₂ @Si(HIPE)
Intrusion volume (mL.g ⁻¹)	5.41	6.5	7.75	7.48
Porosity (%)	77	92	89	93
Bulk density (g.mL ⁻¹)	0.15	0.15	0.12	0.13
Median pore aperture (nm)	2090	1669	1655	1730

Table A 21: Summary of ϵ -TiO₂@Si(HIPE)s morphological characteristics, where ϵ is the oil volume fraction, obtained by *nitrogen physisorption* measurements

	ϵ -TiO ₂ @Si(HIPE)			
	0.58-TiO ₂ @Si(HIPE)	0.60-TiO ₂ @Si(HIPE)	0.64-TiO ₂ @Si(HIPE)	0.67-TiO ₂ @Si(HIPE)
BET surface (m ² .g ⁻¹)	506	420	415	397
Microporous volume (mL.g ⁻¹)	0.199	0.167	0.172	0.162

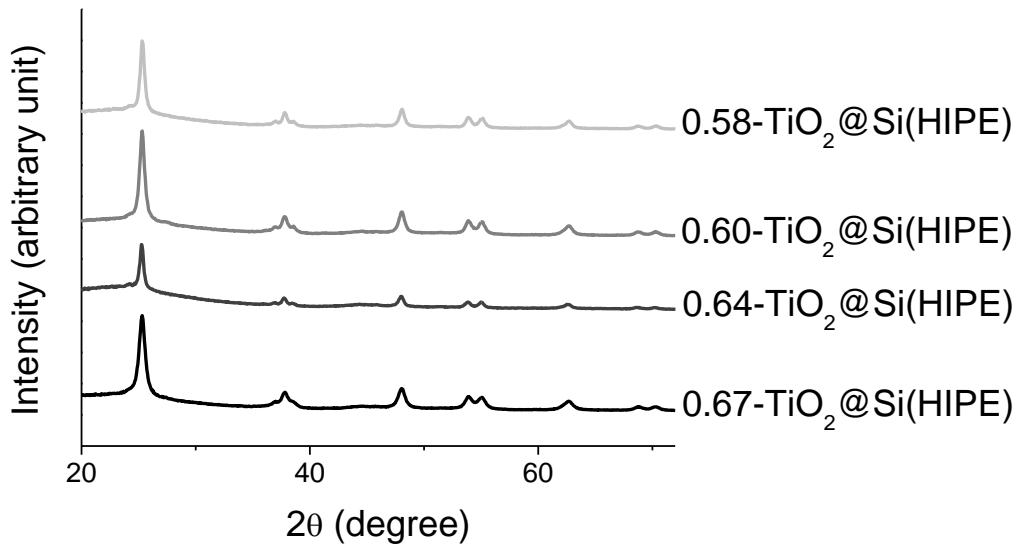


Figure A 12: XRD patterns of ϵ -TiO₂@Si(HIPE)s, where ϵ is the oil volume fraction

Table A 22: Summary of C_x-Si(HIPE)s morphological characteristics, where x is the oil chain length, obtained by *mercury intrusion porosimetry* measurements

	C _x -Si(HIPE)		
	C ₉ -Si(HIPE)	C ₁₂ -Si(HIPE)	C ₁₅ -Si(HIPE)
Intrusion volume (mL.g ⁻¹)	13.47	13.98	13.65
Porosity (%)	94	93	90
Bulk density (g.mL ⁻¹)	0.07	0.07	0.07
Median pore aperture (nm)	1353	1651	2405

Table A 23: Summary of C_x -Si(HIPE)s morphological characteristics, where x is the oil chain length, obtained by **nitrogen physisorption** measurements

	C_x -Si(HIPE)		
	C_9 -Si(HIPE)	C_{12} -Si(HIPE)	C_{15} -Si(HIPE)
BET surface ($m^2.g^{-1}$)	923	942	956
Microporous volume ($mL.g^{-1}$)	0.397	0.416	0.402

Table A 24: Summary of C_x -TiO₂@Si(HIPE)s morphological characteristics, where x is the oil chain length, obtained by **mercury intrusion porosimetry** measurements

	C_x -TiO ₂ @Si(HIPE)		
	C_9 -TiO ₂ @Si(HIPE)	C_{12} -TiO ₂ @Si(HIPE)	C_{15} -TiO ₂ @Si(HIPE)
Intrusion volume ($mL.g^{-1}$)	7.95	7.75	7.17
Porosity (%)	92	89	72
Bulk density ($g.mL^{-1}$)	0.12	0.12	0.10
Median pore aperture (nm)	1511	1655	1800

Table A 25: Summary of C_x -TiO₂@Si(HIPE)s morphological characteristics, where x is the oil chain length, obtained by **nitrogen physisorption** measurements

	C_x -TiO ₂ @Si(HIPE)		
	C_9 -TiO ₂ @Si(HIPE)	C_{12} -TiO ₂ @Si(HIPE)	C_{15} -TiO ₂ @Si(HIPE)
BET surface ($m^2.g^{-1}$)	472	415	472
Microporous volume ($mL.g^{-1}$)	0.191	0.172	0.193

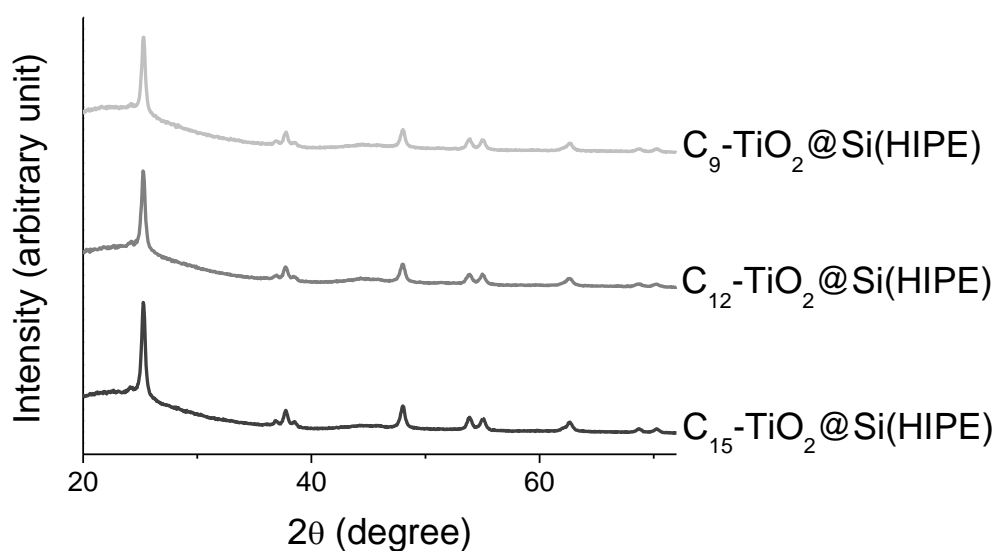


Figure A 13: XRD patterns of C_x -TiO₂@Si(HIPE)s, where x is the oil chain length

Table A 26: Summary of **T-Si(HIPE)**s morphological characteristics, where *T* is the calcination temperature in °C, obtained by **mercury intrusion porosimetry** measurements

	T-Si(HIPE)			
	550-Si(HIPE)	650-Si(HIPE)	750-Si(HIPE)	850-Si(HIPE)
Intrusion volume (mL.g ⁻¹)	13.92	13.98	-	9.78
Porosity (%)	93	93	-	63
Bulk density (g.mL ⁻¹)	0.07	0.07	-	0.07
Median pore aperture (nm)	1193	1651	-	1054

Table A 27: Summary of **T-Si(HIPE)**s morphological characteristics, where *T* is the calcination temperature in °C, obtained by **nitrogen physisorption** measurements

	T-Si(HIPE)			
	550-Si(HIPE)	650-Si(HIPE)	750-Si(HIPE)	850-Si(HIPE)
BET surface (m ² .g ⁻¹)	1144	942	-	359
Microporous volume (mL.g ⁻¹)	0.516	0.416	-	0.140

Table A 28: Summary of **T-TiO₂@Si(HIPE)**s morphological characteristics, where *T* is the calcination temperature in °C, obtained by **mercury intrusion porosimetry** measurements

	T-TiO ₂ @Si(HIPE)			
	550-TiO ₂ @Si(HIPE)	650-TiO ₂ @Si(HIPE)	750-TiO ₂ @Si(HIPE)	850-TiO ₂ @Si(HIPE)
Intrusion volume (mL.g ⁻¹)	-	7.75	7.08	8.54
Porosity (%)	-	89	88	87
Bulk density (g.mL ⁻¹)	-	0.12	0.13	0.10
Median pore aperture (nm)	-	1655	1080	1009

Table A 29: Summary of **T-TiO₂@Si(HIPE)**s morphological characteristics, where *T* is the calcination temperature in °C, obtained by **nitrogen physisorption** measurements

	T-TiO ₂ @Si(HIPE)			
	550-TiO ₂ @Si(HIPE)	650-TiO ₂ @Si(HIPE)	750-TiO ₂ @Si(HIPE)	850-TiO ₂ @Si(HIPE)
BET surface (m ² .g ⁻¹)	452	415	360	117
Microporous volume (mL.g ⁻¹)	0.183	0.172	0.142	0.038

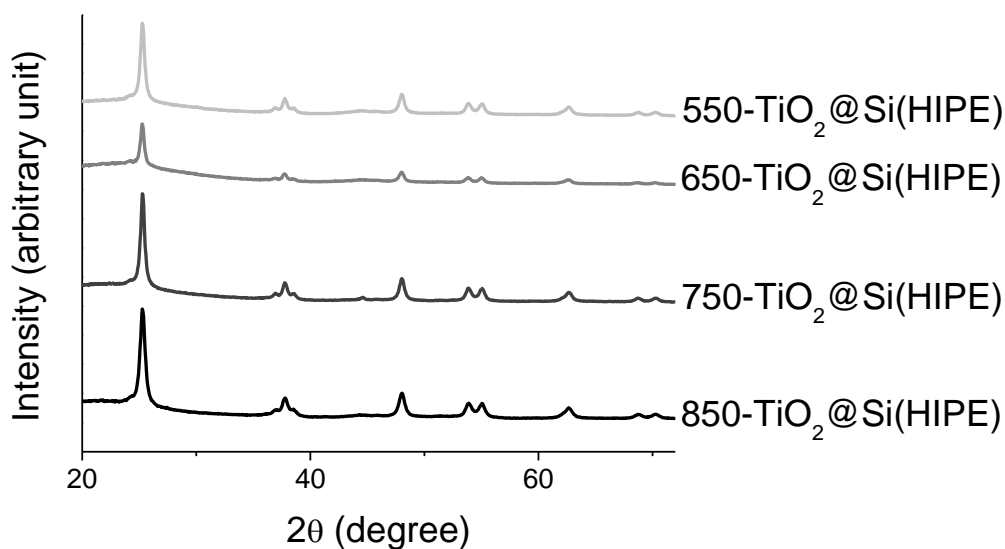


Figure A 14: XRD patterns of T - TiO_2 @ $\text{Si}(\text{HIPE})$ s, where T is the calcination temperature in $^\circ\text{C}$

Table A 30: Summary of v - $\text{Si}(\text{HIPE})$ s morphological characteristics, where v is the local shear in rpm, obtained by **mercury intrusion porosimetry** measurements

	v-Si(HIPE)		
	150-Si(HIPE)	200-Si(HIPE)	250-Si(HIPE)
Intrusion volume ($\text{mL}\cdot\text{g}^{-1}$)	3.69	-	16.2
Porosity (%)	26	-	88
Bulk density ($\text{g}\cdot\text{mL}^{-1}$)	0.07	-	0.12
Median pore aperture (nm)	4454	-	300

Table A 31: Summary of v - $\text{Si}(\text{HIPE})$ s morphological characteristics, where v is the local shear in rpm, obtained by **nitrogen physisorption** measurements

	v-Si(HIPE)		
	150-Si(HIPE)	200-Si(HIPE)	250-Si(HIPE)
BET surface ($\text{m}^2\cdot\text{g}^{-1}$)	928	-	1030
Microporous volume ($\text{mL}\cdot\text{g}^{-1}$)	0.387	-	0.465

Table A 32: Summary of v - TiO_2 @ $\text{Si}(\text{HIPE})$ s morphological characteristics, where v is the local shear in rpm, obtained by **mercury intrusion porosimetry** measurements

	v- TiO_2 @Si(HIPE)		
	150- TiO_2 @Si(HIPE)	200- TiO_2 @Si(HIPE)	250- TiO_2 @Si(HIPE)
Intrusion volume ($\text{mL}\cdot\text{g}^{-1}$)	4.12	4.77	10.67
Porosity (%)	37	85	92
Bulk density ($\text{g}\cdot\text{mL}^{-1}$)	0.10	0.18	0.19
Median pore aperture (nm)	3038	881	269

Table A 33: Summary of $v\text{-TiO}_2\text{@Si(HIPE)}$ s morphological characteristics, where v is the local shear in rpm, obtained by **nitrogen physisorption** measurements

	$v\text{-TiO}_2\text{@Si(HIPE)}$		
	150- $\text{TiO}_2\text{@Si(HIPE)}$	200- $\text{TiO}_2\text{@Si(HIPE)}$	250- $\text{TiO}_2\text{@Si(HIPE)}$
BET surface ($\text{m}^2\cdot\text{g}^{-1}$)	596	546	655
Microporous volume ($\text{mL}\cdot\text{g}^{-1}$)	0.245	0.225	0.274

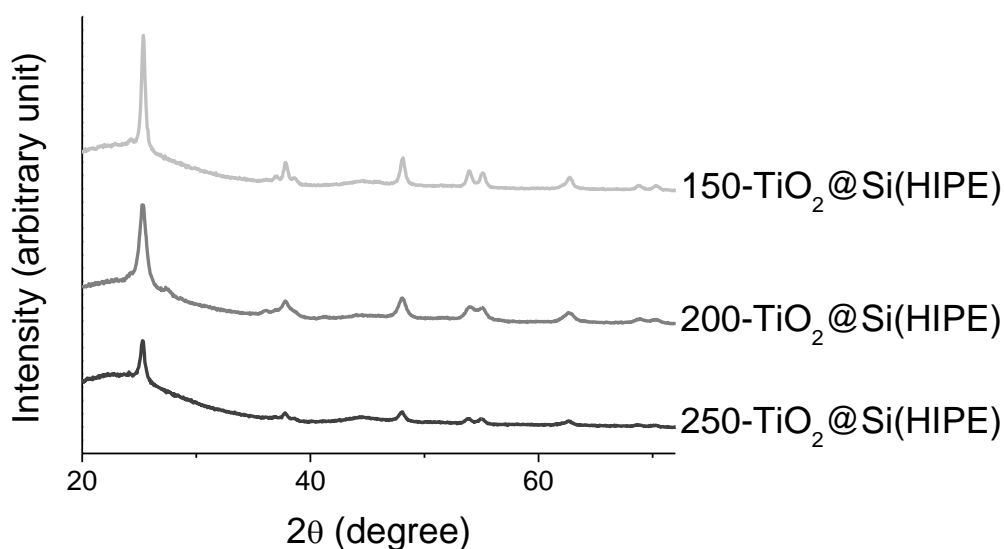


Figure A 15: XRD patterns of $v\text{-TiO}_2\text{@Si(HIPE)}$ s, where v is the local shear in rpm

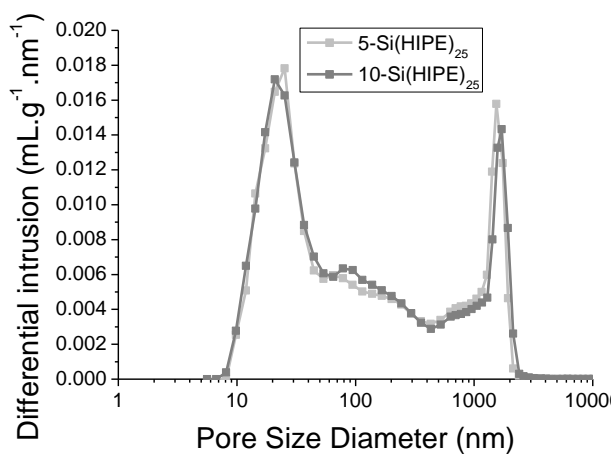


Figure A 16: Pore size distributions of $t\text{-Si(HIPE)}$ s (Batch 25), where t is the poured sol thickness in mm

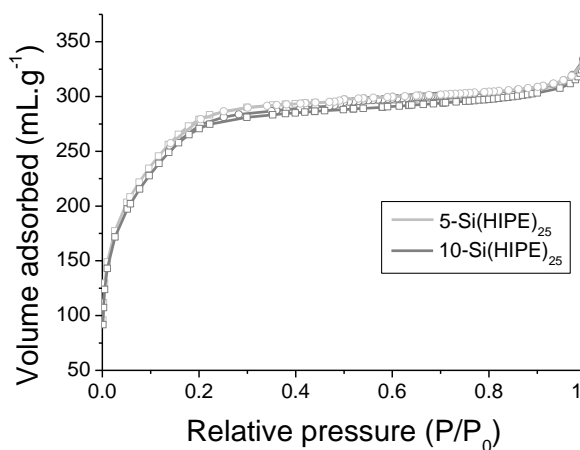


Figure A 17: Nitrogen adsorption (\square) and desorption (\circ) isotherms of $t\text{-Si(HIPE)}$ s (Batch 25), where t is the poured sol thickness in mm

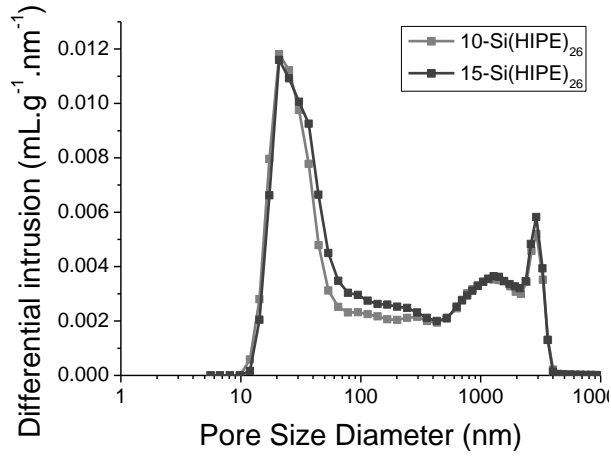


Figure A 18: Pore size distributions of t -Si(HIPE) s (Batch 26), where t is the poured sol thickness in mm

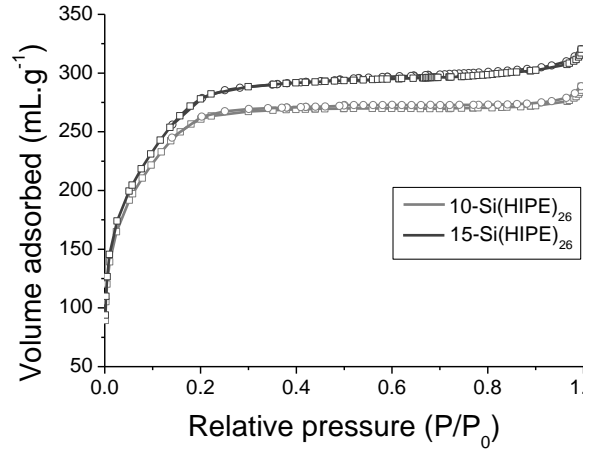


Figure A 19: Nitrogen adsorption (\square) and desorption (\circ) isotherms of t -Si(HIPE) s (Batch 26), where t is the poured sol thickness in mm

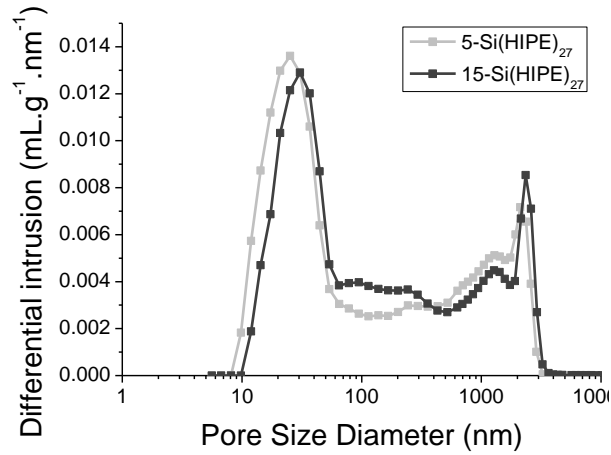


Figure A 20: Pore size distributions of t -Si(HIPE) s (Batch 27), where t is the poured sol thickness in mm

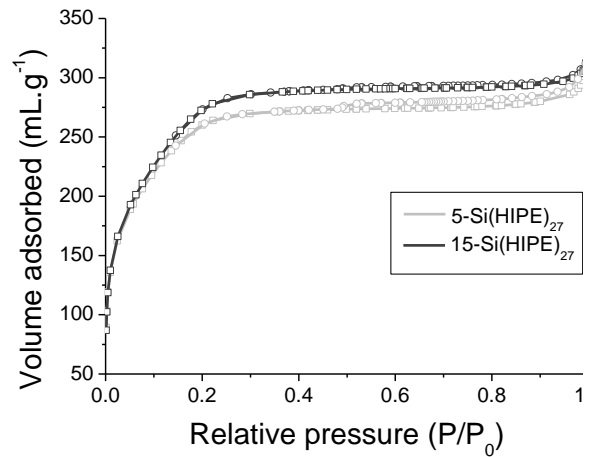


Figure A 21: Nitrogen adsorption (\square) and desorption (\circ) isotherms of t -Si(HIPE) s (Batch 27), where t is the poured sol thickness in mm

Table A 34: Photonic simulation results for each considered sample and median pore aperture diameter

Sample	l_t (m)	l_i (m)	A	B	Chi^2	n_{eff}	L (mm)	l_t (μm)	D (nm)
P25 TiO₂ powder								3.1 ± 0.3	43
experiment #1	3.47E-06	1.00E-03	7.99E-02	1.47E-04	1.69E-02	1.20	2.00		
experiment #2	2.84E-06	7.34E-04	7.99E-02	1.01E-04	1.21E-02	1.20	2.00		
experiment #3	2.85E-06	6.84E-04	7.95E-02	9.88E-05	2.31E-02	1.20	2.00		
mean	3.05E-06	8.06E-04	7.98E-02	1.16E-04	1.74E-02				
standart deviation	2.78E-07	1.29E-04	1.78E-04	2.09E-05	3.82E-03				
TiO₂(IIa)@Si(HIPE)									
I								20.1 ± 1.3	2366
experiment #1	1.92E-05	6.01E-04	3.87E-02	4.63E-03	1.51E-01	1.06	8.47		
experiment #2	1.91E-05	6.88E-04	3.92E-02	5.29E-03	5.64E-01	1.06	8.47		
experiment #3	2.20E-05	6.75E-04	3.85E-02	4.78E-03	7.37E-02	1.06	8.47		
mean	2.01E-05	6.55E-04	3.88E-02	4.90E-03	2.63E-01				
standart deviation	1.27E-06	3.58E-05	2.67E-04	2.60E-04	2.00E-01				
II								16.0 ± 0.6	2052
experiment #1	1.65E-05	8.41E-04	2.06E-02	9.00E-04	5.77E-02	1.05	3.50		
experiment #2	1.65E-05	8.45E-04	2.06E-02	6.88E-04	1.09E-01	1.05	3.50		
experiment #3	1.51E-05	9.80E-04	2.06E-02	9.04E-04	4.32E-02	1.05	3.50		
mean	1.60E-05	8.89E-04	2.06E-02	8.31E-04	6.98E-02				
standart deviation	6.22E-07	6.09E-05	0.00E+00	9.51E-05	2.58E-02				
III								25.6 ± 1.1	2595
experiment #1	2.39E-05	1.59E-03	4.13E-02	6.93E-04	8.57E-02	1.04	5.00		
experiment #2	2.56E-05	1.95E-03	4.15E-02	5.12E-04	2.83E-02	1.04	5.00		
experiment #3	2.72E-05	2.77E-03	6.79E-02	1.60E-04	5.60E-03	1.04	5.00		
mean	2.56E-05	2.10E-03	5.02E-02	4.55E-04	3.99E-02				
standart deviation	1.11E-06	4.44E-04	1.18E-02	1.97E-04	3.06E-02				

Table A 35: Key parameters describing P25 TiO₂ powder and TiO₂@Si(HIPE) systems as tested

	P25 TiO ₂ powder	TiO ₂ (P25)@Si(HIPE)
TiO₂ content (%wt)	100	18
Anatase/Rutile ratio	80/20	90/10
Anatase crystallite size (nm)	19.2	20.5
Rutile crystallite size (nm)	31.1	33
Bed thickness (mm)	0.4	3.6
Irradiated surface (cm²)	5.31	9.08
TiO₂ mass (g)	0.061	0.066

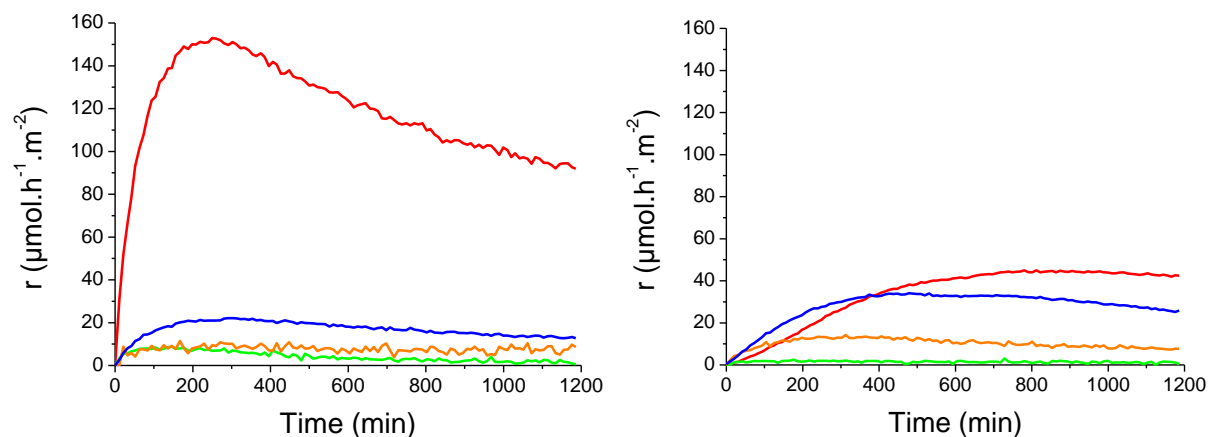


Figure A 22: Production rates of all detected products as a function of time on stream for TiO_2 powder (left) and for the $\text{TiO}_2(\text{P25})@\text{Si}(\text{HIPE})$ (right): H_2 (red), CO (orange), CH_4 (blue) and C_2H_6 (green)

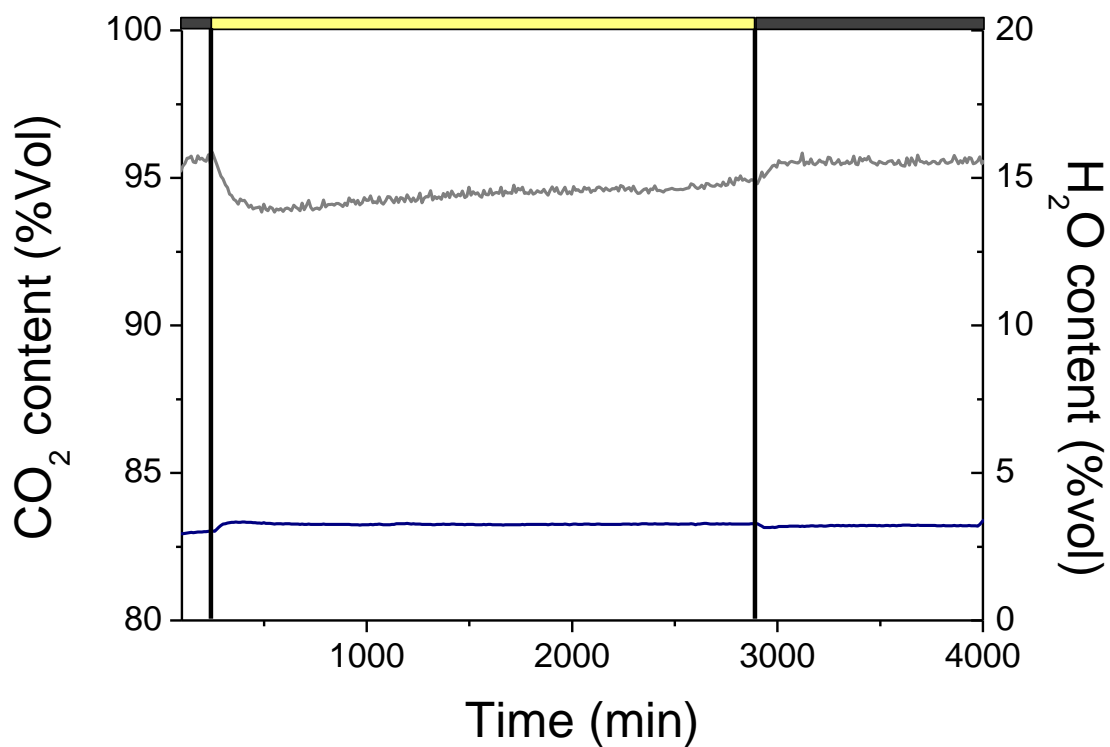


Figure A 23: Reactant contents at first without light, then with light over 44 hours, and finally without light over 24 hours. Photocatalyst: 0.15g of P25 TiO_2 powder. Species: CO_2 (gray) and H_2O (dark blue)

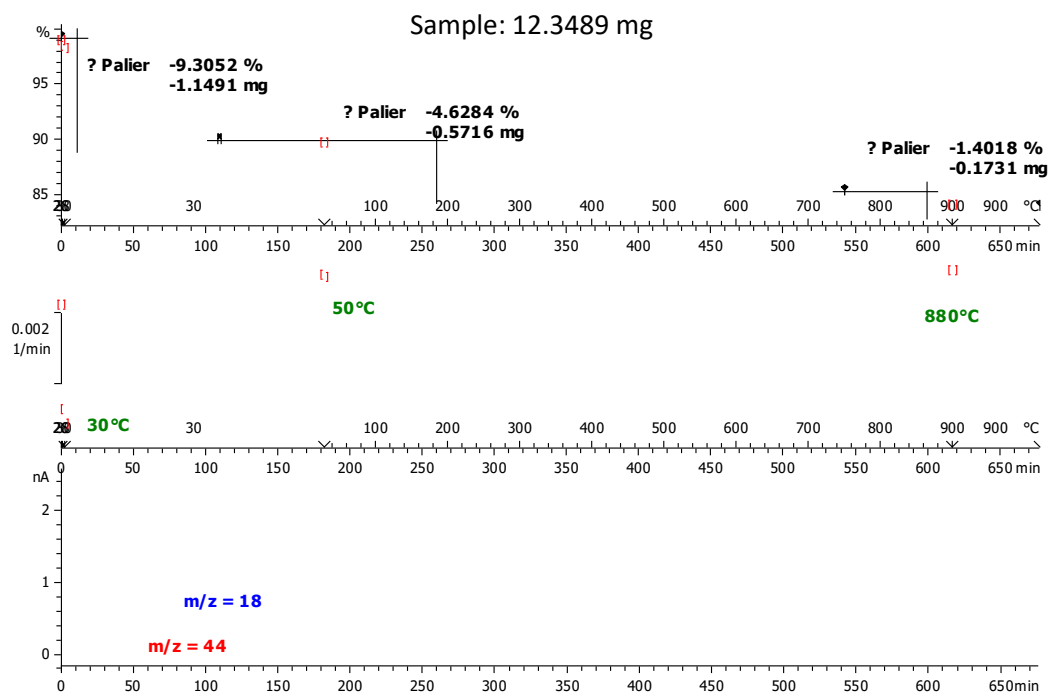


Figure A 24: Mass profil recorded by TGA/MS analysis of $\text{TiO}_2@\text{Si}(\text{HIPE})$

Table A 36: Summary table of the differences between the three $\text{TiO}_2@\text{Si}(\text{HIPE})$ s during impregnation steps

Materials		$\text{TiO}_2@\text{Si}(\text{HIPE})$		
		I	II	III
1 st solution	TTIP concentration (M)	0.29	0.29	0.22
	Age (h)	2	2	2
2 nd solution	TTIP concentration (M)	0.29	0.29	0.22
	Age (h)	2	38	2

Table A 37: Diffuse reflectance UV/Visible spectroscopy, XRF and XRD data of the four studied materials

Materials	TiO ₂ @Si(HIPE)			P25 TiO ₂
	I	II	III	Powder
Bandgap energy (eV)	3.1	3.1	3.1	3.1
%wt TiO ₂ content (%)	32	29	21	100
Anatase/Rutile ratio	100/0	60/40	100/0	80/20
Anatase crystallites size (nm)	7	6.4	12.1	19.2
Rutile crystallites size (nm)	-	6.5	-	31.1
Crystallinity (%)	24	10	44	100

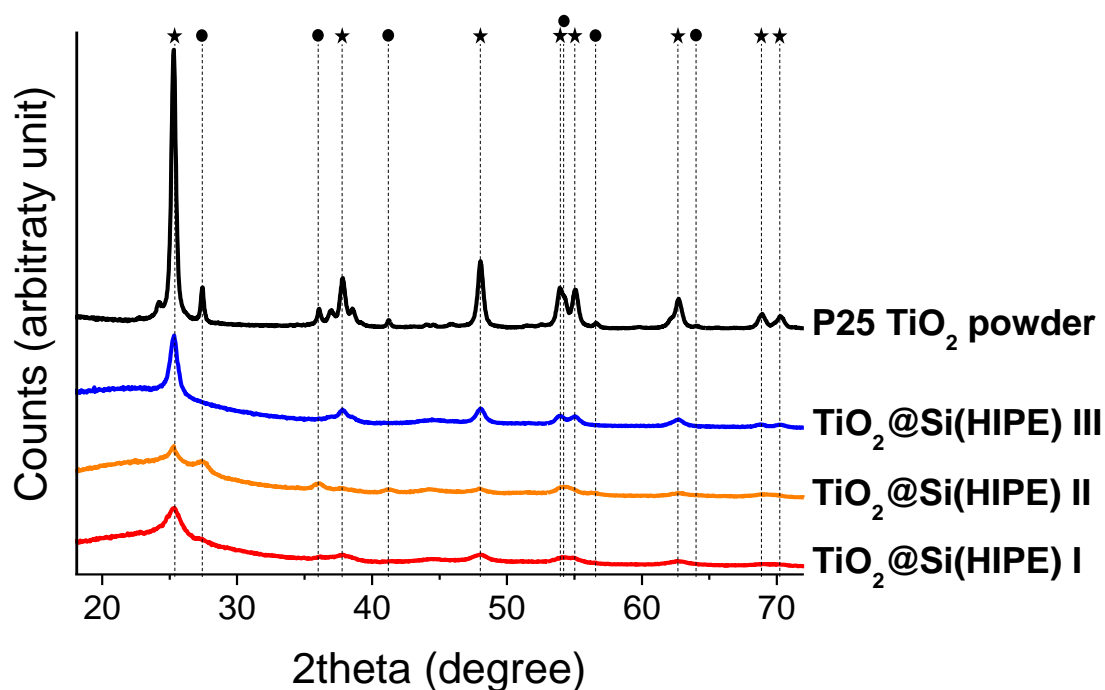


Figure A 25: XRD patterns of the tested photocatalytic materials; depicting a mixture of anatase (★) and rutile (●) crystalline phases for TiO₂@Si(HIPE) II and P25 TiO₂, whereas monoliths TiO₂@Si(HIPE) I and III provide only the anatase crystalline phase

Table A 38: Mercury intrusion porosimetry data [a] value calculated from bed and TiO₂ densities, [b] value measured from the mass and volume of tested materials, and [c] value calculated from cubic close packing approximation considering bed density and average particles size of TiO₂ P25 of 21 nm

Materials	TiO ₂ @Si(HIPE)			P25 TiO ₂
	I	II	III	Powder
Intrusion volume (mL.g ⁻¹)	6.31	6.23	6.47	-
Porosity (%)	74	71	79	92 ^[a]
Bed density (g.mL ⁻¹)	0.12	0.12	0.12	-
Bed density (g.mL ⁻¹) ^[b]	0.115	0.137	0.125	0.321
Median pore aperture (nm)	2366	2052	2595	43 ^[c]

Table A 39: Nitrogen physisorption data and TiO₂ Specific Surface Area (SSA) contribution, calculated as described in §2.2.a

Materials	TiO ₂ @Si(HIPE)			P25 TiO ₂
	I	II	III	Powder
BET surface (m ² .g ⁻¹)	459	259	350	52
Microporous volume (mL.g ⁻¹)	0.189	0.106	0.146	-
TiO ₂ SSA contribution	0.037	0.027	0.033	1

Table A 40: Photocatalytic tests results for each considered sample. When the sum of selectivities does not reach 100%, this indicates traces of C_3 products

Sample	h (mm)	m_{catalyst} (g)	m_{TiO_2} (g)	TiO_2 loading (kg.m ⁻²)	r_{e-} (mol.s ⁻¹)	r_{e-} ($\mu\text{mol.h}^{-1}.\text{m}^{-2}$)	r_{e-} ($\mu\text{mol.h}^{-1}.\text{g}_{\text{TiO}_2}^{-1}$)	Selectivities (%)			
								H ₂	CO	CH ₄	C ₂ H ₆
P25 TiO ₂ powder	0.21	0.04	0.04	0.07	3.29E-11	223	3.31	29	12	48	10
	0.36	0.06	0.06	0.12	4.62E-11	313	2.71	53	3	30	12
	0.65	0.11	0.11	0.21	2.97E-11	202	0.97	48	11	30	11
	1.00	0.17	0.17	0.32	1.37E-11	93	0.29	46	40	8	4
TiO ₂ @Si(HIPE) monolith I	2.0	0.18	0.06	0.07	1.56E-10	697	9.47	0	0	90	10
	2.7	0.25	0.08	0.10	2.35E-10	1050	10.57	4	1	86	7
	3.0	0.28	0.09	0.11	2.53E-10	1134	10.27	0	0	78	22
	4.0	0.37	0.12	0.15	3.16E-10	1416	9.62	1	1	85	13
monolith II	3.0	0.33	0.10	0.12	3.46E-11	155	1.30	8	0	85	11
	4.0	0.44	0.13	0.16	4.09E-11	183	1.15	16	0	76	7
	5.0	0.55	0.16	0.20	5.23E-11	234	1.18	18	0	77	4
	6.0	0.66	0.19	0.24	6.34E-11	284	1.19	16	8	70	6
	7.0	0.77	0.22	0.28	5.18E-11	232	0.83	7	8	80	5
	8.0	0.88	0.26	0.32	4.47E-11	200	0.63	7	8	71	12
	9.0	0.99	0.29	0.36	4.41E-11	197	0.55	15	8	68	8
monolith III	3.0	0.30	0.06	0.08	3.04E-11	136	1.73	8	21	71	0
	4.0	0.40	0.08	0.11	3.62E-11	162	1.55	9	18	73	0
	6.0	0.60	0.13	0.16	5.27E-11	236	1.50	4	5	87	4
	7.0	0.70	0.15	0.18	4.82E-11	216	1.17	3	10	78	9

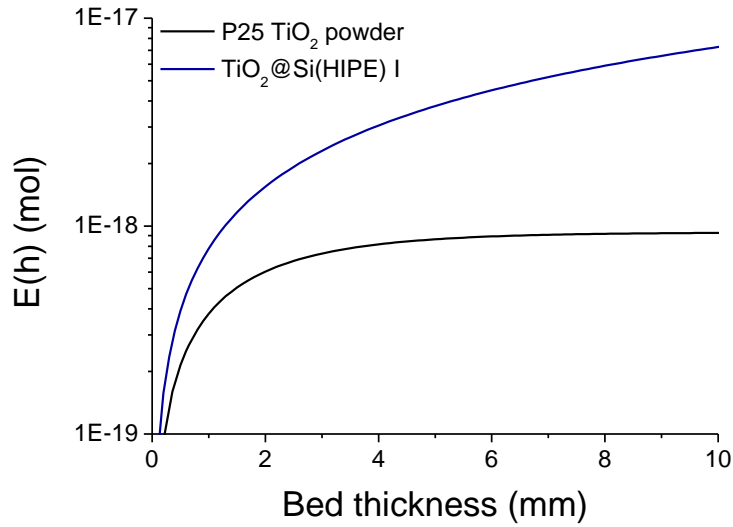


Figure A 26: Profiles of 315-400 nm photon quantity (mol) as a function of bed thickness extracted from α value related to the kinetic model for bed powder and TiO₂@Si(HIPE). Only TiO₂@Si(HIPE) I is represented for the sake of clarity, as their α values are closed compared to powder bed.

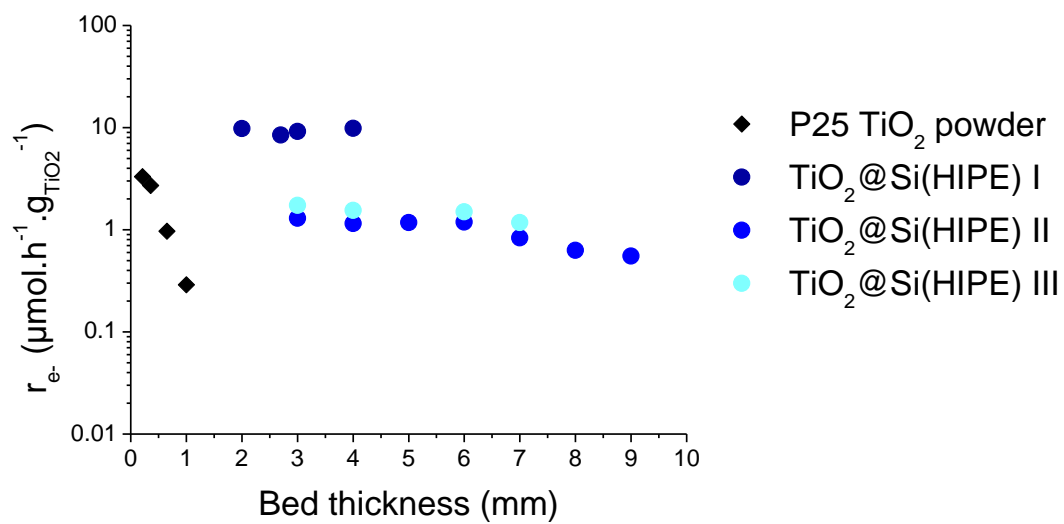


Figure A 27: Global activity per mass of TiO_2 as a function of bed thickness for TiO_2 powder bed and $\text{TiO}_2@Si(\text{HIPE})$ s.

Table A 41: Useful value summary for k_0 calculating of materials from the ε -TiO₂@Si(HIPE) series, where ε is the oil volume fraction

ε	0.6	0.64	0.67
TiO₂ content (%wt)	43	24	45
Crystallite size (nm)	15.8	20.6	13.1
TiO₂ SSA (m².g⁻¹)	40.5	18.3	54.4
S_{BET} (m².g⁻¹)	420	415	397
Median pore size diameter (nm)	1669	1655	1730
m_{TiO2} (g)	0.1223	0.1224	0.2646
h (mm)	2.9	5.1	4.5
S_{irr} (cm²)	7.0	9.8	8.6
α (m⁻¹)	45.4	46.3	41.4
Porosity (%)	92	89	93
v (m.s⁻¹) (*E+08)	2.89	2.87	2.90
D_{TiO2}	0.10	0.08	0.12
E(h) (mol) (*E-18)	1.72	4.08	3.17
C_{irr} (mol) (*E-04)	1.46	1.07	3.72
K (mol⁴) (*E-69)	0.478	1.04	0.262
r_e (mol.h⁻¹) (*E-08)	5.77	17.3	4.13
k₀ (mol⁻¹.h⁻¹) (*E+14)	2.34	5.03	0.485

Table A 42: Useful value summary for k_0 calculating of materials from the T-TiO₂@Si(HIPE) series, where T is SiO₂ calcination temperature (°C)

T	650	750	850
TiO₂ content (%wt)	24	34	36
Crystallite size (nm)	20.6	18.5	15.4
TiO₂ SSA (m².g⁻¹)	18.3	28.4	35.5
S_{BET} (m².g⁻¹)	415	360	117
Median pore size diameter (nm)	1655	1080	1009
m_{TiO₂} (g)	0.1224	0.1078	0.1385
h (mm)	5.1	2.6	3.3
S_{irr} (cm²)	9.84	8.55	7.35
α (m⁻¹)	46.3	110	122
Porosity (%)	89	88	87
v (m.s⁻¹) (*E+08)	2.87	2.85	2.83
D_{TiO₂}	0.078	0.087	0.105
E(h) (mol) (*E-18)	4.08	1.78	1.82
C_{irr} (mol) (*E-04)	1.07	1.02	1.50
K (mol⁴) (*E-69)	1.04	0.621	0.022
r_e (mol.h⁻¹) (*E-08)	17.2	12.7	4.84
k₀ (mol⁻¹.h⁻¹) (*E+14)	5.03	7.12	2.64

Table A 43: Useful value summary for k_0 calculating of materials from the $v\text{-TiO}_2\text{@Si(HIPE)}$ series, where v is the rotation speed (rpm)

v	150	200	250
TiO₂ content (%wt)	24	50	20
Crystallite size (nm)	21.3	11.4	20
TiO₂ SSA (m².g⁻¹)	16.9	39.6	15.5
S_{BET} (m².g⁻¹)	596	546	655
Median pore size diameter (nm)	3038	881	269
m_{TiO₂} (g)	0.0628	0.1200	0.0601
h (mm)	2.7	3.7	5.9
S_{irr} (cm²)	7.55	6.79	6.61
α (m⁻¹)	5.8	148	370
Porosity (%)	37	85	92
v (m.s⁻¹) (*E+08)	2.27	2.82	2.91
D_{TiO₂}	0.076	0.141	0.081
E(h) (mol) (*E-18)	2.33	1.81	1.43
C_{irr} (mol) (*E-04)	0.589	1.63	0.246
K (mol⁴) (*E-69)	1.31	0.682	1.41
r_e (mol.h⁻¹) (*E-08)	5.35	4.99	5.87
k₀ (mol⁻¹.h⁻¹) (*E+14)	3.98	1.72	16.8

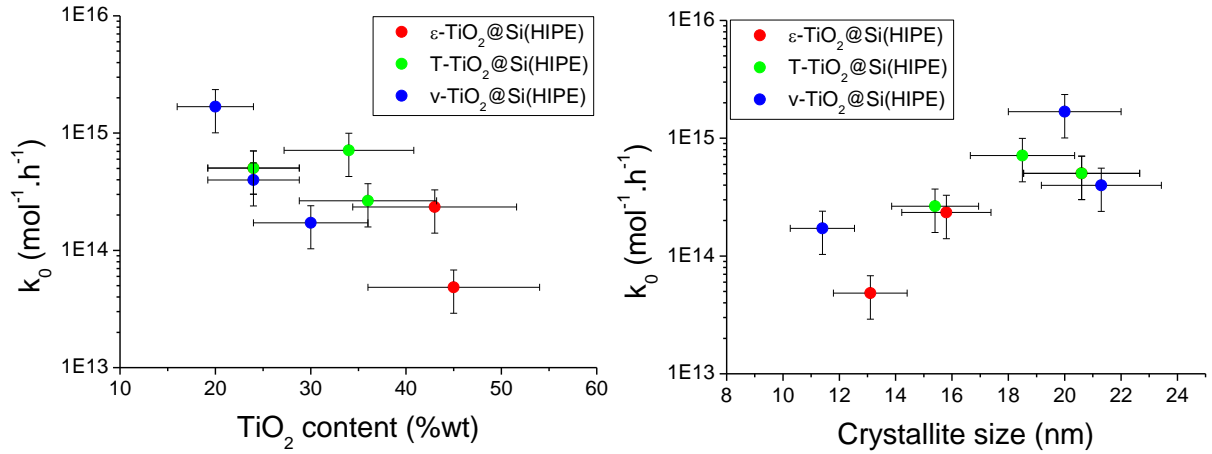


Figure A 28: k_0 values for (ϵ -, T -, and v -)TiO₂@Si(HIPE) series as a function of TiO₂ content (**left**) and crystallite size (**right**)

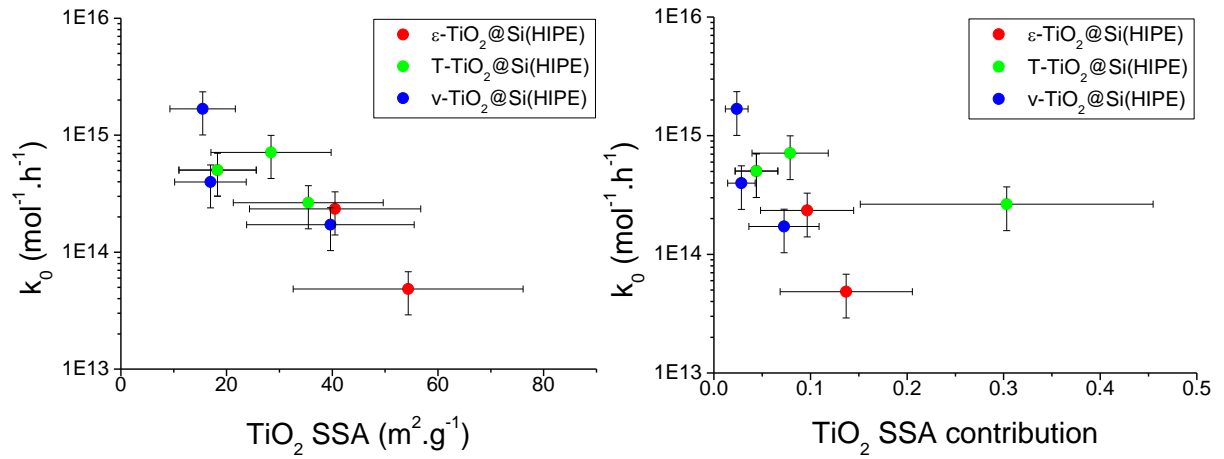


Figure A 29: k_0 values for (ϵ -, T -, and v -)TiO₂@Si(HIPE) series as a function of TiO₂ SSA (**left**) and TiO₂ SSA contribution (**right**)

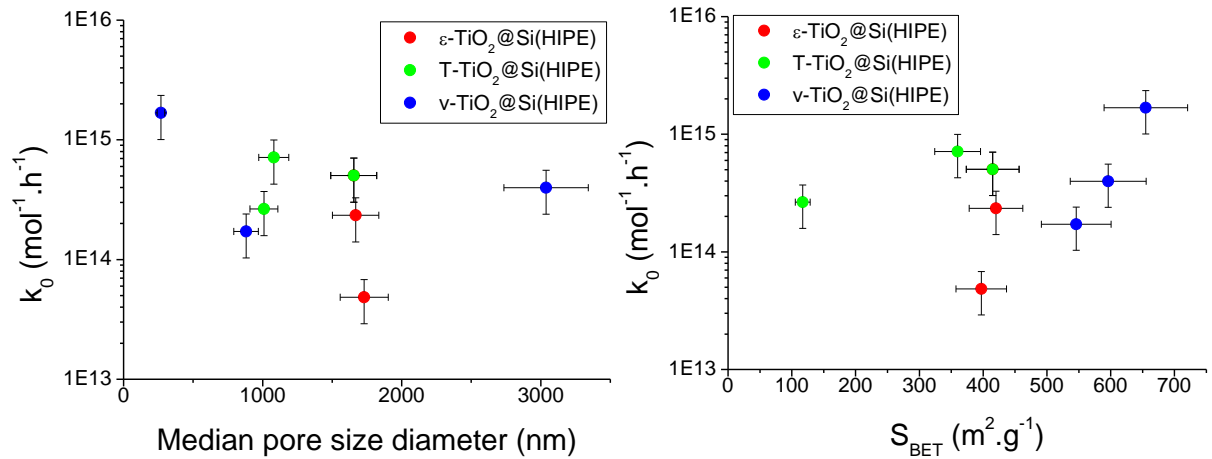


Figure A 30: k_0 values for (ϵ -, T -, and v -)TiO₂@Si(HIPE) series as a function of median pore size diameter (**left**) and BET surface area (**right**)

Titre : Conversion photocatalytique du CO₂ sur monolithes poreux

Résumé : Dans le contexte actuel de développement de nouvelles sources d'énergie non fossiles tout en minimisant l'impact environnemental, la production de carburants solaires par la valorisation des émissions anthropiques de CO₂ apparaît comme une solution à fort potentiel. Le principal défi dans les processus artificiels photo-induits concerne le caractère bidimensionnel des systèmes utilisés, en raison de la faible profondeur de pénétration des photons. Ce travail de thèse se concentre sur le développement de mousses solides alvéolaires, issues de la chimie intégrative, présentant une porosité hiérarchiquement organisée. A travers l'imprégnation de précurseurs de TiO₂, des photocatalyseurs autosupportés ont été synthétisés et ont montré une augmentation de la pénétration des photons d'un ordre de grandeur. D'autre part, ces solides limitent les réactions inverses par un effet de dilution, tout en assurant une sélectivité élevée envers la génération d'alcane. Un modèle cinétique, basé sur un formalisme mixte de Langmuir-Hinshelwood et Eley-Rideal, est proposé pour décrire le comportement des matériaux.

Mots clés : Photocatalyse, Carburants solaires, Monolithes poreux, Modèle cinétique, Chimie intégrative, Catalyse hétérogène

Title: CO₂ photocatalytic conversion through porous monoliths

Abstract: In the current context of developing novel non-fossil energy sources while minimizing the environmental impact, solar-driven-fuel-production by exploiting anthropogenic CO₂ emissions appears to be a solution with great potential. The main challenge in artificial photo-induced processes concerns the two-dimensional character of the systems used, due to the low photon penetration depth. This thesis work focuses on the development of alveolar solid foams, derived from integrative chemistry and bearing a hierarchically organized porosity. By TiO₂ precursor impregnation, self-standing photocatalysts were synthesized and provided a photon penetration increase by an order of magnitude. Moreover, these solids limit back-reactions by a dilution effect, while ensuring high selectivity towards alkane generations. A kinetic model, based on a mixed formalism of Langmuir-Hinshelwood and Eley-Rideal, is proposed to describe material behavior.

Keywords: Photocatalysis, Solar fuels, Porous monoliths, Kinetic model, Integrative chemistry, Heterogeneous catalysis

Unités de recherche

Centre de Recherche Paul Pascal (CRPP), CNRS – UMR 5031
115, avenue du Docteur Albert Schweitzer, 33600 Pessac

IFP Energies Nouvelles
Rond-point de l'échangeur de Solaize, 69360 Solaize